Investigation of Multiphase Flow in Porous Micromodels using Micro-PIV Experiments and Numerical Simulations

Thesis submitted in fulfilment of the

requirements for the degree of

DOCTOR OF PHILOSOPHY

by

Vikas Kumar Sharma

Roll No. (176107010)

Under the supervision of

Prof. Anugrah Singh

Dr. Pankaj Tiwari

Department of Chemical Engineering

Indian Institute of Technology Guwahati

Guwahati -781039

May 2023

Investigation of Multiphase Flow in Porous Micromodels using Micro-PIV Experiments and Numerical Simulations

Vikas Kumar Sharma

Department of Chemical Engineering
Indian Institute of Technology
Guwahati- 781039

STATEMENT

I do hereby declare that the content embodied in this thesis entitled "**Investigation of Multiphase Flow in Porous Micromodels using Micro-PIV Experiments and Numerical Simulations**" is the result of investigations carried out by me at the Department of Chemical Engineering, Indian Institute of Technology Guwahati, Guwahati, India, under the supervision of Prof. Anugrah Singh and Dr. Pankaj Tiwari. In keeping with the general practice of reporting scientific observations, due acknowledgements have been made wherever the work described is based on the findings of other investigators.

Date: 12-05-2023

Vikas Kumar Sharma

Department of Chemical Engineering
Indian Institute of Technology
Guwahati- 781039

CERTIFICATE

This is to certify that the thesis entitled **"Investigation of Multiphase Flow in Porous Micromodels using Micro-PIV Experiments and Numerical Simulations"** submitted by **Mr. Vikas Kumar Sharma (Roll No.: 176107010)** for the award of the degree of Doctor of Philosophy has been carried out under our guidance and supervision. The work documented in this thesis has not been submitted to any other University or Institute for the award of any degree.

Date: 12-05-2023

Dr. Anugrah Singh
Professor
Department of chemical engineering
Indian Institute of Technology Guwahati
Guwahati 781039, India

Dr. Pankaj Tiwari
Associate Professor
Department of Chemical Engineering
Indian Institute of Technology Guwahati
Guwahati 781039, India

Dedicated to my loved father and mother

Acknowledgments

I would like to express my gratitude to all those who helped me in different ways to complete this research work. First and foremost, I would like to express my deepest gratitude to my supervisors Prof. Anugrah Singh and Dr. Pankaj Tiwari, for their continuous support and guidance throughout the entire course of my work. Their uncompromising approach for completing experimental and numerical work, data analysis, and preparing manuscripts has helped me to achieve my research objectives. I am grateful for their valuable suggestions and constant encouragement, without which I could not complete this research work.

I would like to thank my doctoral committee: Dr. Raghvendra Gupta, Dr. R. Anandalakshmi from the Department of Chemical Engineering, and Dr. Suresh A. Kartha from the Department of Civil Engineering at the Indian Institute of Technology Guwahati for their valuable comments and suggestions towards the improvement of my research work.

I am also thankful to the analytical lab staff and teaching assistants in the Department of Chemical Engineering for their cooperation in the analytical laboratory. I would like to thank the Central Instrument Facility of the Indian Institute of Technology for allowing me to carryout Micro-PIV, NMR, FETEM, FESEM, and XRD analysis which are crucial in this research. In this regard, I would like to acknowledge the members of CIF for their assistance. I would like to acknowledge support from the DST-FIST Grant (SR/FST/ETII-071/2016) for PIV facilities.

I would like to express my heartiest thanks to my past and present lab members of the Flow Visualization Lab (Dr. Ajeeth Prabhu, Dr. Bhasker Medhi, Dr. Nazrul Haque, Mr. Deepak Mishra, Mr. Rupak Bhowmik, Mr. Indrajeet Kumar, Mr. Bineet Kumar, Ms. Shivangi Tripathi, Mr. Pervez Alam, Ms. Smita Gupta). I would also like to thank Dr. Rahul Saha, Dr. Bhargav Baruah, and all the labmates from the Energy Conversion Technology Lab (ECTL). Last but

not the least, I would like to express my deepest gratitude to my parents and family members for their continuous support and motivation throughout the journey of my life. Their love, courage, and sacrifice have made it possible for me to come so far.

Abstract

Multiphase flow through a porous medium has several applications in science and engineering, including enhanced oil recovery (EOR), CO_2 capture and storage, subsurface hydrology, gas hydrates, geothermal energy extraction, and hydraulic fracturing, to name a few. Enhanced oil recovery is the subject of interest in the current research work. Primary and secondary recovery processes result in the recovery of only one-third of oil from the reservoir rock, leaving a significant portion of oil trapped in the small constrictions such as dead-ends, pore-throats, and contraction expansion regions. It has been investigated that the parameters, including interfacial tension, wettability, in-situ emulsification, aspect ratio, and flow rate, affect the trapping and mobilization of oil through the porous medium. The entire work in the thesis has been divided into five different sections as effects of various chemicals (low salinity water, polymer, alkali-polymer, and alkali-surfactant-polymer solution); effect of silica nanofluid; effect of flow rate, viscosity, and heterogeneity; parameters affecting oil recovery from complex geometries; effect of particle migration and trapping on oil recovery at the pore scale. Two-phase flow has been studied using micro-particle image velocimetry and fluorescence microscopy in porous micromodels fabricated using soft lithography. The pore-scale flow dynamics and displacement processes during two-phase flow are investigated and visualized to optimize different flooding processes for oil recovery.

Silica nanoparticles in an alkaline solution significantly enhanced the mobilization of trapped oil in the porous medium. The pore-scale flow dynamics during alkaline flooding and nanofluid injection are not completely understood. Silica nanoparticles reduce the interfacial tension between crude oil and nanofluid to ultra-low value (0.01 mN/m) and contact angle up to 22° (extremely water wet condition). The pore-scale flow field is obtained to understand the flow pattern, desirable (piston-like displacement), and undesirable pore-scale events (viscous

fingering) during crude oil and nanofluid interaction within the porous medium. During drainage experiments with an alkaline solution, viscous fingering is observed. As crude oil interacts with the silica nanofluid during the imbibition experiment, a stable micro-emulsion is formed in the porous medium, resulting in a regular piston-like displacement.

The effect of displacing phase viscosity and flow rate on the trapped fluid displacement has been investigated using heterogeneous and homogeneous micromodels. The phenomena of shear-induced circulations and viscous instability are observed during the displacement of the trapped non-wetting phase through the porous domain. Breakage and coalescence of the droplets of the non-wetting phase were also observed during the displacement process. The velocity vector maps show frequent flow reversal of ganglia, leading to an unsteady flow behavior. It is observed that an increase in the flow rate reduces the trapped non-wetting fluid saturation in the porous medium by disintegrating large ganglia into small droplets. Increasing either the flow rate or viscosity increases the shear stress at the interface of the trapped ganglion and displacing phase, leading to shear-induced circulations, and the strength of the vortex is found to increase. These circulations inhibit further displacement of the trapped fluids. It is observed that a heterogeneous micromodel causes significant trapping and lesser mobilization of the non-wetting phase compared to a homogeneous one.

Dead-end pores contribute to 34-51 % of the pore volume of the reservoir rocks and cause significant trapping of oil in the porous medium. Hence, numerical simulations of immiscible two-phase flow are performed at pore-scale for complex pores such as dead-ends and contraction expansion to understand the displacement mechanisms and parameters affecting the oil recovery. The effect of displacing phase injection velocity, viscosity ratio, interfacial tension, wettability alteration, the viscosity of trapped oil, and geometric ratio on the trapped oil recovery has been investigated. The results show that decreasing the contact angles has a

marginal effect on the recovery of trapped fluid until a critical contact angle is reached. The complete displacement of trapped oil is observed when the oil-water interface reaches the bottom of the dead-end before it reaches the rupture point at the junction of the pore-throat channel and dead-end. Increasing the displacing phase injection velocity significantly increases the oil recovery from the dead-end pores. On the other hand, decreasing the injection velocity increases the oil recovery from the contraction expansion pore.

Microscopic studies of low salinity water flooding followed by chemical floodings are performed in a 2D porous micromodel to visualize and quantify the displacement process and the oil recovery. The phenomena such as fluctuating flow, flow direction reversal, viscous fingering, film formation around cylinders, unsteady flow behavior, and sudden velocity jumps are observed during low salinity water flooding. Polymer flooding results in no significant change in the trapped oil configuration. Alkali-polymer solution injection improves oil recovery as it interacts with crude oil, which results in higher in-situ emulsification, interfacial tension reduction, and change in the contact angle to extremely water-wet conditions. Core flooding experiments are performed to understand the recovery potential of different flooding processes in simultaneous and separate injection modes. The core flooding (macro-scale) results showed that the overall heavy oil recovery is 75.37% by simultaneous injection of chemical slugs; however, a separate injection of individual chemical slugs yields lower oil recovery in the case of alkali-surfactant-polymer flooding.

During oil production, particles disintegrated from the unconsolidated rocks, flow through the porous medium, and cause permeability impairment. Therefore the knowledge of suspension flow behaviour through the porous medium is essential. The porous micromodels of homogeneous, heterogeneous, and fractured geometry are used to visualize the suspension flow. Single particle flow dynamics is investigated, which shows that the initial location of the

mobile particle strongly influences the particle trajectories. When the particle is flowing close to the grain, the particle retention time significantly increases because of the highly tortuous path. The effect of particle concentration within the suspension showed that the highly concentrated (20%) suspension flow causes severe cluster formation and collision, resulting in a positive drift in the velocity magnitude along the flow direction. Shear-induced particle migration is observed in the fractured porous medium because the particles experience high shear at the cylinder wall resulting in particle movement towards the center of the fractures where the shear is small. The phenomena of pore bridging, trapping, and shear-induced particle migration are observed during multiphase flow in the heterogeneous porous medium. This study will help understand the fluid flow behavior through an unconsolidated porous medium.

This thesis develops an understanding of suspension flow behavior, different pore-scale phenomena, displacement mechanisms, and parameters affecting trapped oil recovery during different chemical floodings such as low salinity water, alkali, polymer, alkali-polymer, alkali-surfactant-polymer, and silica nanoparticle assisted alkaline solution both at micro and macro scale to optimize the oil recovery.

Table of Contents

List of Tables

Chapter 2

Chapter 3

Chapter 4

Chapter 5

Chapter 6

Chapter 7

List of Figures

Chapter 1

Chapter 2

Chapter 3

Chapter 4

Chapter 5

Chapter 6

Chapter 7

Abbreviations

Abbreviations	Name
AP	Alkali-Polymer
API	American petroleum institute
ASP	Alkali-surfactant-polymer
CBM	Coalbed Methane
CCD	Charged coupled device
CCS	Carbon capture and storage
CMOS	Complementary metal oxide semiconductor
DEM	Discrete element method
DIW	Deionized water
DNS	Direct numerical simulations
EOR	Enhanced oil recovery
FESEM	Field emission transmission electron microscope.
FETEM	Field emission scanning electron microscope
FPS	Frames per second
HPAM	Hydrolyzed polyacrylamide
I.A.	Interrogation area
IFT	Interfacial tension
IMB	Immersed moving boundary
LBM	Lattice Boltzmann method

LDV	Laser Doppler velocimetry
LED	Light emitting diode
LSM	Level set method
LSW	Low salinity water
Micro-PIV	Micro-Particle image velocimetry
MRI	Magnetic resonance imaging
NAPL	Non-aqueous phase liquid
NOA	Norland optical adhesive
NMR	Nuclear magnetic resonance
OOIP	Original oil in place
PDMS	Polydimethylsiloxane
PFM	Phase field method
PIV	Particle image velocimetry
PMMA	Polymethylmethacrylate
PNM	Pore network modeling
PTV	Particle tracking velocimetry
PV	Pore volume
RF	Recovery factor
RIM	Refractive index matching
ROI	Region of interest
SDS	Sodium dodecyl sulfate
SEM	Scanning electron microscopy
SNF	Silica nanofluids
SW	Saline water

TFPM	Tree-shaped fractured porous medium
VOF	Volume of Fluid
μ-CT	Micro-computed tomography

Symbols

Symbols	Name
φ	Phase field parameter
Δx	Displacement
U	Fluid velocity
γ	Mobility
λ	Mixing energy density
ε	Oil-water interface thickness
χ	Mobility parameter
h_c	Maximum grid size
V_{fw}	Volume fraction of water
V_{fo}	Volume fraction of oil
ρ_p	Particle density
ρ_w	Density of water
ρ_o	Density of oil
μ_w	Viscosity of water
μ_o	Viscosity of oil
ρ	Density of the mixture/ Fluid density
μ	Viscosity of the mixture / Fluid viscosity
F_{st}	Surface tension
F	Volume force factor
P	Pressure
G	Chemical potential

ψ	Phase field help variable
P_c	Capillary pressure
θ	Contact angle
σ	Interfacial tension
L	Length
W	Width
H	Height
φ	Porosity
d_p	Bead diameter / Particle diameter
Q	Flow rate
C	Particle concentration in suspension
D	Distance from the center line
U	Velocity magnitude
T	Absolute temperature of fluid
Δt	Time delay between the images
ω_z	Vorticity
γ	Shear rate
N	Normal to the interface
K	Curvature of the interface
V_S	Particle settling velocity
ε_B	Error due to Brownian motion
δ_Γ	Dirac delta function

Chapter 1. Introduction and Literature Review

Introduction;

Micromodel fabrication;

Flow visualization techniques;

Pore-scale phenomena;

Parameters affecting trapping and mobilization;

Literature on two-phase flow through the porous medium;

Objectives;

Thesis organization

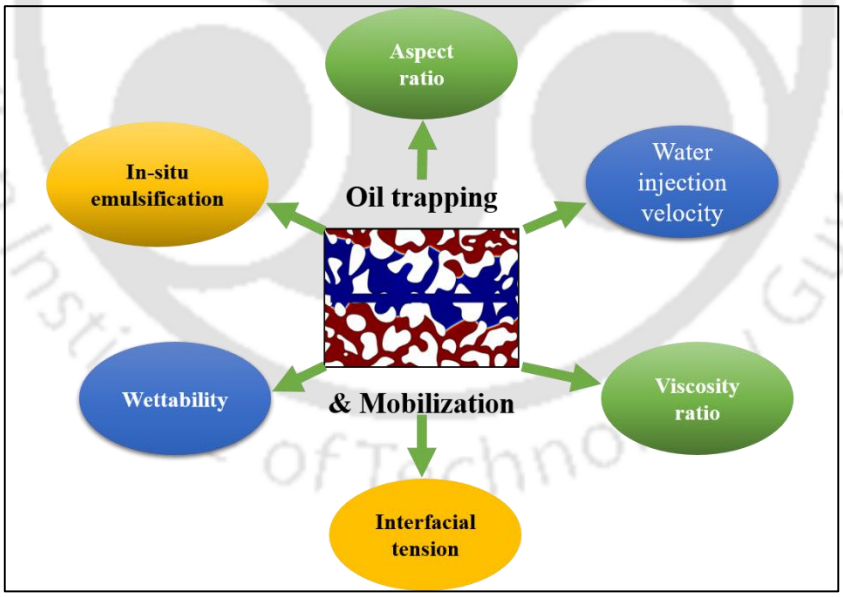

1.1 Introduction

The application of fluid flow through porous media is common in various science and engineering fields. These applications include enhanced oil recovery, carbon capture, and storage (Ge et al., 2022), gas production from the hydrate-bearing formation (Jung et al., 2012), non-aqueous phase liquid (NAPL) contamination of groundwater or groundwater remediation (Muecke, 1979), geothermal energy production (You et al., 2015), and hydraulic fracturing for shale gas recovery (Song et al., 2014), to name a few. Knowledge of two-phase or multiphase flow through the porous medium is crucial in the above fields. The present work is more aligned toward enhanced oil recovery. Understanding flow behavior through the porous media is not yet fully developed. It is critical to understand the displacement process at micro and macro scales within a porous media to optimize the enhanced oil recovery (EOR) process. The pore-scale displacement mechanisms, fluid-fluid, and fluid-solid interactions are challenging to visualize in the reservoir rocks because of their opaque nature. Microfluidics plays a crucial role in fabricating porous micromodels, replicating the real reservoir rocks. Micromodels with different geometries (including homogeneous, heterogeneous, and fractured) have been fabricated to visualize pore-scale flow dynamics and quantify two-phase flow. Optical methods such as micro-particle tracking velocimetry (micro-PTV) (Zarikos et al., 2018), particle image velocimetry (PIV), and micro-particle image velocimetry (micro-PIV) have been used over the years to visualize and quantify the flow in 2D porous micromodels (de Winter et al., 2020; Ekanem et al., 2020). The micro-particle image velocimetry (μ-PIV) is an accurate and well-established optical technique for quantifying microscopic flows with a good spatial resolution (Breuer, 2005; Mielnik and Saetran, 2004; Song et al., 2019).

During secondary and tertiary recovery processes, a significant amount of oil is trapped within the small pore throats and dead-ends in the form of droplets, blobs, and ganglia. The mobilization of trapped crude oil depends on several parameters, including displacing fluid

flow rate and viscosity (Heshmati and Piri, 2018), capillary number (Zarikos et al., 2018), trapping number (Oughanem et al., 2015), aspect ratio, size of ganglion (Oughanem et al., 2015), interfacial tension (Saha et al., 2018b), in situ emulsification (Liu et al., 2019b), and wettability alteration (Maghzi et al., 2011). The displacement of trapped crude oil from the porous media requires viscous forces to overcome the capillary forces to produce crude oil (Hilfer and Øren, 1996; Zhang et al., 2011). Various desirable and undesirable pore-scale phenomena occur during two-phase flow through the porous medium. The phenomena include Haines Jump (Edery et al., 2018), snap-off (Follesø, 2012), shear-induced circulations (Sharma et al., 2022; Zarikos et al., 2018), ganglia breakage and coalescence (Datta et al., 2014a; Datta et al., 2014b; Krummel et al., 2013), fluctuating flow during imbibition, in-situ emulsification (Broens and Unsal, 2018; Unsal et al., 2016), and co-current and counter-current spontaneous imbibition in the fractured porous medium (Jafari and Rokhforouz, 2020; Zhu et al., 2021a), film formation, capillary fingering, viscous fingering (Zhang et al., 2011), and viscous coupling (Roman et al., 2020). These phenomena are discussed in detail in section 1.4.

Particle migration during fluid flow through the pores causes permeability impairment. Research areas such as produced water reinjection in the reservoir (Xia et al., 2022), nanofluids injection for enhanced oil recovery (Hendraningrat et al., 2013), and sand control during flow through unconsolidated formation all require the knowledge of suspension flow through the porous medium. Hence, the transport of suspended particles through a porous medium is the subject of investigation in various experimental and simulation studies (De and Singh, 2021; Yousif et al., 2017; Zhou et al., 2018). The particle migration in the porous medium causes the trapping of fine particles in tiny pore throats, resulting in pore clogging, permeability impairment, and productivity decline (Feia et al., 2015; Jung et al., 2018; Liu et al., 2019a; Xia et al., 2022; Zhou et al., 2018). The primary factors influencing the mobilization and trapping

of the particles within the porous medium include the hydrodynamic and adhesive forces, salinity, temperature, pH, flow rate, and nanoscale heterogeneity (Yang et al., 2022). Bridging and clogging in the porous medium depends on the pore throat to particle size ratio, particle concentration, and flow rate (Jung et al., 2018). The models such as the Lattice Boltzmann Method (LBM), Discrete Element Method (DEM), and Immersed Moving Boundary (IMB) have been coupled to investigate the suspension flow through the porous medium (Zhou et al., 2018).

Several numerical simulation techniques have been utilized to investigate the two-phase flow in the porous medium. These techniques include Pore Network Modeling (PNM), the Lattice Boltzmann method (LBM), and the Direct Numerical Simulations (DNS) method. The direct Numerical Simulations (DNS) method is a reliable approach to handle complex pore geometries by solving the Navier–Stokes equations using finite difference, finite element, and finite volume methods**.** The most popular interface-capturing methods include the Volume of Fluid (VOF), Level-Set, and phase-field methods. Phase field method can conserve the mass, is computationally less expansive and it can handle complex geometries efficiently. Several parameters, such as wettability, rock heterogeneity, viscosity ratio, interfacial tension, capillary number, injection velocity, and fractures, affect the oil recovery factor through the porous medium. When the system is oil-wet, a significant amount of oil remains trapped in the porous medium. However, the water invades even tiny pores at lower contact angle and improve sweep efficiency. Maintaining a proper viscosity ratio eliminates the viscous fingering and improves the oil recovery. Displacing phase injection velocity affects the residual oil recovery from the porous medium. Oil recovery is low at a higher displacing phase injection velocity because of smaller breakthrough time. In the forthcoming sections, all the points raised in this section are thoroughly discussed.

1.2 Micromodel fabrication

One of the initial porous micromodel was developed in 1952 to visualize pore-scale fluid behavior (Chatenever and Calhoun, 1952). A porous micromodel can be defined as "An artificial 2D replica of the porous medium (a network of interconnected pores, measuring in tens of microns) made up of transparent material, through which the movement of colloids and multiphase flow can be visualized" (Karadimitriou and Hassanizadeh, 2012). The micro model has an inlet, outlet, and flow network with feature size at the microscale with an overall dimension of a few centimeters. Microfluidics serves as a vital tool for acquiring insights into diverse pore scale flow mechanisms, including wettability alteration (Gong et al., 2016), and enhancing understanding of oil recovery by visualizing multiphase flow in 2D or 3D porous micromodels (Gunda et al., 2011; Jahanbakhsh et al., 2020; Karadimitriou and Hassanizadeh, 2012; Lake et al., 2015; Yun et al., 2017).

These micromodels are fabricated either using Polydimethylsiloxane (PDMS), Polymethylmethacrylate (PMMA), glass, or silicon wafer. The advantage of using PDMS is that it is cheap, optically transparent and no capital-intensive equipment and clean room facility are required for micromodel fabrication. PDMS micromodels can be fabricated using Soft lithography technique, which is a rapid, and low cost process of micromodel fabrication. PDMS is a relatively inert material with good chemical resistance but its compatibility with organic solvents depends on duration of exposure and temperature conditions. In general, PDMS is compatible with organic solvents, including alcohols and hydrocarbons. However, it may not be compatible with solvents that are highly polar and have strongly acidic and basic properties.

The limitation of this polymeric material is that it has mixed wettability and compatible with temperatures upto 200-250℃. When exposed to high differential pressures, PDMS can undergo

deformation or rupture. If the differential pressure exceeds 4 bars, which is relatively high pressure, PDMS can undergo significant deformation or even rupture.

Numerous methods have been developed to date for micromodel fabrication. These methods include photolithography, soft lithography, 3D printing (Dimou et al., 2021), laser micromachining (Mohammadi et al., 2020b), and wet and dry etching, to name a few. Literature shows micromodels fabricated using glass with active clay minerals (montmorillonite) deposited at the surface to study the effect of low salinity at the pore scale (Bartels et al., 2017).

1.2.1 Micromodel fabrication using soft-lithography process

A micro model is commonly composed of two slabs. One slab contains the pore network, and the other slab, which is featureless, is used as a cover to create a closed network of pores. The flow network and the inlet and outlet areas are designed for micromodel fabrication using Delaunay triangulation. The design is transferred to a mask. Further, the design is transferred from the mask to the silicone wafer using photolithography. It is a technique in which an ultraviolet light source is used to transfer a pattern onto the silicone substrate or glass (Ziaie et al., 2010). The wafer after photolithography is termed a master with printed features used during the soft lithography process for micromodel fabrication. A soft lithography is a low-cost approach to rapid prototyping of both micro and nanoscale devices using soft substrates (polymers, gels, or organic monolayers) without capital-intensive equipment (Qin et al., 2010). A silicon elastomer base (Dow Corning Slygard 184) is mixed with an elastomer curing agent at a mass ratio of 10:1 for a few minutes. The mixture is full of trapped air bubbles after the mixing process. Hence the cup with the mixture is put into a vacuum chamber to remove the trapped air. The cup's content is poured over the master silicon wafer in a Petri dish, with the design of the micro model pointing upward. A layer of PDMS is poured into another Petri dish to form a plain slab without any features. This PDMS slab is used as the sealing layer of the micromodel. The two petri dishes are put in the vacuum chamber to remove any trapped air.

After degassing, the two petri dishes are put in an oven at 68℃ for at least 2 hr to cure and solidify liquid PDMS. The PDMS slabs are allowed to reach ambient temperature after curing. The PDMS slab needs to be separated from the silicon wafer so that it will not destroy the wafer's features. The wafer is gently separated from PDMS. The inlet and outlet holes are punched at the flanks of the cured polymer layer for fluid entry and exit, respectively. The two PDMS slabs had to be put together and bonded. The plain PDMS slab is placed so that its surface that was in contact with the Petri dish would form the inner side of the micromodel. The bonding techniques, such as oxygen plasma and corona discharge can be used to bond the two slabs (Ziaie et al., 2010). In order to make the micromodel more rigid, using the same bonding procedure, a microscope glass slide is bonded to the side of the micro model that did not have inlet and outlet holes. This way, the micro model is fabricated using soft-lithography technique (Figure 1.1). Micromodel fabrication using the soft lithography technique is also performed by Haque et al.,2021. Various micromodels have been fabricated over the years to investigate multiphase flow behavior. The micromodels with analogous geometry of the porous medium, such as homogeneous, partial regular, dual porosity medium (Yun et al., 2017), fractured, and heterogeneous porous medium has been fabricated to investigate the pore scale flow dynamics and oil recovery.

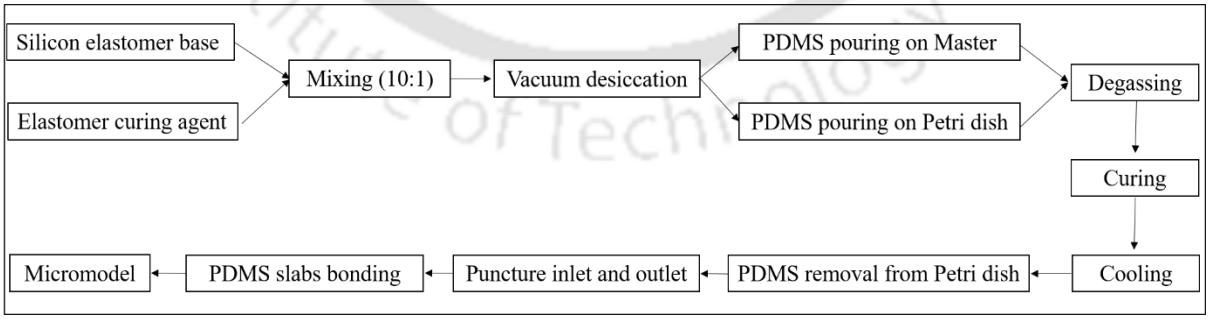

Figure 1. 1 PDMS-based micromodel fabrication process

1.3 Flow visualization techniques

Flow visualization methods are selected based on the type of porous medium, whether opaque or transparent. The flow visualization in an opaque medium can be performed using Nuclear Magnetic Resonance (NMR) (Dijk et al., 1999; Lebon et al., 1996), Magnetic Resonance Imaging (MRI) (Ogawa et al., 2001), and synchrotron-based X-ray Micro-Computed Tomography (μ-CT) (Berg et al., 2013) imaging method to visualize the flow. X-ray PIV and Infra-Red Micro-PIV are also used for flow visualization in an opaque flow cell or micromodel (Kim and Lee, 2006; Liu et al., 2005). Optical flow visualization methods such as Laser Doppler Velocimetry (LDV) (Johnston et al., 1975), Particle Tracking Velocimetry (PTV), Particle Image Velocimetry (PIV), and Micro-Particle Image Velocimetry are used for transparent porous medium. One of the limitations of Laser Doppler Velocimetry (LDA) is that it is used to obtain instantaneous velocity measurements in a single volume/point in space (Sinton, 2004). PTV is used to get the velocity field by tracking individual particles (Huang et al., 2008). In contrast, PIV requires approximately 10 particles per interrogation area to produce one velocity vector. Particle image velocimetry (PIV) is an optical, non-intrusive measurement method that probes spatially and temporally resolved velocity vector fields. This technique is well established for macroscopic flow measurement with a maximum resolution ranging from 0.2-1 mm (Breuer, 2005; Kazemifar et al., 2015; Lu et al., 2018; Roman et al., 2016; Wereley and Meinhart, 2010). Refractive index matching is required between transparent solids and fluids to eliminate image distortion (Wiederseiner et al., 2011).

Micro-particle image velocimetry, a subset of the standard PIV, was introduced by Santiago et al., 1998. This technique is well-established for microscopic flows with a spatial resolution of tens of microns. This technique has been used to obtain the spatially and temporally resolved pore-scale velocity map of immiscible two-phase flow in the porous medium. The main difference between μ-PIV and standard PIV is based on the illumination method (Mielnik and

Saetran, 2004). In standard PIV, a sheet of light is generated to illuminate the particle at the measurement plane. In contrast, for μ-PIV, volume illumination is performed to illuminate the particle at the focal plane (Heshmati and Piri, 2018; Kazemifar et al., 2015; Lu et al., 2018; Roman et al., 2016; Santiago et al., 1998; Wereley and Meinhart, 2010). In this technique, working fluid is seeded with micron-size, neutrally buoyant fluorescent tracer particles. Micro PIV technique is used to track these micro-particles in the flowing fluid as the particles have a similar velocity to the flowing fluid. The resolution of micro-PIV is on the order of a few microns. The length scale of the micro-PIV is typically in the range of tens to hundreds of microns, which is suitable for studying fluid flow in microfluidic devices. An inverted microscope, high-speed camera, light source, syringe pump, and porous micromodel are utilized to execute the experiment and capture the images. The schematic diagram of the micro-particle image velocimetry setup is shown in Figure 1.2. Image processing is executed to improve the image quality and extract the relevant quantitative information using a commercial software dynamic studio (Dantec dynamics) or Freeware Software PIVLab. Image processing comprises of image calibration, pre-processing, background removal, image masking, adaptive PIV algorithm for vector calculation, and post-processing of velocity vectors to extract the parameters such as velocity magnitude, vorticity, and shear rate (Figure 1.3). A number of literatures discussed various image processing algorithms to improve the image quality and get a velocity vector field (Haque et al., 2021; Lindken et al., 2009; Sharma et al., 2022; Sharma et al., 2023; Wereley et al., 2002).

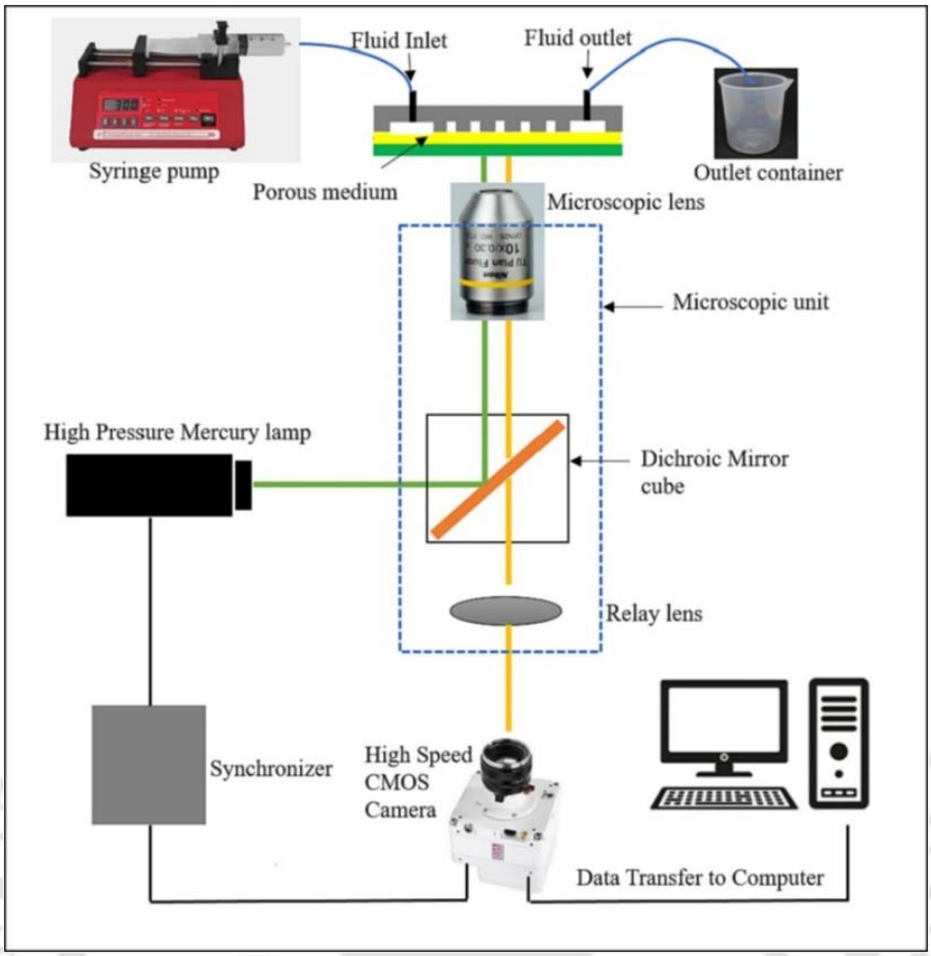

Figure 1. 2 Schematic of Micro-particle image velocimetry experimental set-up

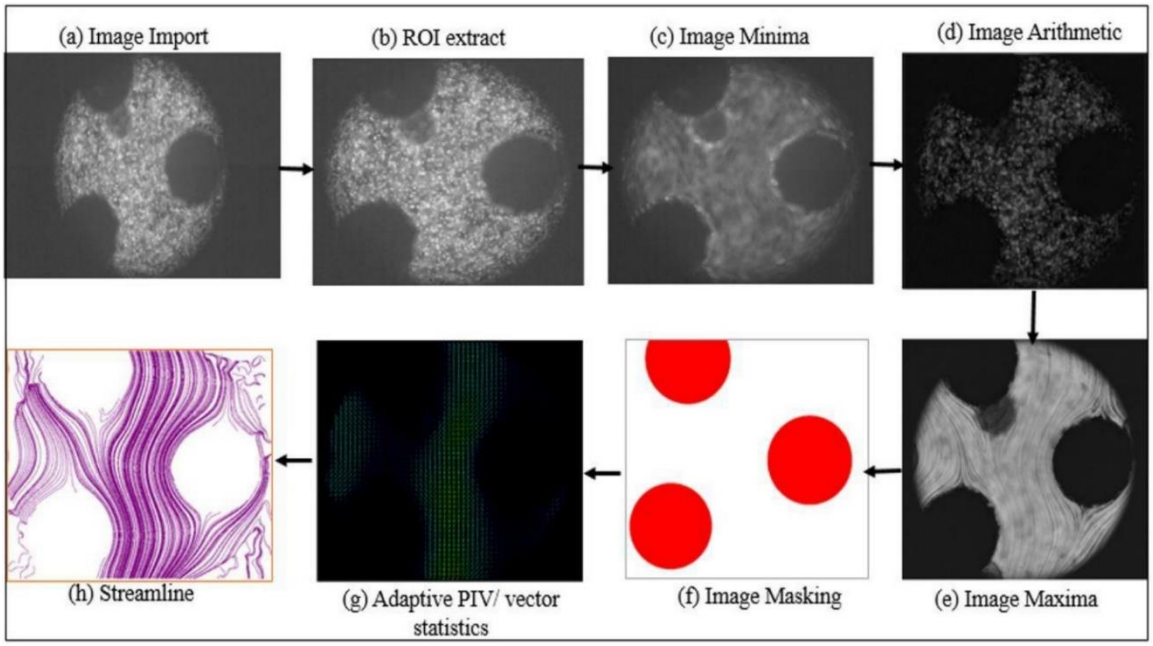

Figure 1. 3 Image processing steps using dynamic studio software.

1.4 Pore-scale phenomena

A number of pore-scale phenomena and events have been illustrated in various literature on two-phase flow in the porous medium. These phenomena include Haines Jump (Edery et al., 2018), snap-off (Follesø, 2012), shear-induced circulations (Heshmati and Piri, 2018; Zarikos et al., 2018), ganglia breakage and coalescence (Datta et al., 2014a; Datta et al., 2014b; Krummel et al., 2013), in-situ emulsification (Broens and Unsal, 2018; Unsal et al., 2016), and co-current and counter-current spontaneous imbibition in the fractured porous medium (Jafari and Rokhforouz, 2020; Zhu et al., 2021a), film formation, capillary fingering, viscous fingering (Zhang et al., 2011), piston-like displacement, bifurcation, confluence (Blois et al., 2013; Blois et al., 2015), wettability alteration (Gong et al., 2016; Saha et al., 2018a; Saha et al., 2018b), In-situ emulsification (Dong et al., 2012; Pei et al., 2011), IFT reduction (Pei et al., 2013b), and viscous coupling (Roman et al., 2020).

1.4.1 Haines Jump

The velocity burst is often observed during two-phase flow through the porous medium. The pore-scale velocity bursts phenomena were first pointed out in 1930 (Haines, 1930). According to his observation, the motion of a fluid front can be highly unsteady and is characterized by pore-scale jumps, known as Haines jumps or Rheon. It consists of energetic, pore-scale velocity bursts that displace the fluid from a pore throat into a wider pore space and is associated with a sudden drop in capillary pressure. The identification of these unsteady phenomena has mainly relied upon high-speed imaging and monitoring of capillary pressure (Moebius and Or, 2012; Yuan and Swanson, 1989). During Haines Jump, fluid can achieve velocities about three orders of magnitude higher than the bulk flow velocity (Moebius and Or, 2012), resulting in Reynolds numbers (Re) in the turbulent flow regime (Re > 500) (Hlushkou and Tallarek, 2006). This unsteady phenomenon is undesirable because sudden velocity jumps result in viscous fingering phenomena, leaving a significant amount of oil trapped in the porous medium. Similar phenomena are confirmed by several recent observations from Berg et al., 2013; Kazemifar et al., 2015; Blois et al., 2015; Li et al., 2017; Edery et al., 2018. According to Edery et al., 2018 a non-wetting fluid invades a pore filled with a wetting fluid when the driving pressure exceeds the capillary pressure at the pore throat. The non-wetting phase continues to flow until it reaches another pore throat, where the capillary pressure is sufficiently high to stop the further flow. This rapid local flow between stable configurations is called a Haines jump. The local variations of the surface tension, which leads to localizing capillary instabilities that drive the Haines jumps to occur in pores. Figure 1.4 shows some of the evidences of Haines jump recorded during experimental observations.

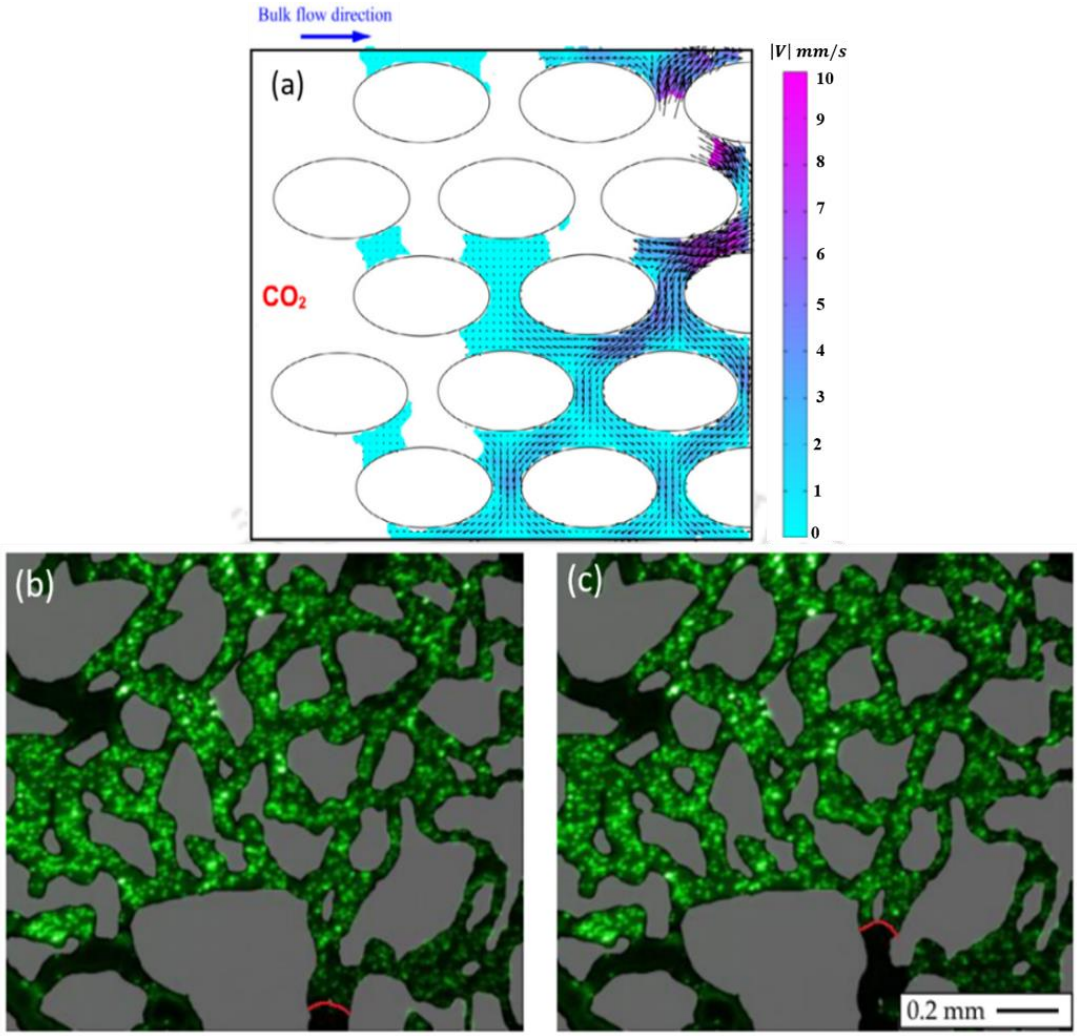

Figure 1. 4 Haines jumps, (a) Velocity jumps clearly evident ahead of the growing finger (Kazemifar et al., 2016) (b) the red curves denote the locations of the interfaces before the Haines jump (c) location of interface after the Haines jump event (Li et al., 2016).

1.4.2 Snap off

The snap-off phenomenon is desirable as it contributes to the oil recovery from the small pore constrictions. Snap-off occurs when CO_2 enters from the pore throat to the pore body region, in the form of a bubble and advances instantly into the middle of the oil-filled pore. From here, it expanded outwards and displaced the oil through the continuous spreading layer or by piston

displacement through adjacent throats (Follesø, 2012). This expansion continues until only the spreading layer remains, which typically takes few to tens of seconds.

1.4.3 Spontaneous imbibition

Spontaneous imbibition (SI) is the primary mechanism for oil recovery from the rock matrix in naturally fractured reservoirs. In this spontaneous imbibition, the wetting fluid (water) is injected into the porous rock matrix, and the oil is expelled from the matrix and flows into the fractures. The spontaneous imbibition can be classified as co-current and countercurrent imbibition (Jafari et al., 2017; Zhu et al., 2021a; Zhu et al., 2021b). In naturally fractured reservoirs, co-current spontaneous imbibition occurs when water and oil flow concurrently in the fractures. However, it is termed counter-current spontaneous imbibition when both phases flow in opposite directions (such as water flow from fracture to the matrix and oil flow from matrix to fracture). Figure 1.5 clearly illustrates the counter-current and co-current SI in the fractured porous medium.

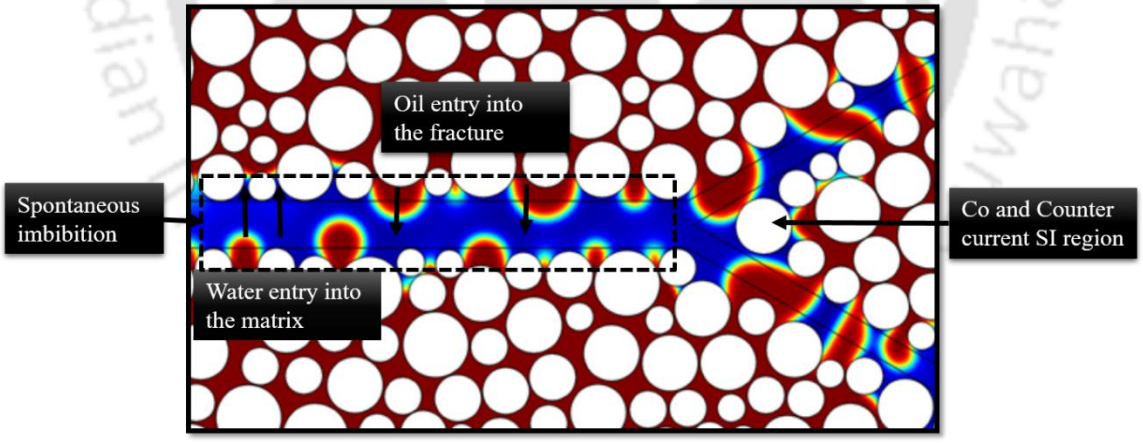

Figure 1. 5 Co-current and counter-current spontaneous imbibition in the bifurcated fractured porous medium (Zhu et al., 2021a).

1.4.4 Shear-induced circulations

During the secondary recovery process, a significant amount of the non-wetting phase is still trapped within small constrictions, pore throats, and dead-end zones in the form of droplets, blobs, and ganglions due to viscous fingering. With a continuous flow of the wetting phase (water) in the porous medium, a shear force acts on the interface of displacing and trapped fluid, causing a partial momentum transfer to the trapped non-wetting phase. This leads to shear-induced circulations in the trapped non-wetting phase (Heshmati et al., 2018). The pressure force by the displacing fluid is not sufficient enough to displace the trapped non-wetting phase (blob or ganglion). These vortices or recirculations can be visualized when the trapped fluid is stagnant. Once the trapped fluid starts to move from the pores, these circulations slowly disappear (Zarikos et al., 2018). Even if the flow rate of the displacing fluid is slightly increased, only the magnitude of the rotation increases, but the trapped fluid is not displaced from the porous medium. Vortex formation thus resists the pressure force supplied by the displacing phase to flush out the trapped non-wetting phase.

1.4.5 Ganglion/droplet breakage and coalescence

The reason for the disintegration of the droplets from large ganglia is the higher flow rates of displacing phase, resulting in higher capillary numbers (2×10^{-4}). The increase in viscous force at the high capillary number is consistent with the change in the interfacial energy, resulting in ganglia disintegrating into several droplets or blobs (Pak et al., 2015). The magnitude of rotation of trapped non-wetting phase ganglia increases with an increase in the flow rate, resulting in the center of mass of ganglia moving close to the interface between displacing phase and trapped non-wetting ganglia. The interfacial stresses applied by the displacing phase disintegrated the droplet from the ganglia. At high flow rates (high capillary number), the oil continually breaks up into discrete ganglia. The ganglia are then advected through the pore

space by the flowing wetting fluid. This is a dynamic process; the oil ganglia continually break up and coalesce, temporarily becoming immobilized at some pore entrances and eventually being pushed through others, ultimately becoming mobilized from the medium (Datta et al., 2014a).

1.4.6 In situ emulsification

During water flooding, a significant fraction of the oil remains in the water-swept region of the porous reservoir rock. The aqueous phase preferentially flows through the connected water path that surrounds the oil phase trapped by capillary forces.

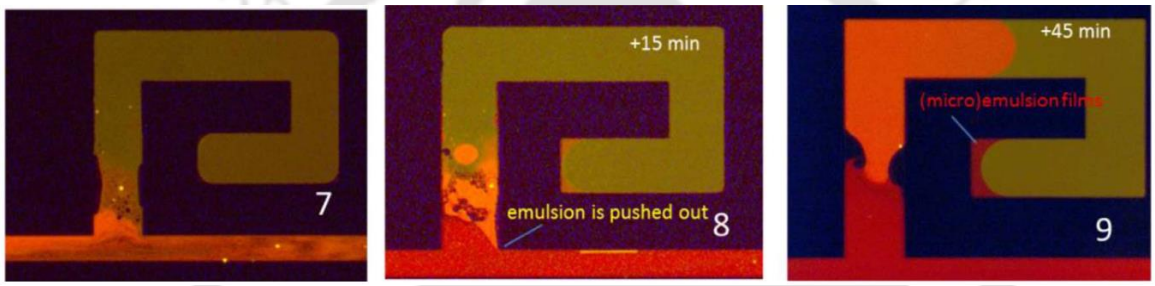

Figure 1. 6 Emulsification process in the dead-end channel, which is initially filled with colored n-decane (green). As emulsification takes place, the red zone form (Broens and Unsal, 2018)

During surfactant flooding interaction of surfactant mixed water with crude oil results in the formation of micro emulsion at the interface, leading to the miscibility between the phases. The micro-emulsion reduces the interfacial tension up to the ultra-low value (10^{-2} mN/m), which is required to generate the miscibility (Broens and Unsal, 2018; Sharma et al., 2021; Unsal et al., 2016). Broens and Unsal, 2018 investigated oil recovery using in-situ emulsification from the microchannel with a dead-end. Image analysis of the dead-end channels indicated that the Marangoni effects contributed to the emulsification process (Figure 1.6). The oil recovery is controlled by the rate at which the surfactant is delivered and dependent on the flow rate of the aqueous solution in the main channel. At higher rates, the surfactant delivery is more efficient. A phase diagram has been developed which elucidates the relationship between emulsion

properties and oil recovery (Lenormand, 1990) (Figure 1.7). Additional oil recovery could result from various driving mechanisms that influence the flow regime, i.e., mobilization of capillary-trapped oil, solubilization of oil, changes in wettability, and/or shifts in effective phase mobility.

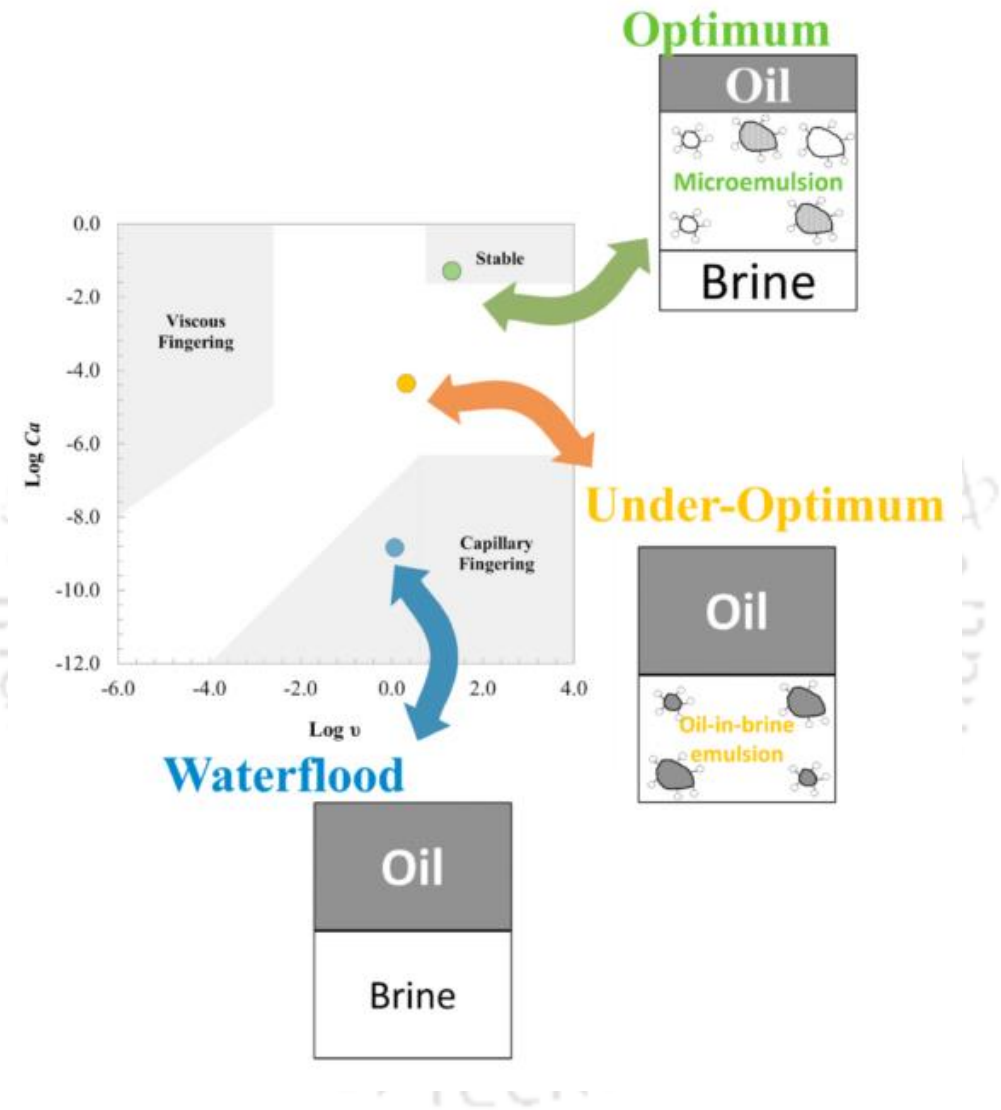

Figure 1. 7 Lenormand phase diagram based on Capillary number (Ca) and viscosity number (υ). The oil/brine diagrams highlight the different emulsion systems created at optimum and under-optimum conditions (Alzahid et al., 2020).

1.5 Parameters affecting the trapping and mobilization of the non-wetting phase

The porous medium is initially saturated with the brine. The non-wetting phase (crude oil) displaces the wetting phase to irreducible water saturation, called the **drainage** process. During secondary and tertiary recovery processes, the non-wetting phase in the porous medium is displaced by wetting phase injection (**imbibition** process). However, a significant amount of oil remained trapped in the small pore constrictions after the flooding. Numerous parameters affect the trapping and mobilization of the non-wetting phase through the porous medium. These parameters include displacing phase injection velocity, viscosity ratio, capillary number, wettability alteration, IFT reduction, aspect ratio, porosity, medium heterogeneity, in-situ emulsification, and effect of fractures.

1.5.1 Flow rate

Heshmati and Piri, 2018 investigated the flow rate and viscosity effect on the trapped oil within the heterogeneous porous medium. They observed that at higher flow rates, there is a higher probability of producing the trapped non-wetting fluid globules. However, the trapped non-wetting fluid could not be mobilized at lower flow rates. Introducing a droplet of the non-wetting phase into the porous medium could result in the perturbation and movement of the trapped non-wetting phase, resulting in its displacement through the porous medium. There are few simulation studies which investigated the effect of displacing phase injection velocity on oil recovery (Gu et al., 2019; Jafari et al., 2017; Jafari and Rokhforouz, 2020; Zhu et al., 2021b). It has been investigated that the oil recovery is high at a lower injection velocity through the porous medium because of lower breakthrough time (Figure 1.8).

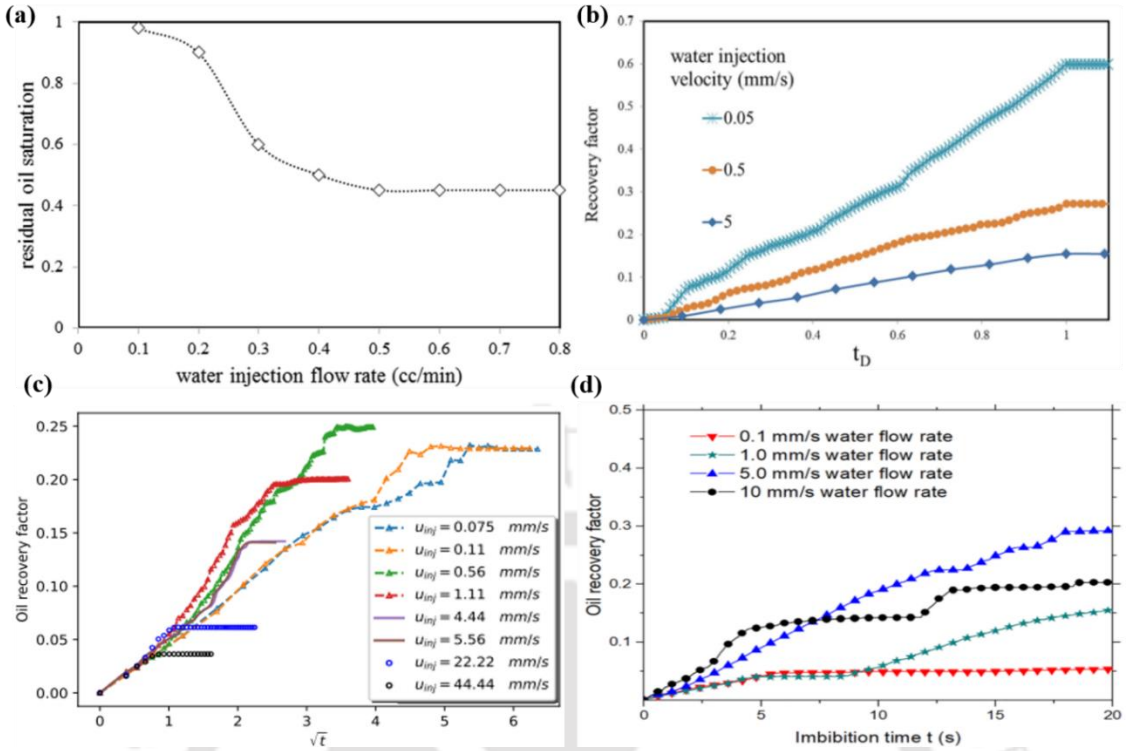

Figure 1. 8 Effect of displacing phase injection velocity on oil recovery, (a) Steady-state residual oil saturation versus water injection flow rate (Jafari et al., 2017), (b) oil recovery factor as a function of dimensionless time for three models with different water injection velocities of 0.05, 0.5, and 5 mm/s (Jafari and Rokhforouz, 2020), (c) Time evolution of the oil recovery factor for different injection velocities of 0.075 mm/s, 0.11 mm/s, 0.56 mm/s, 1.11 mm/s, 4.44 mm/s, 5.56 mm/s, 22.22 mm/s, and 44.44 mm/s (Gu et al., 2019), (d) Effect of water flow rate on the oil recovery factor during the first 20 s (Zhu et al., 2021b).

1.5.2 Viscosity ratio

The viscosity ratio is the ratio of the viscosity of water to the viscosity of oil ($M = \mu_w/\mu_o$), where w and o denote the water and oil, respectively. Numerous simulations have been performed to investigate the effect of viscosity ratio on oil recovery (Amiri and Hamouda, 2014; Gu et al., 2019; Maaref et al., 2017; Rokhforouz and Akhlaghi Amiri, 2017). Amiri and Hamouda, 2014 found that the oil recovery is highest at a critical viscosity ratio (Figure 1.9a).

Oil recovery is generally low at the low viscosity ratio because of the difference in the viscosity of the displacing phase and the resident phase in the porous medium. Maaref et al., 2017 investigated that at a higher viscosity ratio, the oil recovery is significantly increased because of the viscous force applied by the displacing phase (Figure 1.9b). Rokhforouz and Amiri, 2017 observed that the oil recovery is not sensitive to changes in the viscosity ratio at early times. The maximum oil recovery is observed at the viscosity ratio M = 1 (Figure 1.9c). Gu et al., 2019 also found that the oil recovery is highest at a critical viscosity ratio (M = 0.5) (Figure 1.9d).

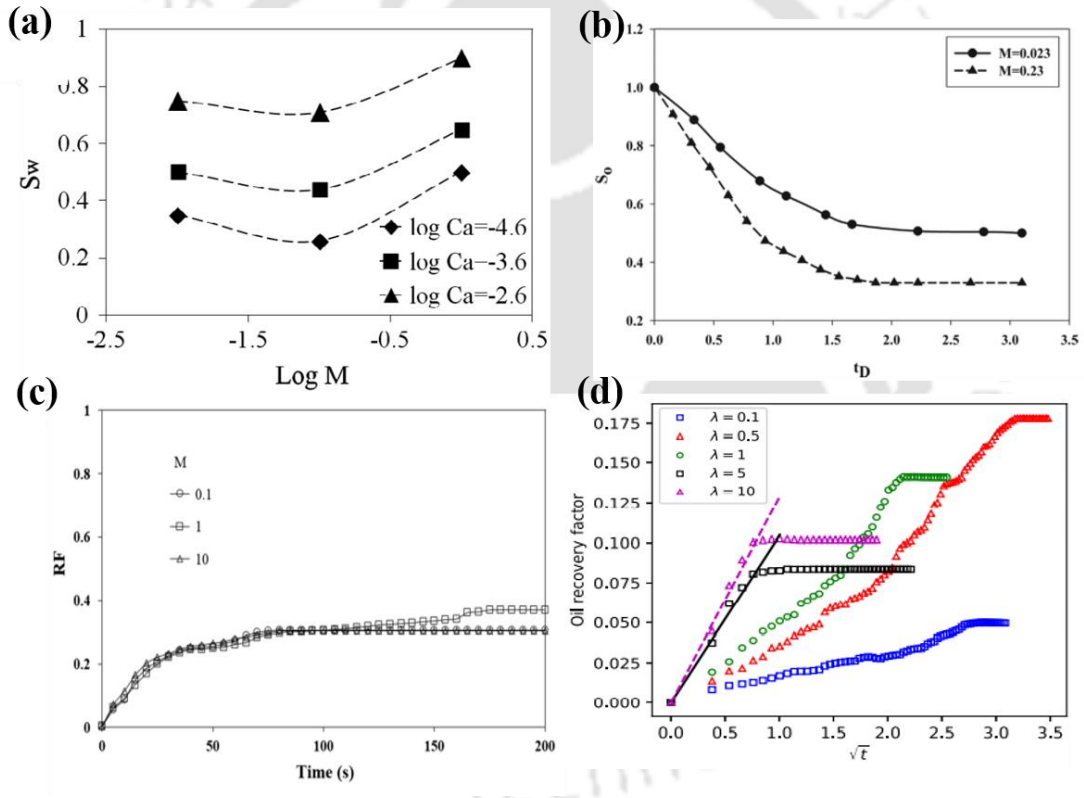

Figure 1. 9 Effect of viscosity ratio on oil recovery(a) Water saturation (S_w) as a function of viscosity ratio (log M) (Amiri and Hamouda, 2014), (b) Oil saturation versus dimensionless time for two different viscosity ratios (Maaref et al., 2017), (c) Oil recovery factor (RF) as a function of time for three models with viscosity ratios of 0.1, 1, and 10 (Rokhforouz and

Akhlaghi Amiri, 2017), (d) Time evolution of the oil recovery factor for the viscosity ratios of 0.1, 0.5, 1, 5, and 10 (Gu et al., 2019).

1.5.3 Wettability

Wettability is the preference of any solid surface (rock, glass, or PDMS) to be wetted or adhered with one fluid in the presence of other immiscible fluids. The relationships between wettability and capillary pressure ($P_c = 2\sigma\ Cos\theta/r$) is critical for improving the oil recovery factor at the pore scale. If the contact angle is between 0°- 80°, 80°-100°, 100°-160°, and 160°-180°, then reservoir rock is characterized accordingly as water-wet, intermediate wet, oil-wet, and strongly oil-wet, respectively. Wettability alteration is one of the most critical mechanisms of oil recovery using low-salinity water flooding (Saw and Mandal, 2020). The reason for contact angle reduction is that the thermodynamic equilibrium between the crude oil and rock gets disturbed in the presence of low salinity water, resulting in cation desorption from the rock surface. The system's pH increases with the release of cations, resulting in the removal of organic materials from the rock surface. A significant reduction in the contact angle up to 38° is reported in the literature when an alkali polymer solution is used as a displacing phase. The reason for wettability alteration is the emulsification process between crude oil and alkali-polymer solution, which results in trapped oil recovery from emulsion from small pore constrictions (Mehranfar and Ghazanfari, 2014). The nanoparticles help in wettability alteration depending on the choice of nanoparticles. The layer of deposited nanoparticles applies a disjoining pressure over the crude oil droplets, which detaches the oil droplet from the surface. Simulations have been performed to investigate the effect of wettability. Zhu et al., 2021a; Jafari et al., 2020 and Maaref et al., 2017 investigated the wettability effect on residual oil recovery from the porous medium. They also observed that the displacing phase enters smaller pore bodies and sweeps out the oil more efficiently because of low capillary resistance

at water-wetting conditions (at θ= 45°- 18°). They observe a decrease in the residual oil saturation with a reduction in the contact angle. Jafari et al., 2020 reduced the contact angle from 90° to 18° and observed that decreasing the contact angle to more water-wet conditions results in additional oil recovery. The oil recovery at a contact angle of 90° is only 11%, whereas the oil recovery at a contact angle of 18° is about 40% (Figure 1.10a). Decreasing the contact angle delays the breakthrough time. Zhu et al., 2021a also investigated the effect of wettability on the oil recovery factor in a bifurcated fractured porous medium and observed maximum oil recovery at a contact angle of 15° and minimum oil recovery at a contact angle of 90° (Figure 1.10b).

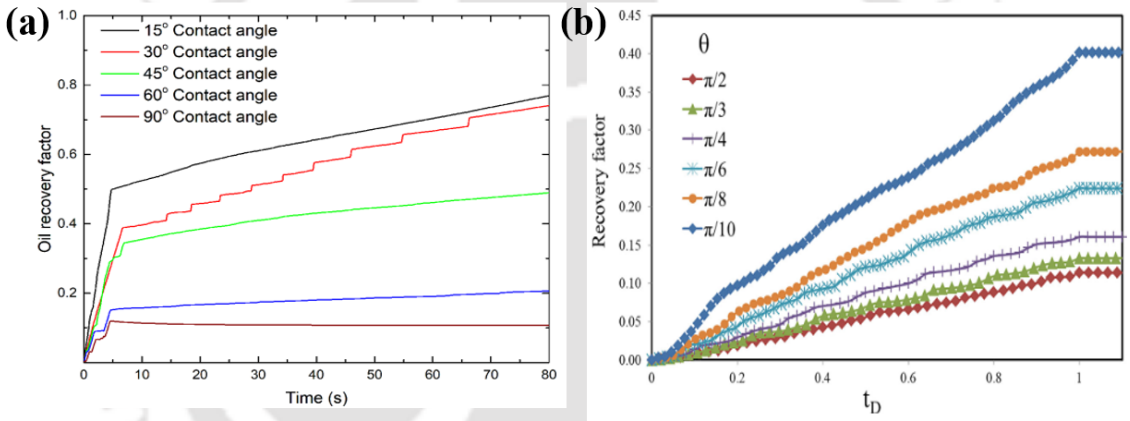

Figure 1. 10 wettability alteration effect on oil recovery factor, (a) The effect of wettability on the oil recovery factor in BFPM (first 80 s) (Zhu et al., 2021a), (b) Oil recovery factor as a function of dimensionless time for different contact angles (Jafari and Rokhforouz, 2020).

1.5.4 Interfacial tension (IFT)

Interfacial tension reduction is one of the most crucial mechanisms of trapped oil recovery from smaller pore constrictions. Several chemical-laden fluids significantly increase the fluid-fluid interactions. The fluids such as low saline water, alkali-polymer, alkali-surfactant polymer, and nanofluids consisting of silica, alumina, and titanium dioxide particles significantly reduce the interfacial tension between the two phases. During low-salinity water injection, the organic

material's solubility increases in the aqueous phase (salting-in effect). This reduces IFT between the two phases (Strand et al., 2009). The IFT is reduced to 17.18 mN/m using low salinity water in the porous medium. The interfacial tension decreases to a significantly low value using an alkali-polymer solution as a displacing phase.

Usually, the alkaline solution interacts with the acidic part (carboxylic acid) of the crude oil and forms an in situ surfactant. The in situ surfactant (petroleum soap) accumulates at the interface of alkaline solution and crude oil, thereby reducing the interfacial tension. The in situ surfactants diffuse into the crude oil or aqueous solution depending on their affinity (Pei et al., 2013a). The significantly lowest IFT (0.20 mN/m) is achieved for an alkali-surfactant-polymer solution and crude oil. The significant IFT reduction is because of emulsion formation between the surfactant and crude oil. The droplet size in the emulsion remains small as the surfactant coats the emulsion droplets during the interaction, which reduces the coalescence of the droplets in the emulsion. Silica nanoparticles form a layer at the water and crude oil interface, causing a decrease in the interfacial tension between the immiscible phases. Therefore, silica nanoparticles can recover additional crude oil by reducing the IFT to an ultralow value. There are some simulations studies which discussed about the effect of interfacial tension on oil recovery (Gu et al., 2019; Jafari and Rokhforouz, 2020; Rokhforouz and Akhlaghi Amiri, 2017; Zhu et al., 2021a).

1.5.5 Effect of fractures

The fractures promote additional oil recovery from the reservoir rocks. In the case of low porosity and permeability formations, the oil did not get enough way to come out of the rocks. Hence the artificial fractures are induced by hydraulically or acid fracturing of the rock. Therefore, the permeability significantly increases, resulting in improved oil recovery. Several experimental and simulation literature shows the effect of fracture morphology, aperture,

width, bifurcation angle, tortuosity, fracture spacing, and fracture angle on oil recovery. Jafari et al., 2017 and Jafari and Rokhforouz, 2020 investigated the effect of fracture aperture on oil recovery. It is observed that the model with the narrowest aperture had the highest oil recovery in the early times. The model with the fracture aperture of 0.90 mm showed higher oil recovery at earlier times than the model with the fracture aperture of 1.25 mm. However, they had a similar ultimate recovery factor (almost 0.25). It can be concluded that the decreasing fracture aperture results in a higher oil recovery at the earlier times, but it does not affect ultimate recovery dramatically (Jafari et al., 2020).

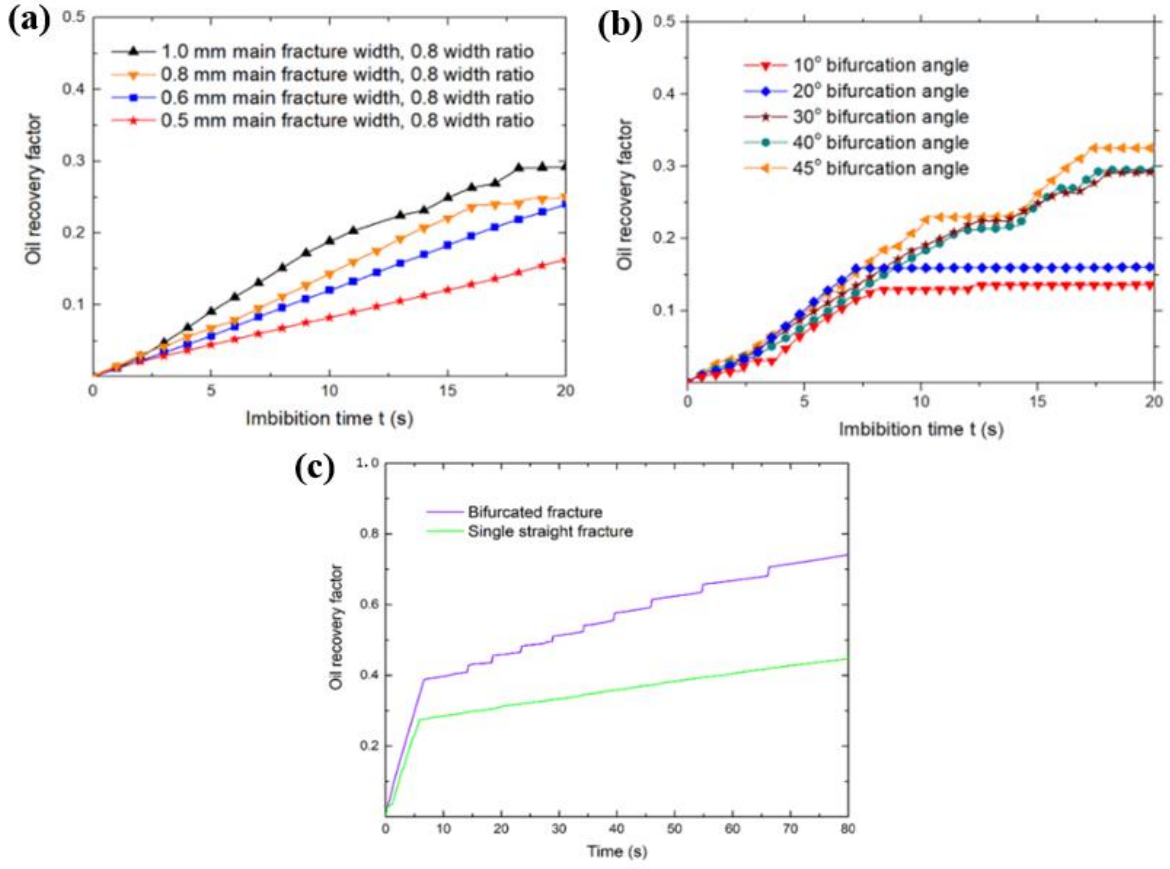

Figure 1. 11 (a) effect of fracture width on the trapped oil recovery (Zhu et al., 2021b), (b) effect of bifurcation angle (Zhu et al., 2021b), (c) effect of fracture morphology (Zhu et al., 2021a).

Zhu et al., 2021b also investigated the effect of fracture width on the oil recovery factor through a tree-shaped fractured porous medium. The fracture width was taken as 0.5 mm, 0.6 mm, 0.8 mm, and 1 mm. The increase in the fracture width enables more of the wetting phase (i.e., water) to participate in imbibition. Meanwhile, it also reduced the flow resistance when fluids migrated in the fracture (Figure 1.11a). The imbibition power in the media increased when the fracture bifurcation angle was increased from 10° to 40°. At a fracture bifurcation angle of 10°, some residual oil remained in the matrix. However, at a fracture bifurcation angle of 40°, a considerable portion of the oil in the matrix was recovered (Figure 1.11b). This is because, as the fracture bifurcation angle increased, the number of matrix pores involved in imbibition increased (Zhu et al., 2021a). Zhu et al., 2021a investigated the effect of fracture morphology on residual oil recovery. They observed that in the presence of a bifurcated fracture, the amount of residual oil in matrix pores is significantly lower than that for a single fracture. One reason is that the fracture bifurcation allows the participation of an increased number of pores in the imbibition process and provides more water (Figure 1.11c).

1.6 State of the art of two-phase flow through the porous medium

1.6.1 Pore-scale flow dynamics during nanoparticle-assisted alkaline flooding

Flow through porous medium has applications in tertiary oil recovery process, subsurface hydrology, carbon capture and storage in geological formations, and methane production from the hydrate-bearing formations, to name a few (Lindken et al., 2009; Lu et al., 2018; Lu et al., 2020; Roman et al., 2016; Sen et al., 2012). However, the knowledge of flow behavior through the porous media is not yet fully developed. It is critical to understand the displacement process

at micro and macro scales within a porous media to optimize the EOR process. Hence, porous micromodels have been fabricated using materials like PDMS, glass beads, and Geomaterials with soft lithography or 3D printing technique to investigate multiphase flow dynamics and pore-scale events such as Haines jump and shear-induced circulation. Numerous experiments and simulations have also been performed to investigate the pore-scale flow physics during two-phase flow in the porous medium (Alzahid et al., 2020; Armstrong et al., 2014; Basirat et al., 2017; Haque et al., 2021; Unsal et al., 2019). The micro-particle image velocimetry (μ-PIV) has been used to obtain the pore-scale velocity vector map of immiscible two-phase flow in a porous medium. Cross-correlating the successive images yields the displacement of the tracer particles. The ratio of displacement and the time delay between successive images gives the velocity of tracer particles, representing the velocity of the flowing fluid (Breuer, 2005; Heshmati and Piri, 2018; Roman et al., 2016). Several studies have been conducted to investigate pore-scale dynamics of single and two-phase flow through a porous medium (Kazemifar et al., 2016; Terzis et al., 2019). The results of single-phase flow showed a periodic flow pattern, symmetrical flow around the micro-posts, bifurcation, convergence, and stagnation zones (Blois et al., 2015; Roman et al., 2020). High flow velocity has been observed at pore throats, whereas low at pore enlargement (Perrin et al., 2005; Zerai et al., 2005). In an experimental study, de Winter et al., 2020 demonstrated a three-dimensional two-component (3D2C) measurement of velocity field using a confocal laser scanning microscope in a T junction and presented porous media coupling models for single-phase flow. In their study, single-phase flow is performed to know the complexities in flow within the porous media. Several literatures have visualized displacement mechanisms during two-phase flow within a 3D porous micromodel (Datta et al., 2014a; Datta et al., 2014b; Krummel et al., 2013). Krummel et al., 2013 investigated the effect of flow conditions on both drainage and imbibition processes. At low capillary numbers (ca $\sim 10^{-6} - 10^{-4}$), the oil menisci displace the wetting fluid

through a series of abrupt bursts into the pores and develop a threshold pressure in the oil to displace the wetting phase out of the pore. However, at high capillary numbers, bursts occur simultaneously in the flow direction, causing domination of viscous force. During the imbibition process, the wetting fluid snap-off threads of oil at multiple pore constrictions at low capillary numbers. Wetting fluid flows through a tortuous network, forming disconnected oil ganglia. At higher capillary numbers (ca $\sim 10^{-4}\ -10^{-3}$), the nonwetting fluid breaks into discrete ganglia and is displaced by the flowing wetting fluid. Kazemifar et al., 2015; Kazemifar et al., 2016 and Li et al., 2017 identified three distinct flow stages during two-phase flow through the porous medium. These stages are pre-front passage, front passage, and post-front passage. The velocity field results showed an unstable and highly perturbed flow during the front passage stage because of abrupt changes in the velocity and direction (Blois et al., 2015; Heshmati and Piri, 2018; Roman et al., 2016). During this stage, viscous fingering instabilities have been visualized during water flooding. The application of polymers (such as HPAM) in the aqueous phase suppresses viscous fingering and increases its viscosity to improve mobility ratio and displacement efficiency (Gutiérrez et al., 2020). One disadvantage of polymers is their retention in pore throats and constriction, which impair the permeability and porosity of porous medium (Ekanem et al., 2020; Li et al., 2019; Parsa et al., 2020). The pore-scale event, such as Haines jump that promotes viscous fingering instability, has been visualized during multiphase flow (Kazemifar et al., 2016). Edery et al., 2018 identified that the Haines jump occurs due to the depletion of surfactant concentration at a high flow rate of displacing phase. Generation of in-situ surfactant during the EOR process can eliminate the Haines jump. During the post-front passage, some oil saturation remained trapped within the small pore throats and dead-ends in the form of droplets, blobs, and ganglions. The mobilization of trapped crude oil depends on several parameters, including displacing fluid

flow rate and viscosity (Heshmati and Piri, 2018), capillary number (Zarikos et al., 2018), trapping number (Oughanem et al., 2015), aspect ratio (ratio of pore body to pore throat), size of ganglion (Oughanem et al., 2015), interfacial tension (Saha et al., 2018a), in situ emulsification (Liu et al., 2019b), and wettability alteration (Maghzi et al., 2011). The displacement of trapped crude oil from the porous media requires viscous forces to overcome the capillary forces to produce crude oil (Hilfer and Øren, 1996; Zhang et al., 2011). Dutta et al., 2014b investigated the mobilization of the trapped nonwetting phase through a 3D porous medium. The trapped ganglia configurations and residual oil saturation are dependent on a capillary number. At low capillary numbers, there is no variation observed in ganglion configuration and residual oil recovery (Datta et al., 2014b). An increase in the capillary number creates a pressure gradient and momentum transfer from the wetting phase to the trapped ganglion of the nonwetting phase resulting in rupture of the ganglion into several small ganglions, blobs, and droplets (Zarikos et al., 2018). The ruptured ganglion is displaced by the flowing wetting phase and produced (Datta et al., 2014b). Heshmati et al., 2018 investigated that high displacing phase viscosity and increased flow rate help overcome the capillary force to mobilize the trapped nonwetting phase. A low aspect ratio within the rock structure results in higher nonwetting phase recovery. In situ emulsification also helps in producing the trapped oil from the dead-end zones. Broens and Unsal, 2018 studied the flow dynamics and emulsification kinetics in a conductive channel with dead-end extensions. There are certain chemicals (alkali) and nanoparticles, which can control and optimize the parameters for maximizing the crude oil recovery. Interaction of alkaline solution and acidic part of crude oil cause in situ surfactant generation at the interface. The problems such as the Haines jump are eliminated due to in situ surfactant generation during alkaline flooding (Ott et al., 2020). Use of silica nanoparticle in alkaline solution further decrease the IFT to ultralow value upon interaction with crude oil. The high viscosity of emulsion (formed due to crude oil and silica

nanofluid interaction) helps maintain the mobility ratio, eliminating viscous fingering instability and increasing displacement efficiency. Nanoparticles (silica) also have a significant role in rheology modification, wettability alteration, and interfacial tension reduction for residual oil recovery (Ali et al., 2018; Rostami et al., 2020; Saha et al., 2018b).

1.6.2 Immiscible two-phase flow in the heterogeneous porous medium

A significant amount of crude oil remains trapped in the reservoir pores after water flooding due to high capillary forces (Alvarado and Manrique, 2010; Carcoana, 1982; Carcoana, 1992). Although experimental and simulation studies have been performed to study the macroscopic behavior of immiscible displacement, there is a need to develop a pore-scale understanding of the displacement process and flow features to optimize different Enhanced Oil Recovery (EOR) processes.

Microfluidics plays a crucial role in providing knowledge about the various pore-scale flow mechanism such as wettability alteration (Gong et al., 2016), and oil recovery through flow visualization of the multiphase flow in 2D or 3D porous micromodels (Jahanbakhsh et al., 2020; Karadimitriou and Hassanizadeh, 2012; Lake et al., 2015; Yun et al., 2017). Optical methods, including Particle tracking velocimetry (PTV) (Zarikos et al., 2018), Particle image velocimetry (PIV) (Zerai et al., 2005), and Micro PIV (Kazemifar et al., 2015; Li et al., 2017), are used for flow visualization and quantitative study of two-phase flow at the pore level. Micro-PIV is a non-destructive technique used to directly probe and measure multiphase flow in porous media. It is a non–intrusive, optical flow measurement technique and allows the measurements of the velocity field at a length scale of 100 µm and spatial resolution of 1-10 µm in microfluidic devices (Breuer, 2005; Mielnik and Saetran, 2004).

The displacement process during multiphase flow in the porous medium has been reported in the literature to provide both qualitative and quantitative information on fluid flow at the pore scale. Qualitative information, including film formation, wettability alteration, in-situ emulsification, flow pattern (Blois et al., 2015), viscous and capillary fingering (Kazemifar et al., 2016) have been investigated using porous micromodels (Elyaderani and Jafari, 2019; Pei et al., 2011; Pei et al., 2013a; Pei et al., 2013b). A vast amount of literature also reports the use of core flooding to assess the displacement process and recovery potential of crude oil through porous domain using a combination of chemical slugs (Saha et al., 2018a; Saha et al., 2018b). However, only a few studies provide quantitative measurements of pore-scale flow phenomena such as velocity burst and recirculations (Heshmati and Piri, 2018; Roman et al., 2020; Zarikos et al., 2018). These undesirable events promote the viscous instability and trapping of the non-wetting phase in the porous medium. There are mainly three forces: capillary force, viscous force, and gravity force (Zhang et al., 2011), responsible for trapping and mobilizing the oil within the porous medium. The aspect ratio (Follesø, 2012), and in-situ emulsification (Broens and Unsal, 2018; Unsal et al., 2016) significantly contribute in the trapping and mobilization of oil. Blois et al., 2015 performed experiments in a 2D porous micromodel with uniform cylindrical micro-posts in the porous medium. They found that a significant amount of glycerol water solution is still trapped during and after silicone oil injection. The non-wetting phase trapping in the porous medium is due to the capillary force in the pores, unfavorable mobility ratio, and low capillary number during the flooding process. The pore-scale events such as viscous instability, capillary fingering, shear-induced circulations (Roman et al., 2020), and Haines jump are responsible for the trapped non-wetting phase in the porous medium. The problem of Haines jump generated due to high flow rate leads to viscous instability during two-phase flow leaving behind the high saturation of non-wetting phase in a porous medium (Edery et al., 2018). Roman et al., 2016 performed PIV analysis for

immiscible two-phase flow in heterogeneous micromodel. They identified the highly perturbed flow leading to dissipative events such as shear-induced circulations causing a significant amount of residual non-wetting phase saturation in the porous medium.

The viscous and capillary forces dominate during the displacement of resident fluid by displacing fluid in a two-phase flow through the porous medium. The residual phase develops resistance to prevent displacement from reservoir pores. The non-wetting phase is also trapped in the dead ends. During two-phase flow, the interaction of both the displacing and trapped phase causes shear-induced circulation in the trapped non-wetting phase because of the shear applied by the displacing phase at the interface. Heshmati and Piri, 2018 used heterogeneous porous micromodel and pore doublet micromodel to investigate the effect of wetting phase flow rate and viscosity in mobilizing the non-wetting phase from the porous medium using micro PIV. Increasing the viscosity of the invading fluid elevated the contribution of the small globules to the final non-wetting phase saturation. Literature shows a high-pressure drop in low-porosity rocks during the fluid flow process due to the trapping of the non-wetting phase within the porous medium (Lu et al., 2018). The aspect ratio (size of the pore body to the size of the pore throat) also plays a crucial role in trapping and mobilizing the non-wetting phase through the porous medium.

1.6.3 Two-phase flow in complex pores

Understanding the displacement mechanism and pore-scale phenomena during two-phase flow in complex pores such as dead-ends and contraction-expansion pores is essential. Certain experimental studies have investigated the effect of various chemicals and nanofluids on pore-scale flow dynamics and displacement processes (Elyaderani and Jafari, 2019; Sharma et al., 2023). It is difficult, expensive, and time-consuming to experimentally investigate the fluid flow dynamics at the pore scale. However, it is feasible to investigate the pore-scale processes

using numerical simulations. Several numerical simulation techniques have been utilized to investigate the two-phase flow in the porous medium (Figure 1.12). Pore network modeling (PNM) is the most desired method for fluid flow simulations. However, it cannot handle complex geometries properly. Numerous literature exists where the Lattice Boltzmann method (LBM) has been employed to model two-phase flow in complex geometries. However, in this method, there is limited understanding of the relation between the Navier–Stokes equations and interaction forces among the particles (Basirat et al., 2017). Direct Numerical Simulations (DNS) method is a reliable approach to handle complex pore geometries by solving the Navier–Stokes equations using finite difference, finite element, and finite volume methods (Raeini et al., 2012). The most popular interface-capturing methods include the Volume of Fluid (VOF), Level-Set, and phase-field methods (Ambekar et al., 2021). One of the limitations of the level-set method is that it cannot conserve mass. Phase field method can conserve mass, be computationally less expansive and handle complex geometries efficiently (Amiri and Hamouda, 2013).

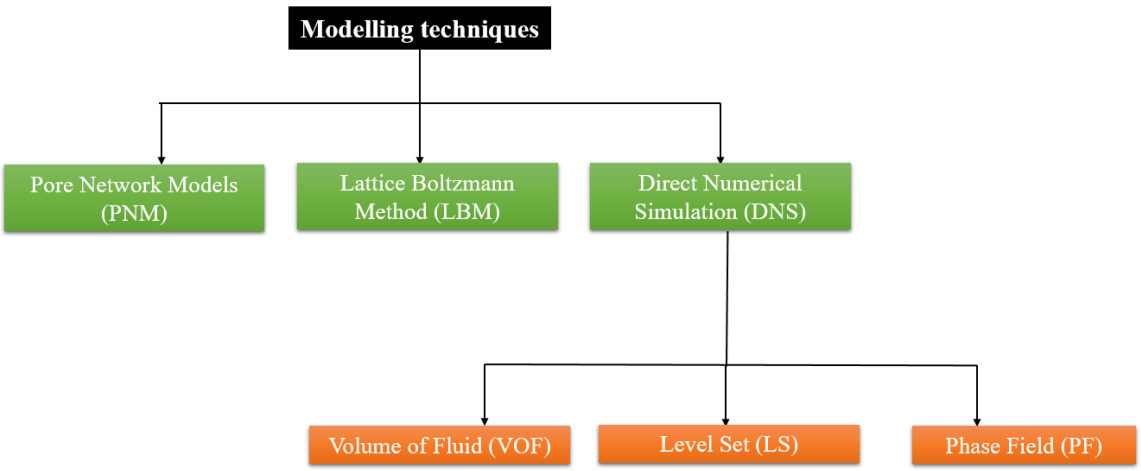

Figure 1. 12 List of techniques used in numerical simulation of two-phase flow through the porous medium.

Several parameters, such as wettability, rock heterogeneity, viscosity ratio, interfacial tension, capillary number, injection velocity, and fractures, affect the oil recovery factor through the porous medium. Wettability significantly affects the oil recovery factor (Amiri and Hamouda, 2014). Maaref et al., 2017 investigated the effect of contact angle variation on residual oil saturation in a heterogeneous medium. They observed that water invades in more pore bodies at a neutrally wet condition and sweeps efficiently due to lower capillary resistance than oil wet medium. However, in the oil-wet mediums, the water splits into fingers, and breakthrough time increases significantly, resulting huge amount of oil remaining trapped in the medium. The viscosity ratio also significantly impacts trapped oil recovery through the porous medium. Many experimental and simulation literature showed viscosity's effect on oil recovery from the porous medium (Amiri and Hamouda, 2014; Gu et al., 2019; Maaref et al., 2017; Rokhforouz and Akhlaghi Amiri, 2017). Amiri et al., 2014 and Gu et al., 2019 observed that the oil recovery is generally low at a low viscosity ratio (due to the difference in the viscosity of the displacing phase and the resident phase). In contrast, it is highest at a critical viscosity ratio. Rokhforouz et al., 2017 used three different viscosity ratios of 0.1, 1, and 10 to investigate their effect on oil recovery during the imbibition process in the porous medium. The oil recovery is not susceptible to changes in the viscosity ratio at early times. The lowest oil recovery of about 30% is observed during the viscosity ratio of 0.1. The maximum oil recovery is observed at the viscosity ratio M = 1. Maaref et al., 2017 and Rokhforouz, and Amiri, 2017 found that at a higher viscosity ratio, the oil recovery is significantly high due to the viscous force enforced by the displacing phase. An experimental study by Heshmati et al., 2018 shows that an increment in the displacing phase viscosity and flow rate applies a viscous force on the residual non-wetting phase. The viscous force results in a momentum transfer to the trapped phase, resulting in it being mobilized. The capillary number (ratio of viscous to capillary force) plays

a crucial role pore-scale displacement mechanism. Basirat et al., 2017; Zarikos et al., 2018; Heshmati et al., 2018; Zhang et al., 2011; and Amiri and Hamouda, 2014, studied the effect of capillary number on the pore-scale displacement process. They observed that increasing the capillary number increases the nonwetting phase displacement, and sweep efficiency is significantly improved. The response of injection velocity on the residual oil saturation has been investigated in the fractured porous medium as a function of time during the imbibition process by varying it from 0.05 mm/s to 5 mm/s (Jafari et al., 2017). At the highest injection rate (5 mm/s), the recovery factor was highest (15%) in the early times. However, the lowest recovery was observed after the total injection period because of the early water breakthrough. However, the maximum oil recovery of 25% was observed at an injection rate of 0.5 mm/s because of the reduction in breakthrough time due to low injection velocity. Similarly, Jafari and Rokhforouz, 2020, Zhu et al., 2021a and Gu et al., 2019 found that at a critical displacing phase injection rate, the recovery factor will be highest. The higher or lower injection velocity does not affect the higher recovery factor. Porous medium structure, be it homogeneous, heterogeneous, or fractured, affects the distribution of the non-wetting phase during the displacement process. Maaref et al., 2017 used homogeneous and heterogeneous porous mediums to understand the effect of heterogeneity on RF. It is observed that the injected water displaces most of the non-wetting phase from the homogeneous porous medium (residual oil 37%). However, injected water creates several fingers or branches in the non-wetting phase saturated porous medium, resulting in significant oil trapping (residual oil 50%). Similar results are also obtained by Amiri et al., 2014. The pore-level imbibition process has been investigated in a 2D fractured porous medium, and observed oil film thinning and rupture, and oil drop detachment (Rokhforouz and Akhlaghi Amiri, 2017). Fractures significantly contribute to the additional oil recovery from the porous medium. The effect of fracture morphology has been observed on counter-current imbibition in the fractured porous medium (Zhu et al., 2021a; Zhu

et al., 2021b). It is observed that the bifurcated fractures in the porous medium produce about 30% more oil than the single fracture, and decreasing the contact angle results in an increase in the oil recovery. The velocity magnitude in the bifurcated fracture was significantly higher than in the matrix. Enlarging the fracture width could increase the oil recovery from tree-shaped fractured porous medium (TFPM) (Zhu et al., 2021b). The sweep efficiency increases as the fracture bifurcation angle increases. Tortuosity does not have a significant effect on oil recovery initially during imbibition. However, it affects the distribution of trapped oil. Roman et al., 2020 and Broens and Unsal, 2018 studied the displacement mechanism in dead-end pores. Broens and Unsal, 2018 et al. investigated emulsification kinetics to recover the trapped fluid from the dead-end. Roman et al., 2020 performed micro-PIV studies for pore-scale flow visualization to understand the displacement process.

1.6.4 Low salinity water and chemical flooding for heavy oil recovery

The heavy oils have significantly lower API gravity (10° - 22.3°) and higher viscosity, resulting in the complexity of recovering the oil from the porous medium (Mohammadi et al., 2020a). Heavy oil recovery through water flooding in the reservoir produces only 5-10% of initial oil saturation. The higher mobility of the aqueous phase (water) bypasses a substantial volume of heavy oil in the reservoir rock. It is essential to control water mobility and improve fluid-fluid and fluid-rock interaction. It is critically important to understand the pore-scale flow dynamics during water flooding and different chemical slug injection to optimize heavy oil recovery processes. The micromodels (glass, PMMA, PDMS, or bead-based) replicating reservoir rocks have been fabricated to boost cognizance of fluid flow through a porous medium at the pore-scale (Karadimitriou and Hassanizadeh, 2012). Micro-particle image velocimetry has been extensively used to investigate displacement mechanisms, pore-scale processes, periodic flow patterns, symmetric flow, bifurcation, convergence, and temporally consistent velocity

magnitude during fluid flow in porous micromodels (Blois et al., 2015; Roman et al., 2016). The intricacies of flow behavior in a free-flow channel coupled with a porous medium have been investigated with the help of confocal laser scanning (de Winter et al., 2020; Terzis et al., 2019). The two-phase flow studies (drainage, imbibition, and water flooding processes) have been conducted in many previous studies (Datta et al., 2014b; Heshmati and Piri, 2018; Kazemifar et al., 2015; Zarikos et al., 2018). The microscopic flow dynamics, such as recirculations and Haines jump, promote viscous instability (during two-phase flow), leading to a high amount of oil trapped in the porous medium. A substantial volume of heavy crude oil remains trapped in the forms of disconnect ganglia, blobs, and droplets in the dead-ends and pore throats of the porous medium after the water flooding process. It is critical to modify fluid-fluid (IFT, in-situ emulsification) and fluid-solid interactions (wettability alteration) to recover the trapped fluid from the porous medium. Various chemical flooding processes have been executed in the past to recover the trapped fluid by changing fluid-rock and fluid-fluid interactions (Chen et al., 2015; Dong et al., 2012; Pei et al., 2012a; Pei et al., 2011; Pei et al., 2013a; Pei et al., 2012b; Pei et al., 2014; Sedaghat et al., 2013; Sharma et al., 2021; Tang et al., 2013). During alkaline flooding, an alkaline solution is introduced into the porous medium, where it reacts with the petroleum acids in the crude oil, resulting in in-situ surfactant generation at the crude oil and injected fluid interface. The in-situ surfactant cause emulsification and results in interfacial tension (IFT) reduction (Saha et al., 2018a). The emulsion has very high viscosity compared to water and oil, resulting in flow in multiple directions without any preferential flow path and eliminating the water channeling. The high-pressure gradient generated by emulsion overcomes the capillary force trapping the residual oil in pore throats or dead-ends, thereby further reducing residual oil saturation (Dong et al., 2012; Kalita et al., 2022; Pei et al., 2011). High emulsion viscosity also creates resistance to water flow and eliminates the preferential flow path, leading to a notable boost in sweep efficiency

and oil recovery (Dong et al., 2012; Pei et al., 2011). Pie et al., 2013 investigated the effect of different injection parameters on sweep efficiency. It has been observed that tertiary oil recovery increases with an increment in the alkali concentration. Higher oil recovery is achieved in the case of continuous alkaline injection compared to cyclic alkaline injection in the porous medium. The flooding results describe that the alkaline solution with 1 wt.% NaOH results in an oil recovery of 20%. Alkaline flooding is feasible for the development of highly viscous heavy oil reservoirs. It has been investigated that heavy oil with a high-viscosity of 3450 mPa.s performed well in both the low- and medium-permeability sand packs (Du et al., 2013).

There are certain disadvantages of applying inorganic alkali (NaOH and Na_2CO_3) injection in the porous medium because of permeability reduction, scale formation, and corrosion. Organic alkali can be an alternative to inorganic alkali during the enhanced oil recovery process because it eliminates scale formation, corrosion, and viscosity reduction of the polymer solution. Chen et al., 2015 conducted organic alkaline polymer flooding in porous micromodel and core-flooding to augment heavy oil recovery. They observed that the application of inorganic alkali (NaOH and Na_2CO_3) caused a decrease in the viscosity of the polymer. However, using organic alkali (ethylene diamine) results in a slight increase in polymer viscosity. The ethylene diamine–HPAM flooding results in higher oil recovery than Na_2CO_3-HPAM flooding. The addition of surfactant in an alkali-polymer solution significantly decreases the IFT, alters wettability, and improves sweep efficiency. Alkali-surfactant-polymer flooding has been used in various studies for significant wettability alteration and IFT reduction. Fractures in the porous medium further result in additional oil recovery. Alkali-surfactant-polymer (ASP) flooding has been performed in fractured five-spot micromodel, and understood that irrespective of fracture orientation to the actual flow direction, fractures within the porous

medium cause an increase in the ultimate oil recovery because of increased porosity and permeability due to fracture (Sedaghat et al., 2016). The injecting fluid breakthrough time rises dramatically if the fracture is perpendicular to the flow. However, an early breakthrough is observed in the case of fracture parallel to the flow direction. Nanofluids have a significant role in enhanced heavy oil recovery (Elyaderani and Jafari, 2019; Sharma et al., 2021). Elyaderani and Jafari, 2019 examined the impact of silica nanoparticles to enhance heavy oil recovery and found that the alkaline-nanoparticle solution alters the wettability of the medium from oil-wet to water-wet. It has been reported that the additional oil recovery of (26.40%) is obtained over water flooding using surfactant-stabilized SiO_2-based nano-emulsion (Kumar and Mandal, 2020).

1.6.5 Suspension transport through the porous medium

Suspension is generally defined as the dispersion of solid particles in a continuous fluid medium (Hunter, 2001). The migration of suspended particles in the porous medium has been observed in numerous fields of science and engineering. Areas such as produced water reinjection in the reservoir (Xia et al., 2022), CO_2 sequestration (Ge et al., 2022), nanofluids injection for enhanced oil recovery (Hendraningrat et al., 2013), sand control during flow through unconsolidated formation (Papamichos et al., 2001), groundwater extraction (Muecke, 1979), geothermal energy production (You et al., 2015), gas production from hydrate-bearing sediments (Jung et al., 2012) and hydraulic fracturing using proppant laden fracturing fluid for shale gas recovery (Song et al., 2014), all require the knowledge of suspension flow through the porous medium. Microfluidics plays a significant role in fabricating the replica of reservoir rocks in terms of 2D or 3D porous micromodels to visualize and quantify the suspension flow behavior through the porous medium (Anbari et al., 2018; Gunda et al., 2011; Lifton, 2016). The transport of suspended particles through a porous medium is the subject of investigation in various experimental and simulation studies (Auset and Keller, 2004; De and Singh, 2021;

Yousif et al., 2017; Zhou et al., 2018). Preferential flow is a significant problem during water flooding or CO_2 sequestration due to the significantly low viscosity of displacing phase compared to the displaced phase. Hence, Lei et al., 2022 developed a novel method for preferential flow control in heterogeneous porous media by concentration-manipulated rheology of micro gel particle suspension with polymer/colloid duality (Lei et al., 2022). The suspension/particle migration in the porous medium causes the trapping of fine particles in tiny pore throats, resulting in pore clogging, permeability impairment, and productivity decline (Feia et al., 2015; Jung et al., 2018; Liu et al., 2019a; Xia et al., 2022; Zhou et al., 2018). Different chemical and physics factors have been reviewed which are responsible for particle migration (Kaolinite, chlorite, silica, and quartz) through the porous medium (Yang et al., 2022). Particle disintegration from the rock occurs under imbalanced torques arising from hydrodynamic and adhesive forces exerted on attached particles (VanNess et al., 2019). The drag force acting on the spherical particle can be calculated by $F_d = C_h \times 6\pi\mu_w\tau_w r_s(r_s - h)$, where μ_w is the water viscosity, τ_w is the hydrodynamics shear, r_s is the particle radius, h is the distance between the particle and surface, and C_h is dimensionless function. The primary factors influencing the mobilization and trapping of the particle within the porous medium include the hydrodynamic and adhesive forces, salinity, temperature, pH, flow rate, and nanoscale heterogeneity. For multiphase flow, wettability and interfacial tension also contribute to particle migration through the porous medium (Ge et al., 2022). Jung et al., 2018 Studied the particle migration during multiphase flow using a microfluidic pore model to investigate the effects of pore throat to particle size ratio, particle concentration, and flow rate on clogging or bridging in porous media. They observed that the bridging and clogging would not happen at a low pore throat-to-particle size ratio. But clogging easily occurred at a lower pore throat to fine particle size ratio. A decrease in the flow rate results in clogging or bridging

because of particle deposition. During the multiphase flow of CO_2 and water in the porous medium, particle accumulates at the interface (CO2/water) and results in bridging and clogging in the pores (Jung et al., 2018). Liu et al., 2019 showed different dimensionless numbers such as adhesion number, Archimedes number, stokes number, Reynolds number, and geometric ratio to define the domains of particle bridging, adhesion, and retardation (Liu et al., 2019a).

Numerical simulations are also performed to investigate the suspension flow through the porous domain. The three models, the Lattice Boltzmann method (LBM), Discrete element method (DEM), and Immersed moving boundary (IMB), are coupled to investigate the suspension flow behavior in the porous medium. In this framework, LBM simulates fluid flow, DEM simulates particle migration, and IMB couples fluid-solid interaction (Zhou et al., 2018). Zhou et al. 2018 studied the effect of particle diameter, flow rate, particle volume fraction, and injection amount on particle retention and permeability impairment during suspension flow through the porous medium using LBM–DEM–IMB Simulation Method. Smaller particles can pass through the porous medium; however, intermediate-sized particles experience more particle retention, resulting in severe permeability impairment. Higher concentration causes more retained particles and more severe permeability reduction. A lower flow rate results in more and closer particle retention, while a higher flow rate obtains a more dispersed distribution of retained particles. Besides, the particle retention and permeability impairment become more severe as the total amount of injection particles increases (Zhou et al., 2018). Like Zhou et al. 2018, Feia et al. 2015 experimentally investigated the retention of the particles in the core sample caused an increase in the pressure, resulting in a decrease in the sample's permeability (Feia et al., 2015). Xia et al. 2022 investigated the effect of particle size distribution and different porous media during the reinjection of the produced water using coupled LBM-DEM simulation method. Clogging with mixed different-sized particles causes a severe porosity and permeability reduction. The reinjected water should be filtered enough

to eliminate the mixed clogging in the pores of the reservoir rock (Xia et al., 2022). The structure of the porous medium affects particle transport and deposition. Pore throat dimension, tortuosity, and path connection are the main parameters governing particle transport.

The deposition rate increases until a critical flow velocity, beyond which it decreases. At higher flow rates, hydrodynamic forces are applied to the particles, which dominate the gravitational forces, thus enhancing lift and drag forces and reducing the suspended particles' deposition (Benamar et al., 2007). Literature also shows the application of Stokesian dynamics simulations to investigate suspension flow through the homogeneous and heterogeneous porous medium. De and Singh, 2020 investigated suspension flow through a porous medium using Stokesian dynamics simulations. The results showed that the hydrodynamic and repulsive forces between the moving and fixed grain particles strongly influence the particle trajectories. A comparative study of suspension flow in a straight channel and porous medium suggested that the presence of grain particles alters the shear-induced particle migration in the porous medium (De and Singh, 2020). De and Singh, 2021 investigated the particle migration during suspension flow through a multilayer heterogeneous porous medium. Particles migrate from a higher concentration to a lower concentration layer and from a low porous to a higher porous layer. Furthermore, exciting phenomena like channel formation of suspended particles, trapping, and bridging in the low porosity regions are described (De and Singh, 2021).

1.7 Research Gaps

1.7.1 Nanofluid flooding

The combined effect of alkali (sodium carbonate) and silica nanoparticles in crude oil recovery from the porous medium is not very well-known and needs to be explored. Also, to the best of

our knowledge, there are no measurements of the pore-scale flow field in 2D porous micromodel for alkaline flooding and silica nanoparticle-assisted alkaline flooding. The pore-scale flow field is required to understand the flow pattern in the porous medium, desirable (piston-like displacement), and undesirable pore-scale events (viscous fingering, shear-induced circulations). Knowledge of these events can help us in developing strategies to optimize the oil recovery. Therefore, the present work investigates the combined effect of alkali (sodium carbonate) and silica nanoparticles in the recovery of crude oil from the porous medium. Their effect on IFT reduction, emulsification, rheology, and wettability alteration is also investigated. The quantitative study of alkaline and nanoparticle-assisted alkaline flooding is performed to understand the displacement mechanisms at the microscale using a 2D porous micromodel. Drainage and imbibition experiments are conducted to quantify the flow behavior and pore-scale phenomena in the 2D porous micromodels.

1.7.2 Immiscible two-phase flow

A proper understanding of various parameters responsible for trapping and mobilizing the non-wetting phase in the porous medium at the microscale is not yet developed. The unsteady flow behavior originating due to the integration and disintegration of droplets during the displacement process is also not properly understood. The microscopic study of flow physics and the effect of different parameters, such as displacing phase viscosity, flow rate, and heterogeneity on trapping and mobilization of the non-wetting phase in heterogeneous porous micromodels, are not completely understood. This study also analyses the unstable flow behavior due to droplet integration and disintegration during the immiscible displacement process. Homogeneous and heterogeneous micromodels are fabricated using beads and shadow mask-based soft lithography techniques.

1.7.3 Fluid flow in complex pores

Although there is numerous literature available on two-phase flow through the porous medium. However, these literatures do not explain the displacement mechanisms and different parameters affecting the trapped oil recovery from complex pores, such as dead-ends and contraction-expansion pores. Understanding the displacement mechanism of trapped fluid through these geometries is essential, as 34-51% of the pore space consists of these dead-ends. So the study of pore-scale displacement mechanisms and parameters affecting the trapped oil recovery from the complex geometries, such as dead-ends and contraction-expansion models, need to be investigated. Parameters such as displacing phase velocity, viscosity ratio, wettability, interfacial tension, and geometric ratio have to be for their effects on trapped oil recovery from dead-ends and contraction expansion pores.

1.7.4 Chemical flooding

The quantitative study of pore-scale phenomena and displacement mechanisms of heavy oil from the porous medium using low salinity water flooding (LSW) and slightly miscible chemical flooding is not yet well understood. So, LSW flooding and chemical floodings such as polymer, alkali-polymer, and alkali-surfactant-polymer must be performed at the micro and macro scale to investigate the pore-scale flow dynamics and their effectiveness in residual oil recovery from the porous medium quantitatively. The different flooding methods need to be compared for their displacement mechanism and oil recovery. Physiochemical properties such as wettability alteration (static and dynamic), interfacial tension, emulsification, and droplet size distribution should be evaluated. Simultaneous and direct injection schemes of saline water and chemical solutions in different experiments need to be performed to know the oil recovery potential of different flooding processes.

1.7.5 Suspension flow through the porous medium

There is limited literature available showing the flow dynamics and pore scale phenomena of low to concentrated suspension flow through different homogeneous, fractured, and heterogeneous porous mediums. The field of suspension flow needs to be explored as it has applications in various areas of science and engineering, such as subsurface hydrology and geothermal energy production. The effect of particle concentration on suspension flow behavior through different porous medium needs to be investigated. The current work experimentally validates the Stokesian dynamics simulations conducted to investigate suspension flow through the porous medium by De and Singh, 2020. Single particle dynamics, suspension flow through homogeneous, heterogeneous, and fractured porous medium, and the effect of grain particles on shear-induced particle migration are quantitatively investigated using velocity magnitude, shear rate, and vorticity profiles. The present study also illustrated the shear-induced particle migration, bridging, and clogging phenomena during multiphase flow in the heterogeneous porous medium. The current work provides an understanding of suspension flow through different types of porous medium at different concentrations both quantitatively and qualitatively to optimize the particle control at the time of multiphase flow for enhanced oil recovery.

1.8 Objectives

The effect of chemicals (alkali, polymer, surfactant) and nanoparticles (silica, alumina, and titanium dioxide) on the trapped oil recovery have been studied at the macroscale in previous literature. The quantitative effect of these chemicals, nanoparticles, and their mechanisms on pore-scale displacement behavior and flow dynamics are not completely understood. Even the combined effect of alkali and nanoparticles in crude oil recovery from the porous medium is not very well-known and needs to be explored. Investigation of the best suitable nanoparticles working in synchronization with the alkali must be known to improve the trapped oil recovery.

Experimental and numerical studies available in the literature showed that there are several parameters, such as capillary force, viscous force, flow rate, viscosity ratio, interfacial tension, wettability alteration, aspect ratio, and in-situ emulsification, which are responsible for trapping and mobilization of non-wetting phase through the porous medium. The effect of these parameters and the pore scale phenomena on non-wetting phase recovery is not completely understood. After water flooding, most of the oil remained trapped in the dead-end and pore constrictions. The dead-ends contribute about 34-51% of the rock's pore space, resulting in significant non-wetting phase trapping. The mechanism of oil recovery and the effect of different parameters on oil recovery through dead-ends and small pore constrictions need to be understood to optimize various enhanced oil recovery processes. During oil recovery through a porous medium, the unconsolidated sediments break from the rock and flow with the oil. But these particles trapped in the small constrictions result in reduced porosity and permeability. Sand production is also a problem during oil production through loosely consolidated sediments. Hence, the flow behavior of suspension through a porous medium must be understood to eliminate the permeability impairment and optimize the sand control.

The objectives of this work are designed as given below:

- **Pore-scale velocity field measurement during nanoparticles-assisted alkaline flooding**

  An experimental investigation of pore-scale flow dynamics during two-phase flow (alkaline flooding and nanofluid injection) in a micromodel using the microscale particle image velocimetry (μ-PIV) technique will be conducted. The combined effect of alkali (sodium carbonate) and nanoparticles (silica) on oil recovery will be investigated using interfacial tension, rheology, emulsification, contact angle, chemical flooding, and micro-PIV measurement.

- **An investigation of immiscible fluid displacement process in randomly distributed bead-based porous micromodels.**

  The porous micromodels with heterogeneous and homogeneous geometry will be fabricated to understand the immiscible fluid displacement process. The effect of displacing phase viscosity, flow rate, and heterogeneity will be investigated on the trapped fluid displacement.

- **Numerical simulations of two-phase flow in complex pores.**

  The numerical simulation of two-phase flow in the complex pores will be performed to understand the pore scale flow dynamics and oil recovery using the phase field method. The effect of displacing phase flow rate, viscosity ratio, interfacial tension, wettability alteration, and the geometric ratio on the trapped oil recovery from the dead-end will also be investigated.

- **A pore-scale flow dynamics and heavy oil recovery using low saline water and chemical flooding.**

  Pore-scale flow dynamics and displacement mechanisms during different flooding processes will be studied at the micro and macro-scale for enhanced heavy oil recovery. Microscopic studies (including low saline water followed by chemical floodings) will be performed using micro-particle image velocimetry, and macroscopic studies will be conducted using Core flooding.

- **Experimental investigation of suspension transport through the porous medium.**

  The suspension flow through the porous medium will be studied, and the effect of particle concentration on flow through different porous mediums (homogeneous, fractured, and heterogeneous) will be investigated.

1.9 Organization of Thesis

Chapter 2 summarizes the materials and methods used in the experimental work and the mathematical modeling of fluid flow through the porous medium. The experimental work includes crude oil characterization, interfacial tension, wettability alteration, stability, and in-situ emulsification analysis. The image acquisition during micromodel flooding and its post-processing steps are also discussed in the chapter.

Chapter 3 presents the findings on pore-scale flow dynamics during alkaline flooding and silica nanoparticle-assisted alkaline flooding. The combined effect of alkali (sodium carbonate) and nanoparticles (silica) on oil recovery is investigated using interfacial tension, rheology, emulsification, contact angle, chemical flooding, and micro-PIV measurement.

Chapter 4 discusses the immiscible fluid displacement through a heterogeneous porous medium and investigates the effect of displacing phase viscosity, flow rate, and heterogeneity on the pore-scale displacement mechanism.

Chapter 5 presents numerical simulations of two-phase flow in a dead-end model to understand the pore scale flow dynamics and oil recovery using coupled Cahn–Hilliard phase field and Navier–Stokes equations, solved by a finite element method.

Chapter 6 summarizes heavy oil recovery at the micro and macro-scale using low salinity water flooding and different chemical floodings. The effect of low salinity water, polymer, alkali-polymer, and alkali-surfactant-polymer on oil recovery has been investigated in terms of mechanisms and oil recovery using IFT, wettability, in-situ emulsification, micromodel flooding, and core flooding.

Chapter 7 presents the suspension flow dynamics through the homogeneous, heterogeneous, and fractured porous medium. The effect of particle concentration on suspension flow behavior through a porous medium has been investigated.

Chapter 8 summarizes the conclusions of the conducted research work and the possibility of extending the research work in the future.

Chapter 2. Materials and Methodology

Materials and Methods;

Experimental Procedures;

Image processing;

Mathematical modeling

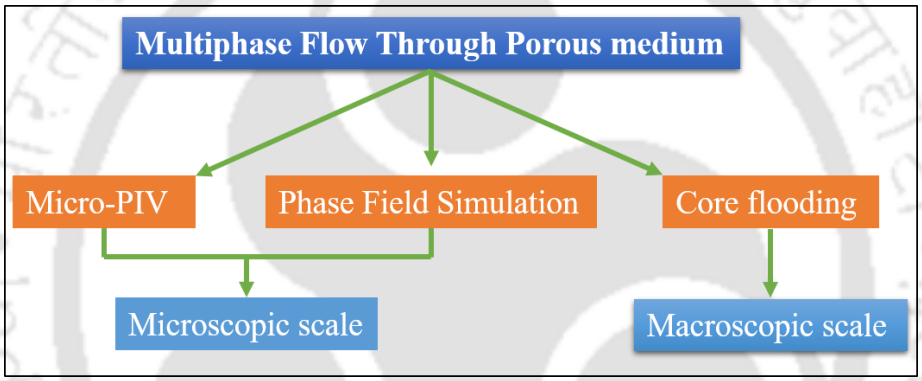

Materials and Methodology

In this chapter, different chemicals, tracer particles, experimental methods, and mathematical modeling of simulation work have been described to understand microscopic and macroscopic fluid flow dynamics. The physiochemical properties of crude oil, such as its composition, density, viscosity, interfacial tension, and acid value, are evaluated in this chapter. Similarly, morphological characterization of cores and nanoparticles using XRD, EDX, FESEM, and FETEM are also executed. The fabrication method of different types of micromodels replicating porous medium used during the research work is explained here thoroughly. The micro-particle image velocimetry technique used to visualize multiphase flow through a porous medium is presented here with the image acquisition and their processing. Finally, the macroscopic study of multiphase flow through a porous medium is performed on the different core samples using the core-flooding method, which is also explained here.

2.1 Materials

The intermediate and heavy crude oil samples are taken from the Assam oil fields (Oil India Limited). Heavy crude oil has a density of 0.925 g/cm^3, viscosity of 20.1 mPa.s at 30℃, acid value of 2.72 mg KOH/g of sample and surface tension of 30.63 mN/m. Silicone oils of viscosity 10 cSt and 50 cSt are procured from Sigma Aldrich, whereas Silicone oil of 345 cSt are procured from Himedia Pvt. Ltd. The anhydrous glycerol was procured from Merck India. Sodium chloride (Merck India), HPAM polymer (Sigma Aldrich), sodium carbonate alkali (Merck India), and sodium dodecyl sulfate surfactant (Sigma Aldrich) are used in the formulation of the non-wetting phase for micromodel flooding. Hydrophilic silica nanoparticles (mol. wt. 60.08, average particle size ~15 nm supplied by Sisco Research Laboratory Pvt. Ltd.) are used to prepare nonwetting fluid. Polymer beads (Dynoseeds TS 500) of diameter 500–600 μm are procured from Microbeads to form the matrix in the bead-based

micromodel. PMMA (Polymethylmethacrylate) particles of size 40 μm and density 1.18 gm/cm^3 are purchased from Microbeads AS to formulate the suspension with varying particle concentrations. Fluorescent polystyrene particles of size 1 μm and density 1.055 gm/cm^3 are purchased from Thermofisher scientific to seed the displacing phase. These particles are used as tracer particles at low concentration ranging from 0.04%-0.06% (by volume) to track the flow within the porous micromodel. The seeding particles are selected based on the three parameters: particle response time (τ_s), settling velocity (v_s), and mean displacement error due to Brownian motion (ε_B). The particle response time of polystyrene particles for the flow is 6.5 μs, which is short enough for nonintrusive flow. These particles faithfully follow the flow, and no sedimentation is observed due to low particle settling velocity (2.14×10^{-8} μm/s), which can be considered significantly low for sedimentation. Due to the small size of the particles, an error of about 0.3% in velocity vector measurement is estimated. This error due to Brownian motion is so small that it can be neglected (Sharma et al., 2021). The refractive index mismatch have been observed between the water and oil because of the different optical paths for each liquid, resulting in different focal plane lengths. This RI mismatch caused opaque or unclear visuals of the two phases. Therefore, anhydrous Glycerol (Refractive index 1.47) was added to the water phase (Refractive index 1.33) to match the refractive index of the silicone oil (RI 1.405). Polydimethylsiloxane (PDMS) is purchased from Dow chemicals for micromodel fabrication. The Berea and Idaho cores are purchased from Kocurek Industries, Inc., Caldwell, USA for the core flooding process.

Intermediate crude oil (supplied by Oil India Limited) has a viscosity, density, and acid number of 33.4 mPa s, 0.894 g/cm^3, and 3.40 mg KOH/g crude oil, respectively. These properties were measured at room temperature (25 °C) and atmospheric pressure. The crude oil is further characterized for its composition using Fourier-transform infrared spectroscopy (FTIR) and 1H

nuclear magnetic resonance (NMR) studies. A typical IR spectrum of crude oil is shown in Figure 2.1a. The functional groups on the IR spectra of the oil include CH stretching of the saturate (2921.98 and 2856.85 cm^{-1}) and C−H symmetric deformation of the saturate (1376 cm^{-1}). The peak in the range of 1600−1720 cm^{-1} shows the CO stretch of the carboxylic acid (Pauchard et al., 2009; Samanta et al., 2011). The peak observed in the range of 700−1000 cm^{-1} correlates the out of the plane bending of the C−H aromatic ring (Pauchard et al., 2009; Saha et al., 2018a; Samanta et al., 2011).

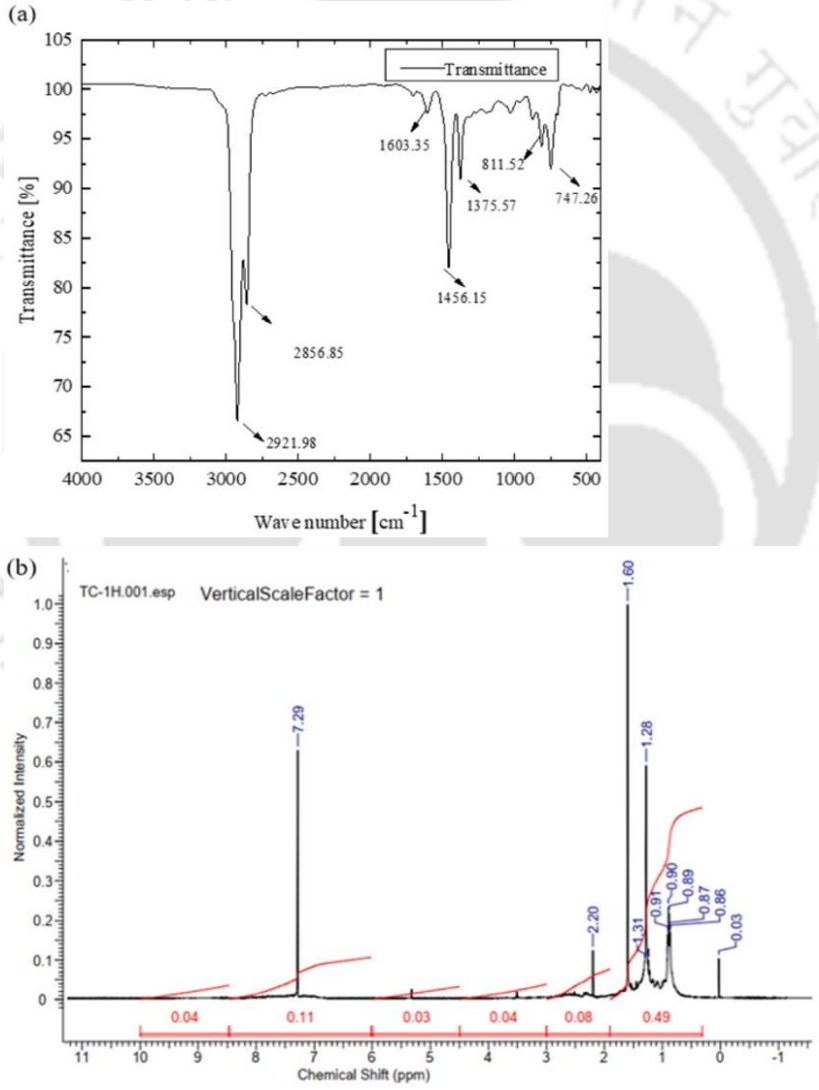

Figure 2. 1 Crude oil compositional analysis, (a) FTIR analysis of the crude oil, and (b) nuclear magnetic resonance (NMR) analysis of crude oil.

Table 2. 1 Crude oil composition investigation using nuclear magnetic resonance (NMR) analysis.

S.N.	Compound detected	Chemical shift	Percentage (%)
1.	Alkanes	0.3-1.9	62.02
2.	Aliphatic heteroatoms	1.9-3.0	10.13
3.	α-CH_2 and α-CH_3 to aromatics	3-4.5	5.06
4.	Methoxy and Carbohydrates	4.5-6.0	3.80
5.	Aromatics	6-8.5	13.92
6.	Ester and carboxylic acid	8.5-10	5.06

2.2 Experimental methods

2.2.1 Bead-based heterogeneous micromodel fabrication

The flow visualization experiments are conducted using bead-based porous micromodels (Figure 2.2). Polydimethylsiloxane (PDMS from Kevin Electrochem Pvt. Ltd.) is used for micromodel development because of its highly transparent nature during the optical flow visualization process. A soft lithography process has been adopted for micromodel fabrication. It is a low-cost approach to rapid prototyping micro and nanoscale devices using soft substrates (polymers, gels, or organic monolayers) without capital-intensive equipment (Qin et al., 2010). Polymer beads (Dynoseeds TS 500) of diameter 500-600 μm are used to form the matrix in the micromodel. Micromodel development starts with mixing the silicone elastomer base with curing liquid in a prescribed weight proportion (10:1) for at least 10 minutes. The mixing process resulted in significant air bubbles in the solution, which were later removed using a

vacuum desiccator. After degassing, the polymer mix (silicone elastomer base with curing agent) is poured into a petri dish and kept in the oven for 25 min at 60°C for premature curing. The premature curing results in stickiness on the surface of the PDMS slab. When the microbeads (from Dynoseeds TS 500) of diameter 500-600 μm are poured onto the premature PDMS slab, they stick on the PDMS slab. It is again kept for curing at 60°C for 1.5 hours resulting in microbeads to stick and tightly reinforce their ends in the PDMS slab. Cured PDMS is taken out from the oven and cooled at room temperature for 10 minutes. Next, a layer of PDMS is poured into another Petri dish to form a plane slab without any feature and kept in the oven for 25 min at 60°C for premature curing. This plain PDMS slab is placed on top of the previously cured PDMS slab to seal. This complete assembly is again kept in the oven for curing at 60°C for 1.5 hours.

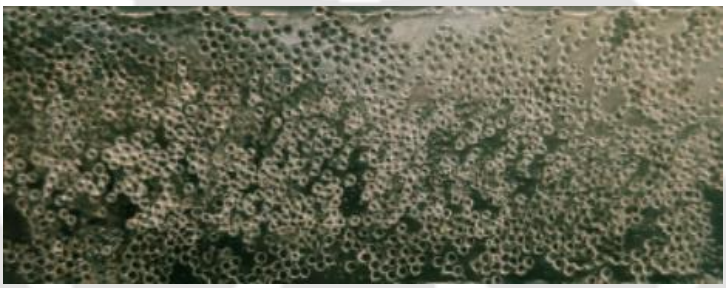

Figure 2. 2 Bead-based heterogeneous porous micromodel

The inlet and outlet holes are punched at the left and right corners of the top slab for fluid entry and discharge. A silicone sealant is put at the junction of both PDMS slices and kept for 6 hrs at the ambient condition to ensure the system is leakage-free. The fabricated micromodel has an inlet, heterogeneous porous medium (4.05 cm × 1.95 cm; length × width), and an outlet. The porous medium contains a random distribution of microbeads (500 μm - 600 μm in diameter) with a porosity of 54%. The effective depth of the micromodel is approximately 400 μm. The depth of the micro model can be controlled by selecting the size (smaller- higher) of microbeads. The depth of the micromodel also depends on the degree of curing of the PDMS

base slab. There are various parameters which can control the micromodel properties (Shirazi et al., 2022).

2.2.2 Beads size selection for micromodel fabrication

The size of the bead mentioned in the current study (500-600 μm) is larger than the typical grain size in the geological porous media. The larger grain size and pore throat dimensions provide better flow visualization using microscopic techniques. A number of literature shows applications of bead-based porous micromodels to investigate the pore-scale velocity field measurement in the porous medium (Datta et al., 2014b; Huang et al., 2008; Lu et al., 2018; Lu et al., 2020; Sabbagh et al., 2020; Sen et al., 2012). The beads size ranges from a few μm to several mm depending on the microscopic or macroscopic flow visualization in the porous medium. The depth of the micro model can be controlled by selecting the size (smaller- higher) of microbeads (Shirazi et al., 2022). The depth of the micromodel also depends on the degree of curing of the PDMS base slab. for example, if the PDMS slab is semi-cured, the beads easily stick and engrave into the semi-cured PDMS slab.

Table 2. 2 Literature on the application of microbeads for micromodel fabrication and flow visualization.

S.N.	Authors	Beads size used for micromodel fabrication
1.	Sen et al., 2012	Microspheres of 200 μm diameter (corpuscular, 0200)
2.	Lu et al., 2018, 2020	50 μm diameter transparent glass sphere and 500 μm diameter food grade sodium chloride.
3.	Huang et al., 2008	Polymethyl methacrylate (PMMA) with a diameter of 7 mm.
4.	Dutta et al., 2014	Hydrophilic glass beads of diameter 76 μm
5.	Sabbage et al., 2020	Spherical borosilicate glass sphere of average diameter 1 mm.

6.	Current work	Polymer beads of diameter 500-600 μm

There are also several literatures available showing the use of 2D porous micromodels with differently shaped micro-posts (de Winter et al., 2020; Haque et al., 2021; Roman et al., 2016; Sharma et al., 2021; Terzis et al., 2019; Wang and Wang, 2017; Zarikos et al., 2018; Zhang et al., 2011). The size (diameter) of the micro-posts ranges from 40 μm to 850 μm.

Table 2. 3 Application of differently shaped micro posts in the porous micromodels.

S.N.	Authors	Micro post size in 2D Porous micromodel
1.	Terzis et al., 2019	Square pillars of 240 μm
2.	Zarikos et al., 2018	Octagonal pillars with a minimum diameter of 92 μm and a maximum diameter of 178 μm.
3.	Zhang et al., 2011	Cylindrical micro-posts with a diameter of 300 μm each.
4.	DeWinter et al., 2020	Square pillars of 240 μm
5.	Haque et al., 2021	Cylindrical-shaped pillar diameter 788 μm, and 850 μm, respectively.
6.	Roman et al., 2016	Cylindrical grains of diameter 40 μm
7.	Wang et al., 2017	Cylindrical micro-posts of diameter 100 μm

2.2.3 Homogeneous micromodel fabrication

Micromodels are fabricated using polydimethylsiloxane (PDMS) with the soft lithography technique. A shadow mask (Master) with a uniform porous structure is used for the fabrication. PDMS base is mixed well with the curing agent in a 10:1 proportion for 10 minutes. The mixture solution (polymer) is degassed under a vacuum using a vacuum desiccator. The shadow mask is put into the petri dish, and the mixture solution is poured over the shadow

mask. The solution is put into the oven for 4 h at 60 °C for curing. Once the solution is cured, the polymer (cured PDMS) is peeled off from the shadow mask. The porous network of the shadow mask is now printed on the cured PDMS. The PDMS slab with the porous network is placed on a thin pre-cured PDMS slab to seal the network. The holes are drilled onto the cured PDMS slice at the left and right corners to provide fluid entry and exit ports. This way, a 2D porous micromodel with uniform cylindrical micro-posts is fabricated (Figure 2.3). Additional information about micromodel fabrication is provided by Haque et al., 2022 and Karadimitriou et al., 2012.

Table 2. 4 Geometrical Characterization of homogeneous porous micromodels

S.N.	Parameters	Micromodel 1	Micromodel 2
1.	micromodel length	4.05 cm	4.05 cm
2.	micromodel width	1.95 cm	1.95 cm
3.	cylinder height	400 μm	400 μm
4.	cylinder diameter	1000 μm	500 μm
5.	pore throat size	400 μm	500 μm
6.	inlet and outlet port diameter	3 mm	3 mm
7.	porosity (φ)	68%	80%

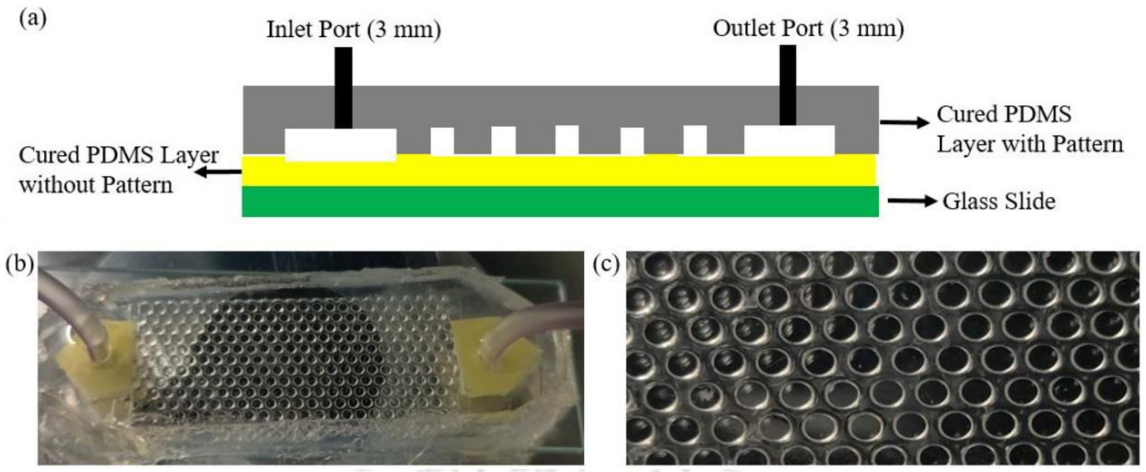

Figure 2. 3 2D porous micromodel (a) schematic diagram of 2D porous micromodel with uniform cylindrical grains, (b) micromodel consisting of cylindrical pillars, and (c) enlarged view of porous media.

2.2.4 Micro-particle image velocimetry

Micro-particle image velocimetry is used to visualize the multiphase flow through the porous medium. Micro-PIV is a non-destructive technique used to probe and measure multiphase flow in porous media directly. It is a non–intrusive, optical flow measurement technique and allows the measurements of the velocity field at a length scale of 100 µm and spatial resolution of 1-10 µm in microfluidic devices (Breuer, 2005; Mielnik and Saetran, 2004). This technique has been used to obtain the pore-scale velocity vector map of immiscible two-phase flow in a porous medium.

2.2.4.1 Principle of micro-PIV

The working fluid is seeded with micron-size, neutrally buoyant fluorescent tracer particles. The micro-PIV technique tracks these micro particles in the flowing fluid as the particles will have a similar velocity to the flowing fluid. A light source (laser or a mercury lamp) is used to volumetrically illuminate the fluid flow and excite the fluorescent tracer particles. In this technique, two successive images of tracer particles in the flowing fluid are captured at a time

delay (Δt) using a high-speed camera. These images are divided into several interrogation windows. Positions of tracer particles are compared in successive images. Cross-correlating the successive images yields the displacement of the tracer particles. The ratio of displacement and the time delay between successive images gives the velocity of tracer particles, representing the velocity of the flowing fluid.

The tracer particles are selected for flow visualization based on certain conditions. The particles should faithfully follow the flow; particles should have a density closely matching that of the suspending fluid; the particles should be large enough to dampen the effects of Brownian motion. When seed particles become sufficiently small, particle-fluid interactions give rise to random particle movement, preventing particles from following the flow faithfully. The effects of Brownian motion on μ-PIV measurements were considered by Santiago et al. [3]. With D being the Stokes-Einstein diffusion coefficient of a particle suspended in a fluid moving at a uniform velocity u, the relative error ε_B in the measured particle displacement during a time interval, Δt may be estimated as:

$$\varepsilon_B = {}^{1}/_{u}\sqrt{{}^{2D}/_{\Delta t}} \quad (1)$$

The equation shows that the effect of Brownian motion becomes lesser important as the flow velocity increases. The error arising from Brownian motion is random and may be considerably reduced by averaging over a population of particles.

2.2.4.2 Micro-PIV system components

The schematic diagram of the μ-PIV experimental setup is shown in Figure 2.4. A syringe pump (New Era NE-1000) connected to a liquid vessel (containing a wetting or nonwetting phase) applies a constant injection rate into the 2D micromodel. A porous micromodel is placed under the inverted microscope IX-83 (Olympus) for flow visualization. The objective lens with

magnifications of 4×,10×, and 20×, with numerical apertures of 0.10, 0.25, and 0.45, respectively, are used in the experiments for flow visualization. The fluorescence illumination source (high-pressure mercury lamp) is used to illuminate the desired region of interest in the micromodel. A high-speed CMOS (complementary metal oxide semiconductor) camera, Phantom VEO 640 L (maximum resolution 2560 × 1600), is used to capture the image sequence, and dynamic studio (Dantec dynamics) software is used for pre-processing and post-processing of the images. Experiments are conducted at room temperature and atmospheric pressure.

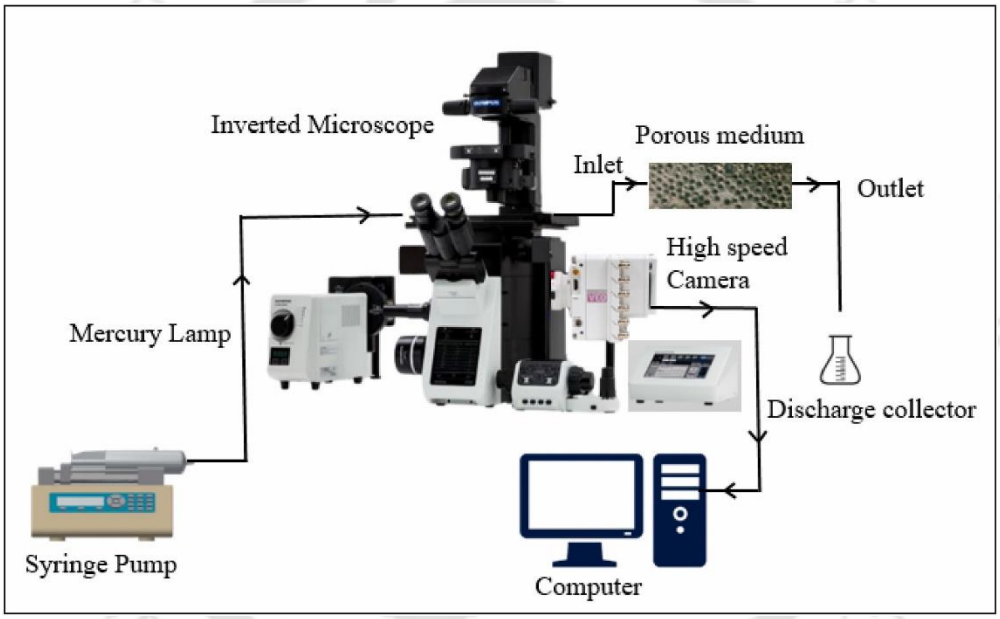

Figure 2. 4 Schematic diagram of micro-particle image velocimetry system

2.2.4.3 Image processing

Image processing is executed to improve the image quality and extract the relevant quantitative information using a commercial software dynamic studio (Dantec dynamics). Image processing comprises of image calibration, pre-processing, background removal, image masking, adaptive PIV algorithm for vector calculation, and post-processing of velocity vectors to extract the parameters such as velocity magnitude, vorticity, and shear rate (Figure 2.5). An

ensemble of 300 images captured during fluid flow in a heterogeneous porous micromodel are imported and calibrated using a scale factor. Image pre-processing is performed to increase the resolution and contrast to improve image quality. The background removal process is executed to remove noise from the image sequence. This process involves the calculation of image minima, showing the background noise due to settled particles and reflection from the boundaries. The image minima is subtracted from an ensemble of raw images to eliminate the background noise and improve the signal-to-noise ratio. The image maxima is calculated and used to apply the mask to eliminate the region of no interest or no fluid flow regions. An adaptive PIV algorithm is applied for velocity vector calculations using the image sequence. The set of the pre-processed image is divided into several interrogation windows. The average displacement of a group of particles (Δx) in the interrogation window from successive images is measured using cross-correlation. The frame rate of the images gives the value of the time delay between the images (Δt). The ratio of particles displacement in an interrogation window from one image to the next image by time delay (Δt) between the successive images gives the velocity vector ($\vec{v} = \frac{\Delta x}{\Delta t}$) in that interrogation window. Similarly, the velocity vectors for all the interrogation regions are obtained to get the velocity vector field. The false or spurious vectors are removed using a universal outlier detector and substituted based on a normalized median test using neighboring vectors. A grid step size of 16×16 and an interrogation area range of 32×32 to 64×64 are used during image post-processing. The vector statistics is calculated to give a mean velocity vector field which is used to calculate streamlines, two orthogonal components (U and V) of the velocity vector, velocity magnitude, and its contours, vorticity, and shear rate. The following equation defines the vorticity at a point (3D motion),

$$\bar{\omega} = \nabla \times \bar{U} = \left(\frac{\partial W}{\partial y} - \frac{\partial V}{\partial z}\right)\bar{\imath} + \left(\frac{\partial U}{\partial z} - \frac{\partial W}{\partial x}\right)\bar{\jmath} + \left(\frac{\partial V}{\partial x} - \frac{\partial U}{\partial y}\right)\bar{k} \quad (2)$$

Here, *U*, *V*, and *W* are velocity's x, y, and z components. In 2D (having only the x- and y components of velocity), the fluid element rotates about the z-axis, and the vorticity is given by

$$\omega_z = \frac{\partial V}{\partial x} - \frac{\partial U}{\partial y} \quad (3)$$

The following expression evaluates the shear rate γ.

$$\gamma = \frac{\partial V}{\partial x} + \frac{\partial U}{\partial y} \quad (4)$$

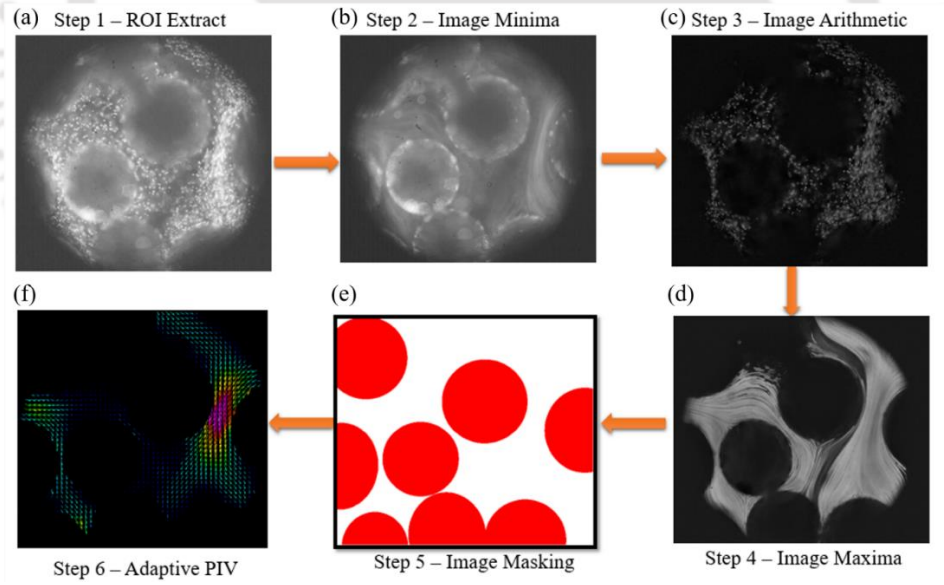

Figure 2. 5 Image processing sequence: (a) Region of interest (ROI) extract, (b) Image minima of an ensemble of images, (c) Image arithmetic process, (d) Image maxima of a set of images, (e) Masking of regions without fluid flow, (f) Vector calculation using adaptive PIV algorithm.

2.2.5 Core flooding

The macroscopic investigation of oil recovery during different flooding processes is executed using the Idaho core sample purchased from Kocurek Industries (Texas). Core flooding setup consists of a high-pressure syringe pump, two floating piston accumulators (for crude oil and aqueous phase), a hassler core holder, a manual hydraulic pump, and a core of size 1 inch × 4 inch (Figure 2.6). The syringe pump injects light paraffin oil through piping in the floating piston accumulator, where the oil pushes the piston upward to displace the test fluid (Low saline water, polymer solution, alkaline-polymer solution, and alkali-surfactant-polymer solution) out of the accumulator towards the core holder assembly. Two pressure transducers are installed at the inlet and the outlet of the core holder to investigate the differential pressure during the flooding process. A hand-operated hydraulic pump gives the overburden pressure in the core holder using hydraulic oil, and the pressure can be monitored using a pressure gauge. The core flooding procedure involves several steps. The core plug dry weight and dimensions are measured for porosity calculation. The core plug is saturated in saline water with 0.5 wt.% NaCl for 2 hours using a vacuum desiccator. The wet weight of the core plug is measured, and the pore volume of the core is calculated using the difference between the wet and dry weight to saline water density. The ratio of pore volume to bulk volume gives the porosity of the sandstone core. The apparent permeability of the core plug is measured by setting up the core flooding system for a single-phase flow. The brine is introduced at 0.5 ml/min in the Idaho core to get the pressure difference across the core plug system. The apparent permeability of the core plug is measured using core plug dimension, flow rate, brine viscosity, and pressure differential. The drainage process is initiated by saturating the core with the crude oil at a flow rate of 0.2 ml/min until no more brine is produced. The drainage process creates a reservoir-like condition for fluid distribution in the porous domain.

The core is saturated with 95% crude oil and 5% connate water saturation using 3-4 PV of the crude oil injection. Imbibition experiments are conducted by injecting 1.2 PV low salinity water at 0.1-0.5 ml/min in the core until no more oil is produced. The overburden pressure of 2000 psia and back pressure of 515 psia are used during the core flooding process. A considerable volume of residual oil remained confined after low salinity water flooding. After that, 0.7 PV of polymer solution (HPAM) is injected at 0.1-0.2 ml/min in the core plug to displace the residual oil after water flooding. A small fraction of the crude oil is produced using polymer flooding. The alkali-polymer flooding process is also performed to maximize residual oil recovery from the porous medium. Alkali-polymer solution (1.1 PV) and alkali-surfactant-polymer solution (2.64 PV) are injected one after another at a rate of 0.1-0.2 ml/min in the core plug, and the amount of residual oil produced is measured.

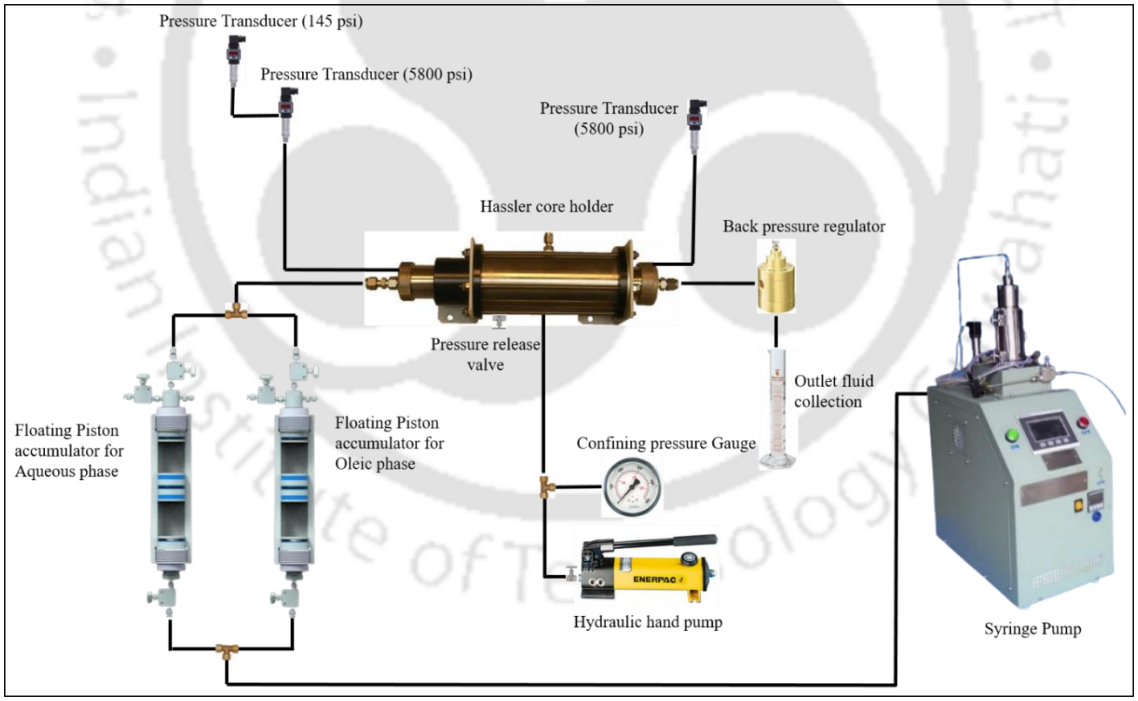

Figure 2. 6 Schematic diagram of core flooding experimental set-up.

2.2.6 Density and API gravity of crude oil

The crude oil's density is measured using a specific gravity bottle / Pycnometer. Initially, the specific gravity of the crude oil relative to water is measured. The specific gravity of the crude oil is measured by the ratio of crude oil density to water density. The following formula is used to calculate the API gravity of the crude oil (Ahmed et al, 2001);

$$°API = (141.5/SG) - 131.5 \quad (5)$$

2.2.7 Acid value

The acid value is defined as the amount of KOH in mg required to neutralize one gram of the sample. It was evaluated using the American oils chemistry society (AOCS) official methods (Te TA-64, 1997). The following formula is used to measure the acid value of crude oil (Zhang et al., 2015).

$$Acid\ value = (N \times V \times 56.1)/M_s \quad (6)$$

Where N, V and M_s Normality of NaOH, the volume of titrant (ml), and mass of sample (gm), respectively.

2.2.8 Viscosity and emulsification test

The viscosity of crude oil, chemicals, and emulsions is analyzed using Rheometer (Anton Paar, MCR 301). The viscosity of the samples is measured using a 1° cone and plate geometry at room temperature (25℃) by varying the shear rate from 0 – 200 s^{-1}. The viscosity of most of the samples is reported at a 1 s^{-1} shear rate. All the data is stored and extracted by Rheoplus V3.1 software. Crude oil–alkaline solution and crude–nanofluid emulsions are prepared by

mixing them in equal proportion using an ultrasonic homogenizer. The viscosity of the emulsion is measured using Rheometer.

2.2.9 Surface and interfacial tension

The surface tension of different alkali solutions and crude oil-treated alkali solutions was analyzed using a tensiometer (Kwoya – DY300) by the Wilhelmy plate method. Initially, the plate was cleaned by burning red hot to remove the impurities. The alkaline solution is poured into a glass vessel up to a level and placed at a dedicated place in the instrument. The system is calibrated to initialize the experiment. The measurement button on the instrument was pressed so that the plate automatically dipped into the alkaline solution and pulled out of it. The reading on the instrument represents the surface tension of the aqueous phase. The same equipment was also used to measure the interfacial tension between glycerol water solution and silicone oil of 10 cSt, 50 cSt, and 345 cSt. During IFT measurement, the dense phase (Glycerol-water solution) is first poured into the glass vessel. Thereafter, the light phase (silicone oil) is poured on top of the dense phase without disturbing the surface. At the time of IFT measurement, the Du Nouy ring is dipped in the sample up to the interface. Once this ring moves up the interface, IFT reading is obtained.

The dynamic interfacial tension between the crude oil and aqueous phases, such as alkaline solution and silica nanofluids, was measured using a spinning drop tensiometer (Kruss- Site 100) at the atmospheric condition. The heavier phase (ρ_h) was poured into the cylinder connected to the capillary tube, and a micro syringe injected lighter-phase (ρ_l) crude oil into the capillary tube. The angular velocity is represented by ω. The rotation per minute (rpm) was maintained at 4000-5000 rpm, and the droplet length (L)-to-diameter (D) ratio to be ≥ 4. The IFT value is calculated using the following formulation (Saha et al., 2018a).

$$\sigma = r^3\omega^2(\rho_h - \rho_l)/4 \quad ; \quad L/D \geq 4 \qquad \textbf{(7)}$$

2.2.10 Field emission scanning electron microscope (FESEM) and Energy Dispersive X-ray (EDX)

Field emission scanning electron microscope (FESEM) analysis was performed using Zeiss sigma equipment by placing the powdered sample of nanoparticles and sandstones in the carbon tape attached to the sample holder, also called stub. The sample is coated with gold to reduce the charging. EDX analysis is performed with an EDX detector to determine the elemental composition of the samples, such as nanoparticles and rock powders.

2.2.11 Particle size analyzer and zeta potential

The nanofluid stability is measured based on the zeta potential and the particle size analysis. It is measured by dynamic light scattering using particle size analyzer (Beckman Coulter- Delsa Nano). The nanofluid sample was poured into the cuvette and placed inside the instrument at its dedicated place. A laser beam was illuminated, and the fluctuations in the laser beams due to Brownian motion were detected to calculate the particle size distribution and the zeta potential.

2.2.12 Contact angle measurement

The contact angle is measured using an in-house built setup consisting of a high-speed camera (Phantom VEO 640 L), a LED light, and XYZ hallmarc stage to put the cylindrical rock pellet. The drop shape analysis plugin of Image J software is used to find out the contact angle from the images. The Berea core pellet is cut into pieces and saturated with crude oil for three weeks at 60℃. The oil-saturated pellet is further saturated with the nanofluids for 24 hrs. and washed with deionized water. The rock sample was then dried at 40℃ for 24 hrs. The rock sample was submerged in the water container, and an oil droplet was placed carefully on the pellet's surface. The images of the drop are captured, and the contact angle is measured in the image J software using the drop shape analysis plugin.

2.3 Simulation methods

2.3.1 Phase field method

The phase field method is a dynamic numerical simulation (DNS) method. It is popular due to its ability to handle complex pore geometries and topological changes. The phase field method (PFM) realistically captured phenomena related to viscous and capillary forces with a reasonable computational time. PFM not only addresses the interface in the flow but also ensures that the system's total energy is minimized. For modeling two-phase flow in pore geometries, the phase-field method is advantageous as it ensures both mass conservation and accurate representation of interface curvature. In this method, the Navier-Stokes equation is coupled with the Cahn-Hilliard equation and numerically solved using the finite element method. The Cahn-Hilliard equation tracks the diffuse interface separating the immiscible phases.

2.3.2 Mathematical modeling of Phase field method

The displacement of oil by water from the dead-end pore is investigated using the Phase Field method. The following assumptions are considered while performing the simulations. Water and oil are assumed to be Newtonian, incompressible, and there is no mass transfer across the interface. The fluid properties, such as viscosity, density, and surface tension are assumed to be constant. The gravity is neglected as numerical simulations are performed in a 2D geometry. The bond number (ratio of gravitational force to surface tension force) is calculated for the fluid flow in complex pores such as contraction-expansion pores. A significantly small value of bond number 2.08×10^{-5} is obtained, showing the gravitational force is low enough. Hence gravity term is neglected during numerical simulations. The two-phase flow dynamics are governed by a Cahn-Hilliard equation in the Phase Field method. In this method, the Navier-Stokes equation is coupled with the Cahn-Hilliard equation and numerically solved using the

finite element method. The Cahn –Hilliard equation tracks the diffuse interface separating the immiscible phases. The fourth-order Cahn–Hilliard equation is decomposed by the COMSOL solver into two second-order equations using an auxiliary parameter (ψ).

At the oil-water interface, the Cahn-Hilliard equation can be represented as

$$\frac{\partial \varphi}{\partial t} + u.\nabla\varphi = \nabla.\frac{\gamma\lambda}{\varepsilon^2}\nabla\psi \tag{8}$$

$$\psi = -\nabla.\varepsilon^2\nabla\varphi + (\varphi^2 - 1)\varphi \tag{9}$$

Where φ is the phase-field parameter. It represents the oil-water interface when $-1 < \varphi < 1$. u is the fluid velocity (m/s). γ is the mobility (m^3.s/kg), λ is the mixing energy density (N), ε represents the oil-water interface thickness (mm), ψ is the phase-field help variable. $\gamma = \chi\varepsilon^2$, where χ is the mobility parameter, which determines the timescale for Cahn-Hilliard diffusion. For good initial approximation, χ is considered as 1.

The surface tension (σ) coefficient depends on oil-water interface thickness (ε) and mixing energy density (λ) which can be represented by

$$\sigma = \frac{2\sqrt{2}\lambda}{3\,\varepsilon} \tag{10}$$

The interface thickness (ε) can be estimated as half of the maximum grid size (h_c).

The volume fraction of individual fluids is calculated using the following equations,

$$V_{fw} = \frac{(1-\varphi)}{2} \tag{11}$$

$$V_{fo} = \frac{(1+\varphi)}{2} \tag{12}$$

Where, V_{fo} is the volume fraction of crude oil and V_{fw} is the volume fraction of water.

Density and viscosity of the mixture to vary smoothly over the interface,

$$\rho = \rho_w + (\rho_o - \rho_w)V_{fo} \quad (13)$$

$$\mu = \mu_w + (\mu_o - \mu_w)V_{fo} \quad (14)$$

Where, ρ_w is the density of water, ρ_o is the density of crude oil, V_{fo} is the volume fraction of crude oil, μ_w is the dynamic viscosity of crude oil, and μ_w is the dynamic viscosity of water.

Mass and Momentum Transport

The two-phase flow in the porous medium can be depicted by Navier- Stokes equations. The surface tension term has been added to the model to account for capillary effects.

The momentum and continuity equations can be expressed as

$$\rho\frac{\partial u}{\partial t} + \rho(u.\nabla)u = \nabla.[-pI + \mu(\nabla u + (\nabla u)^T)] + F_{st} + \rho g \quad (15)$$

$$\nabla.u = 0 \quad (16)$$

Where ρ denotes the fluid density (Kg/m^3), μ is the dynamic viscosity (mPa.s) of the fluid, u represents the fluid velocity (m/s), F_{st} is the surface tension force acting at the oil-water interface, p denotes the pressure (pa), and g is the gravity vector (m/s^2).

The surface tension F is given by,

$$F_{st} = G\nabla\varphi \quad (17)$$

Where G is the chemical potential

$$G = \lambda\left[-\nabla^2\varphi + \frac{\varphi(\varphi^2-1)}{\varepsilon^2}\right] = \frac{\lambda}{\varepsilon^2}\psi \quad (18)$$

The boundary conditions applied to the dead-end and contraction-expansion pore model include velocity (**u** = 0.001 m/s) at the pore-throat inlet and pressure (P = 0) at the outlet. A wetted-wall boundary condition is applied to all the walls of the pore models. In this boundary condition, the motion of the oil-water interface at the wetted-wall boundary is zero, indicating a no-slip condition (**u** = 0). The contact angle is dependent on the phase field variable (φ) and capillary width (ε), which is representative of interface thickness.

$$\boldsymbol{n}.\varepsilon^2\nabla\varphi = \varepsilon^2 cos\theta|\nabla\varphi| \quad (19)$$

$$\boldsymbol{n}.\gamma\nabla(\zeta) = 0 \quad (20)$$

Where θ is the contact angle through the oil medium and **n** is the normal vector.

Chapter 3. Pore-scale velocity field measurement during nanofluid-assisted alkaline flooding

Micromodel;

Enhanced Oil Recovery;

Microscale Particle Image Velocimetry;

Nanofluid flooding;

Porous medium

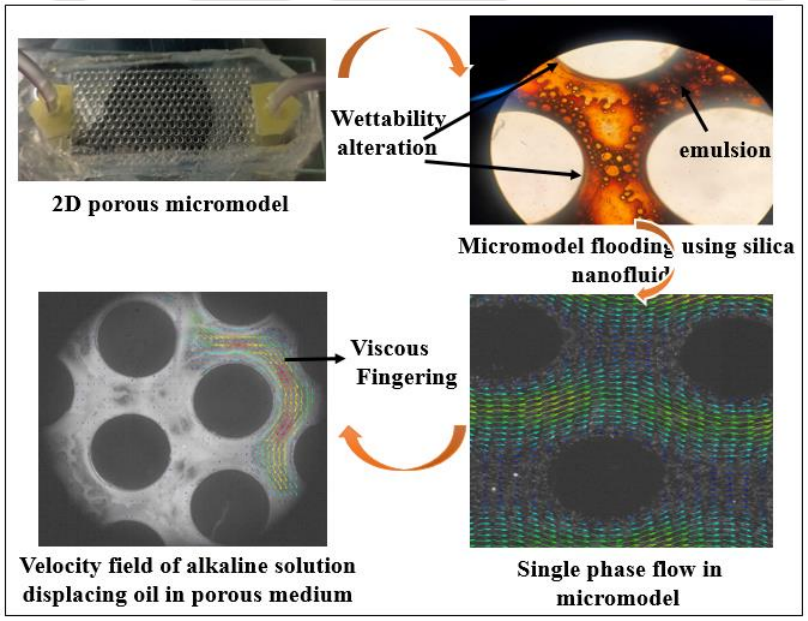

Pore-scale velocity field measurement during nanofluid-assisted alkaline flooding

In this chapter, we report experimental investigations on pore-scale flow dynamics during two-phase flow in a micromodel using the microscale-particle image velocimetry (μ-PIV) technique. The combined effect of alkali (sodium carbonate) and nanoparticles (silica) on oil recovery is investigated using interfacial tension, rheology, emulsification, contact angle, chemical flooding, and micro-PIV measurement. Dynamic interfacial tension (IFT) measurement shows that silica nanoparticles reduce the interfacial tension between crude oil and nanofluid to ultra-low value (0.01 mN/m). Reduction in IFT results in a stable micro-emulsion formation. A microscopic study reveals that the silica nanoparticle reduces the average droplet size to 3 μm in the emulsion by covering oil droplets all over, resulting in the reduced coalescence of droplets. Silica nanoparticles significantly altered the wettability by changing the contact angle from 71.5° (DI water) to 22° (0.15 wt.% SiO_2). The literature is unavailable regarding the quantitative measurement of the pore-scale velocity field in 2D porous micromodel for alkaline and silica nanofluid flooding. Therefore, a pore-scale flow field is obtained to understand the flow pattern, and pore scale events including piston-like displacement, and viscous fingering during crude oil and nanofluid interaction within the porous medium. Silica nanoparticles and Na_2CO_3 help in IFT reduction, emulsification, wettability alteration, and mobility control by rheology modification, which assists in the stable displacement of oil from the porous medium.

3.1 Interfacial tension analysis

Dynamic IFT behavior is analyzed for crude oil/alkaline solution (0.2, 0.4, 0.5, 0.6, 0.8, 1.0 wt.% of sodium carbonate), and the results are shown in Figure 3.1a. Results showed that the minimum interfacial tension (0.052 mN/m) is achieved using an alkaline solution with 0.6 wt.% of sodium carbonate. Usually, the alkaline solution interacts with the acidic part (carboxylic acid) of the crude oil and forms an in-situ surfactant. The in-situ surfactant (petroleum soap) accumulates at the interface of alkaline solution and crude oil, thereby reducing the interfacial tension. The in-situ surfactants either diffuse into the crude oil or aqueous solution, depending on their affinity (Pei et al., 2013a). In the present study, as alkali (Na_2CO_3) interacts with the crude oil at their first contact, minimum IFT is observed. With time, the generation rate of the in-situ surfactant at the interface decreases compared to the diffusion rate into either the aqueous phase or oil. As soon as the surfactant generates, it diffuses into the aqueous or oleic phase depending on its affinity, which results in an increase of interfacial tension as a function of time (Figure 3.1). A similar trend for dynamic interfacial tension values between alkali (Na_2CO_3) and heavy crude oil has also been observed in previous literature (Ge et al., 2012).

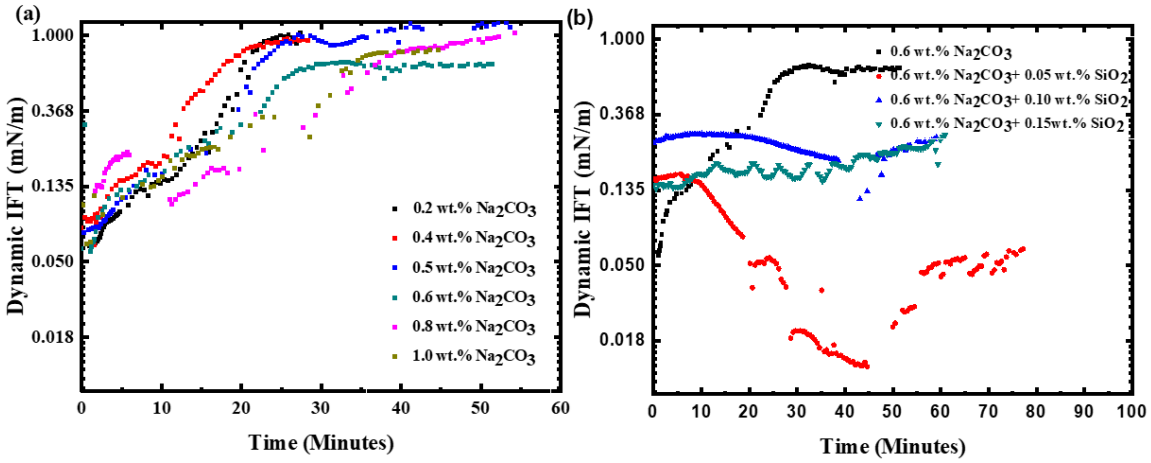

Figure 3. 1 Dynamic IFT measurement (a) Dynamic IFT between crude oil and alkaline solution without silica nanoparticles (b) Dynamic IFT between crude oil and silica nanofluid.

The generation of in-situ surfactant can be observed by performing surface tension analysis of the emulsion and FTIR analysis (Figure 3.2).

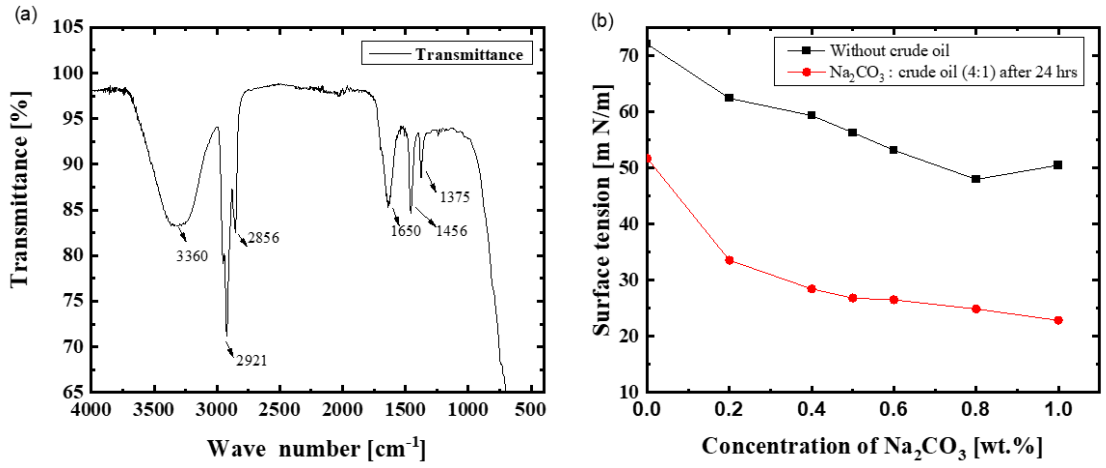

Figure 3. 2 Investigation of generation of in-situ surfactant using (a) FTIR analysis of crude oil/ alkaline solution (1:4) emulsion, (b) Surface tension analysis.

In-situ surfactant generation is confirmed by FTIR analysis of a mixture of crude oil and alkaline solution. After treatment of the crude oil with Na_2CO_3 solution, its IR spectrum is analyzed. The spectrum around 1650 cm^{-1} indicates the formation of petroleum soap or surfactant, which plays a crucial role in reducing the IFT value (Samanta et al., 2011) (Figure 3.2a). Surface tension tests are performed to analyze the generation of in-situ surfactant during alkali crude oil interaction. Initially, the surface tension of alkali (Na_2CO_3) at 0.2, 0.4, 0.5, 0.6, 0.8, and 1 wt.% is measured, which shows reduced surface tension from 62.39 to 50.5 mN/m. Crude oil is treated with an alkaline solution and aged for 24 hrs. The surface tension value of alkali-treated crude oil is drastically reduced from 33.57 mN/m to 22.87 mN/m, as shown in Figure 3.2b. The difference in surface tension of alkaline solution (50.5 mN/m) and alkali-treated crude oil (22.87 mN/m) is because of in-situ surfactant generation in the case of alkali-treated crude oil. The effect of silica nanoparticles on interfacial tension between the crude oil

and alkaline solution has been studied. Three samples of silica nanofluid are formulated by adding silica particles at a concentration of 0.05, 0.10, and 0.15 wt.%. IFT was reduced to a value of 0.01 mN/m using 0.05 wt.% of silica nanoparticles (Figure 3.1b). Silica nanoparticles form a layer at the water and crude oil interface, causing a decrease in the interfacial tension between the immiscible phases. Therefore, silica nanoparticles can be used to recover additional crude oil by reducing the IFT to an ultra-low value.

3.2 Wettability alteration

The nanoparticles help in wettability alteration depending on the choice of nanoparticles. The Silica nanoparticles in an alkaline solution settle at the solid surface with time, forming a wedge shape. The layer of deposited nanoparticles applies a disjoining pressure over the crude oil droplets, which results in the detachment of the oil droplet from the surface (Rostami et al., 2020). The contact angle is measured on the crude oil-saturated sandstone rock slice, which shows a contact angle reduction from 71.56° (DI water) to 38.3° (0.8 wt.% Na_2CO_3). The contact angle is reduced from 71.56° (DI water) to 22° using a silica nanoparticle-assisted alkaline solution (Figure 3.3). The range of fluctuation in the contact angle for different formulations was 1.4°-2.6°. In the Figure, DIW, SW, and SNF stand for deionized water, saline water, and silica nanofluid/ silica nanoparticle-assisted alkaline solution, respectively. The contact angle of alkaline solution with 0.6 wt.% Na_2CO_3 is measured as 56.48° on a PDMS slice. This way, silica nanoparticles alter wettability, and additional crude oil can be recovered.

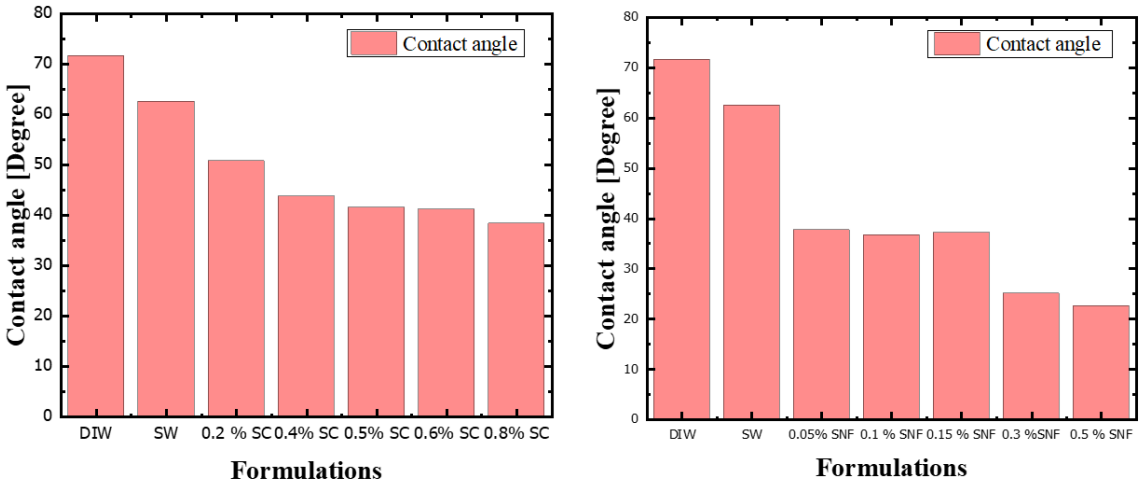

Figure 3. 3 Contact angle measurement for (a) increasing concentration of alkali (sodium carbonate), (b) increasing concentration of silica nanoparticle-assisted alkaline solution.

3.3 Viscosity and microstructure of emulsion

The interaction of crude oil and alkaline solution (at 0.1, 0.3, 0.5, 0.7, 0.9, 1 wt. % of sodium carbonate) in the porous medium results in in-situ emulsification. The rheology of this emulsion is analyzed, and the results are shown in Figure 3.4a. The rheological study shows the shear-thinning behavior of the emulsion. The viscosity of the emulsion is found to increase with an increase in the concentration of alkali (Na_2CO_3). The observation also confirms that the viscosity of the emulsion is significantly high, which causes the displacement of crude oil to be nearly uniform and reduces the severity of viscous fingering.

The effect of silica nanoparticles on the physicochemical properties of the emulsion is also studied. The silica nanoparticles are added in alkaline solution at a concentration of 0.05, 0.1, 0.3, and 0.5 wt.%. The emulsions formed by the interaction of these silica nanofluids with crude oil are analyzed, and the result is shown in Figure 3.4b. Silica nanoparticles in the emulsion further increase the viscosity. As nanoparticle concentration is increased, the emulsion viscosity is further increased. A shear-thinning behavior of emulsion is observed

during viscosity measurement. The higher viscosity of emulsion results in a good sweep efficiency, eliminates viscous fingering and delays the breakthrough of the aqueous phase.

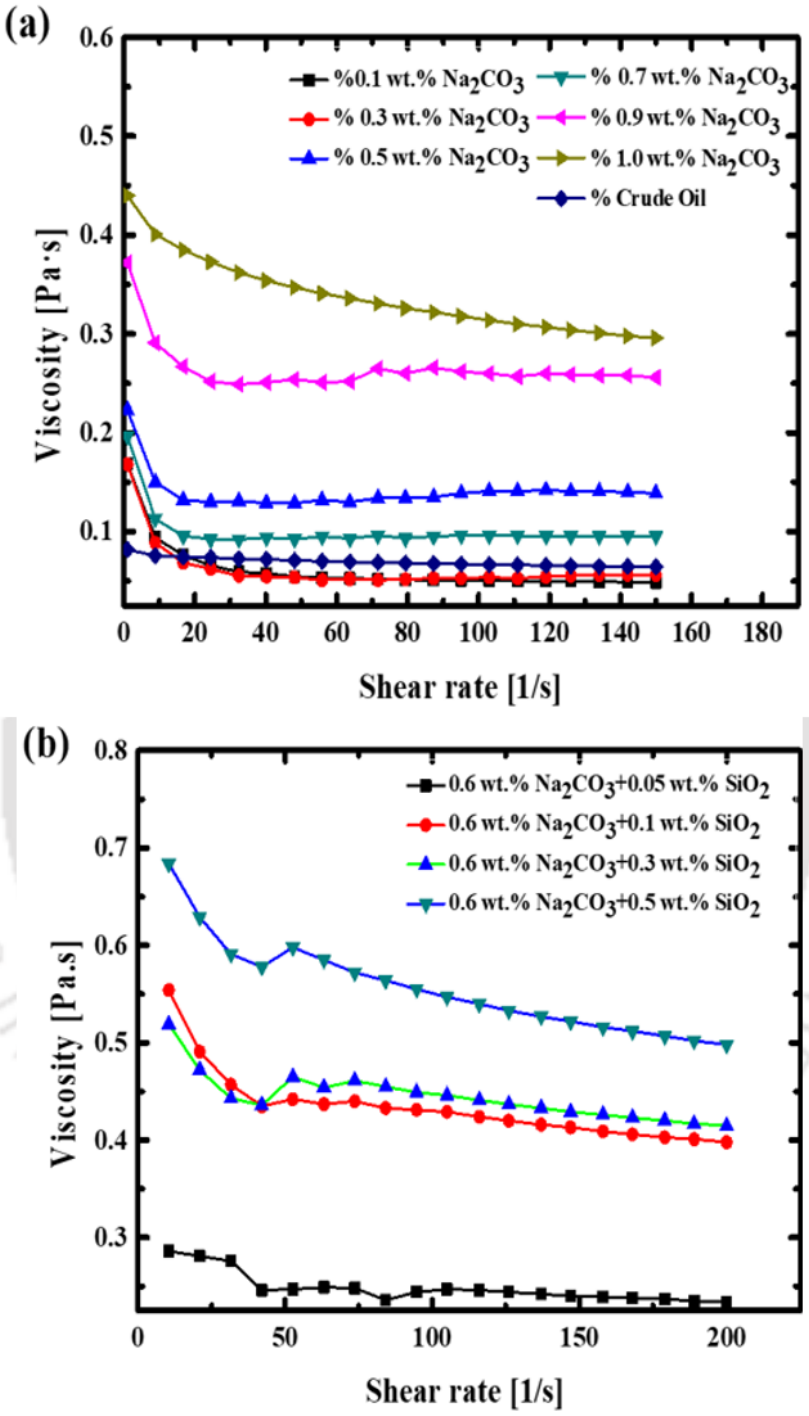

Figure 3. 4 (a) Viscosity of the water-oil emulsion at various concentrations of Na_2CO_3, (b) Effect of silica nanoparticles on the shear viscosity of the emulsion.

The formation of thermodynamically stable emulsion is essential for additional crude oil recovery. Microemulsion can be differentiated from regular emulsion based on the IFT between the two phases, droplet size within the emulsion, long-lasting property, and thermodynamic stability (Unsal et al., 2016). Several studies have reported that in a microemulsion, the IFT between the two phases reaches an ultra-low value (10^{-2} to 10^{-3} mN/m), and the typical droplet size should be less than 100 μm (Koh and Wong, 2019; Unsal et al., 2016; Unsal et al., 2019). In the present study, the dynamic interfacial tension between the crude oil and silica nanofluid is obtained in the range of 10^{-2} to 10^{-3} mN/m (Figure 3.1b), and the average droplet size is 3 μm (Please see Figure 3.5b, d for the droplet size distribution).

The quality of any emulsion can be based on the IFT value between the two phases, droplet size within the emulsion, long-lasting properties, and thermodynamic stability. The rheological study of the emulsion between nanofluid and crude oil at temperatures 50℃ and 60℃ confirms its thermal stability (Figure 3.6).

The emulsion formed due to the interaction of crude oil and the aqueous alkaline solution is visualized under the microscope (Figure 3.5a). The droplet size distribution of emulsion shows that the average droplet diameter of emulsion (crude oil /alkaline solution) is 13 μm (Figure 3.5c). It is observed that the droplet diameter of the emulsion increases with time due to the coalescence of droplets, indicating an unstable emulsion. The effect of silica nanoparticles on emulsion is also visualized in this study (Figure 3.5b). Although a few studies suggest that the microemulsion has droplet size in the nanometre range. In this study, the droplet size distribution of emulsion shows that few droplets are near the nanometre range, whereas some droplets are in the micrometer range with an average droplet size of 3 μm (Figure 3.5d). The variance of the emulsion (crude oil /alkaline solution) droplets without silica nanoparticles is

66.12 µm. However, the variance of emulsion droplets with silica nanoparticles decreased to 1.40 µm. It can be observed that the droplet size and their numbers are changing significantly by adding silica nanoparticles. The addition of silica nanoparticles in the alkaline solution causes a decrease in the droplet size and an increase in the number of droplets. During the interaction of silica nanofluid and crude oil, nanoparticles adsorb at the liquid-liquid interface and stabilize the emulsion. Silica particles enhance the strength of the mechanical barrier effect around oil droplets by covering them all over, resulting in the reduced coalescence of droplets. In the presence of alkali (Na_2CO_3) and silica nanoparticles, electrostatic and steric effects are the leading cause for the stability of the emulsion. The addition of silica nanoparticles reduces the interfacial tension between the two phases, thereby decreasing the droplet size and improving emulsion stability by stabilizing the droplet size (Pal and Mandal, 2020).

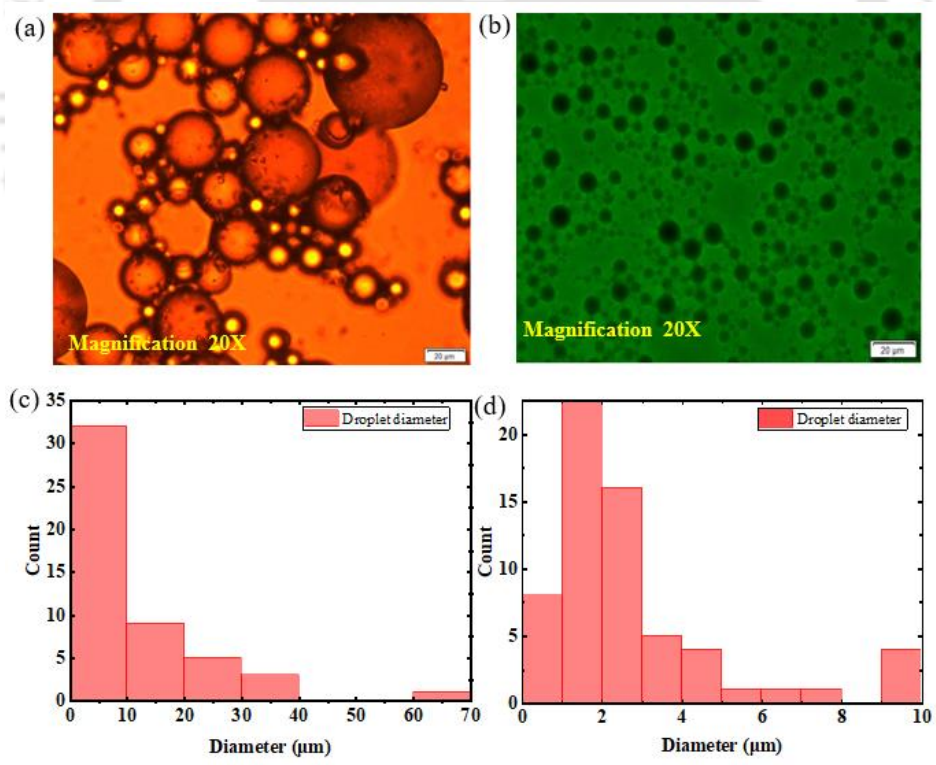

Figure 3. 5 Microscopic analysis of crude oil and alkaline solution emulsion, (a) Without silica nanoparticles, (b) With silica nanoparticles, (c) Droplet size distribution of emulsion without silica nanoparticles, (d) Droplet size distribution of emulsion with silica nanoparticles.

The stability of the emulsion is measured using dynamic light scattering and zeta potential. Zeta potential measures the electrostatic repulsion between the charged droplet surface. Its value should be ±30 mv for sufficient repulsion between the charged droplets (Kumar and Mandal, 2018; Maurya and Mandal, 2018). Zeta potential value of emulsion formed using crude oil and 0.05 wt. % silica nanofluid is -45 mv, which confirms the stability of the emulsion. The emulsion stability is measured as a function of time which shows that the emulsion is stable after 12 days (Figure 3.7).

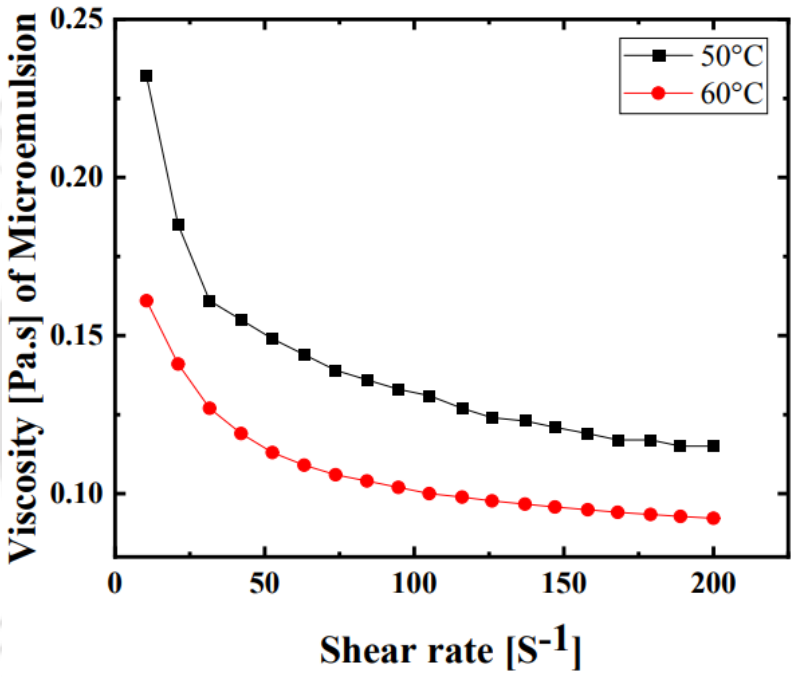

Figure 3. 6 Microemulsion stability as a function of time and temperature.

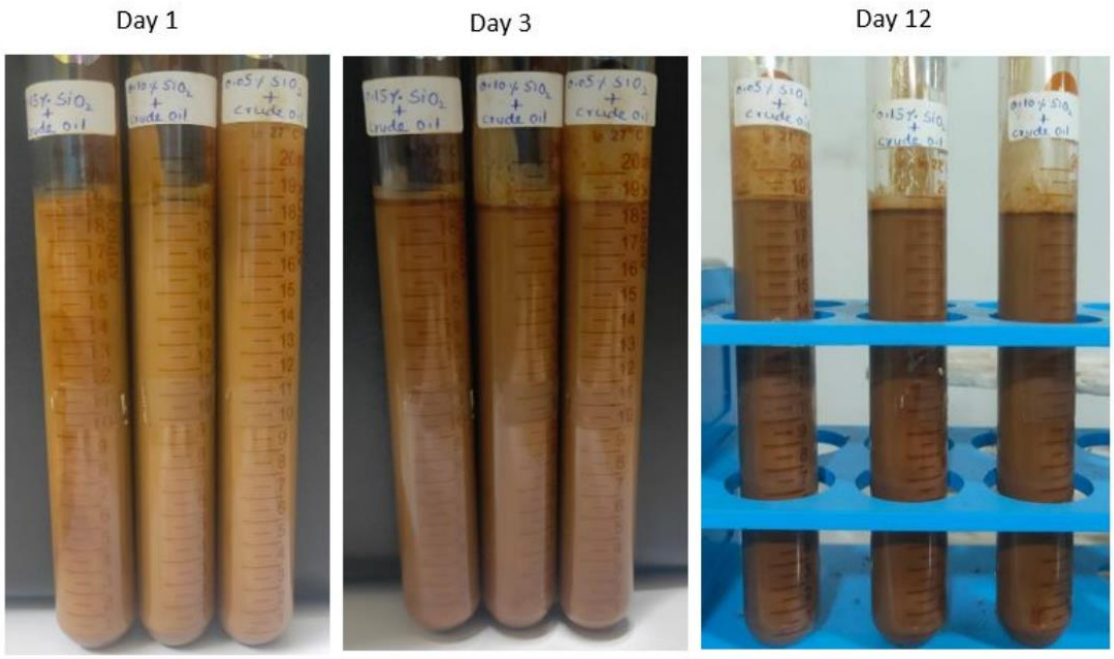

Figure 3. 7 Emulsion stability as a function of time.

3.4 Flow visualization of alkaline flooding

Two sets of flooding experiments are performed in which aqueous phases, including alkaline solution and silica nanofluid, are considered as a non-wetting phase, whereas crude oil is used as a wetting phase. Alkaline flooding experiments are performed with the 2D porous micromodel, and the results are visualized in Figures 3.8a and 3.8b. Results showed the growth of fingers (viscous fingering phenomena) due to the significant difference in the viscosity of crude oil and alkaline solution leading to an unfavorable mobility ratio. Oil film on the cylinder wall is visualized during and after flooding, which confirms that significant wettability alteration has not happened in the case of alkaline flooding. A considerable amount of residually trapped crude oil is also visualized in the pore throat zones (Figure 3.8a, 3.8b). Silica nanofluid flooding is also performed in a 2D porous micromodel to understand the effect of silica nanoparticles on wettability alteration, and results are shown in Figure 3.8c. It is observed that the oil film is absent at some places within the porous medium (or partially available) around the cylinder, which means that the wettability is significantly altered.

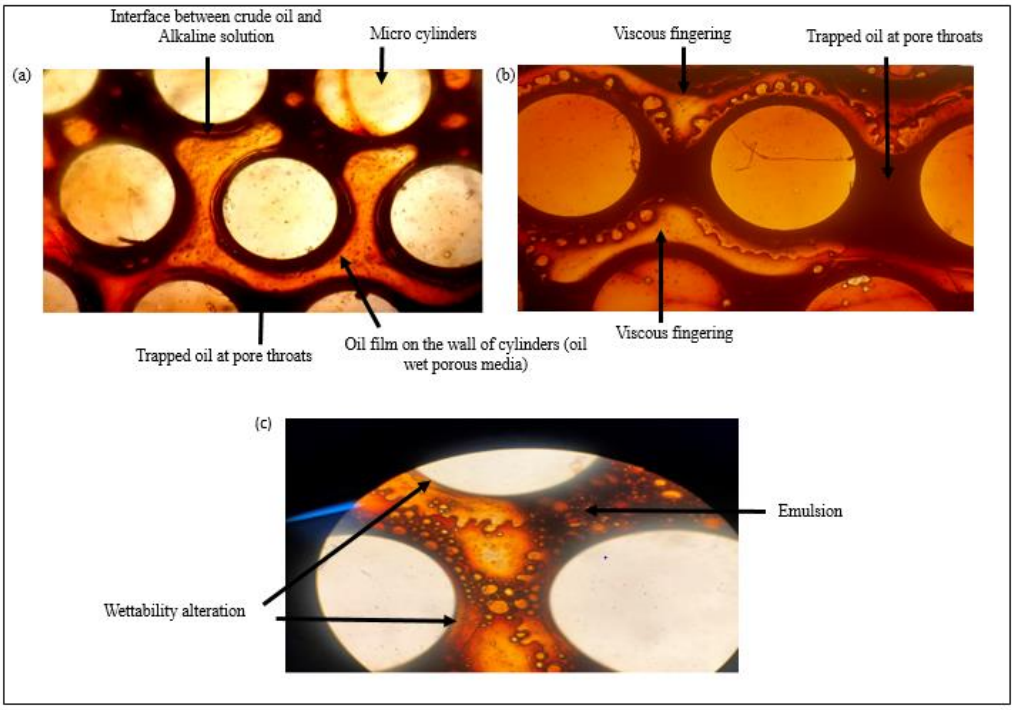

Figure 3. 8 Visualization of two-phase flow in porous micromodel (a) oil film formation around micro-cylinders during alkaline flooding in porous micromodel, (b) formation of viscous fingers, (c) wettability alteration by silica nanofluid in the micromodel.

3.5 Single-phase flow (Micro-PIV experiments)

Low salinity water seeded with fluorescent particles is injected into a 2D porous micromodel. The fluid flow is visualized using an inverted microscope, and an ensemble of images is captured using a high-speed camera. PIV Image Processing is performed using a commercial software, Dynamic studio 6.3 (Dantec Dynamics). The flow field is obtained from the cross-correlation method using the micro-PIV technique (Figure 3.9). To prepare the cross correlation map each image is divided into a number of square-shaped interrogation windows. Then a reference interrogation window is taken from the first image and move it across the subsequent image to find the corresponding region with the highest similarity. For each interrogation window, the normalized cross-correlation coefficient is calculated between the

reference interrogation window and the corresponding region in the subsequent frame. Normalize the cross-correlation coefficients by dividing them by the maximum value obtained in the correlation calculation. Fourier transform is used to prepare the normalized cross-correlation map.

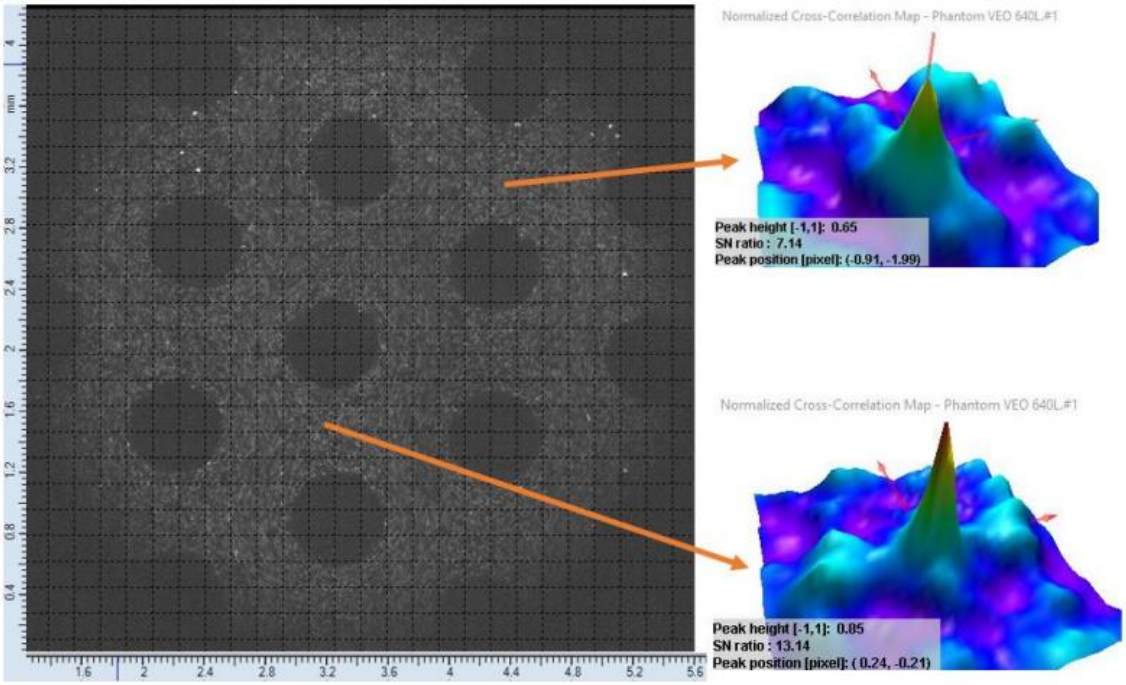

Figure 3. 9 Normalized cross-correlation map showing the signal-to-noise ratio in the flow path.

Figure 3.10 represents the velocity vector map of single-phase flow acquired by cross-correlating the PIV image pairs. The circular dark regions are considered micro-pillars, while the space around these pillars is the voids where the fluid flows. The fluid flow shows the consistency of the velocity magnitude (with time) in the entire field of view. The flow accelerates at pore throat regions and decelerates at pore enlargements. Maximum velocity magnitude is obtained at the center of the flow path while it decreases in near-wall regions. It is to be noted that PDMS is hydrophobic in nature, and therefore the cylinder walls do not have a no-slip boundary condition (Berg et al., 2008). A pseudo sinusoidal flow path (wavy flow) is

observed during the fluid flow through the porous medium. Symmetrical flow around the micro cylinders with no flow instability is observed through the velocity vector map (Figure 3.10).

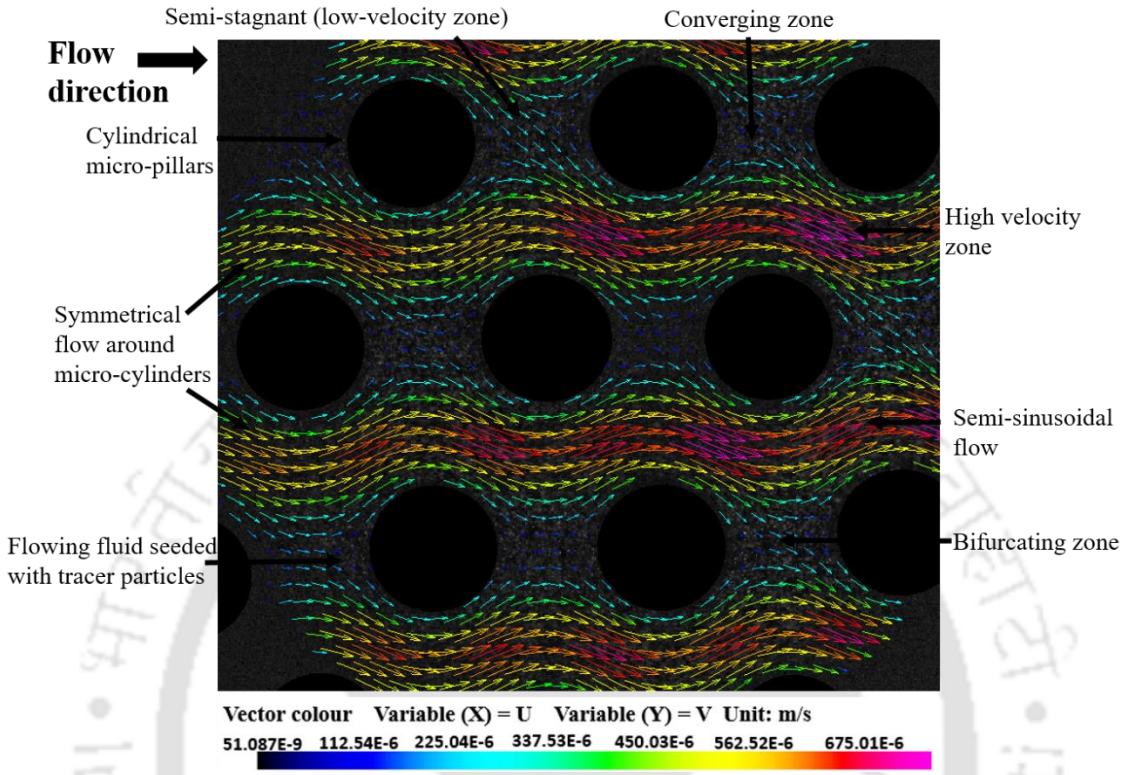

Figure 3. 10 Instantaneous velocity vector field of saline water infiltrating in a 2D porous microfluidic device with a flow rate of 0.1 ml/min (Images were captured at a frame rate of 24 FPS and 4X magnification)

It is also observed that the velocity profile vertical to the flow direction between the cylindrical grains is nearly parabolic. However, slight asymmetry was observed, which we believe could be due to small imperfection in the geometry arising from the experimental artifacts. One can avoid such artifacts in computer simulations where it is possible to design perfect geometry and apply ideal flow conditions.

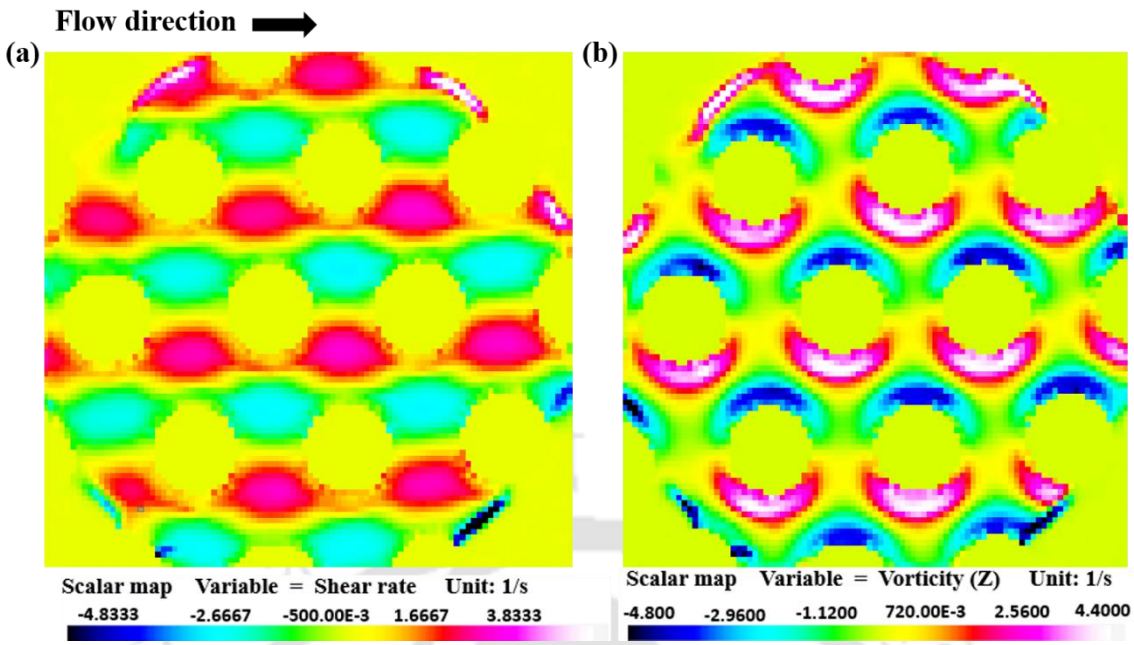

Figure 3. 11 Scalar derivative profiles (a) shear rate profile for single-phase flow in a porous medium (b) Vorticity profile for single-phase flow in the porous medium

The results obtained are similar to Blois et al., 2015 for single-phase flow. The shear rate field is obtained for single-phase flow in a 2D porous micromodel (Figure 3.11a). It is observed that the maximum shear rate is at the wall of the micro cylinders, and the minimum shear rate is obtained at the center of the flow path (porous medium). The center of the flow path is considered as the reference line around which the shear rate is measured. At the top of this line, the shear rate has a positive value, whereas below this line shear rate has a negative value due to the sinusoidal nature of the velocity field. In the case of the capillary tube, the literature says that the shear rate is maximum at the capillary tube wall; however, the velocity is maximum at the center (Berg and van Wunnik, 2017). The vorticity distribution profile for single-phase flow in the porous medium is also measured, and the contours of vorticity magnitude are shown in Figure 3.11b. The symmetrical nature of the shear rate and vorticity field demonstrates the stable and regular nature of the flow field.

Numerical simulations of single-phase flow are performed using COMSOL Multiphysics V5.2a. The Stokes equation representing the creeping flow is used for simulating the fluid motion at a very low Reynolds number. Stokes equation for conservation of momentum and continuity equation for conservation of mass are solved for incompressible fluid flow in a microfluidic device using the finite element method.

Momentum equation

$$0 = \nabla.[-pI + K] + F \tag{21}$$

where, $K = \mu(\nabla u + (\nabla u)^T)$

Mass conservation equation:

$$\rho \nabla . u = 0 \tag{22}$$

In the above equations ρ, F, μ, u are density (kg/m^3), volume force factor (N/m^3), viscosity, and velocity vector (m/s), respectively.

The computational domain has a width of 9500 μm and a height of 5000 μm. The cylinders, representing the matrix, are of 500 μm diameter each. Numerical simulations are conducted using deionized water (density of 1000 $\mathrm{kg/m^3}$, viscosity $0.001\ \mathrm{pa.s}$) as a flowing fluid through the porous medium. The velocity boundary condition is applied at the inlet, and the pressure boundary condition ($P = 0$) at the outlet. No-slip boundary condition is applied at the grain wall, whereas a symmetric boundary condition is used at the top and bottom boundary of the flow domain (Figure 3.12).

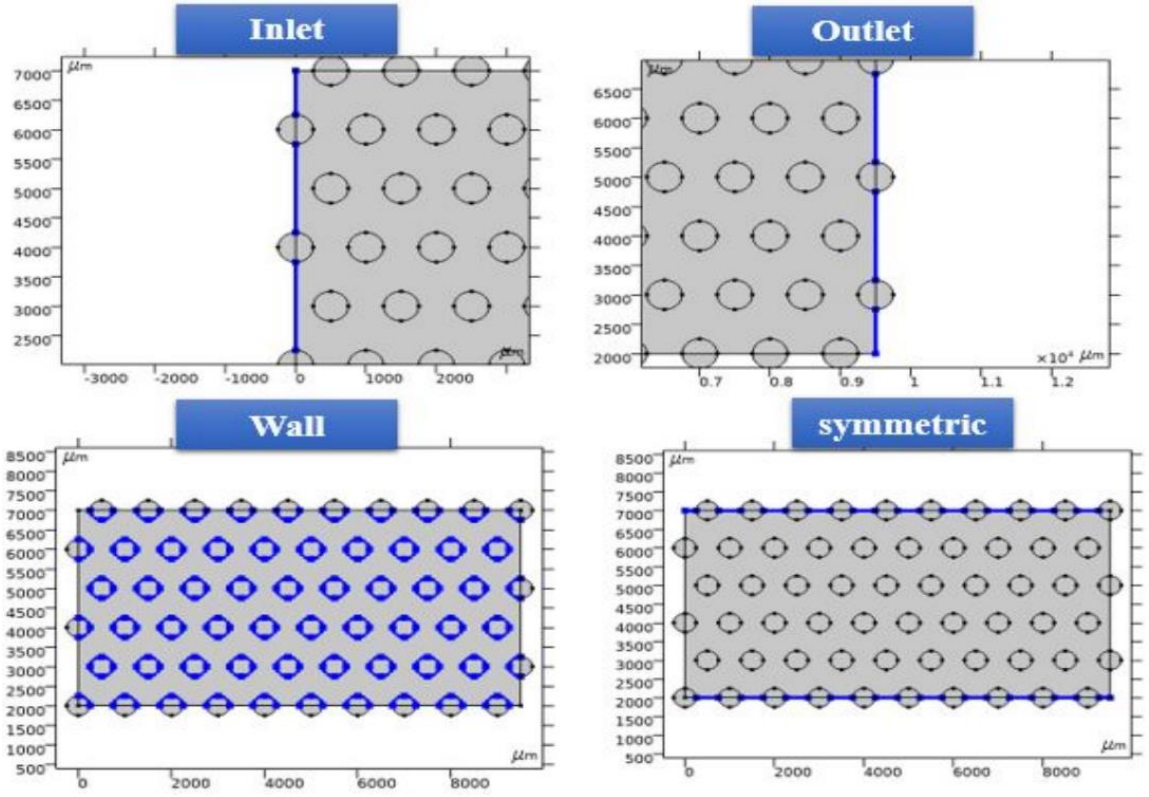

Figure 3. 12 Boundary conditions used during single-phase flow through the porous medium.

The 2D porous micromodel with uniform cylindrical grains meshed extremely fine with triangular mesh using a physics-controlled meshing sequence (Figure 3.13).

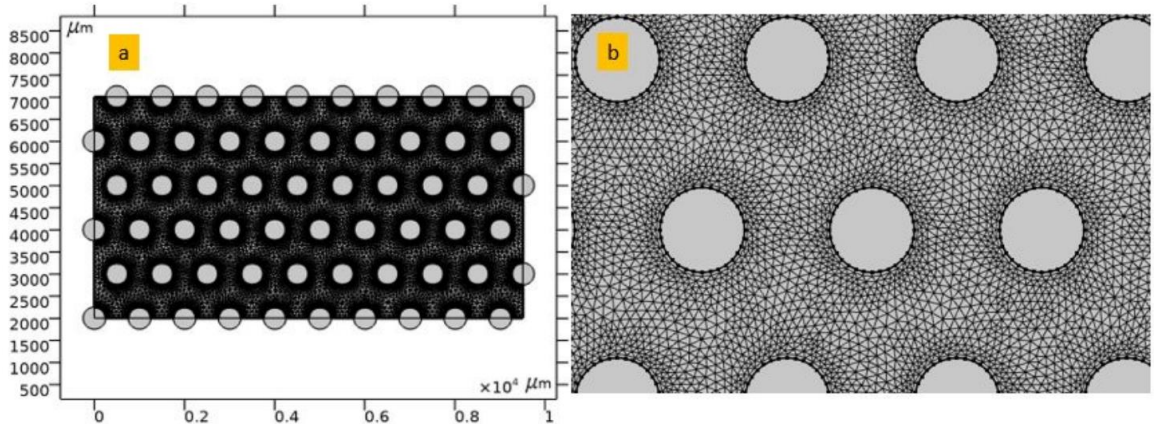

Figure 3. 13 The physics-controlled meshing of the flow domain (a) full view, (b) magnified view of the flow domain.

The number of triangular and quadrilateral elements in the mesh was 35986 and 1520, respectively. The minimum element quality of 0.5147 and average element quality of 0.907 were observed, indicating a good mesh (Table 3.1). The maximum and minimum element sizes were 100 μm and 0.2 μm, respectively.

Table 3. 1 Mesh statistics

S.N.	Description	Value
1.	Minimum element quality	0.5147
2.	Average element quality	0.907
3.	Triangle	35986
4.	Quad	1520
5.	Edge element	1866
6.	Vertex element	216
7.	Maximum element size in the flow domain	100
8.	Minimum element size	0.2
9.	Curvature factor	0.2

PARDISO (Parallel direct sparse solver interface), a direct solver based on LU decomposition, is utilized to obtain the velocity field in the flow domain. The experimental measurements are compared with the numerical simulation results (Figure 3.14). The velocity magnitude of 0.60 mm/s is obtained at the center of the flow path from the simulation. An almost similar velocity magnitude is also observed from the μ-PIV measurements.

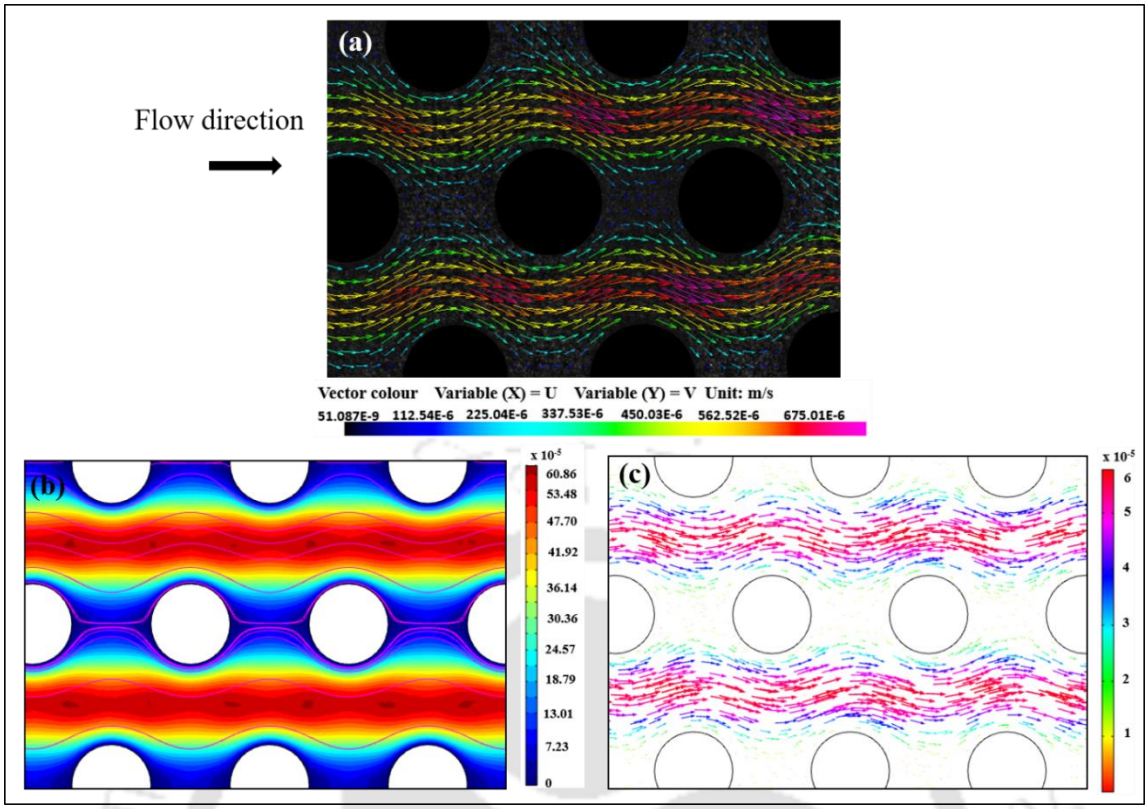

Figure 3. 14 Comparison of experimental and simulation results at 4X magnification: (a) Velocity vector map from single-phase µ-PIV experiments, (b) Velocity contour map obtained from numerical simulations, (c) Velocity vector map obtained from simulations for single-phase flow.

3.6 Two-phase flow (Micro-PIV experiments)

The single-phase flow experiments and simulations performed and validated in the previous section are considered as a reference case for two-phase flow experiments. Two types of experiments have been performed to study the two-phase flow in a porous micromodel. One analysis is conducted using the alkaline solution as a non-wetting phase and crude oil as a wetting phase. The second analysis is performed using silica nanofluid as a non-wetting phase and crude oil as a wetting phase.

3.6.1 Drainage experiments using an alkaline solution

Drainage experiments are performed to displace the wetting phase (crude oil) from the porous media using the non-wetting phase (alkaline solution). In this experiment, the micromodel is first saturated with crude oil. After that, the alkaline solution is injected to displace the crude oil present in the pores of the micromodel. The emulsion formation (primary displacement mechanism during alkaline flooding) is visualized during the interaction of crude oil and alkaline solution. Viscous fingering is also identified during the drainage experiment due to the unfavorable mobility ratio between the aqueous phase and crude oil (Figure 3.15). A large quantity of crude oil is left behind as residual oil due to this finger formation, which elucidates the low sweep efficiency during the injection of alkaline solution. Phase diagrams show the boundaries separating the flow regimes into viscous fingering, capillary fingering, and compact/stable displacement. The boundaries of these regimes have been identified using pore network simulation and experimental observations (Lenormand et al., 1983). The displacement experiments are performed in a water-wet porous micromodel to identify these boundaries of pore-scale flow regimes (Zhang et al., 2011).

Two-phase flow studies in the past have been used to define the phase diagram for identifying viscous fingering, capillary fingering, and stable displacement regions (Chen et al., 2018). In our experiments, the viscosity ratio and capillary number for two-phase flow are calculated considering the viscosity of crude oil (33.4 mPa.s), the viscosity of alkaline solution (0.95 mPa. s), typical velocity in the channels (0.16 mm/sec), and the interfacial tension between crude oil and Na_2CO_3 alkaline solution (0.052 mN/m). The calculated logarithmic value of the viscosity ratio is -1.546, and the logarithmic value of the capillary number is -2.533. Chen et al., 2018 have presented the stability phase diagram by plotting the logarithmic value of the viscosity ratio [$\log_{10}$ M] and capillary number [$\log_{10}$ Ca]. We observed that our values fall in the viscous

fingering regime. The phase boundaries of viscous fingering regimes are also reported by Zhang et al., 2011.

The velocity vector map is obtained during the two-phase flow in the micromodel using the µ-PIV technique. In the middle of the flow channel, the velocity is 0.33 mm/sec, whereas, near the micro cylinders, it is 0.10 mm/sec (Figure 3.15). Flow velocity is maximum at the center of the flow channel, but as soon as we move towards the wall of the micro cylinders, the velocity drastically reduces.

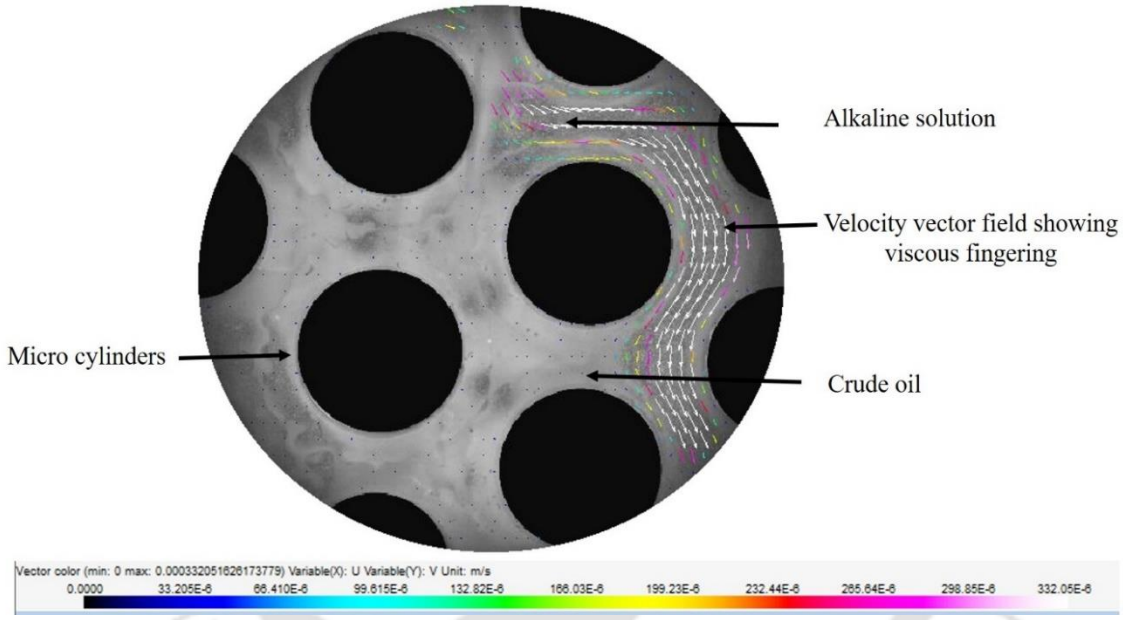

Figure 3. 15 Instantaneous velocity vector field of alkaline solution displacing crude oil in a 2D porous microfluidic device with a flow rate of 0.05 ml/min (images were captured at a frame rate of 24 FPS and 4X magnification).

The velocity vector map also shows the near parabolic flow profile in the viscous fingering path. It is also observed that some of the alkaline solution is trapped between the residual crude oil in small pockets during the injection of the alkaline solution. The fluid in these pockets is almost stationary. A very low velocity of approximately 0.033 mm/sec is obtained in these pockets that too because of the perturbations of the nearby flowing fluid. These pockets of

extremely low velocity are termed as a stagnant zone. During the drainage process, the fluid flow pattern is not periodic.

3.6.2 Imbibition experiments using an alkaline solution

In the imbibition experiment, the micromodel is first saturated with an alkaline solution seeded with fluorescent tracer particles. Crude oil is injected into the porous medium to understand the interaction between the two phases (crude oil and alkaline solution). W/O emulsion formation is observed due to the interaction of crude oil and alkaline solution. This emulsion is visualized under the microscope, which shows the large size of emulsion droplets. The coalescence of these droplets generates bigger droplets, resulting in an unstable emulsion (see Figure 3.5a). As the viscosity of crude oil is high compared to the alkaline solution, no viscous fingering is observed during the imbibition experiment with the alkaline solution. A set of 300 images are captured at a frame rate of 24 FPS at 4X magnification. The interface movement is visualized in the porous micromodel to quantify the two-phase flow during the imbibition experiment (Figure 3.16). The results show that the flow pattern is not periodic due to the perturbations generated by the emulsion. Although bifurcation (a single stream of fluid diverges into two streams), converging (two fluid streams converging into one stream), and stagnation zones (low-velocity regions) are visible during the imbibition experiment, but these are not as regular as they were in the case of single-phase flow. The velocity magnitude is very much affected by the perturbations created by the emulsion. For example, at one pore throat within the flow path, the velocity magnitude is 0.479 mm/sec, whereas, at some other pore throats, the velocity magnitude is 0.095 mm/sec. This significant difference in the velocity magnitude is simply because of the perturbation created by the emulsion. A wavy flow pattern is observed during the experiments using an alkaline solution. Figure 3.16 displays that some

alkaline solution is left behind the interface, which can be seen by the velocity vectors behind the front.

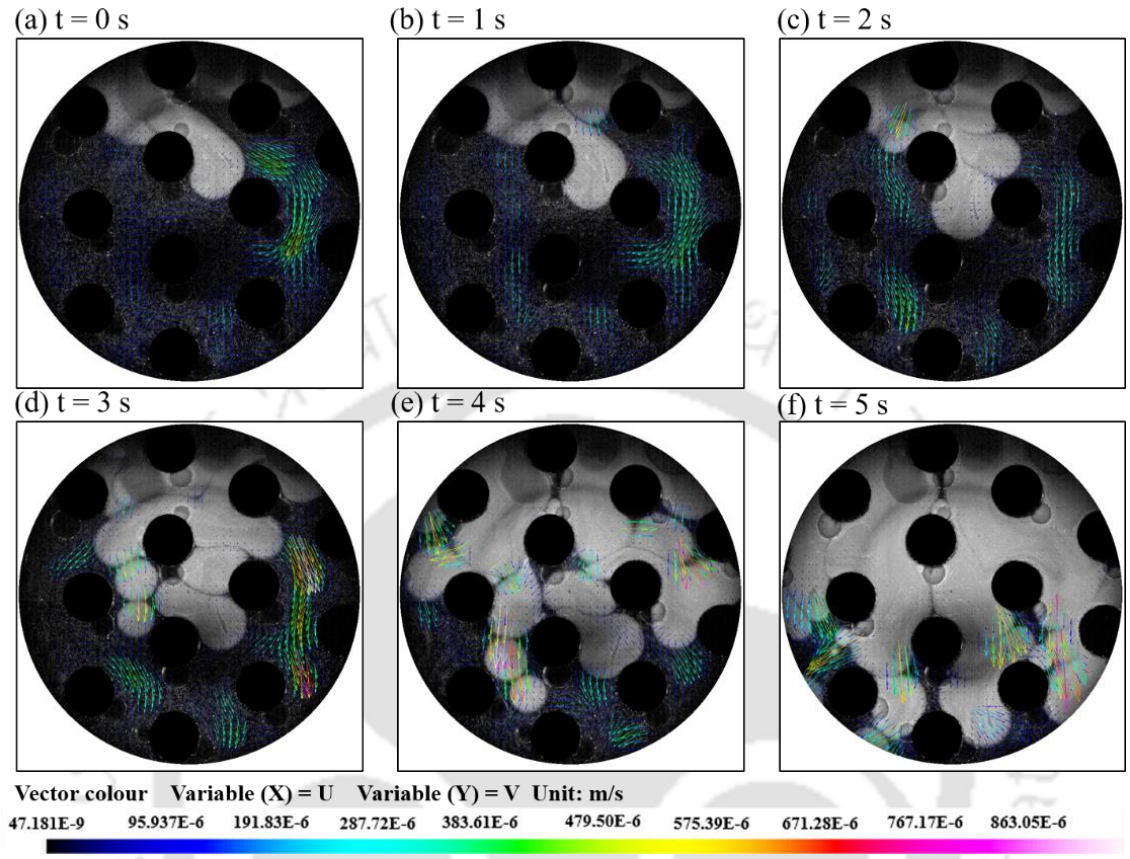

Figure 3. 16 Instantaneous velocity vector field during the imbibition process of crude oil displacing alkaline solution in a 2D porous microfluidic device with a flow rate of 0.1 ml/min. Images were captured at a frame rate of 24 FPS and 4X magnification

3.6.3 Imbibition experiments using silica nanofluid

The 2D porous micromodel is first saturated with silica nanofluid seeded with fluorescent polystyrene tracer particles. After that, crude oil is injected at a rate of 0.08 ml/min to understand the interaction of the two phases (crude oil and silica nanofluid) and displace silica nanofluid out of the porous medium. The two-phase flow within the porous medium is visualized under the microscope. It is observed that as the crude oil interacts with the silica nanofluid, an emulsion is formed in the porous medium. The application of silica nanofluids

reduces emulsion droplet size and increases their number, which helps in developing a stable emulsion. Silica particles enhance the strength of the mechanical barrier effect around oil droplets by covering them all over, resulting in the reduced coalescence of droplets (Pal and Mandal, 2020). In the presence of alkali (Na_2CO_3) and silica nanoparticles, electrostatic and steric effects are the leading cause for the stability of the emulsion. The addition of silica nanoparticles reduces the interfacial tension between the two phases, thereby decreasing the droplet size and improving emulsion stability (Pal and Mandal, 2020). This statement can also be justified by Figure 3.5b and Figure 3.5d showing the microscopic image of emulsion (crude oil/silica nanofluid) and its droplet size distribution. This figure shows that the interaction of crude oil and silica nanofluid results in a stable emulsion consisting of a large number of droplets with an average size of about 3μm.

For the quantitative analysis of two-phase flow, a set of 500 images are captured at a frame rate of 24 FPS at 4X magnification. These images are processed to get the velocity vector field (Figure 3.17). The interface movement is visualized in the porous micromodel to quantify the two-phase flow during the drainage experiment. During the experiment, the use of silica nanofluid causes the uniform movement of the interface. A regular piston-like displacement is observed during the imbibition process due to the low aspect ratio (pore size by throat size). Therefore, viscous fingering phenomena is not visualized in the case of the imbibition experiment using silica nanofluid. The sweep efficiency during the two imbibition processes is investigated and compared. The results showed that silica nanoparticles maximize the sweep and displacement efficiency by forming a stable emulsion and displacing the fluid using regular piston-like displacement.

Although emulsion (of crude oil/silica nanofluid) moves at a low velocity of 0.83 mm/sec, its displacement efficiency is high compared to the emulsion of crude oil/alkaline solution. The

velocity vector map shown in Figure 3.17 indicates the bifurcation (a single stream of fluid diverging into two streams), converging (two fluid streams converging into one stream), and stagnation regions (low-velocity regions) during the imbibition experiment. However, these are not regular as they were in the case of single-phase flow. Unsteady flow behavior (velocity magnitude not temporally and spatially consistent) is observed from the velocity vector map. The velocity vector map shows a near-parabolic flow profile with a maximum velocity of 0.83 mm/sec at the channel center and a minimum velocity of 0.092 mm/sec near the cylinder wall.

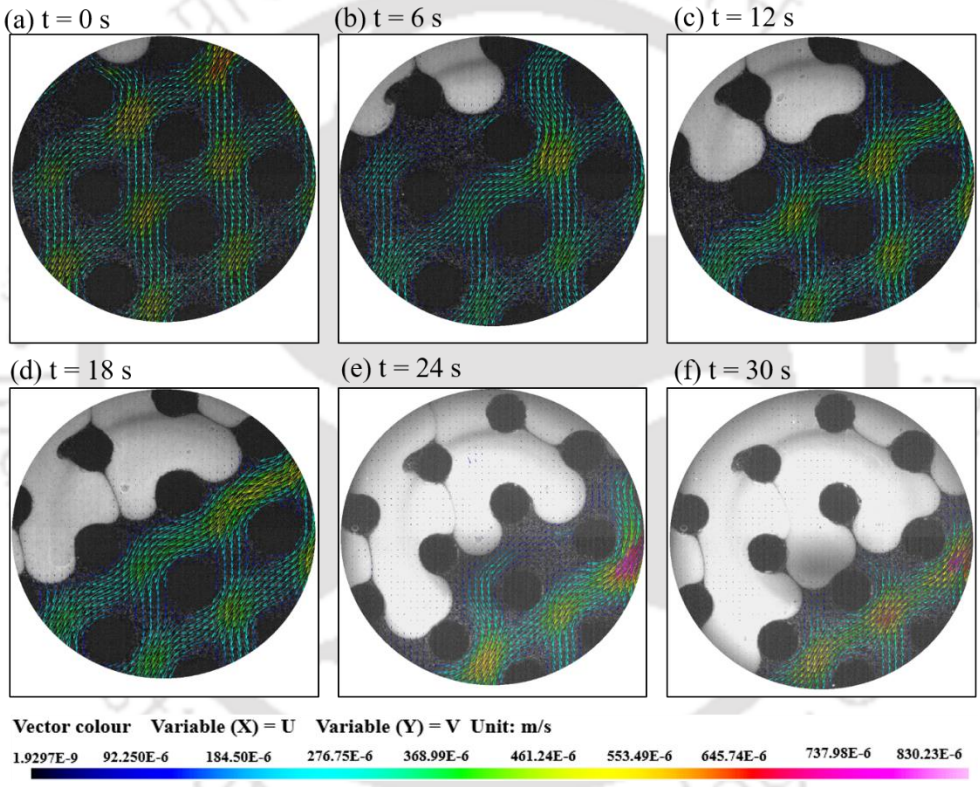

Figure 3. 17 Instantaneous velocity vector field during imbibition process of crude oil displacing silica nanofluid from a 2D porous microfluidic device with a flow rate of 0.08 ml/min. Images were captured at a frame rate of 24 FPS and 4X magnification.

3.6.4 Shear rate distribution for alkaline flooding & nanofluid crude oil interaction

The 2D porous micromodel can be used for understanding the oil mobilization by EOR mechanisms. To gain further insight into the flow phenomena, the shear rate distribution of the flow field is obtained for two cases: during the alkaline flooding in a porous medium and during the interaction of silica nanofluid and crude oil within the porous medium.

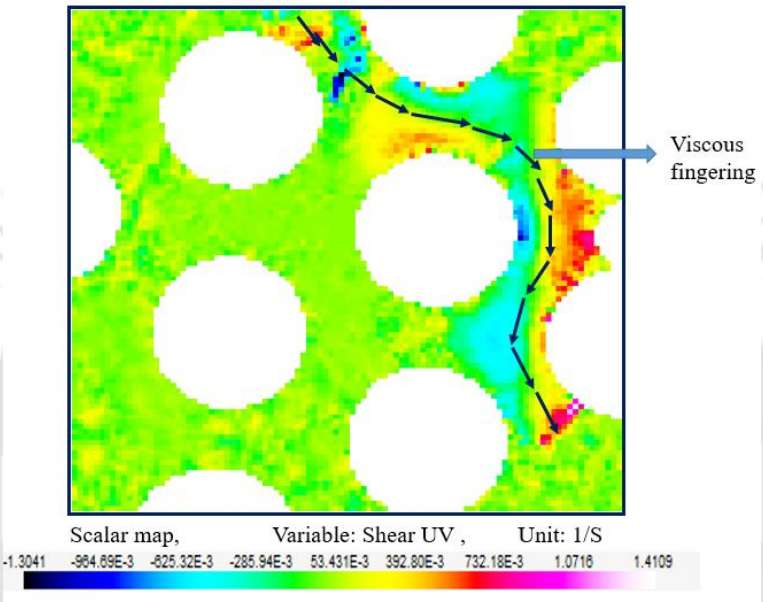

Figure 3. 18 Shear rate profile for alkaline flooding showing viscous fingering phenomena

The shear rate distribution during alkaline flooding demonstrated the viscous fingering phenomena (Figure 3.18). The Centre of the viscous fingering flow path is considered as the reference line around which the shear rate is measured. In the middle of the viscous fingering path, the shear rate value is very low because of the very low-velocity gradient. A maximum shear rate is observed at the wall of the micro-cylinder because of a high-velocity gradient. The positive and negative value of the shear rate represents the direction to the left and right of the reference line.

The shear rate distribution of silica nanofluid and crude oil interaction is demonstrated in Figure 3.19. The temporal movement of the silica nanofluid and crude oil interface is visualized at an interval of 6 seconds. Maximum shear is observed at the interface of the two phases. The shear rate flow field shows uniform displacement/piston-like displacement because of emulsion (crude oil/nanofluid). The shear rate is minimized just behind the front because the emulsion displaces most of the silica nanofluid through the porous medium. Sweep efficiency is high, and viscous fingering is eliminated in the case of silica nanofluid.

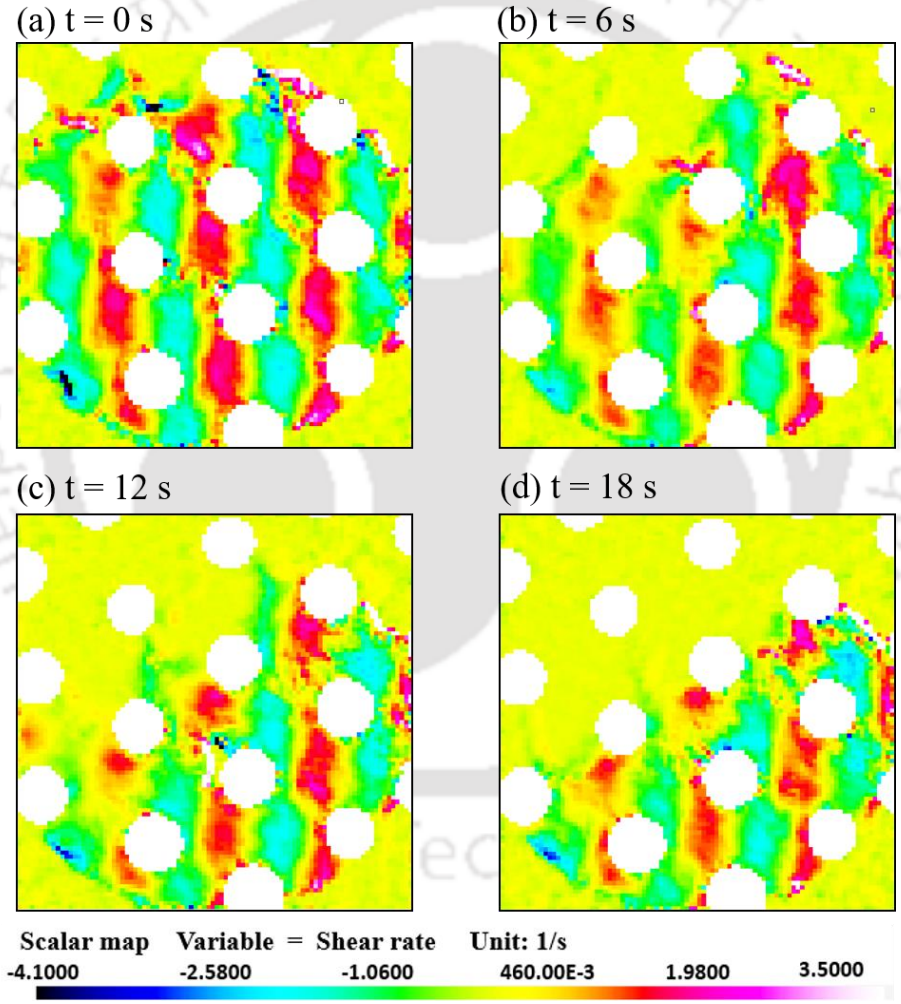

Figure 3. 19 Shear rate profile for silica nanofluid-crude oil interaction in porous micromodel

The studies mentioned above show that 2D micromodels can be effectively used to understand pore-scale flow physics during two-phase flow in porous media. There are several advantages

of using a 2D porous micromodel to gain insight into real 3D porous media. Fluid flow dynamics and pore-scale events such as shear-induced circulation, snap-off, Haines jump, viscous fingering, capillary fingering, and stable or unstable displacement can be visualized and quantified easily in a 2D porous micromodel.

3.7 Summary

Experiments were performed to study single-phase and two-phase flow in a 2D porous micromodel. The effect of the alkali and silica nanoparticles on the displacement process is studied by performing IFT measurements, contact angle measurements, rheological analysis, and micromodel flooding. The dynamic IFT is reduced to a value of 0.01 mN/m at a concentration of 0.05 wt. % of silica nanoparticles. Silica nanofluid alters the wettability by reducing the contact angle from 71.56° (DI water) to 22° (0.15 wt% SiO_2). The quantitative study of single-phase flow shows symmetrical flow around the micro cylinders, semi-sinusoidal flow path, and temporally consistent velocity magnitude. The convergence, bifurcation, high-velocity, and low-velocity zones are also identified during single-phase flow. The single-phase flow results are validated using numerical simulations, which elucidates that the experimental and simulation results are in synergy. These single-phase flow experiments serve as a reference for two-phase flow.

Two-phase flow (Drainage and Imbibition) experiments are conducted using the alkaline solution as a non-wetting phase and crude oil as a wetting phase. During drainage experiments, viscous fingering is observed, which is formed mainly due to the unfavorable mobility ratio between crude oil and alkaline solution. A large quantity of crude oil remained untouched by the alkaline solution and trapped within the porous medium leading to poor sweep efficiency. During the imbibition experiment, w/o emulsion is formed due to crude oil and alkaline solution interaction. The high emulsion viscosity significantly reduced the viscous fingering

during the imbibition experiment. Quantitative results show that the flow pattern is not periodic in the porous medium due to the perturbations generated by the emulsion. Although bifurcation, converging, and stagnation zones are visualized from the velocity vector map, these are not periodic due to unsteady flow behavior in porous micromodel. Imbibition experiment is also conducted using silica nanofluid as a non-wetting phase and crude oil as a wetting phase. During the imbibition experiment, as crude oil interacts with the silica nanofluid, a stable emulsion is formed in the porous medium resulting in a regular piston-like displacement and eliminating viscous fingering phenomena. The bifurcating, converging, and stagnation regions are observed from the velocity vector map.

Chapter 4. Investigation of the immiscible fluid displacement process in randomly distributed bead-based porous micromodels

Pore structure;

Shear-induced circulation;

Porous medium;

Micro-particle image velocimetry;

Microscopic study

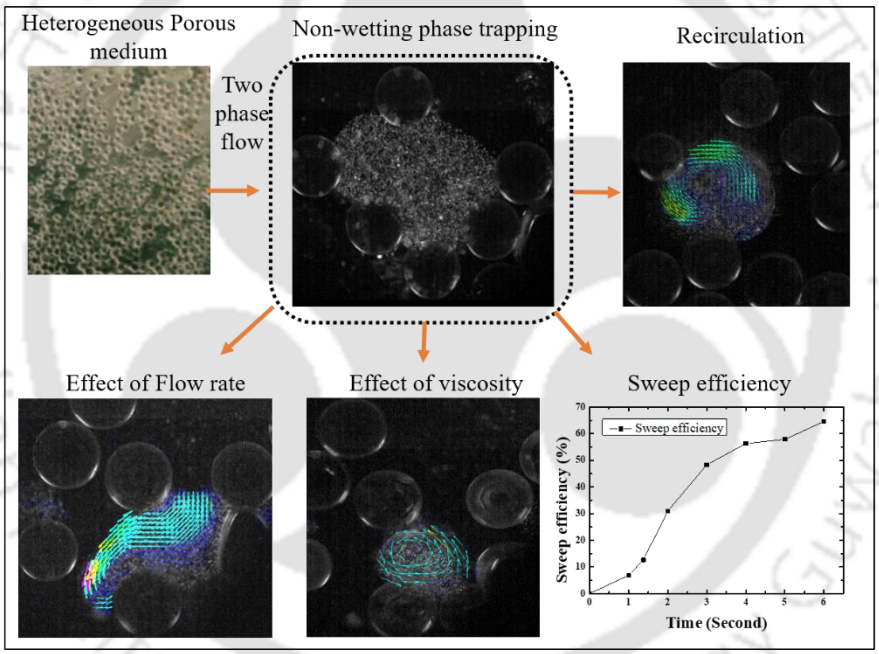

Investigation of immiscible fluid displacement process in randomly distributed bead-based porous micromodels

This chapter reports pore-scale immiscible displacement processes in a bead-based porous micromodel using fluorescence microscopy and micro-particle image velocimetry (μ-PIV). The porous micromodels with heterogeneous and homogeneous geometry are fabricated to investigate the effect of displacing phase viscosity and flow rate on the pore-scale displacement mechanism. The recirculations and viscous fingering are observed during the displacement of the trapped non-wetting phase through the porous domain. It is observed that the breakage and coalescence of the non-wetting phase droplets cause frequent flow reversal of ganglia, leading to an unsteady flow behavior during the displacement process. The effect of flow rate and viscosity on the trapped non-wetting phase is investigated, and the results indicate that an increase in the flow rate reduces the trapped non-wetting fluid saturation in the porous medium by disintegrating large ganglia into small droplets. Increasing either the flow rate or viscosity increases the shear stress at the interface of the trapped ganglion and displacing phase, leading to shear-induced circulations. These recirculations restricts further displacement of the trapped fluids. At a higher flow rate with a more viscous displacing phase, the trapped non-wetting phase ganglion disintegrate into smaller droplets and easily displaced. The porous medium with low porosity and a higher degree of heterogeneity results in more trapping and less recovery of the non-wetting phase.

4.1 Single-phase flow

The fluid flow is viewed by objective lenses of magnification 4 × and 10 × (having numerical apertures of 0.10 and 0.25, respectively) using an inverted microscope. A high-speed CMOS (complementary metal-oxide-semiconductor) camera (Phantom VEO 640L) is utilized to image the flow. The raw images of single-phase flow (DI water doped with fluorescent polystyrene particles) at 0.05 ml/min in a heterogeneous porous medium can be seen in Figure 4.1. The circular dark regions are the solid matrix, whereas the white tracer particle in the flow network around the solid matrix shows the fluid flow in the porous medium. A normalized cross-correlation map is generated to probe the signal-to-noise ratio (Figure 4.1d).

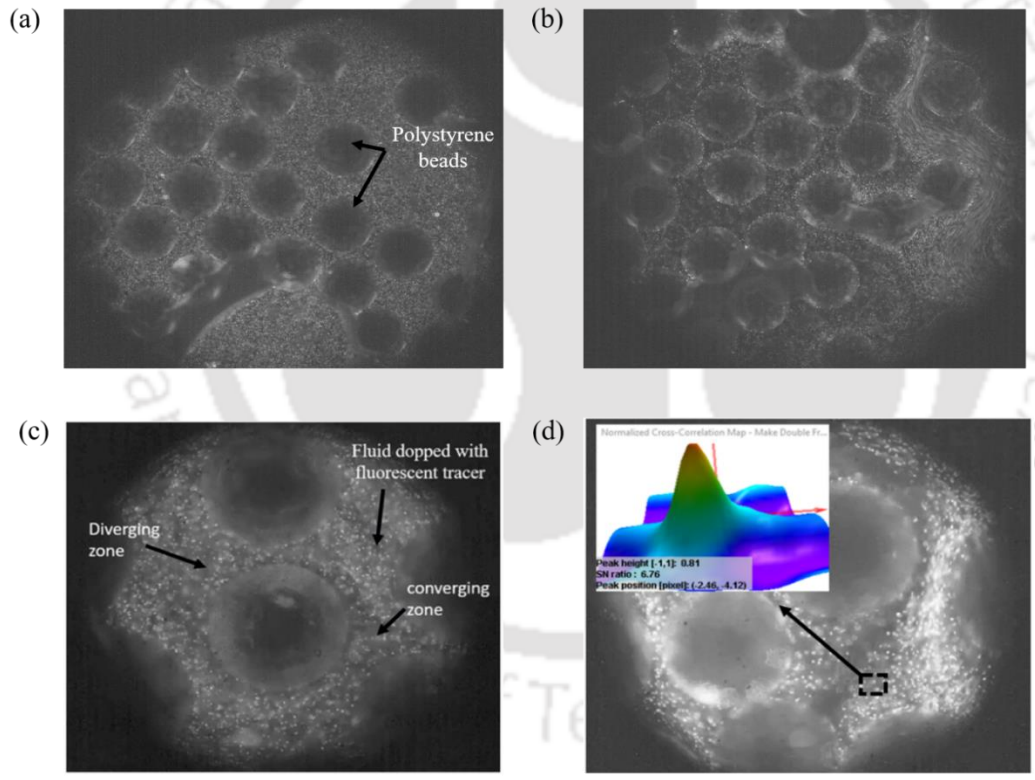

Figure 4. 1 Single-phase flow in the heterogeneous porous domain: (a, b) Single-phase flow captured at 4X magnification, (c) single-phase flow captured at 10X magnification, (d) Signal-to-noise ratio (SNR) in the heterogeneous porous domain during cross-correlation PIV.

Single-phase flow experiments (using deionized water) are carried out as a reference case for the two-phase immiscible displacement studies in bead-based heterogeneous porous micromodels. Figure 4.2 shows the velocity distribution profile of single-phase flow. The flow field shows that the zones of large pore bodies have preferential flow paths. A consistent velocity magnitude with time is observed, indicating steady-state flow in the porous domain. However, there are a few zones with very low or negligible velocity (probably dead-end zones).

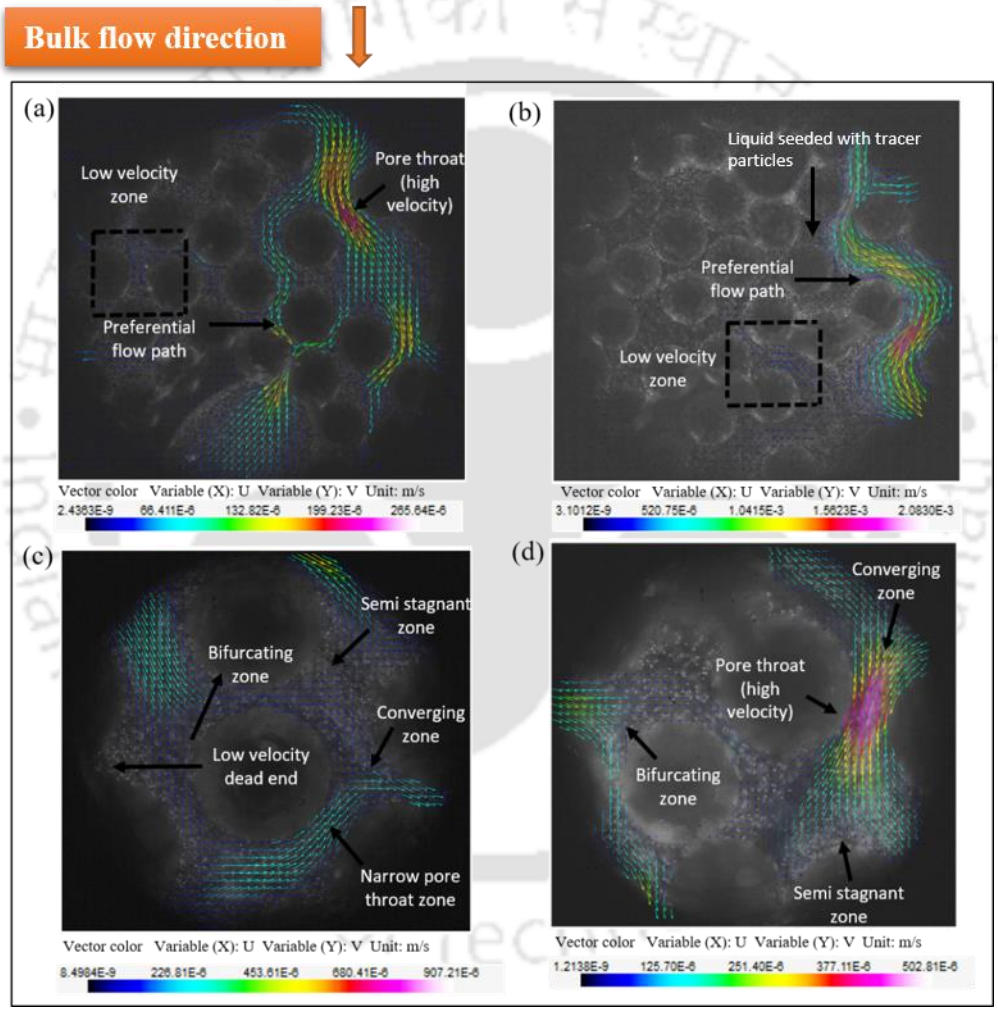

Figure 4. 2 Velocity distribution profile of DI water flow in a 2D heterogeneous micromodel (a, b) Single-phase flow captured at 4× magnification and 24 fps (flow rate 0.2, 0.1 ml/min respectively) (c, d) single-phase flow captured at 10× magnification and 24 fps (flow rate 0.05 ml/min)

The velocity vector field demonstrates the bifurcation zones, converging zones, semi-stagnant zones, low-velocity dead-end zones, and high-velocity pore throat zones. The fluid moves fast at pore constrictions or throats and slowly at pore body. The velocity magnitude is highest in the middle of the throat, while it decreases in near-wall regions due to boundary effects. Flow instability is not observed because the fluid flows under laminar flow conditions.

The single-phase flow experiments of micro-PIV are validated by numerical simulations using COMSOL MULTIPHYSICS V5.2a. The following Stokes equations are solved using the finite element method for single-phase flow in the heterogeneous porous domain.

The momentum equation is given by:

$$\nabla.[-pI + K] + F = 0 \tag{23}$$

where, $K = \mu(\nabla u + (\nabla u)^T)$.

The mass conservation equation is:

$$\rho \nabla . u = 0 \tag{24}$$

In the above equations, ρ, μ, u are fluid density (kg/m^3), viscosity, and velocity vector (m/s), respectively.

The term F in equation (23) represents the surface force acting at the interface between the two fluids and is defined as,

$$\mathrm{F} = \sigma k n \delta_\Gamma \tag{25}$$

Where σ is the surface tension, k is the curvature of the interface, n is normal to the interface, and the Dirac delta function δ_Γ is zero everywhere except at the interface. No interface forms in the case of single-phase flow. Hence the Dirac delta function (δ_Γ) is zero, resulting in the

surface force factor (F) to be zero in the momentum equation (4) for single-phase flow. However, this term will be important in two-phase flow.

The heterogeneous porous domain meshed with the boundary layer meshing sequence, and the PARDISO solver was used. PARDISO (**PAR**allel **DI**rect **SO**lver) solver is a direct sparse solver based on LU decomposition used for solving large sparse symmetric and non-symmetric linear systems of equations. The experimental and simulation results are compared to validate the results of single-phase flow through a heterogeneous porous medium in Figure 4.3.

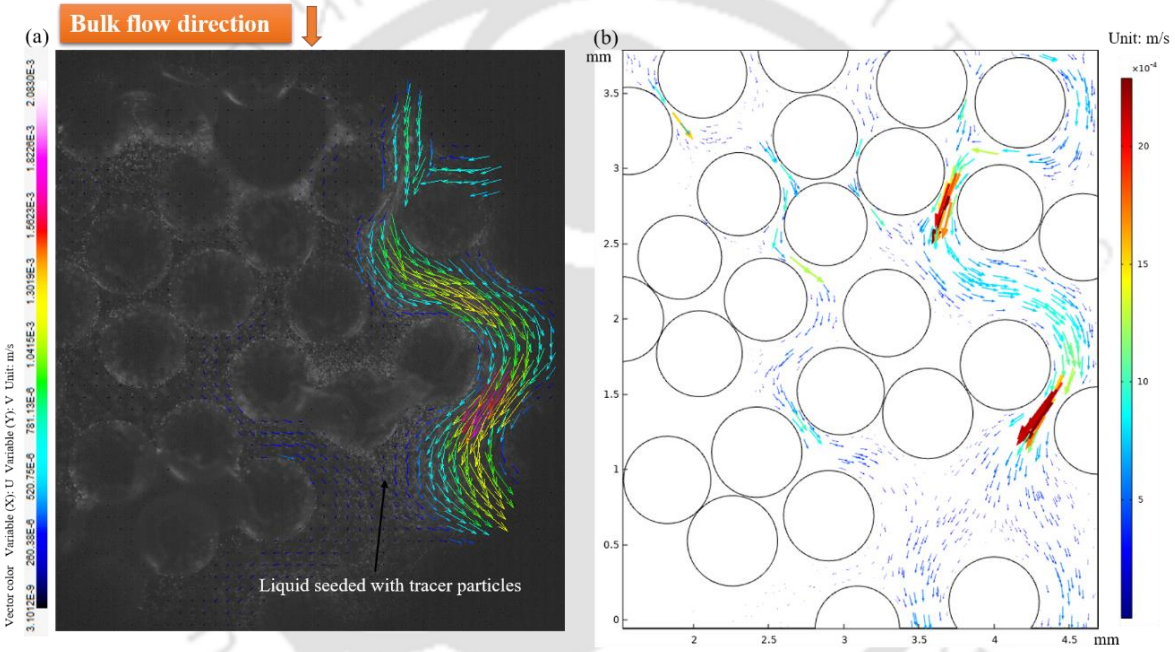

Figure 4. 3 Velocity distribution profile obtained for single-phase flow by (a) µ-PIV experiments, (b) single-phase flow simulation at a flow rate of 0.1 ml/min.

A qualitative agreement of the velocity vector field is obtained between the experimental and simulation results (Figure 4.3). Although, the quantitative symmetry between the two cases is complex. The mean velocity vector map is obtained by averaging over 200 velocity vector maps. The velocity magnitude along a slanted line AB in the flow path is investigated to demonstrate the quantitative similarity between experimental and simulation results (Figure

4.4). In micro-PIV experiments, the average value of velocity magnitude (from the mean velocity vector map) is 0.71 mm/s, whereas, from the numerical simulation, it is 0.80 mm/s. The uncertainty (difference) between the simulation and experimental results is 11.25%. This uncertainty is mainly because of the heterogeneous nature and experimental artefacts of the porous medium.

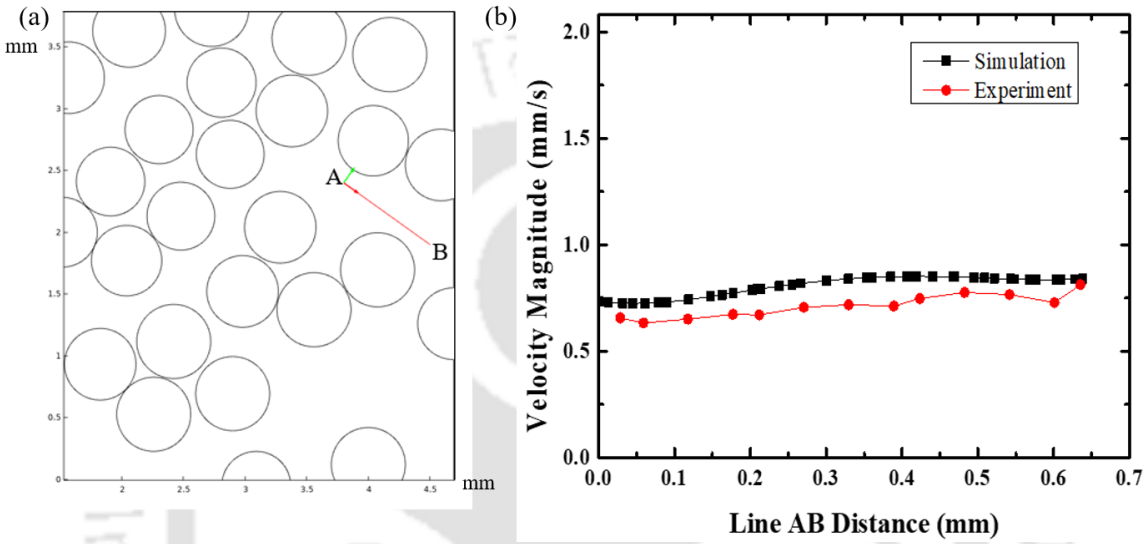

Figure 4. 4 Comparison of experimental and simulation results of velocity magnitude along a slanted line AB in the heterogeneous porous medium.

4.2 Immiscible displacement in heterogeneous porous micromodel

Two-phase flow studies are conducted in the randomly distributed heterogeneous porous micromodel to gain a fundamental understanding of flow dynamics. The study is carried out to probe the flow pattern, microscopic phenomena at the pore level, and interface tracking in the porous media. The viscosity and density values of chemical formulations used during two-phase flow are summarized in Table 4.1.

Table 4. 1: Viscosity and density of all wetting and non-wetting phases used during experiments

Phase	**Viscosity (cSt)**	**Density (g/cm^3) at 25°C**
Wetting phase		
• Silicone oil -I	10	0.93
• Silicone oil - II	50	0.96
• Silicone oil – III	345	0.967
Non-wetting phase		
• Glycerol + DI water (50:50)	119.68	1.137

The glycerol-DI water solution is used as a non-wetting phase, and silicone oil-I as a wetting phase during the imbibition experiment. The microfluidic device is initially saturated using glycerol water doped with fluorescent polystyrene particles. The wetting phase is injected at 0.5 ml/min into the porous medium to mobilize the non-wetting phase, and images are captured at 24 fps. The velocity vector field obtained after post-processing of images shows a non-uniform displacement of the non-wetting phase. Figure 4.5 presents velocity vector maps showing the temporal movement of the interface of glycerol water-silicone oil. A non-uniform (unstable) displacement of the non-wetting phase is caused by the capillary forces. The viscous fingering phenomena can be clearly observed in Figure 4.5.

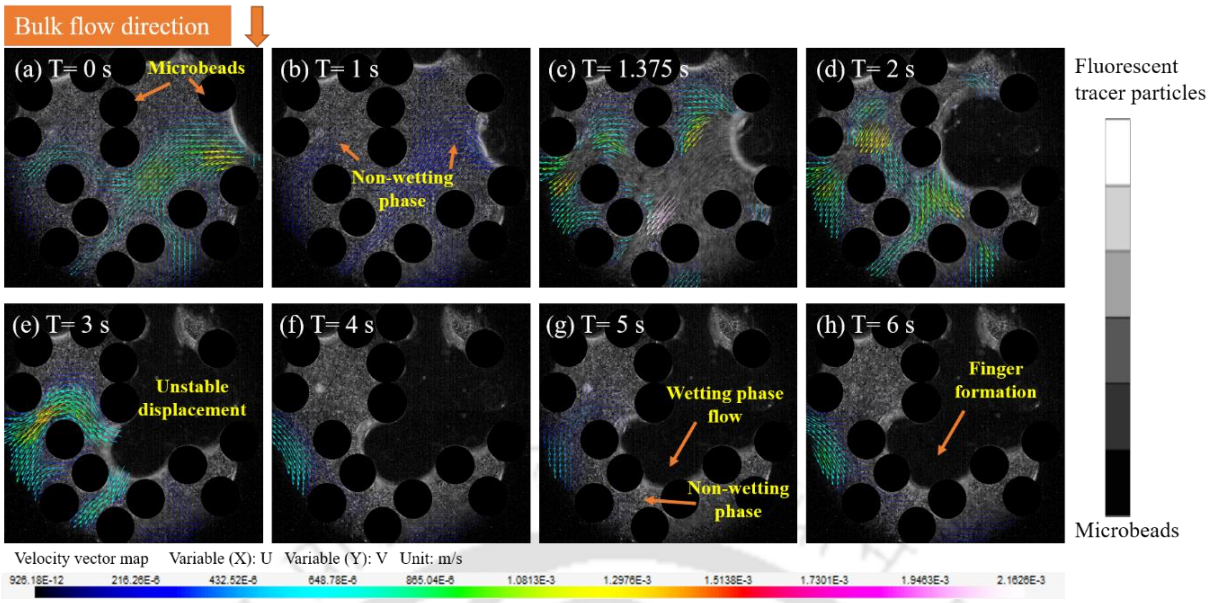

Figure 4. 5 Velocity vector maps showing displacement of non-wetting phase (Glycerol + DI water solution) by injection of wetting phase (Silicone oil - I). The images were captured at 24 FPS and a flow rate of 0.5 ml/min.

It was observed that the maximum velocity at 1.375 s (Figure 4.5c) jumped to 2.16 mm/s from 0.2 mm/s corresponding to that at time, T = 1s (Figure 4.5b), even though the flow rate is only 0.5 ml/min. From these images, the areal sweep efficiency of the wetting phase to displace the non-wetting phase out of the heterogeneous porous medium has been calculated and plotted with time (Figure 4.6). The plot shows that the sweep efficiency is increased up to 64.55% within 6s.

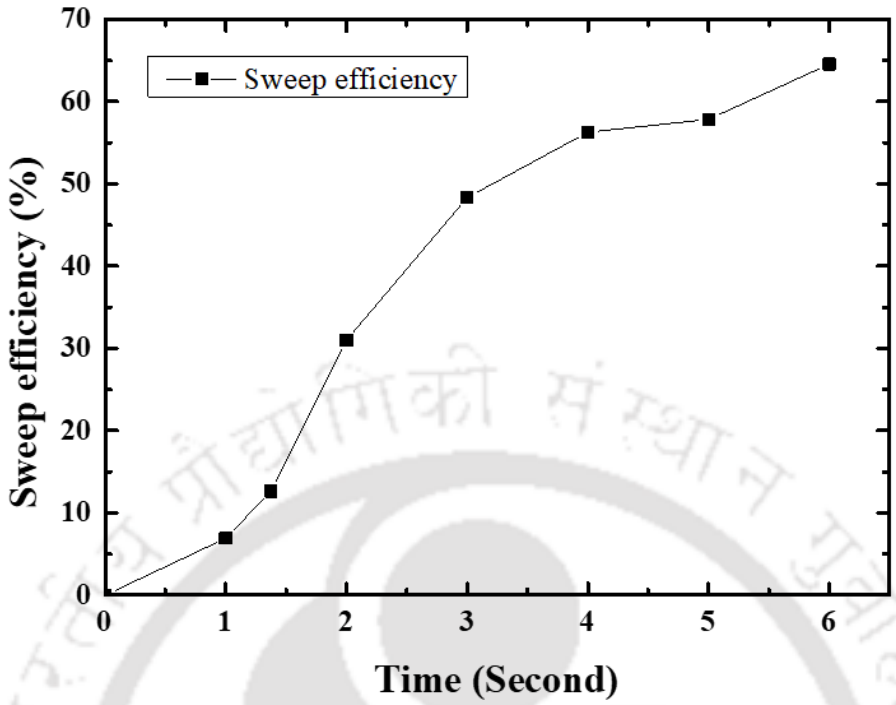

Figure 4. 6 Areal sweep efficiency with time during injection of wetting phase to displace the resident non-wetting phase from the heterogeneous porous medium.

A significant amount of the non-wetting phase is still trapped within small constrictions, pore throats, and dead-end zones in the form of droplets, blobs, and ganglions due to undesirable events such as viscous fingering (Figure 4.7). The trapped fluid bodies smaller than a single pore are known as droplets. Blobs are larger than droplets and fully occupy a single pore. Larger trapped non-wetting phase bodies that occupy more than one pore dimension are called ganglia (Zarikos et al., 2018).

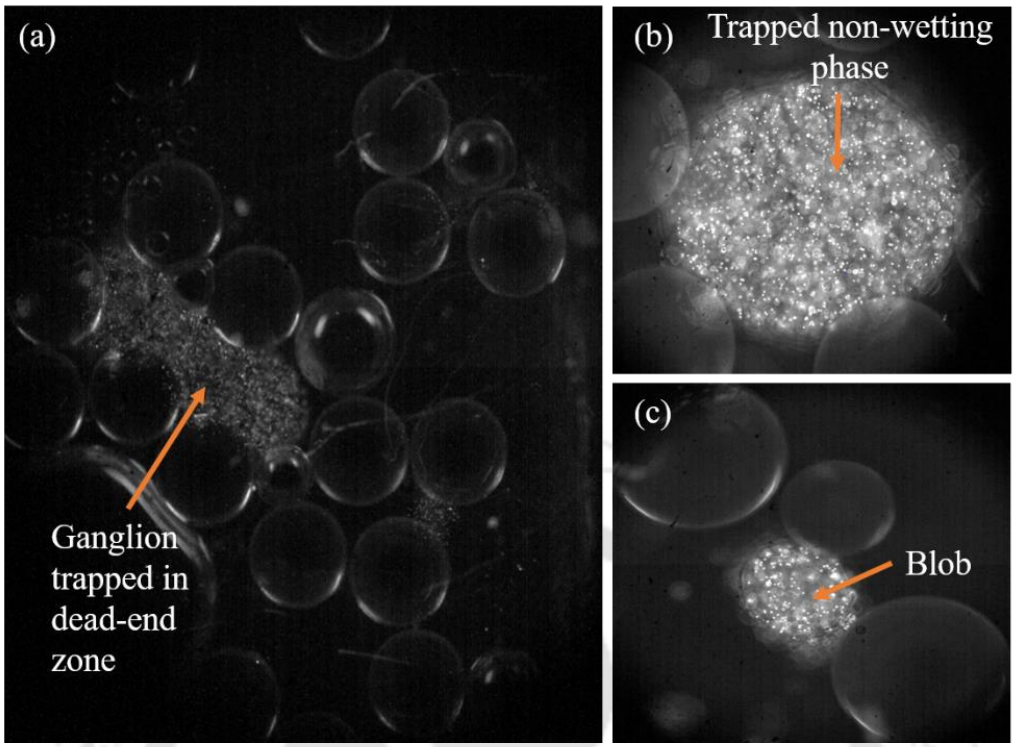

Figure 4. 7 Trapped fluid in the porous medium, (a) ganglion trapped in dead-end, (b) a globule of trapped non-wetting phase, (c) blob.

With a continuous flow of silicone oil in the porous medium, a shear force acts on the interface of displacing and trapped fluid, causing a partial momentum transfer to the trapped non-wetting phase. This leads to a circular motion in the trapped non-wetting phase called shear-induced circulation or vortex formation. The pressure force by the displacing fluid is not sufficient enough to displace the trapped non-wetting phase (blob or ganglion).

These vortices or recirculations can be visualized when the trapped fluid is stagnant. Once the trapped fluid starts to displace from the pores, these circulations slowly disappear, and if the droplet is again trapped during displacement, these recirculations or vortexes reappear. The recirculation or shear-induced circulations cause an additional consumption of energy supplied by displacing phase. It also leads to additional energy dissipation (Roman et al., 2020).

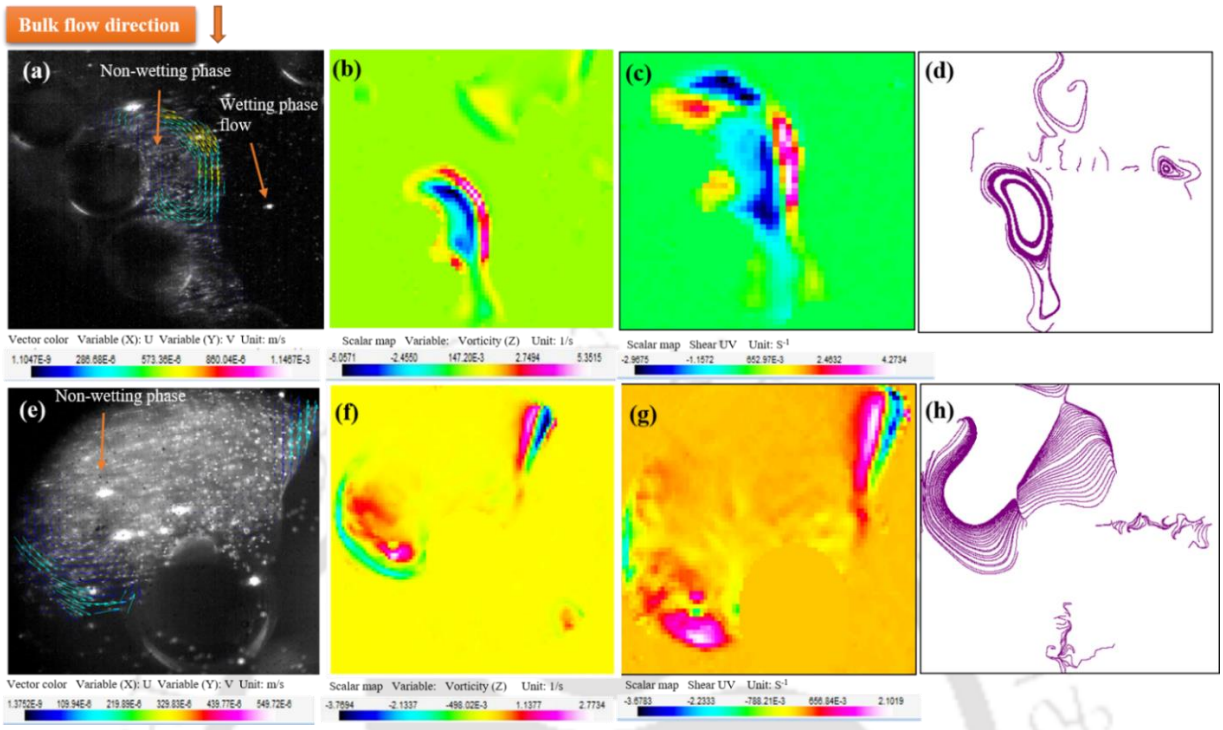

Figure 4. 8 Shear-induced circulations in the non-wetting phase produced by stresses at the interface by wetting phase (Silicone oil - I); (a) & (e) velocity vector maps showing the recirculations and vortex formation, (b) & (f) Vorticity contour map showing the vortex formation during the displacement of trapped non-wetting phase, (c) & (g) Contour maps showing shear rate distribution during two-phase flow, (d) & (h) streamlines showing shear-induced circulations in the non-wetting phase (Glycerol-water solution).

Figure 4.8 shows the formation of shear-induced circulations during the displacement of the trapped non-wetting phase by a continuous flow of the wetting phase. As the displacing phase moves through the porous medium, it applies stress at the boundary of the non-wetting phase. This generates recirculations in the trapped fluid (see Figure 4.8a). Figure 4.8e shows another large circulation. Even if the flow rate of the displacing fluid is slightly increased, only the magnitude of the rotation increases, but the trapped fluid is not displaced from the porous medium. Vortex formation thus resists the pressure force supplied by the displacing phase to

flush out the trapped non-wetting phase. Hence it can be concluded that the vortex formation is highly undesirable from a fluid displacement point of view. However, if the flow rate is significantly increased, there is a breakage of small droplets from the moving ganglion that is produced. Figures 4.8b and 4.8f show the vorticity contour map to quantify the generated shear-induced circulations. The vorticity and shear rate maps are generated using the velocity vector map. The vorticity contours show that the rotation intensity is maximum at the flanks and reduces significantly towards the center. Figure 4.8f shows the fluid rotations near the interface of the wetting and non-wetting phase. Figures 4.8c and 4.8g represent the shear rate contours of displacing and trapped phases, respectively. These plots show that the shear rate is extremely large at the right-side flank of the vortex and minimal at the center of the trapped fluid. Streamlines are drawn by tracing the lines tangent to the velocity vectors. The streamlines further confirm shear-induced circulation during the displacement of the trapped non-wetting phase.

The effect of image processing on the velocity and shear rate prediction is assessed by a sensitivity /uncertainty analysis. Two sets of images are used for velocity and shear rate prediction. One set includes 200 images without pre-processing (without background and noise removal). While the second set contains 200 pre-processed images. Both sets of images are post-processed using dynamic studio software, and velocity vector maps are generated. These maps are used to generate a mean velocity vector map for both sets of images. Shear rate maps are also obtained using these velocity vector maps. The figure 4.9 shows the shear rate and velocity magnitude profiles for images without pre-processing and with pre-processing along line A. Though the profiles are qualitatively similar, there is a significant quantitative difference, emphasizing the need for image pre-processing to improve the accuracy of PIV analysis.

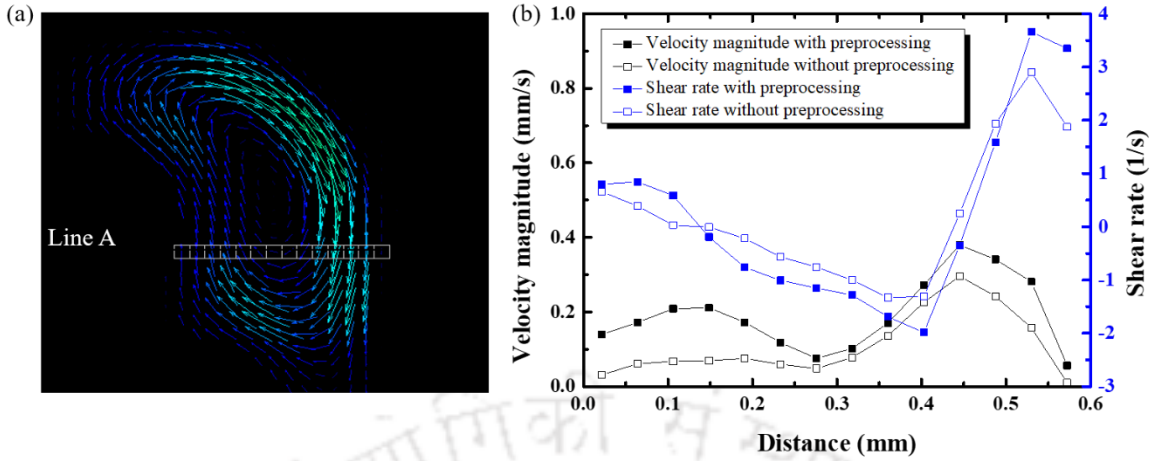

Figure 4. 9 Effect of image pre-processing on shear rate and velocity prediction, (a) line A along which shear rate and velocity magnitude are measured, (b) velocity magnitude and shear rate profiles along line A for without pre-processed images, and pre-processed images, respectively.

4.3 Trapping and mobilization of non-wetting phase

Understanding various parameters responsible for trapping and mobilizing the non-wetting phase in the porous medium is essential to optimize the recovery during enhanced oil recovery processes. Parameters such as displacing phase viscosity and its flow rate, wettability alteration, interfacial tension reduction, in-situ emulsification, aspect ratio, and porosity of the reservoir rocks are crucial for mobilizing the trapped non-wetting phase. In the present study, the effect of flow rate, viscosity, and heterogeneity are discussed quantitatively to understand the trapped fluid mobilization mechanism. To understand the effect of heterogeinity, two micromodels have been used to study the fluid flow. The homogeneous porous medium has uniformly arranged micro cylinders. However, the heterogeneous porous medium contains a random distribution of microbeads of diameter ranging from 500 μm- 600 μm. The porosity of the homogeneous micromodels is about 68%, whereas the heterogeneous micromodel has a porosity of 54%. Table 4.2 shows the list of displacing phases, their flow rates, interfacial tension, and capillary numbers in the heterogeneous and homogeneous micromodels.

Table 4. 2 Displacing phase, their corresponding flow rates, interfacial tension, and capillary number used in heterogeneous and homogeneous porous micromodels to displace the trapped non-wetting phase. (**Note**: Silicone oil II was also injected in the porous medium at 0.05 ml/min and 0.5 ml/min. Similarly, Silicone oil III was also injected at 0.5 ml/min and 1 ml/min. But no change in trapped fluid configuration was observed in both case. So images were not captured corresponding to these flow rates).

Micromodel	**Displacing phase**	**Flow rate (ml/min)**	**Interfacial tension (mN/m)**	**Capillary Number ($v\mu/\sigma$)**
Heterogeneous porous micromodel	Silicone oil - I (10 cSt)	0.05,	35.72	5.15E-08
		0.2		2.06E-07
		0.5		5.15E-07
	Silicone oil – II (50 cSt)	0.05	31.90	2.98E-07
		0.5		2.98E-06
		1		5.96E-06
		5		2.98E-05
		9		5.36E-05
	Silicone oil – III (345 cSt)	0.5	32.93	2.00E-05
		1		4.01E-05
		5		2.00E-04
		8		3.21E-04

Homogeneous porous micromodel	Silicone oil - I (10 cSt)	0.05 0.5	35.72	5.15E-08 5.15E-07
		0.5 1	31.90	2.98E-06 5.96E-06
	Silicone oil – II (50 cSt)	2		1.19E-05

4.4 Effect of flow rate

The effect of the flow rate of the wetting phase on the displacement of the trapped non-wetting phase in the form of small droplets, blobs, and ganglion in the porous medium is investigated. Initially, silicone oil - I (10 cSt) is used at low flow rates. The resultant recirculation and vortex patterns are shown in Figure 4.10. Figures 4.10a-c represent the velocity vector maps in which an increase in the magnitude of shear-induced circulation with an increase in the flow rate (from 0.05 ml/min to 0.5 ml/min) is clearly observed. The velocity at the circumference of the vortex increased from 0.03 mm/s (at a flow rate of 0.05 ml/min) to 0.3 mm/sec (at a flow rate of 0.5 ml/min). The ten-fold increase in the flow rate results in an increase of one order of magnitude in the velocity. The flow rate of the wetting phase is increased to displace the trapped non-wetting phase out of the porous medium. An increase in the flow rate results in an increase in the viscous forces, which apply an additional shear force at the interface of the trapped non-wetting phase and displacing phase. This additional shear force causes a higher momentum transfer to the trapped non-wetting phase and increases the magnitude of shear-induced circulations.

The velocity vector results showed that the maximum velocity is observed at the interface of the wetting and non-wetting phase. Therefore the velocity magnitude is higher at the flanks of the vortex, whereas, minimum, in the center of the vortex. A similar result is also observed by Zarikos et al., 2018. Figures 4.10d, 4.10e, and 4.10f show the vorticity maps at flow rates of 0.05, 0.2, and 0.5 ml/min, respectively. It is observed that with an increase in the flow rate (from 0.05 to 0.5 ml/min), the vorticity increased from 2.23 s^{-1} to 7.60 s^{-1}.

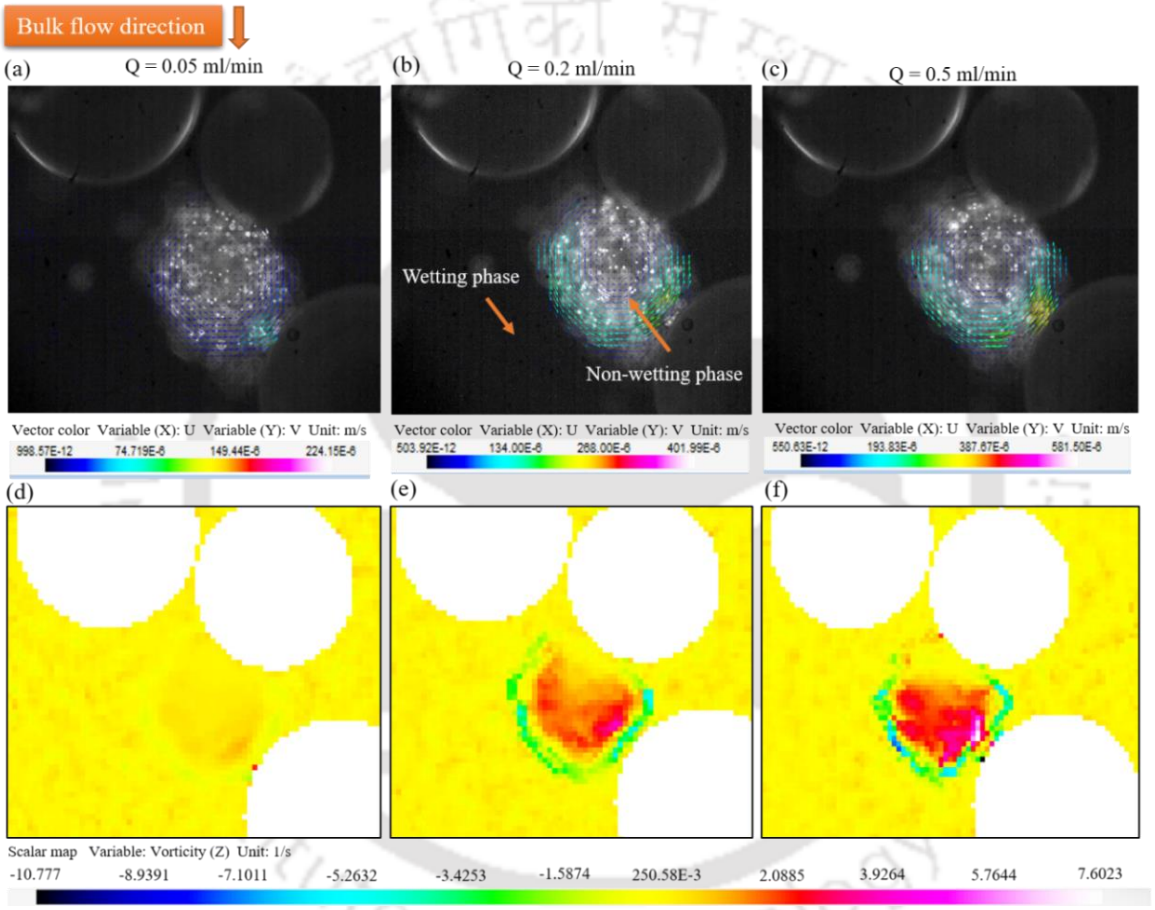

Figure 4. 10 The velocity vector maps quantifying the shear-induced circulations at three flow rates (a) 0.05 ml/min, (b) 0.2 ml/min, and (c) 0.5 ml/min. The vorticity maps corresponding to these flow rates (d) 0.05 ml/min, (e) 0.2 ml/min, and (f) 0.5 ml/min.

4.5 Effect of displacing phase viscosity

Viscosity plays a crucial role in mobilizing the trapped non-wetting phase through pore throats and constriction within the porous medium. Increasing the viscosity of the displacing phase results in controlling the mobility ratio and improving the sweep efficiency. The wetting phase of 10 cSt viscosity in the flow rate range of 0.05 ml/min to 0.5 ml/min could not significantly displace the trapped fluid (section 4.4). In the further experiments, silicone oils of two different viscosity values, 50 cSt (Silicone oil- II) and 345 cSt (Silicone oil -III), are considered. Silicone oil - II is injected at three different flow rates: 1 ml/min, 5 ml/min, and 9 ml/min (Figure 4.11). The flow rates are sequentially increased in the same experiment. The velocity vector and vorticity maps are generated using an image sequence to quantify the shear-induced circulation in the trapped non-wetting phase. The angular velocity is expressed as half of the vorticity ($\frac{1}{2}(\nabla \times \bar{U})$). The results show that at higher flow rates, the vortex size reduces, and angular velocity is high even inside the vortex boundary (outer circumference of the vortex), which is not observed in the case of vortex formed at a low flow rate (1 ml/min). Even at a high flow rate (9 ml/min), the trapped fluid is not displaced, although the strength of the vortex increases. Figures 4.11d, 4.11e, and 4.11f show the maximum vorticity of 3.88 s^{-1}, 8.18 $s^{-1,}$ and 11.6 s^{-1} at a flow rate of 1 ml/min, 5 ml/min, and 9 ml/min, respectively. The maximum angular velocity for the flow rate of 1, 5, and 9 ml/min is calculated as 1.94, 4.09, and 5.8 $s^{-1,}$ respectively, using the formula of angular velocity mentioned above. The vorticity maps in Figure 4.11 are utilized to measure the vortex size with the help of a freeware software image J. The area of the vortex for flow rates 1, 5, and 9 ml/min are measured as 1463615 μm^2, 975043 $\mu m^{2,}$ and 714201 $\mu m^{2,}$ respectively.

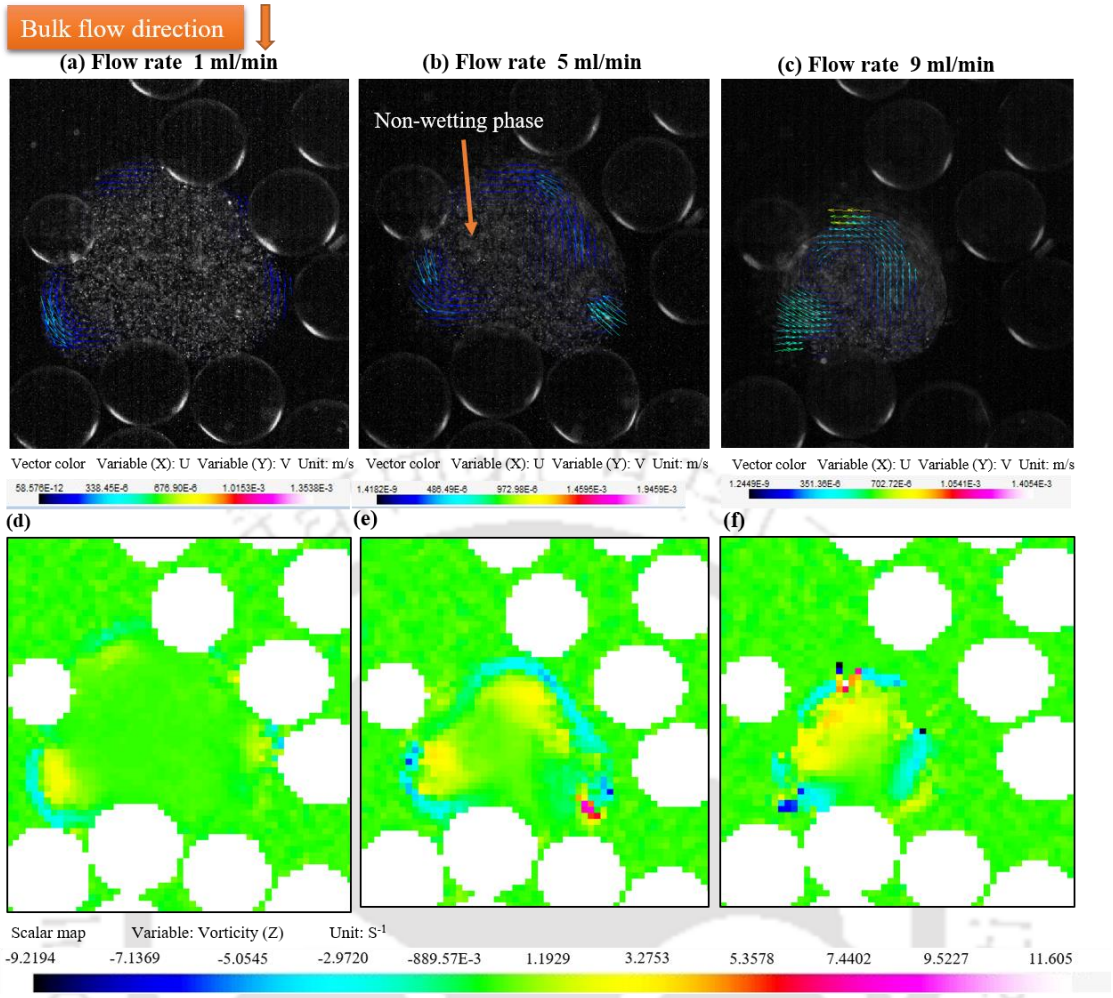

Figure 4. 11 Velocity vector maps showing the shear-induced circulation formed by displacing phase (silicone oil - II) at flow rates of (a) 1 ml/min, (b) 5 ml/min, and (c) 9 ml/min. Vorticity map showing injection of silicone oil II to displace the trapped ganglion (d) flow rate 1 ml/min, (e) flow rate 5 ml/min, (f) flow rate 9 ml/min.

With silicon oil –III (345 cSt), the experiments are carried out at two different flow rates, 5 ml/min and 8 ml/min. In Figure 4.12, the velocity vector map shows the displacement of the trapped ganglia. It is observed that at a flow rate of 5 ml/min, the ganglia mobilizes (Figure 4.12a-d). Due to high viscosity and flow rate, the trapped ganglia disintegrate into smaller droplets and ganglia and hence get mobilized easily. The reason for the disintegration of the

droplets from large ganglia is the higher flow rates of displacing phase, resulting in higher capillary numbers (2×10^{-4}). The increase in viscous force at the high capillary number (due to a higher flow rate) is consistent with the change in the interfacial energy, resulting in ganglia disintegrating into a number of droplets or blobs (Pak et al., 2015). The magnitude of rotation of trapped non-wetting phase ganglia increases with an increase in the flow rate, resulting in the center of mass of ganglia moving close to the interface between displacing phase and trapped non-wetting ganglia. The interfacial stresses applied by the displacing phase disintegrate this droplet from the ganglia.

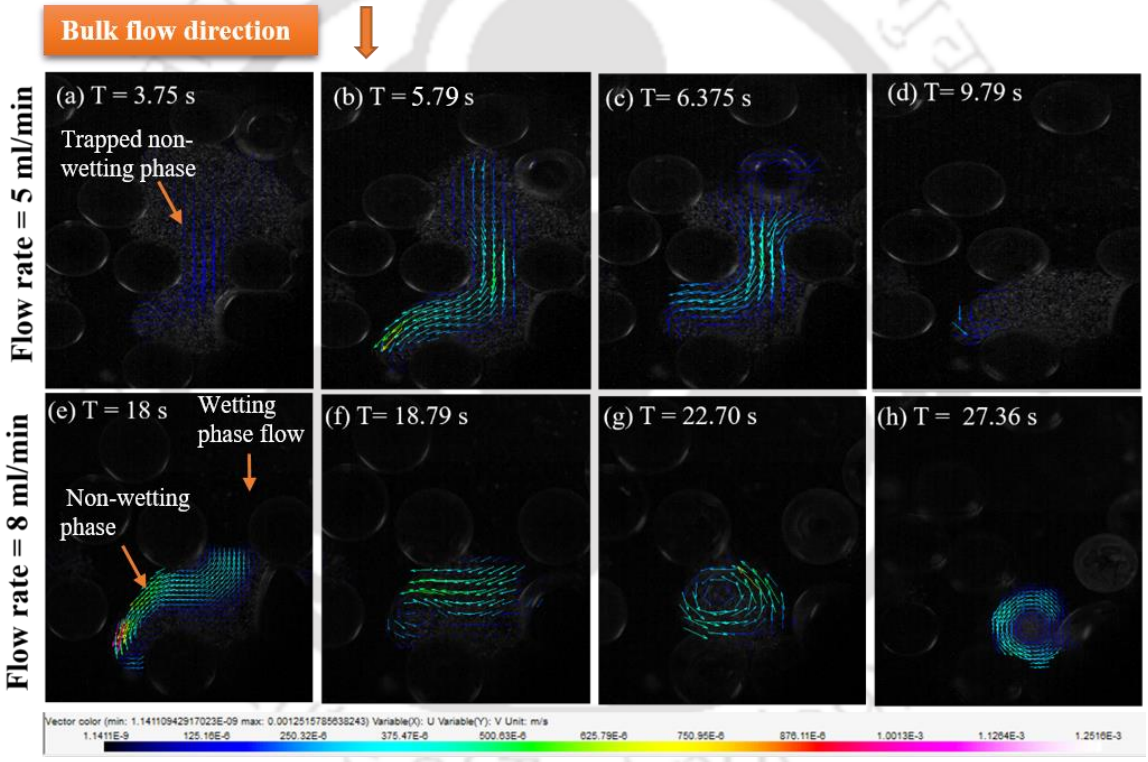

Figure 4. 12 Velocity vector map showing the displacement of trapped ganglia by injecting silicone oil - III (viscosity 345 cSt) for flow rates of (a-d) 5 ml/min and (e-h) 8 ml/min at different time intervals.

During mobilization, shear-induced circulation or vortex is not visualized. However, once the mobilization ceases, the shear-induced circulation is again observed in the trapped ganglia. A

small ganglion has remained trapped at a flow rate of 5 ml/min due to capillary forces (Figure 4.12 d). A further increase in the flow rate (8 ml/min) results in the further disintegration of the small ganglia in many droplets and blobs (Figure 4.12 e-h). These droplets are produced due to the high flow rate; however, small blobs remain trapped (Figure 4.12 h). Hence, the simultaneous increase in the viscosity and flow rate of the wetting phase results in the recovery of the residually trapped non-wetting phase, which maximizes the additional recovery of the non-wetting phase.

4.6 Effect of heterogeneity

For homogeneous reservoirs, the pore size and pore throat sizes are uniform, the non-wetting phase trapping during water flooding is less, and most of the trapped oil after the secondary flooding process can be displaced by increasing the viscosity and flow rate of the displacing fluid. However, in the case of a heterogeneous porous medium (where the pore throat size is significantly smaller), it leads to trapping of the non-wetting phase. Even a very high flow rate could not displace this trapped non-wetting phase completely (Figure 4.12). A displacing fluid with high viscosity and a high flow rate can displace the trapped non-wetting phase but would require much more energy/pressure.

Two micromodels, one heterogeneous porous medium (porosity, 54%) and another homogeneous porous medium (porosity 68%, with uniform cylindrical micro-posts) are considered to study the effects of heterogeneity. Silicone Oil-I and II (10 cSt and 50 cSt) are injected into the porous medium at different flow rates to displace the trapped non-wetting phase droplets, blobs, and ganglia. Initially, silicone Oil-I is injected at a flow rate range of 0.05-0.5 ml/min in the homogeneous porous medium. Most of the non-wetting phase is displaced, but a small quantity remains trapped in the pores in the form of ganglia (Figure

4.13). The non-wetting phase still remained trapped in the porous medium, even at a flow rate as high as 0.5 ml/min of silicone oil (10 cSt).

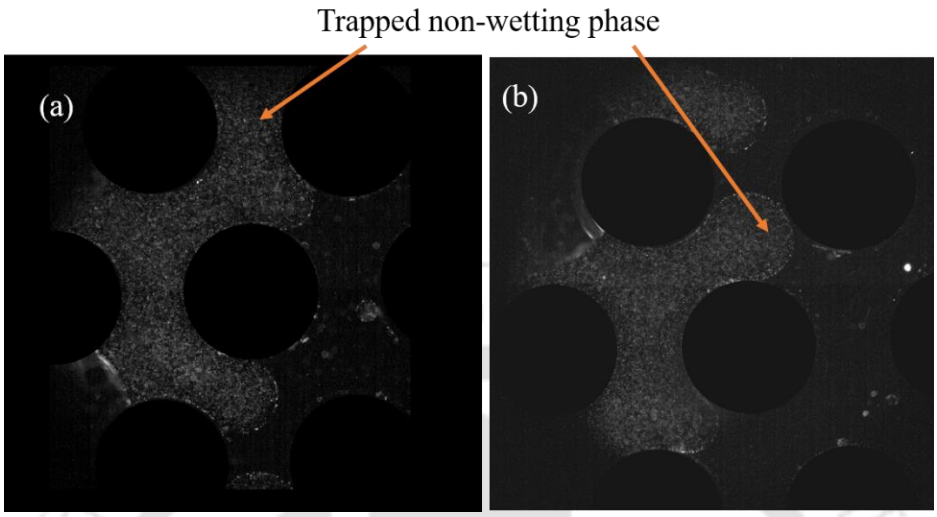

Figure 4. 13 Trapped non-wetting phase in the porous medium during injection of silicone oil (10 cSt) at 0.5 ml/min in the homogeneous porous medium (images were captured at 24 fps)

In further experiments, silicone oil-II (50 cSt) is injected in a homogeneous porous medium at different flow rates of 0.5, 1, and 2 ml/min to displace the trapped non-wetting phase. The flow rates are sequentially increased in the experiment. Initially, the displacing phase is injected at a flow rate of 0.5 ml/min. During displacement of the non-wetting phase from the porous medium, the disintegration of larger ganglia into smaller droplets and vice versa are observed. The integration/disintegration of droplets happens when the viscous forces of displacing fluid overcome the capillary force at some position of trapped fluid. Figure 4.14 shows this phenomenon of small droplet integration into larger ganglion while mobilizing the trapped non-wetting phase. The phenomena of integration and disintegration of droplets help in mobilizing the trapped non-wetting phase.

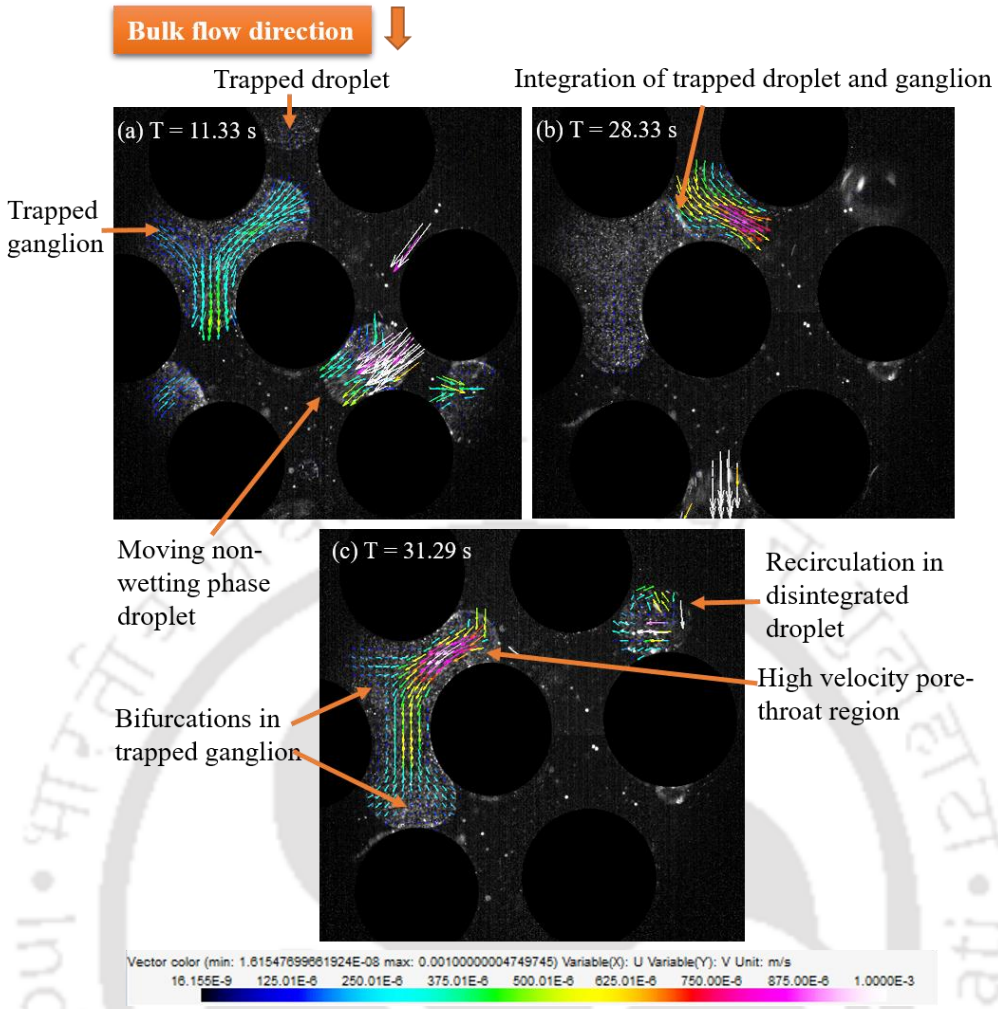

Figure 4. 14 Integration & disintegration of small droplets into/from large ganglion (Flow rate 0.5 ml/min, 24 fps and displacing phase silicone oil - II (viscosity 50 cSt)), (a) non-wetting phase droplet approaching towards ganglion, (b) Integration of non-wetting droplet into large ganglion, (c) recirculation in a trapped disintegrated non-wetting phase droplet.

During the displacement process, fluctuating flow or unstable flow (back and forth fluid motion) is observed in the trapped non-wetting phase. The main reason for this phenomenon is the movement of small droplets and blobs in the porous medium during the displacement process. These droplets affect the displacement of the larger ganglia. Sometimes it applies the shear force on the ganglia to displace from the pores, and sometimes it displaces ganglia in the

pores in opposite to the flow direction, which results in the intermittent change of course (direction) of the trapped non-wetting phase in the porous medium.

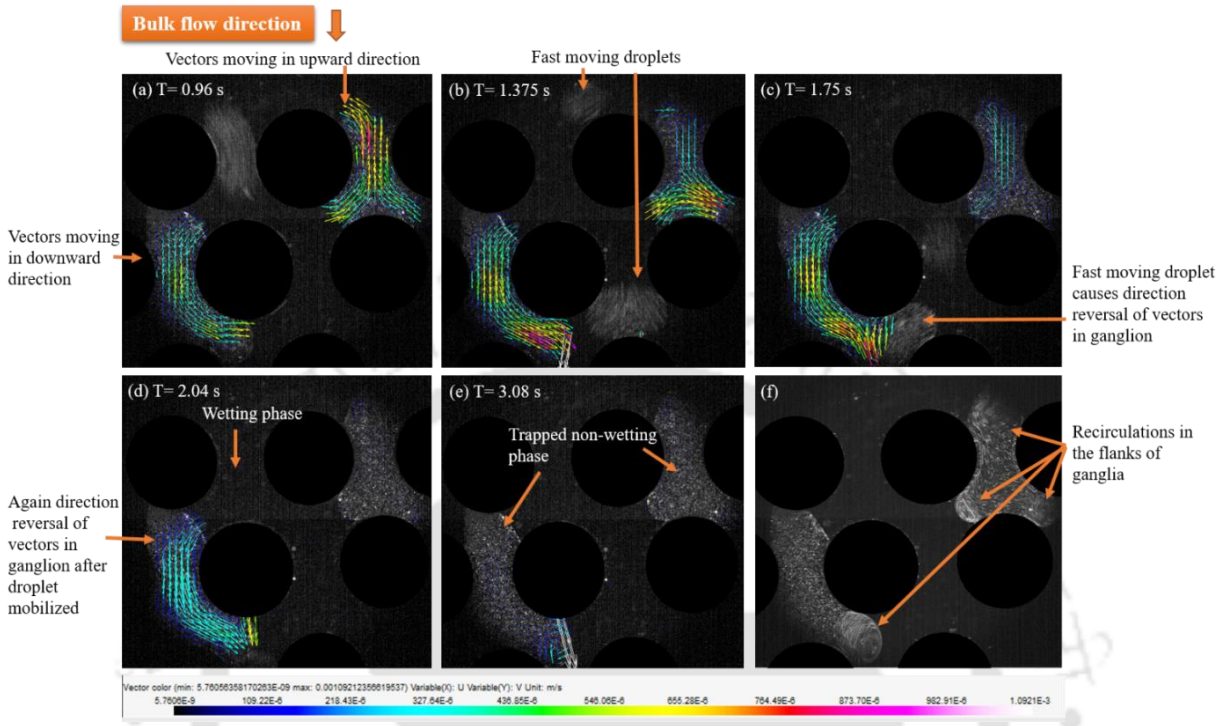

Figure 4. 15 fluctuating flow during displacement of trapped fluid through the porous medium, (a) counter-current movement of velocity vectors because of the displacement of smaller non-wetting phase droplets in the pore, (b) velocity vectors showing the movement in the direction of flow, (c) direction reversal due to fast-moving droplet, (d) movement of the ganglion in the downward direction, (e) recirculations at the low end of the trapped ganglion, (f) image maxima showing the shear-induced circulations in the trapped ganglia. The flow rate was 1 ml/min, and the viscosity of the displacing phase silicone oil-II was 50 cSt.

Figure 4.15 shows the fluctuating motion of the trapped non-wetting phase during the displacement process using silicone oil - II (viscosity 50 cSt) at a flow rate of 1 ml/min in the porous micromodel. Initially (t = 0.96 s), when a droplet suddenly came nearby to the trapped fluid, a movement in the downward direction for fluid trapped in the left, and a movement in the upward direction for fluid trapped in the right is observed (Figure 4.15a). At time t = 1.375

s, the moving droplet is just about to reach the left side trapped non-wetting phase; the flow direction of the non-wetting ganglion is the downward direction (Figure 4.15b). But at time t = 1.75 s, when the droplet reaches beside the trapped ganglion of the non-wetting phase, it obstructs the flow of the ganglion in a downward direction, and the flow is reversed to an upward direction (Figure 4.15c). This means that only at a minimal time between 0.96 s to 1.75 s, the flow direction of the ganglion reversed because of the movement of small droplets. Hence, the movement of small droplets of the non-wetting phase during two-phase flow contributes to the fluctuating (unsteady) flow in the medium. Once the droplet is moved out from the region of interest of the porous domain, the flow is again reversed in the downward direction (Figure 4.15d). If the trapped fluid is not disturbed by the droplet of the non-wetting phase, then at the same flow rate, the non-wetting phase ganglia become stagnant, and only recirculation or vortex is formed at the flanks of the ganglia, which can be easily seen in Figure 4.15e and 4.15f. Hence, the presence of smaller moving droplets affects the movement of larger ganglia. The movement of smaller non-wetting phase droplets cause fluctuating flow in the porous medium. These droplets cause flow direction reversal, contributing to unsteady flow behavior in the porous medium during two-phase flow. At higher flow rates, these droplets merge with the ganglion and start to move. Even if the droplet is not merged with the ganglion, it can change the flow direction of the ganglion.

Even at a flow rate as high as 1 ml/min, the trapped non-wetting phase is not entirely displaced as a small amount of non-wetting phase remained trapped within the porous medium because of capillary forces. The difference in viscosity between glycerol water solution (119.68 cSt) and silicone oil (50 cSt) results in higher mobility of silicone oil, and causes trapping of some non-wetting phase in the porous medium. Therefore, the flow rate is further increased to 2 ml/min, keeping the silicone oil viscosity (50 cSt) constant. In this case, it was observed that

the remaining non-wetting phase trapped in the porous medium is completely displaced. The reason for the displacement of the trapped non-wetting phase is an increase in capillary number up to 1.19×10^{-5} due to an increase in displacing phase flow rate (2 ml/min). An increase in the flow rate causes a further increase in the magnitude of recirculation in the trapped non-wetting phase resulting in movement of the center of mass of trapped ganglia closer to the interface between the displacing phase and trapped non-wetting phase. This results in the disintegration of the ganglia in the smaller droplets. The remaining trapped ganglia are also easily produced because of the high viscous force of the displacing phase at a high flow rate. Figure 4.16 shows the displacement of the remaining non-wetting phase out of the porous medium at 2 ml/min of flow rate by silicone oil - II (50 cSt). Initially, in figure 4.16a (T=3.33s), the recirculations are observed at the flanks of the trapped ganglia. The applied flow rate results in displacing the trapped non-wetting phase. As the trapped ganglia start displacing, the recirculations disappear from the flanks of ganglia at T=8.5 s (figure 4.16b). In figure 4.16c (T= 14.875 s), the ganglion in the left side bifurcated during the displacement process. In figure 4.16d and 4.16e (T= 19.66 s and T= 20 s), it can be seen that the right side ganglion started moving very slowly with some recirculation at the flank. Figure 4.16f (T= 20.25 s) shows a non-wetting phase droplet about to disintegrate from the right side trapped ganglion. In figure 4.16g (T= 24.375 s), the droplet disintegrated from the ganglion in the right side and displaced out of the field of view of this image. The remaining non-wetting phase in figure 4.16h started displacing out of the porous medium by the displacing phase. Finally, it can be clearly seen in figure 4.16i (T= 25.83 s) that the trapped non-wetting phase is almost completely displaced out of the porous medium, and only a small portion of the non-wetting phase is left behind and stuck in the pore corner. Hence it can be concluded that the increased flow rate and resulting droplet disintegration help in displacing the non-wetting phase out of the porous medium. If the displacement in both the micromodels is compared, it can be seen that the non-wetting phase trapped in the

homogeneous porous medium is easily displaced. The trapped non-wetting phase is completely displaced using silicone oil - II (50 cSt) at 2 ml/min. In the case of heterogeneous porous micromodel, the maximum displacement of the trapped non-wetting phase is observed using silicone oil with a viscosity of 345 cSt and at a flow rate as high as 8 ml/min. Hence, a heterogeneous micromodel results in the trapping of more non-wetting phases. The displacement of this trapped non-wetting phase is still difficult, and only a small amount can be displaced at higher flow rates with highly viscous displacing fluid. The trapped fluid saturation in the homogeneous porous medium changed from 26.11% to 0.99% after injecting the wetting phase at 2 ml/min. In the heterogeneous porous medium, trapped fluid saturation changes from 29.69% to 6.75% after injecting silicone oil III (345 cSt) at 8 ml/min flow rate.

A few other parameters are also responsible for mobilizing the trapped non-wetting phase from the porous medium. These parameters include interfacial tension, wettability alteration, and in-situ emulsification. The tendency of a fluid to spread or adhere to a solid surface in the presence of other immiscible fluids is known as wettability. The application of nanoparticles (such as SiO_2, TiO_2, and Al_2O_3), alkali (Na_2CO_3, NaOH), and surfactant (SDS) cause wettability alteration leading to the production of trapped oil in the porous medium. The use of the above chemicals also helps in IFT reduction and in-situ emulsification, which further produces the trapped non-wetting phase. Further pore-scale studies are required to understand the effect of these parameters on the displacement process.

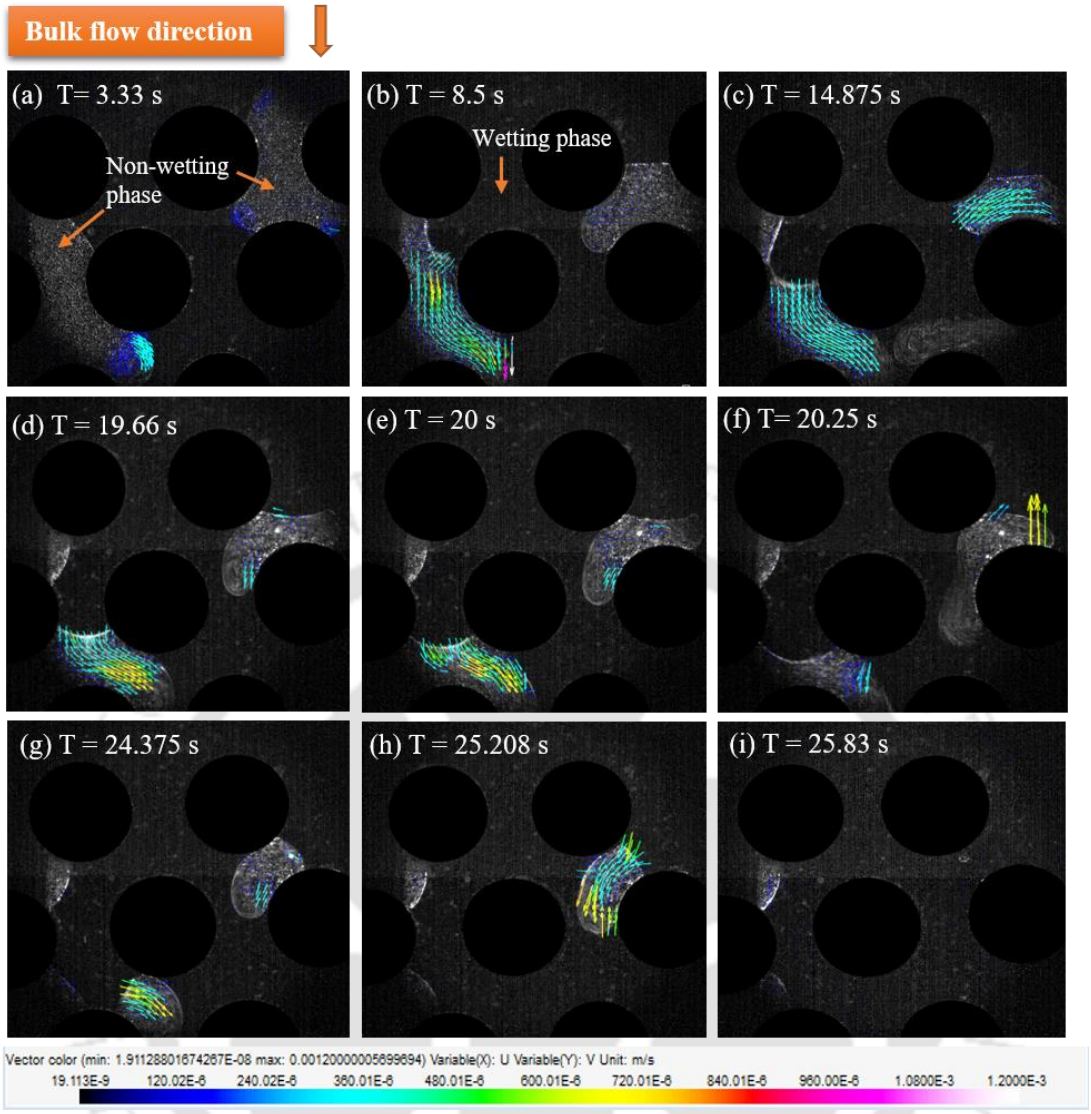

Figure 4. 16 Displacement of non-wetting phase ganglia using silicone oil - II of viscosity 50 cSt at 2 ml/min flow rate: (a) shear-induced circulations at the flanks of the trapped non-wetting phase ganglia, (b) displacement of trapped ganglia, (c) disintegration of ganglia during displacement process; (d), (e) mobilization of trapped non-wetting phase ganglia, (f) detachment of droplet from the parent ganglion; (g), (h): disintegration into smaller droplets, (i) complete displacement of trapped non-wetting phase.

4.7 Summary

Single and two-phase flow experiments are conducted in a bead-based heterogeneous porous micromodel to gain a fundamental understanding of flow dynamics and pore-scale. The single-phase experimental results are validated using numerical simulations as a reference for two-phase flow experiments. The two-phase flow results show an unstable displacement of the non-wetting phase by the wetting phase. The phenomena of shear-induced circulations and viscous fingering are observed during the displacement process. These phenomena are undesirable and result in unstable/unsteady flow behavior in the porous medium. Due to unstable displacement, the non-wetting phase is trapped in small constrictions, pore throats, and dead-end zones in the form of droplets, blobs, and ganglia. It is observed through the experiments that one of the reasons for unsteady flow behavior is the disintegration or integration of droplets from the ganglia. These droplets cause flow direction reversal of ganglia while moving through the constrictions or pore throats, causing fluctuating flow back and forth. The shear-induced circulations are observed during the displacement process in the trapped non-wetting phase due to viscous stresses at the interface. In this study, the effect of various parameters, such as displacing phase flow rate, viscosity, and heterogeneity on mobilizing trapped non-wetting phase, is investigated. The velocity vector map shows that increasing only the flow rate does not displace the trapped non-wetting phase within the tested range of flow rates (0.05 – 9 ml/min). It only increases the intensity of recirculation in the trapped droplet or ganglia. The increase in viscosity of the displacing phase has a greater influence on removing the trapped non-wetting phase. The micromodel flooding in the homogeneous porous medium demonstrates minimal trapping and maximum recovery of the non-wetting phase during the two-phase flow. On the other hand, a heterogeneous micromodel causes excessive trapping and minimum mobilization of the non-wetting phase.

Chapter 5. Numerical simulation of two-phase flow in complex pores

Dead-end;

Contraction expansion;

Shear-induced circulations;

Pore-scale flow dynamics;

Phase field method;

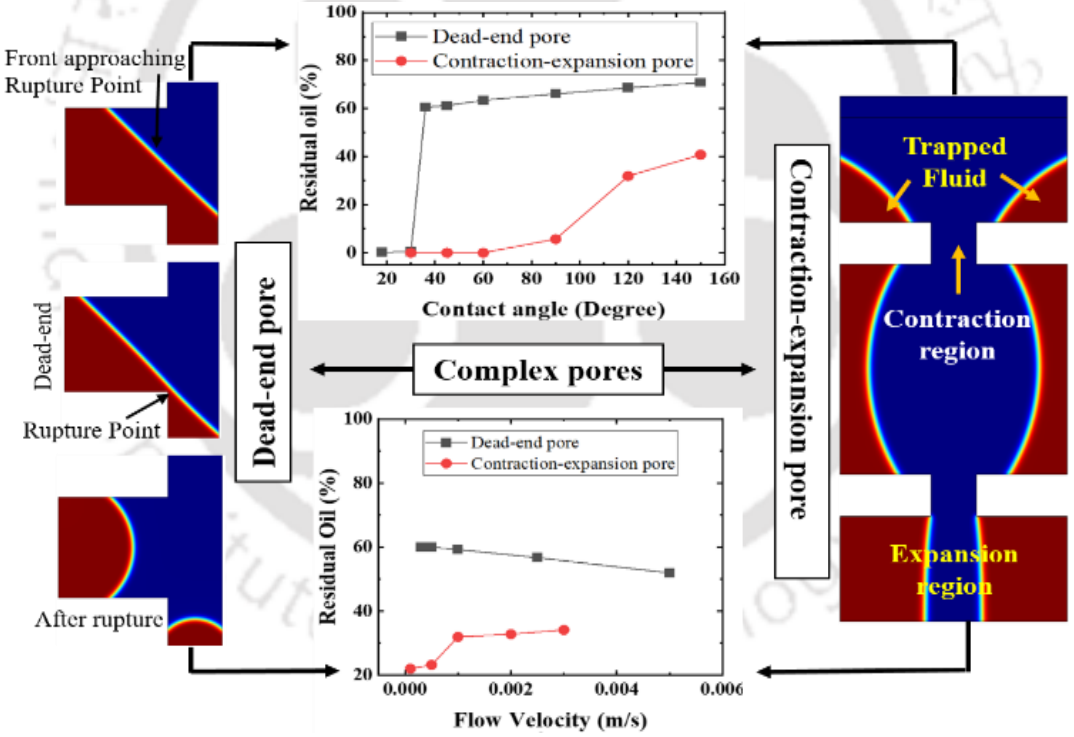

Numerical simulation of two-phase flow in complex pores

This work presents numerical simulations of immiscible two-phase flow at pore-scale for complex pores such as dead-ends and contraction expansion to better understand the displacement mechanisms and parameters affecting the oil recovery. The effect of displacing phase injection velocity, viscosity ratio, interfacial tension, wettability alteration, viscosity of trapped oil, and geometric ratio on the trapped oil recovery has been investigated. The contact angle measurement shows that at a critical contact angle, the oil recovery will be maximum. The complete displacement of trapped oil is observed when oil-water interface reaches the bottom of the dead-end before it reaches the rupture point (junction of pore throat channel and dead-end). The change in the viscosity ratio does not have significant effect on oil recovery in both the complex pores. Oil recovery from the dead-ends increases with an increase in the water injection velocity. Increasing the dead-end depth cause a reduction in the oil recovery. However, reducing the contact angle reduces the residual oil saturation in the dead-ends.

5.1 Phase field method

The phase field method is one of the numerical simulation methods used for the two-phase flow. It is popular due to it's their ability to handle complex pore geometries and topological changes. The phase field method (PFM) realistically captures phenomena related to viscous and capillary forces with a reasonable computational time. The application of the phase-field method is more preferable in terms of both the conservation of mass and capturing the interface curvature for modeling two-phase flow in pore geometries. In this method, Navier-Stokes (N-S) equation is coupled with the Cahn-Hilliard equation and numerically solved using the finite element method. The Cahn–Hilliard equation tracks the diffuse interface separating the immiscible phases. The following assumptions are considered while performing the

simulations. Both the Fluids (water and oil) are assumed to be Newtonian, incompressible, and assume no mass transfer across the interface. The fluid properties such as viscosity, density, and surface tension are assumed to be constant irrespective of pressure, and the system is considered to be isothermal. The gravity is neglected as the numerical simulations are performed in a 2D geometry.

The N-S equation in terms of momentum and continuity equations can be expressed as

$$\rho\frac{\partial \mathrm{u}}{\partial \mathrm{t}} + \rho(\mathbf{u}.\nabla)\mathbf{u} = \nabla.[-\mathrm{pI} + \mu(\nabla\mathbf{u} + (\nabla\mathbf{u})^{\mathrm{T}})] + \mathrm{F_{st}} + \rho\mathrm{g} \tag{26}$$

$$\nabla.\mathbf{u} = 0 \tag{27}$$

Where ρ denotes the fluid density (Kg/m^3), μ is the dynamic viscosity (mPa.s) of the fluid, **u** represents the fluid velocity (m/s), F_{st} is the surface tension force acting at the oil-water interface, p denotes the pressure (pa), and g is the gravity vector (m/s^2).

$$\frac{\partial\varphi}{\partial \mathrm{t}} + \mathbf{u}.\nabla\varphi = \nabla.\frac{\gamma\lambda}{\varepsilon^2}\nabla\psi \tag{28}$$

$$\psi = -\nabla.\varepsilon^2\nabla\varphi + (\varphi^2 - 1) \tag{29}$$

Where φ is the phase-field variable. It represents the oil-water interface when $-1 < \varphi < 1$. u is the fluid velocity (m/s). γ is the mobility (m^3.s/kg), λ is the mixing energy density (N), ε represents the oil-water interface thickness (mm), ψ is the phase-field help variable. $\gamma = \chi\varepsilon^2$, where χ is the mobility parameter, which determines the timescale for Cahn-Hilliard diffusion. For good initial approximation, χ is considered as 1.

5.2 Simulation set-up

The dead-end and contraction-expansion pore models used in the current work are taken from the experimental work of Roman et al., 2020. These models represent the pore body and pore throat configuration present in the reservoir rocks. The pore geometries used are identical to the natural reservoir rock, with pore bodies in the range of hundreds of microns and pore throats

of tens of microns. The dimensions of the dead-end and contraction-expansion models are presented in Figure 5.1. In the dead-end model, the pore throat channel size is 100 μm, and dead-ends have a depth of 200 μm (Figure 5.1a). The different geometries of the dead-end pore model (by varying the pore throat channel width and dead-end depth) are used during numerical simulations. In the contraction expansion model, the dimensions of the expansion region (pore body) and contraction region (pore throat) are 100 μm and 20 μm, respectively (Figure 5.1b).

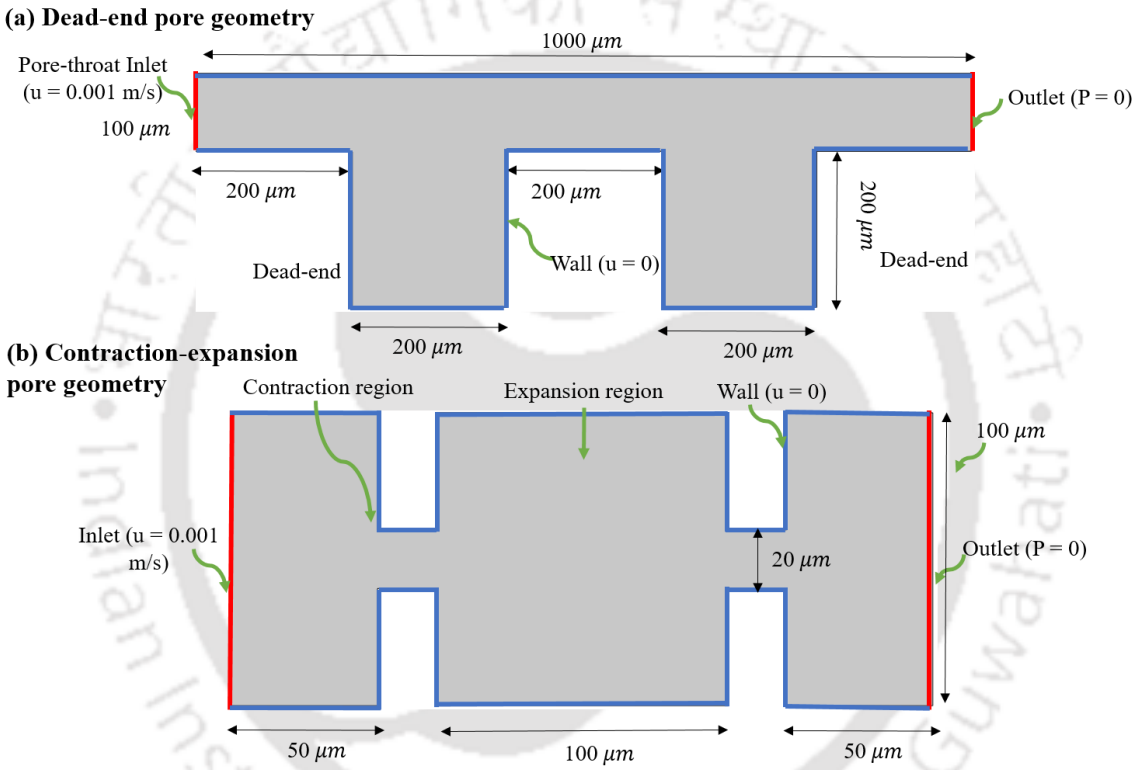

Figure 5. 1 Schematic diagram of (a) dead-end pore, (b) Contraction expansion pore.

Numerical simulations are executed using COMSOL Multiphysics. The Navier-Stokes equation is solved for the velocity and pressure. Both of the pore models are discretized using a physics-controlled meshing sequence. The mesh statistics reveal the total mesh elements of 37369 with minimum and maximum element sizes are 0.045 μm and 3.9 μm, respectively. Tables 5.1 and 5.2 show the mesh statistics of the discretized domain.

Table 5. 1 Mesh statistics

S.N.	Description	Value
1.	Minimum element quality	0.1384
2.	Average element quality	0.9408
3.	Triangle	35755
4.	Quad	1614
5.	Edge element	905
6.	Vortex element	14

Table 5. 2 Size settings

S.N.	Description	Value
1.	Maximum element size	3.9 μm
2.	Minimum element size	0.045
3.	Curvature	0.25
4.	Maximum element growth rate	1.08
5.	Thickness adjustment factor	5
6.	Number of boundary layers	2

Silicone oil of viscosity 0.0046 Pa.s and density 913 kg/m^3 is used as the displaced fluid. However, water with a viscosity of 0.00089 Pa.s and density of 1000 kg/m^3 is used as a displacing phase during water flooding in the pore models. Interfacial tension of 35 mN/m,

inlet velocity of 0.001 m/s, and contact angle of 45° are used for the base case. Several simulations are executed by varying the displacing phase injection velocity (0.0003 m/s – 0.01 m/s), viscosity ratio (0.09 – 10.65), contact angle (150°- 18°), interfacial tension (1 mN/m - 50 mN/m), and different geometric parameters.

The grid-independence test is conducted to obtain the optimized number of mesh elements. For this purpose, the case with a water injection velocity of 0.001 m/s in the oil-saturated dead-end pore model is considered. Four meshes (A, B, C, and D) with different numbers of elements are considered, and the average velocity of the injected fluid near the oil-water interface (50 μm from the inlet) is measured (Figure 5.2). Table 5.3 shows the grid independence test and the relative errors with respect to Mesh A. The minimum velocity measurement error (with respect to Mesh A) of 0.22% is obtained at t = 0.2 s. Hence, Mesh B is used to discretize the pore domain in the model.

Table 5. 3 The results of the grid independence test

S.N.	**Mesh type**	**No. of elements**	**Velocity (m/s) at t =0. 2s**	**Relative error with respect to Mesh A (%)**
1.	Mesh A	131231	9.9797 E-4	0.22
2.	Mesh B	37369	9.9574 E-4	0.83
3.	Mesh C	9896	9.8969 E-4	1.19
4.	Mesh D	6453	9.8609 E-4	

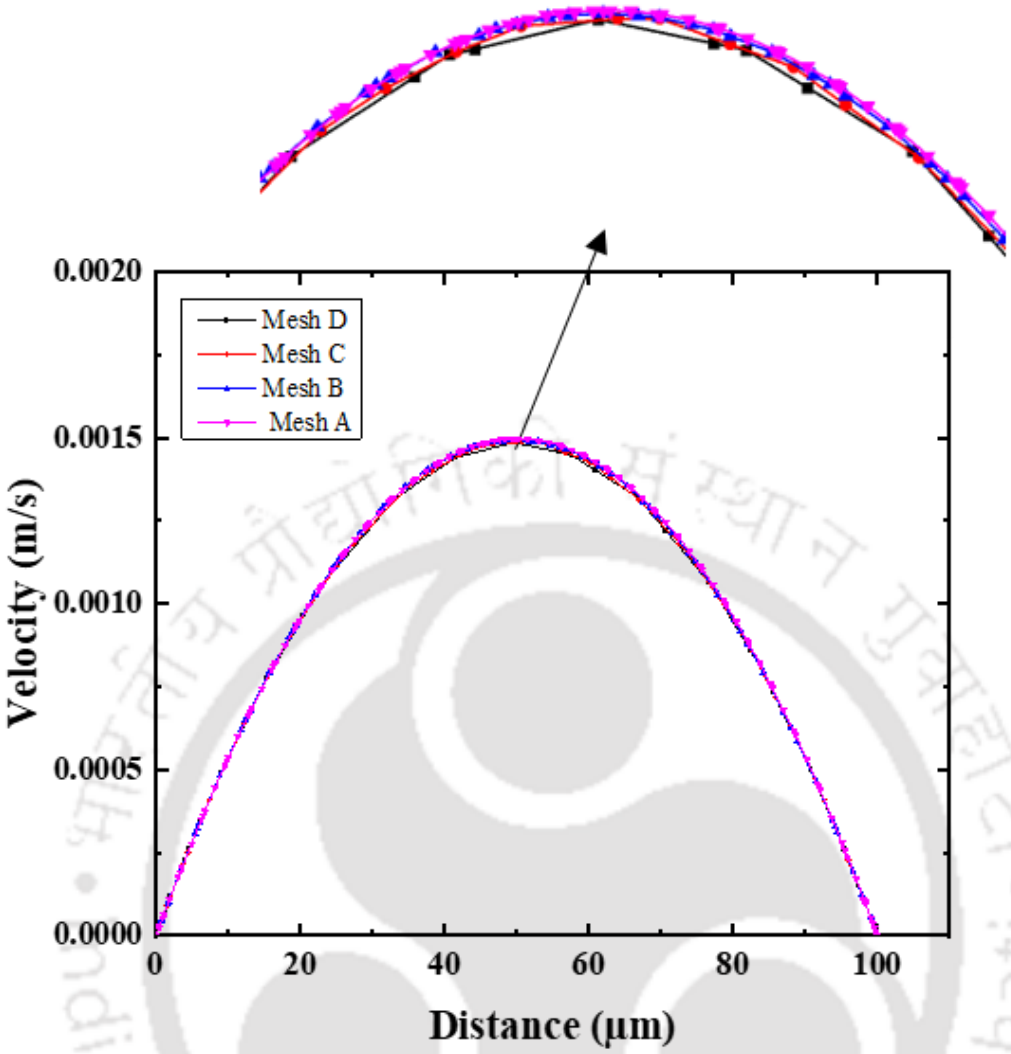

Figure 5. 2 Grid independence test four different meshes A, B, C, and D.

5.3 Validation of the numerical model

The model is validated by comparing the results with the experiments conducted by Roman et al., 2020 in a dead-end geometry to understand phase trapping and mobilization behavior (Figure 5.3a). The numerical simulations are performed using the same fluids as used in the experiments, DI water and glycerol mixture (20:80) be as trapped fluid and oil (5 cSt) as the displacing fluid (Figure 5.3b). The interfacial tension and viscosity ratio values used in the simulations are 15 mN/m and 0.09, respectively. All the parameters taken above are identical to those used by Roman et al., 2020. The dead-end geometry is initially saturated with the DI

water and glycerol solution. Silicone oil is injected into the model at a velocity of 0.00145 m/s (mentioned in Table 1, case 4 Roman et al., 2020).

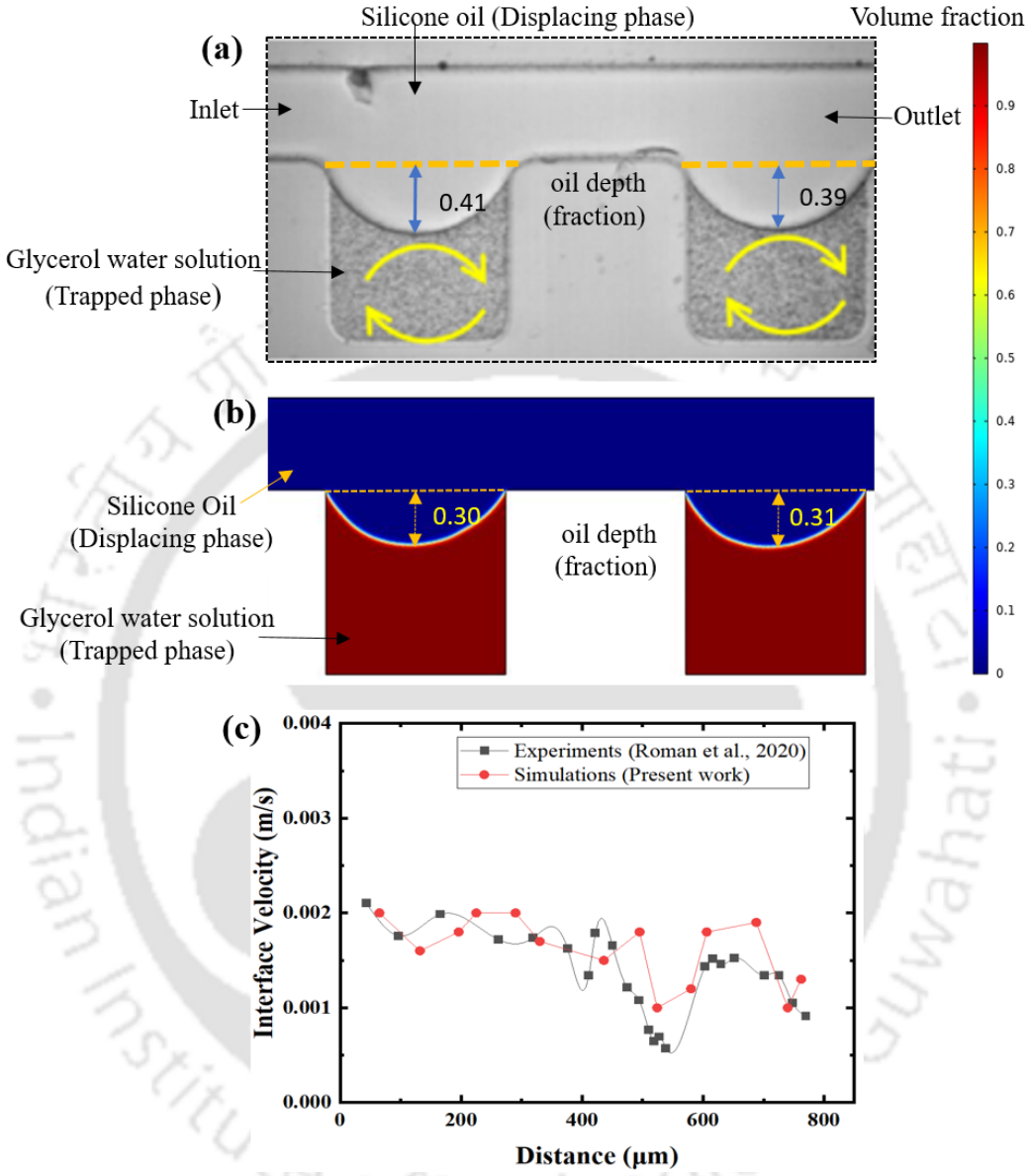

Figure 5. 3 Validation of simulations (a) Oil depth (fraction) in dead-ends 1 and 2 during the experimental study, (b) Oil depth (fraction) during the numerical study, (c) comparison of the interface velocity between the experimental work by Roman et al., 2020, and numerical simulation results in the current study with identical parameters.

Good agreement in the simulations of the current study and experimental work by Roman et al., 2020 is observed. The experiment results showed the ratio of oil depth to dead-end depth is 0.41 and 0.39 in dead-end 1 and 2, respectively (Figure 5.3a). However, the simulations result in the current study reveals that the ratio of oil depth to dead-end depth is 0.30 and 0.31, in dead-end 1 and 2, respectively (Figure 5.3b). Simulation results showed 73.17% accuracy in dead-end 1, while 79.48% in dead-end 2, relative to the experiments conducted in a dead-end with case 4 mentioned in table 1 of Roman et al., 2020. The curvature of the oil-water interface, bulged towards the trapped phase in the dead-ends is almost symmetrical in both the experimental and simulation results. Symmetry is also observed in the interface velocity along the centreline of the main pore throat channel in the dead-end geometry (Figure 5.3c).

5.4 Oil trapping in complex pores

The dead-end pores contribute about 34-51% of the pore space of the reservoir rocks, which causes significant oil trapping in these pore constrictions. A heterogeneous porous medium geometry is taken from Keller et al., 1997, and a fracture has been created horizontally in the middle of the porous medium to understand the severity of oil trapping. The total void space present in the porous medium is 1.18×10^{-7} m^2. Numerical simulations are performed by saturating the medium with silicone oil (5 cSt) and displacing it by injecting water at an injection velocity of 0.001 m/s. A significant amount of oil (49.2%) remained trapped after water flooding in the porous medium. It is noticed that most of the oil is trapped in the dead-ends and contraction-expansion pores (Figure 5.4). The trapped oil needs to be recovered from these small pore constrictions to improve the sweep efficiency.

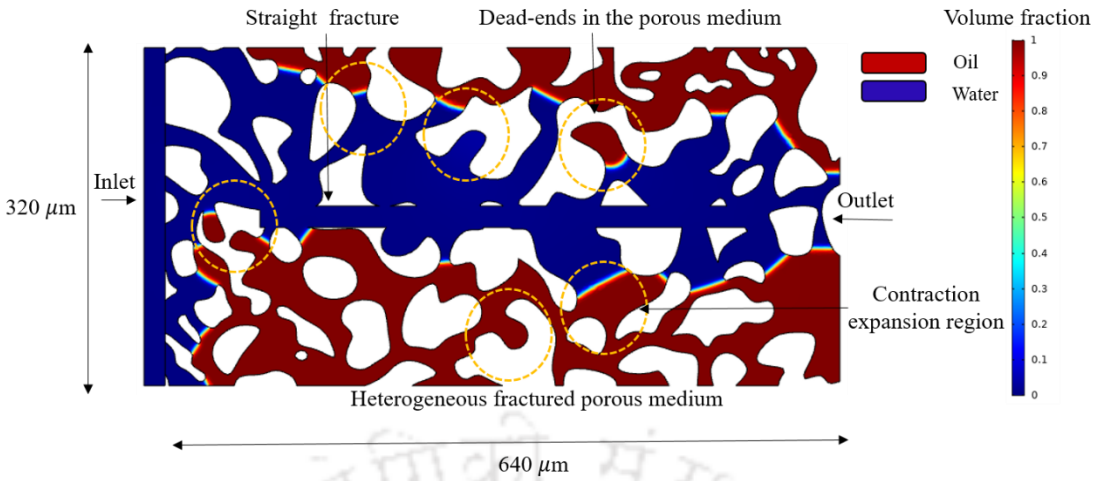

Figure 5. 4 Water flooding in the oil-saturated fractured porous medium, leaving oil trapped in dead-ends and contraction expansion regions.

Several parameters may be responsible for oil displacement through smaller pore constrictions, such as dead-ends. These parameters include wettability, interfacial tension, capillary number, and viscosity ratio (Rokhforouz and Amiri, 2019). Therefore, the current work investigates the effects of wettability alteration, interfacial tension, injection velocity, viscosity ratio, and the effect of geometric parameters on trapped oil recovery from dead-end and contraction expansion pores.

5.5 The effect of contact angle

Wettability substantially affects the displacement process in porous media. The contact angle (θ) is generally used to quantify the degree of wettability, which is a condition used in determining the interfacial shape. The wettability increases with a reduction in the contact angle, and the residual oil is recovered from the complex pores (dead-ends).

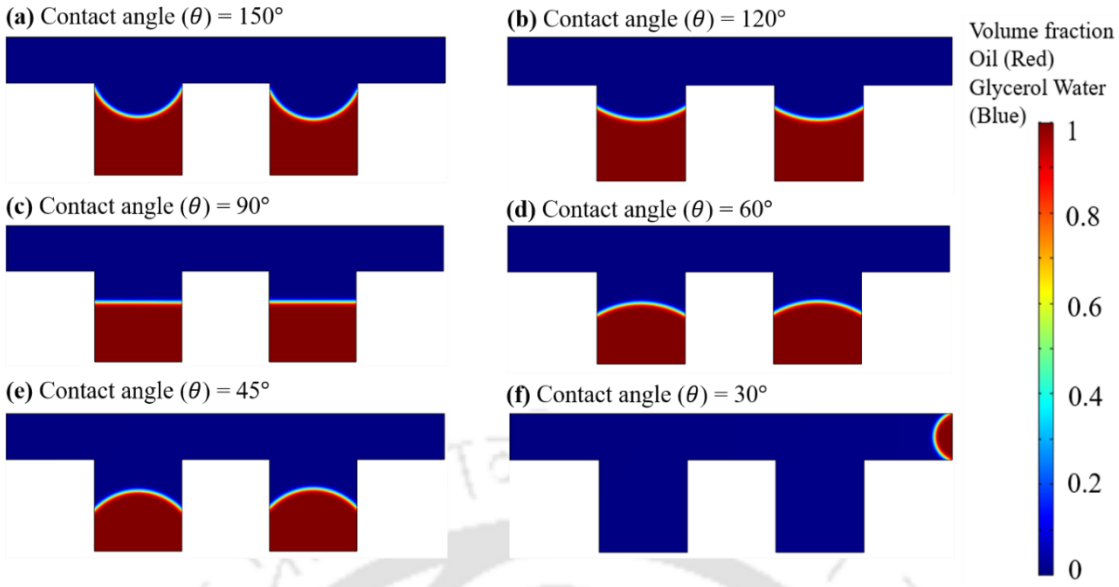

Figure 5. 5 Oil recovery from the dead ends by changing the contact angle from 150°(a) to 30°(f).

Numerical simulations are performed at contact angles ranging from 150° to 18° to understand the effect of contact angle on oil recovery. The volume fraction plots show the distributions of oil and water (red and blue, respectively) in the simulated dead-end model with contact angles varying from 150° to 30° (Figure 5.5). It is observed that almost complete oil is recovered at a contact angle of 30°. Further reducing the contact angle up to 18° also shows the complete displacement, similar to oil recovery at 30°. Figure 5.5 clearly shows that as the contact angle decreases, oil displacement from the dead-ends increases slowly.

The residual oil saturation in the dead-ends is large at a contact angle of 150°. However, decreasing the contact angle to 30° results in almost complete oil recovery from the dead-ends. The low contact angle results in improved wettability, providing easy access for the water to displace oil from the smaller pores by overcoming the capillary pressure and improving sweep efficiency (Sharma et al., 2023). Similarly, Rokhforouz and Amiri, 2017 and Maaref et al., 2017 simulated models with different contact angles to investigate the influence of wettability on residual oil saturation in the porous medium. They also observe that the displacing phase

enters smaller pore bodies and sweeps out the oil more efficiently because of low capillary resistance at water-wetting conditions (at θ= 45° to 18°). They observed a decrease in the residual oil saturation with a reduction in the contact angle. Meanwhile, with a decrease in the contact angle, the increase in oil recovery is not linear. It is observed that changing the contact angle from 150° to 36° recovers only 10.22 % of additional oil from the dead-end. While an additional oil of 60.19 % is recovered at 30° (Figure 5.6). Therefore, it can be concluded that below the critical contact angle, a substantial amount of trapped oil is recovered.

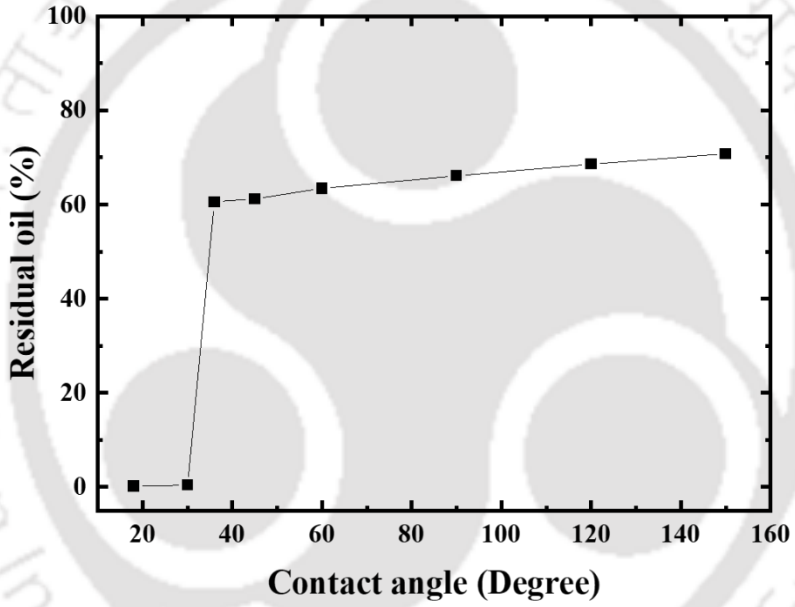

Figure 5. 6 Effect of contact angle on trapped oil recovery in the dead-end pore model.

A decrease in the contact angle from 150° to 30° (or even up to 18°) increases the rupture time (time taken by the oil-water interface to reach the junction point of the dead-end and pore throat channel mentioned in figure 5.7a) of the oil film at both the first and second dead-end. At a contact angle of 150°, the film rupture time is 0.52 s, but at a contact angle of 30°, it increases to 0.59 s (Figure 5.7). No oil film rupture is observed when the contact angle is reduced below

30° because the oil-water interface reaches the bottom of the dead-end, which leads to the complete displacement of oil from the dead-end. It is observed that at higher contact angle (extremely oil-wet condition), the water-oil interface is bulged towards the oil in the flow direction resulting in the bulged interface moving quickly towards the rupture point (Figure 5.7a). Once the oil film is ruptured, the oil is trapped in the dead-ends. As the contact angle is reduced to 45°, the interface is flat and not bulged towards oil or water. This further results in the delay in the rupture of the interface (oil film). When the contact angle is further reduced to 30°, the interface is bulged towards the preceding (displacing) phase, resulting in the delay for the interface to reach the rupture point. As the contact angle is reduced below 30°, displacing phase (water) tries to displace the oil along the dead-end wall first and from the middle of the dead-end for complete displacement (Figure 5.7). If the interface reaches at the bottom of the dead-end before it reaches the rupture point, no oil is left behind. As seen in figure 5.7, this occurs for three contact angles of 30°, 25.71°, and 18°.

5.6 Pore-scale phenomena during displacement

During the displacement process, as the oil-water interface approaches the rupture point, the displacing phase reaches deep inside the dead-end (Figure 5.8a). When the interface is about to touch the rupture point, shear-induced circulations are observed in the middle right corner of the dead-ends (Figure 5.8b). This recirculation is generated because of the partial momentum transferred by the flowing interface in the forward direction. As soon as the interface touches the rupture point, the continuous oil film rupture into two (Figure 5.8c). The rupture results in oil trapping in the dead-ends, where recirculations can be visualized (Figure 5.8d). The recirculation diminishes some time after the oil film rupture because of significantly low/negligible shear stress applied by the displacing phase on the trapped fluid during continuous fluid flow.

5.7 Complete displacement process from dead-end

The complete displacement of oil from the dead-end can be observed in the extremely water-wet condition where the contact angle with the wall is about 30° or less. The displacement mechanisms change with the contact angle. Initially, during displacement, the water-oil interface is reached at the start of the dead-end (Figure 5.9a and 5.9g). After that, the interface jumped into the dead–end to displace oil (Figure 5.9b and 5.9h). Due to the low contact angle (30°), the oil-water interface is bulged towards the water phase, causing a delay in reaching the rupture point. As the interface reaches the dead-end bottom, the water phase starts to displace the oil from the bottom of the dead-end by making an arc shape facing toward the right wall of the dead-end (Figure 5.9c, 5.9i). The residual fluid from the dead-end is recovered by the viscous force of the displacing fluid (Figures 5.9d, 5.9e, 5.9f, and 5.9j, 5.9k, 5.9l). However, significant shear-induced circulation is formed in the middle of the dead-end (Figure 5.9j). Finally, the oil is displaced from the dead-end to the pore throat channel and from the pore throat channel to the second dead-end. Similar phenomena takes place in the second dead-end. In this manner, the complete displacement of the trapped oil occurred from the dead-end. Figures 5.9g, 5.9h, 5.9i, 5.9j, 5.9k, and 5.9l are the velocity magnitude maps complementary to volume fraction maps shown in Figures 5.9a, 5.9b, 5.9c, 5.9d, 5.9e, and 5.9f, respectively.

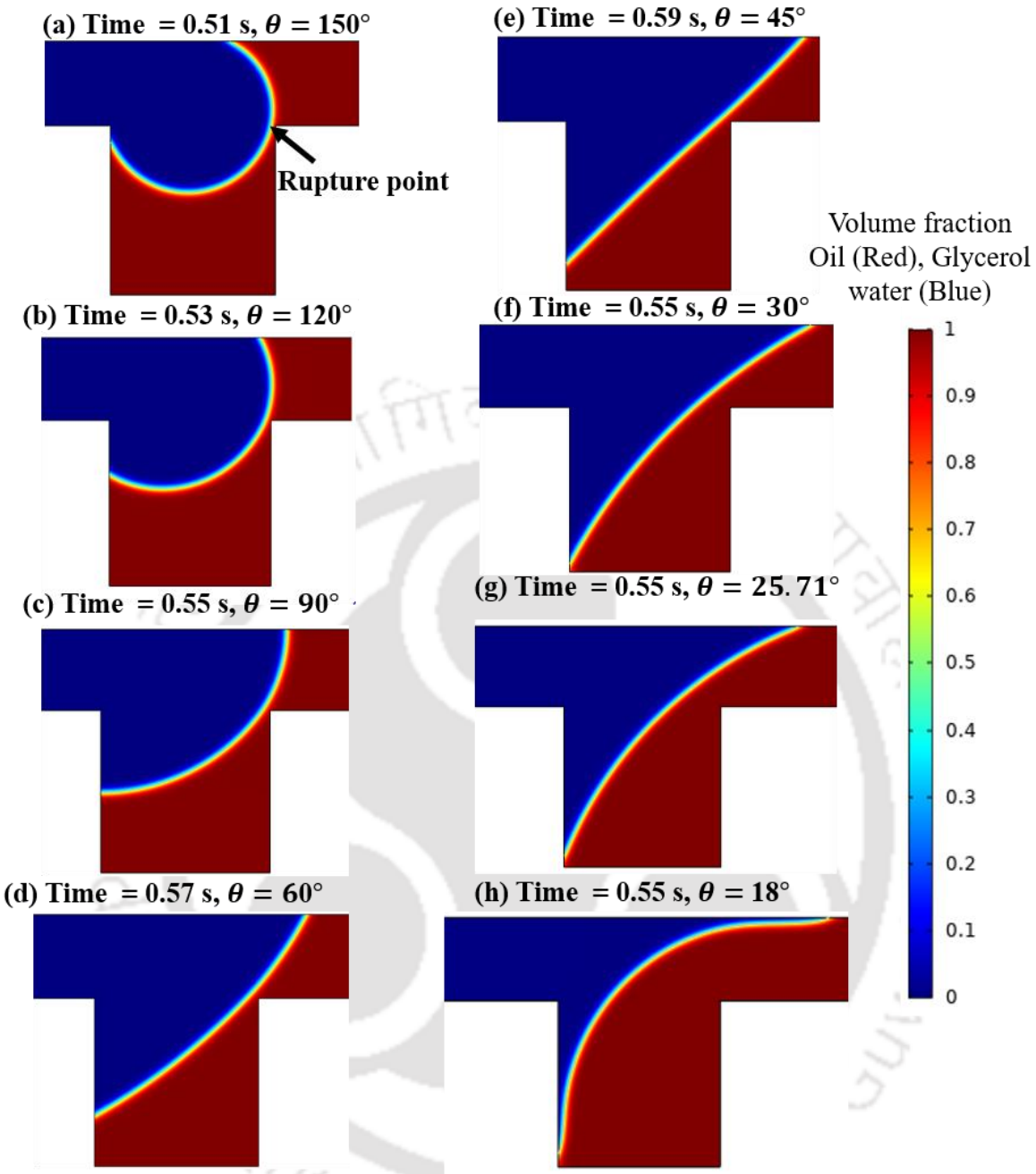

Figure 5. 7 Effect of change in the contact angle from 150° (a) -18° (h) on oil/water interface rupture.

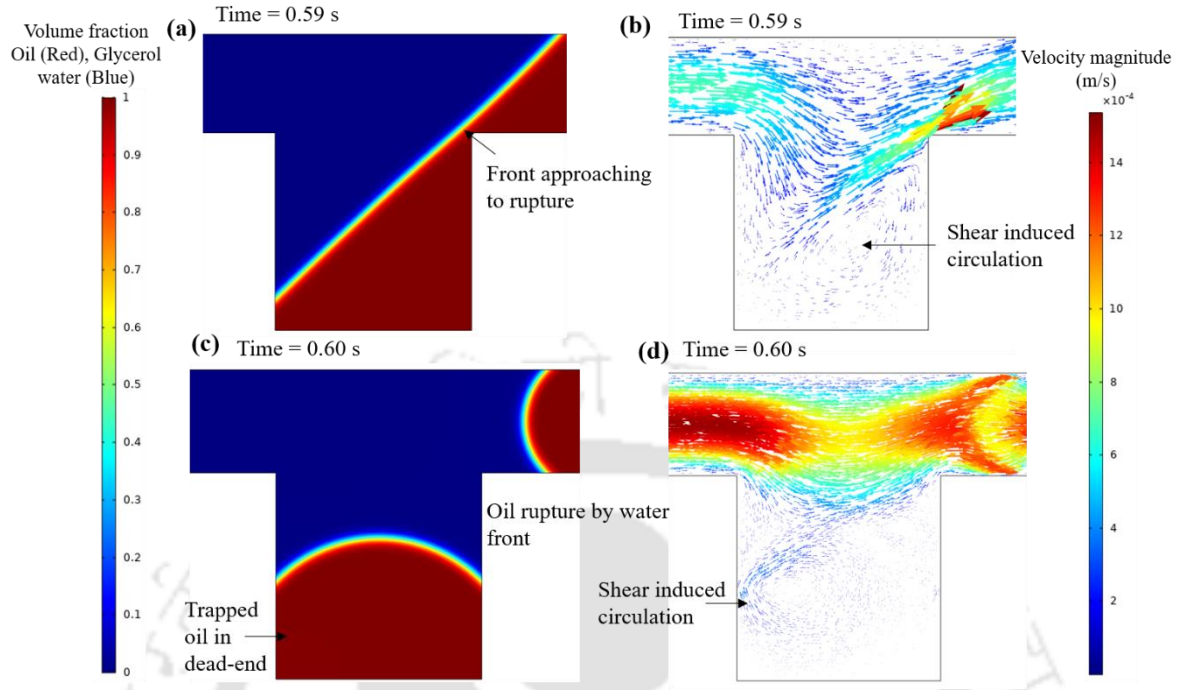

Figure 5. 8 Pore-scale phenomena (oil film rupture and shear-induced circulation) during two-phase flow in the dead-end at a contact angle of 45° ; (a),(c) are showing volume fraction plot, and (b), (d) are showing the velocity magnitude maps.

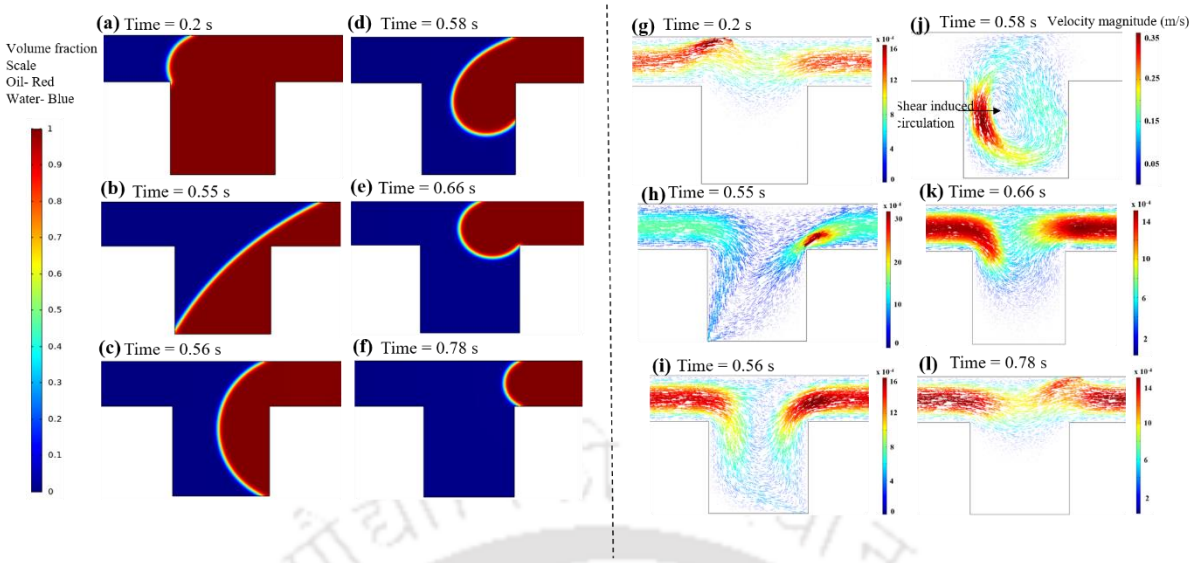

Figure 5. 9 Displacement mechanism during complete displacement at a contact angle of 30°; (a-f) shows volume fraction plots, and (g-l) shows the velocity magnitude maps.

5.8 Effect of viscosity ratio and displacing phase injection velocity

Fluid viscosity is an essential parameter in oil displacement through the dead-ends of the porous medium. The viscosity ratio (M) is the ratio of displacing phase viscosity (water) to the displaced phase (oil) viscosity ($M = \mu_w/\mu_o$). Numerical simulations are performed using six models with viscosity ratios of 0.09, 0.19, 0.93, 1.10, 5, and 10.65 to understand the effect of the viscosity ratio on oil recovery from the dead-end (Figure 5.10a). The lowest residual oil saturation (59.7%) is observed at a viscosity ratio of 0.93. Residual oil saturation is almost similar in all of the remaining five viscosity ratio cases. Rokhforouz and Amiri, 2017 observed maximum oil recovery at the viscosity ratio M = 1. Similarly, Gu et al., 2019 found that the oil recovery is highest at a critical viscosity ratio of 0.5. Residual oil saturation is generally high at low viscosity ratio because of the significant difference in the viscosity of the displacing phase and the displaced phase.

To understand the effect of water injection velocity in the dead-end to recover the trapped oil, the water is injected into the dead-end model at seven different injection velocities of 0.01 m/s,

0.0075 m/s, 0.005 m/s, 0.0025 m/s, 0.001 m/s, 0.0005 m/s, and 0.0003 m/s. The simulation results showed a significant decrease of 14.9% in the residual oil saturation in the dead-end by increasing the displacing phase injection velocity from 0.0003 m/s to 0.01 m/s. (Figure 5.10b). The lowest residual oil saturation (45.1%) is obtained at an injection velocity of 0.01 m/s, whereas the highest residual oil saturation (60%) is observed at an injection velocity of 0.0003 m/s. The maximum recovery (lowest residual oil saturation) is observed at the highest water injection velocity because the high injection velocity applies a high shear and drag force onto the trapped fluids in the dead-ends, forcing it to be displaced into the pore-throat channel. However, the low water injection velocity could not apply sufficient drag force to move out the trapped fluid. The effect of water injection velocity on oil recovery from the dead-ends is completely contradictory to its effect on oil recovery from the regular porous medium. The high injection velocity results in faster oil recovery than the low injection velocity at the early stage, but it results in early water breakthroughs leaving a significant amount of oil trapped in the pore constrictions such as dead-ends. Gu et al., 2019 investigated that the oil recovery will be high at lower injection velocity through the porous medium because of higher breakthrough time. Gu et al., 2019 observed maximum oil recovery from the fractured porous medium at a velocity of 0.0005 m/s.

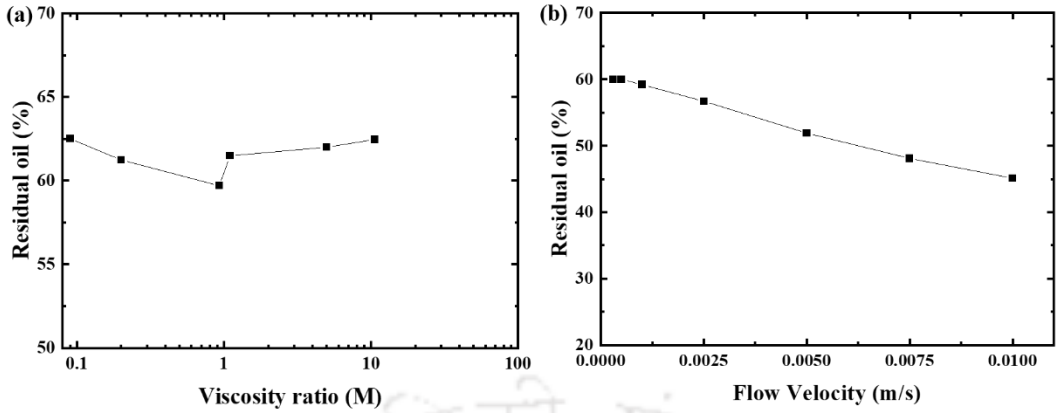

Figure 5. 10 Effect of different parameters on residual oil saturation for contact angle of 45° (base case), (a) Effect of viscosity ratio, (b) Effect of displacing phase injection velocity.

5.9 Effect of trapped fluid density

The petroleum reservoir rock may have different types of oil. Depending on the density and viscosity of the oil, the recovery process also gets more complex. Light oil of 36.5°, medium oil of 23.02°, and heavy oil of 20.19° and 15.45°API are used in the present work to understand the effect of oil API gravity on the oil recovery from the dead-end. The numerical simulations are performed with the base case fluid and rock properties mentioned in section 5.1. The results showed that at a contact angle of 30°, light, and medium oil are almost entirely displaced from the dead-end. However, the heavy oil with an API gravity of 15.45° is not entirely displaced; and, 66.7% of oil remained trapped in the dead-end. Therefore the contact angle is reduced from 30° to 25°, and numerical simulation is performed again, keeping all the simulation parameters the same. It is observed that the oil is almost swept from the dead-end. Therefore, the contact angle or wettability plays a major role in displacing the trapped oil through the porous medium, irrespective of its API gravity. However, the critical contact angle for the complete displacement of oil through dead-end will decrease with an increase in the density or API gravity of the oil. The wettability alteration can reduce the trapped fluid saturation and improve the oil recovery factor.

5.10 Effect of geometric parameters

Several factors, including pore throat width, depth of the dead-ends, and distance between the two dead-ends, can affect the trapping and mobilization of oil. Models with different pore throat widths (100 and 50 μm) and dead-ends depth (200-300 μm) are prepared, and numerical simulations have been performed at different contact angles 18°, 30°, and 60° to understand their effect on the oil recovery. Table 5.4 shows the 11 different models used during numerical simulations.

Table 5. 4 Models with different geometries used in numerical simulations (*model 11 consists of 3 dead-end pores in series).

Model number	**Pore-throat channel width (μm)**	**Dead-end depth (μm)**	**Distance between dead-ends (μm)**	**Residual oil saturation at θ = 60°**	**Residual oil saturation at θ = 30°**	**Residual oil saturation at θ = 18°**
1.	100	200	200	63.87	0.38	0.5
2.	100	225	200	63.15	63.10	0.4
3.	100	250	200	70.76	66.24	0.8
4.	100	300	200	75.85	71.55	1.21
5.	50	200	200	57.29	1.02	0.3
6.	50	225	200	58.65	66.8	0.6
7.	50	250	200	66.00	69.01	0.8
8.	50	300	200	71.45	74.9	1.20
9.	100	200	100	63.30	0.46	0.38
10.	100	200	300	63.40	0.56	0.46
***11.**	100	200	200	63.50	0.57	0.66

The numerical simulations are performed for all the models at contact angles 60°, 30°, and 18°. When the contact angle is 60°, the dead-end depths of 200, 225, 250, and 300 μm for a constant pore throat of 100 μm (model 1-4) show a residual oil saturation of 63.8%, 63.2%, 70.8%, and 75.8%, respectively. Whereas, same variation in the dead-end depths with pore throat size 50 μm (model 5-8), shows residual oil saturation as 57.3%, 58.7%, 66%, and 71.5%, respectively. Decreasing the contact angle from 60° to 30° caused a reduction in the residual oil saturation for the models with a pore throat channel width of 100 μm. At a contact angle of 30°, simulations results of model 1-4 with a constant pore throat size of 100 μm, show residual oil saturation of 0.38%, 63.10%, 66.24%, and 71.55%. Simulation results with models 5-8 having pore throat size 50 μm, show residual oil saturation as 1.02%, 66.8%, 69%, and 74.9% (Figure 5.11). A complete displacement of trapped oil is observed when the contact angle is decreased to 18°, irrespective of pore throat size and dead-end depth. It is observed from the simulation results that as the contact angle decreases, the residual oil saturation also decreases in the dead-ends in the case of models with a pore throat channel width of 100 μm. However, a complete displacement of trapped oil can be observed at a critical contact angle. As the depth of the dead-end increases, it leads to higher saturation of trapped oil in the dead-ends. Oil recovery from the deep dead-ends can be obtained by reducing the contact angle. The contact angle is reduced from 60° to 18° in all the models from 1 to 11, which results in almost complete oil recovery. The complete displacement of trapped oil is observed when the oil-water interface reaches the bottom of the dead-end before it reaches the rupture point (junction of the pore-throat channel and dead-end). The simulation results show that almost complete oil recovery from the dead-ends is obtained for model 5. Reducing the pore throat channel width reduces oil recovery for deeper dead-ends in case of contact angle of 30°. In models 9 and 10, the distance between the two dead-ends is changed from 200 μm to 100 μm and then 300 μm. Numerical simulation results show almost complete displacement of trapped oil from the dead-end at a 30° and 18°

contact angle. Whereas 63.3% and 63.4% of oil are recovered at the contact angle of 60° for both the cases mentioned above. So it can be concluded that increasing the distance between the dead-ends does not have any effect on the residual oil recovery. The simulation results also show that increasing the number of dead-ends does not have any effect on the oil recovery (model 11). Residual oil saturation in model 11 with three dead-ends (63.50%) is almost equal to the residual oil saturation (63.87%) in model 1 with two dead-ends in series. Almost complete displacement of trapped oil from the dead end is observed in model 11 (with three dead-ends in series) with contact angles of 30° and 18°. However, a significant amount of oil (63.50%) remained as residual oil after the displacement process in model 11 at a contact angle of 60°. The flow patterns, and nature of recirculations are almost identical in the three dead-ends.

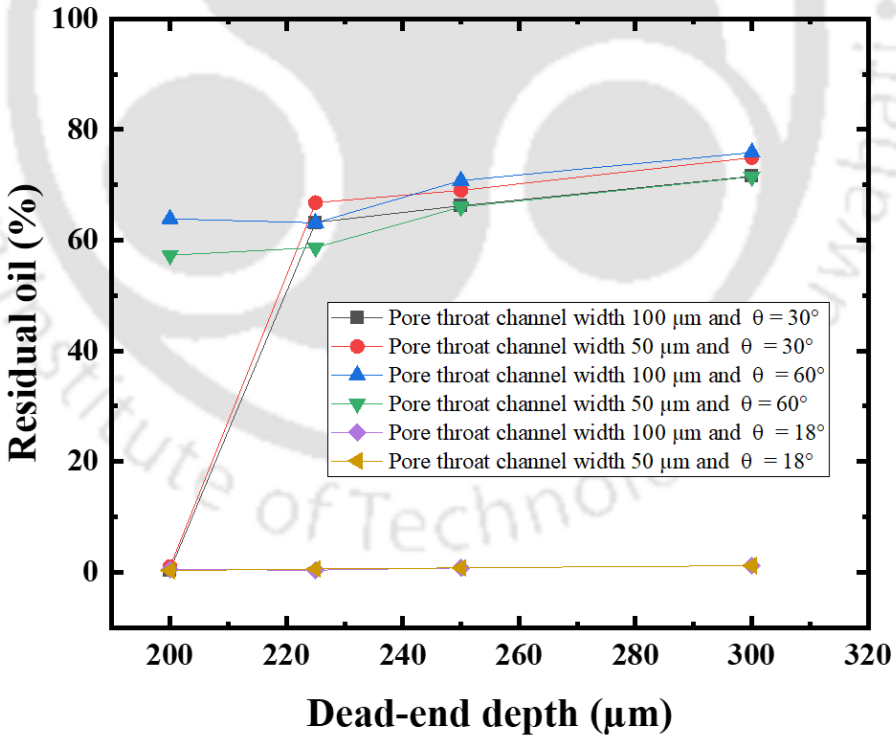

Figure 5. 11 Effect of geometric ratio on the trapped oil recovery from the dead-end at the contact angles of 60°, 30°, and 18°.

Three dead-end widths of 100 μm, 200 μm, and 300 μm were considered to understand the effect of dead-end on trapped oil recovery. The effect of contact angle ranging from 18° to 150° in the presence of different dead-end widths is shown in the figure below. The complete displacement of the oil from the dead-end with widths 100 μm, 200 μm, and 300 μm is observed at a contact angle of 18°, 30° and 60° (Figure 5.12). It is also observed that when the width of the dead-end is decreased from 300 μm to 100 μm, the residual oil recovery will be higher within the dead-ends. The oil trapping will be significantly high at lower dead-end width (100 μm) because the oil-water interface reaches very fast to the rupture point in comparison to the bottom of the dead-end. A higher contact angle may increase the resistance of the flow, resulting in more oil trapping, but this effect may be mitigated by a wider dead-end that allows the fluid to bypass the resistance. The narrower dead-end may increase the flow resistance, but a lower contact angle may reduce this effect.

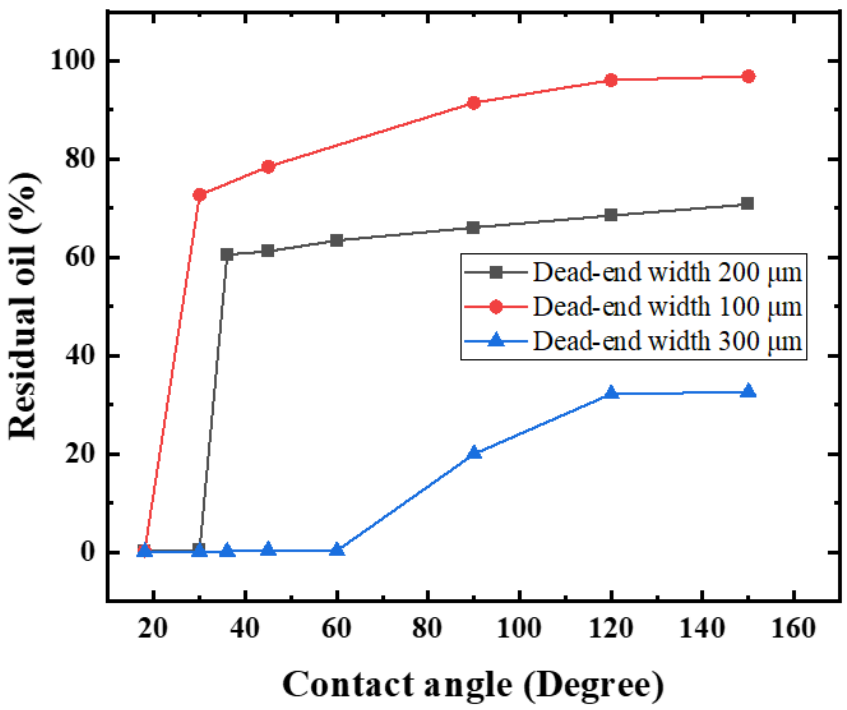

Figure 5. 12 Effect of dead-end width on residual oil saturation at the contact angle ranging from 18° - 150°.

5.11 Displacement in contraction expansion pores

The reservoir rocks consist of different complex pores, such as dead-ends, and contraction expansion pores, where a significant amount of fluid is trapped during the displacement process. During the displacement process in contraction expansion pores, the non-wetting phase is trapped in the corners. Trapping of the fluids can be reduced by identifying the effect of parameters such as wettability, interfacial tension, viscosity ratio, and displacing phase injection velocity. In the present study, we have performed numerical simulations in the contraction expansion geometry. The model is initially saturated with the oil of viscosity 0.0046 mPa.s and density 913 kg/m^3, which is displaced by water. The interfacial tension of 1 mN/m and contact angle of 120° is used during numerical simulations.

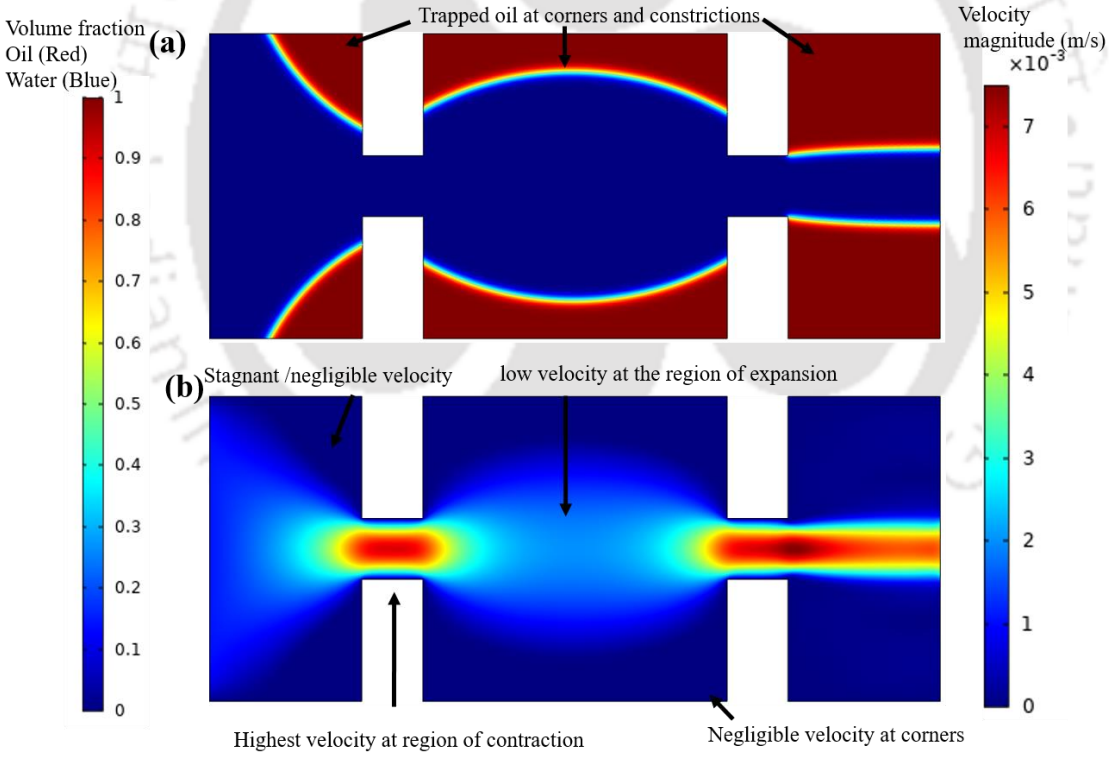

Figure 5. 13 Two-phase flow in contraction-expansion pores at a contact angle of 120°; (a) Volume fraction plot showing oil trapping in the corners and constrictions, (b) Velocity magnitude profile in contraction-expansion geometry.

Figure 5.13 shows the results of simulations in contraction expansion pores. The volume fraction plot shows a significant amount of oil trapping at the corners of the pores (Figure 5.13a). The red indicates the oil, whereas the blue indicates the displacing phase water. The velocity magnitude plot demonstrates the high and low-velocity zones during the displacement process. It is observed that the velocity magnitude is significantly increased in the region of contractions and decreased in the expansion regions. Negligible velocity is observed in the corners of the pore as oil is trapped in this region during the displacement process. Numerical simulations have been performed to investigate the effect of parameters such as wettability, interfacial tension, viscosity ratio, and water injection velocity on the displacement process in the contraction-expansion pores. The impact of wettability is measured by changing the contact angle from 150° to 30° keeping the other parameters same as given in base case (Table 5.5).

Table 5. 5 Base case conditions for simulation in contraction expansion pore.

Name	**Value**
Water density	1000 kg/m^3
Silicon oil	913 kg/m^3
Water viscosity	0.00089 Pa.s
Silicone oil viscosity	0.0046 Pa.s
IFT	35 mN/m
Contact angle	120°

Reducing the contact angle results in displacing trapped oil from the pore corners and constrictions. It is observed that at the contact angle of 30° and 60°, there is complete displacement of oil from the pores. However, a significant amount of oil remained trapped at

120° and beyond. Trapped oil recovery from the contraction-expansion pore is easier than dead-end pores. Because during the displacement process, 61.23% of oil remained trapped in the dead-end pore at the contact angle of 45°. However, complete displacement is observed in the contraction-expansion pore at the same contact angle. Changing the contact angle from 150° to 90° reduces residual oil saturation from 40.8% to 5.67% (Figure 5.14a). Displacing phase flow velocity also affects the displacement process in the contraction-expansion pores. To understand the effect of water injection velocity on oil recovery, the injection velocity is increased from 0.0001 m/s to 0.003 m/s. At low injection velocities, the residual oil saturation is comparatively less because of late water breakthrough (Figure 5.14b). At an injection velocity of 0.001-0.003 m/s, residual oil saturation is high because of early water breakthrough due to high displacing phase (water) injection velocity.

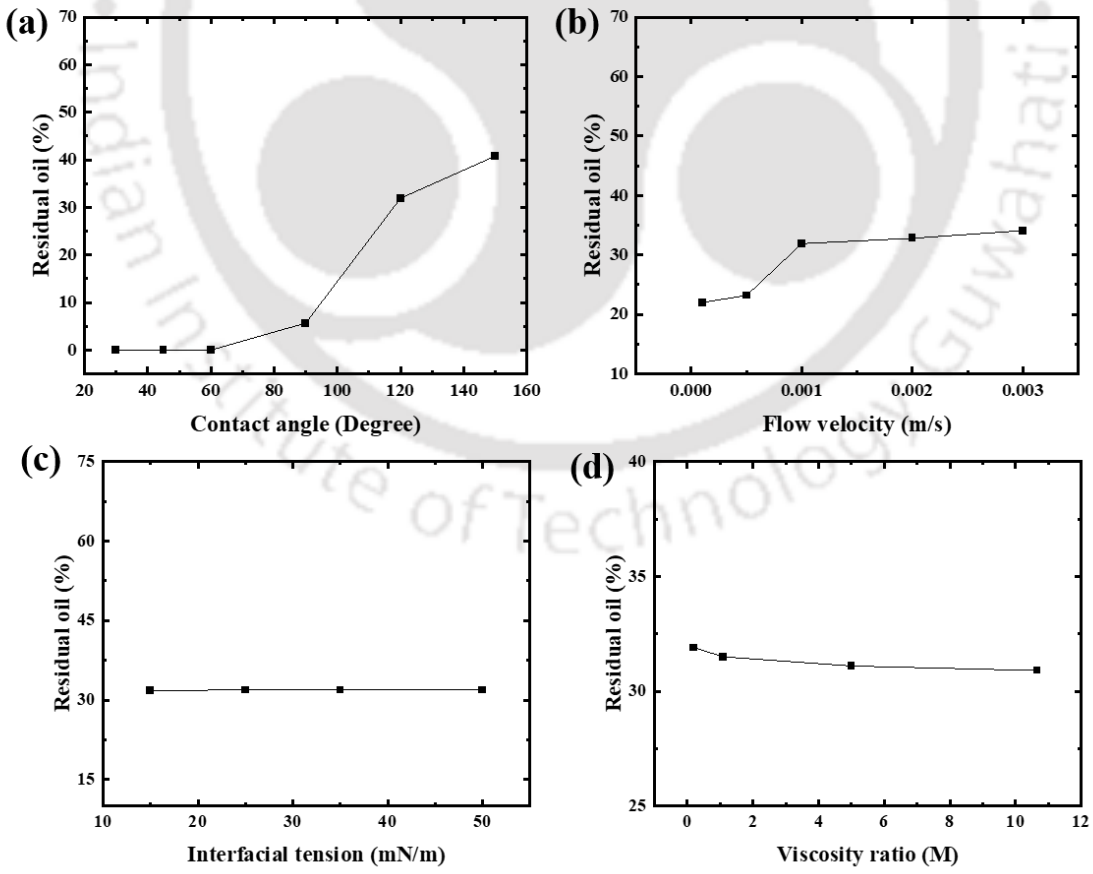

Figure 5. 14 Effect of different parameters on fluid displacement through contraction expansion pores, (a) effect of contact angle, (b) flow rate, (c) interfacial tension, (d) viscosity ratio.

The interfacial tension between the phases and viscosity ratio also affects the oil recovery from contraction-expansion pores. Changing the IFT from 15 to 50 mN/m does not affect oil recovery significantly (Figure 5.14c). Similarly, increasing the viscosity ratio from 0.19 to 10.65 does not substantially affect oil recovery. However, at a higher viscosity ratio, the oil recovery is slightly higher (Figure 5.14d).

Volume fraction and velocity vector plots are prepared with time to understand the oil displacement mechanism through the contraction-expansion pore by injection of displacing phase. Figure 5.15a-d (volume fraction plots) tracks the oil-water interface with time and shows oil trapping at the corners during displacement. Figure 5.15e-h (velocity vector plots) shows the flow behavior in the bulk fluid and at the interfaces. At the initial time (t = 0.002 s), when the displacing fluid front moves from the inlet section, the shear-induced circulation appears at the flanks of the front at both ends (Figure 5.15a, e). The shear-induced circulations are generated because of the high shear force applied by the moving front on the fluids at the corners of the expansion section 1. When the oil-water interface reaches at the start of contraction region 1 (time t = 0.036 s), the low-intensity recirculations are initiated in the trapped fluid of expansion region 1 (Figure 5.15b, f). As the interface moves ahead at the center of the contraction region, 1 (time t = 0.038), the intensity of the shear-induced circulations increases significantly because of the increase in the velocity of the oil-water interface (Figure 5.15c, g). The velocity vector map shows that the velocity at the center of the vortex is the lowest, whereas, at the circumference, it is the highest. However, when the interface enters the expansion region (time t = 0.044 s), the oil-water interface velocity decreases significantly, resulting in the recirculations disappearing from the expansion region 1 (Figure 5.15d, h). The

interface continuously moves ahead in the expansion region, and at time t = 0.109 s, as the interface is about to enter the contraction region 2, a significant amount of oil is left behind (trapped) at the corners, top, and bottom of the expansion region 2. Large recirculations/vortex formation can be visualized in the trapped fluid (oil) at the corners near the contraction region 2 under the effect of partial momentum transfer by the displacing phase water (Figure 5.16a, f). The recirculation phenomena in the trapped fluid have been observed in Zarikos et al., 2018. In their study, the trapped fluid is not getting displaced with increasing the flow rate; only the recirculation intensity increases. When the interface takes exit from the contraction region 2 and enters the expansion region 3, the recirculations in the trapped fluid shift backward due to a change in the fluid configuration (time t = 0.114 s) (Figure 5.16b, g). At time t = 0.136 s, the oil-water interface entered into expansion region three and was about to touch the outlet wall (Figure 5.16c, h). The high-intensity twin vortex formation occurs at time t = 0.137 s when the oil-water interface touches the outlet wall (Figure 5.16d, i). The vortex formation is because of the shear force applied by the displacing fluid (water) on the trapped fluid oil. A steady state condition is obtained when the simulation is continued for 3.5 s. The trapped fluid configuration is only changed with time (Figure 5.16e, j). However, no significant change in the oil recovery has been observed. The trapped fluid is recovered by changing the parameters, such as the contact angle (below 90°). The parameters such as contact angle, interfacial tension, injection velocity, and viscosity ratio change the trapped fluid configuration and displacement process through the complex pores such as dead-end and contraction expansion pores.

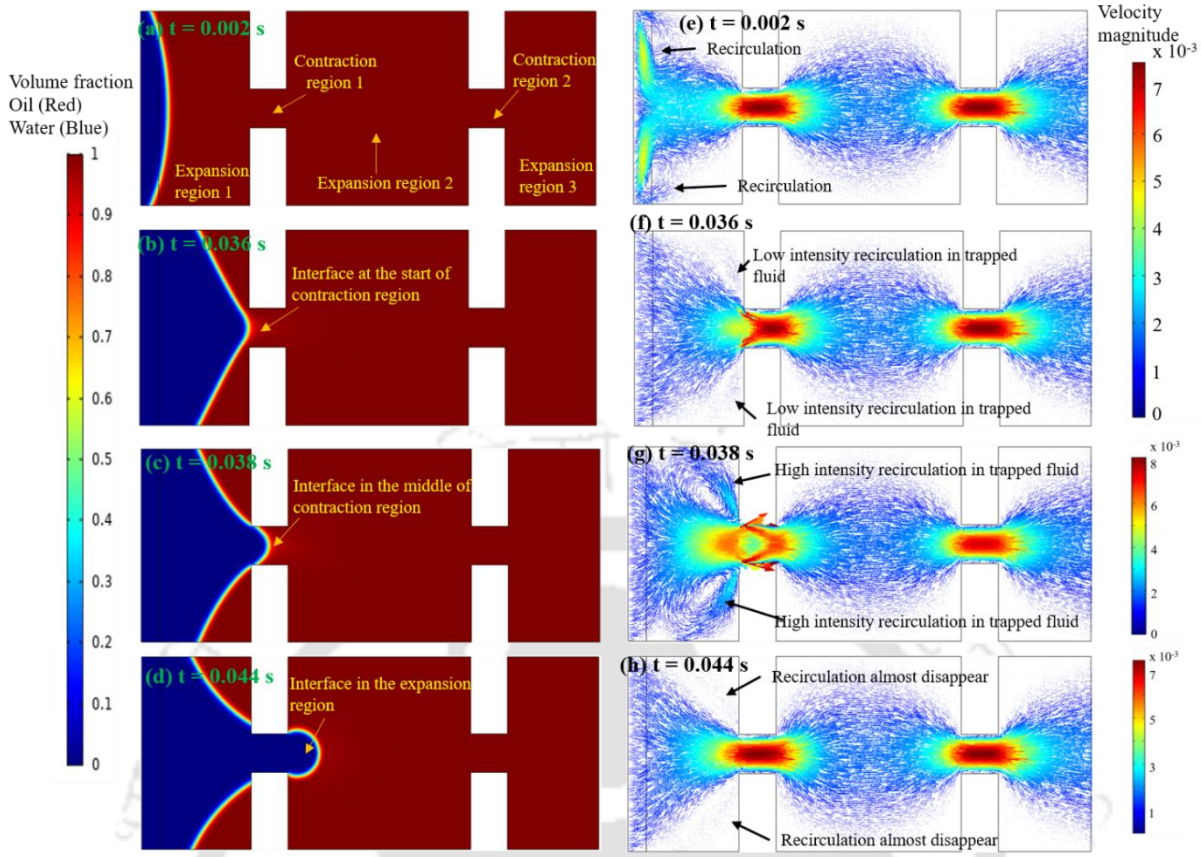

Figure 5. 15 Two-phase flow in the contraction-expansion model at a contact angle of 120° when the oil-water interface entered up to the expansion region 2; (a), (b), (c), (d) are volume fraction plots showing interface tracking with time; (e), (f), (g), (h) are velocity magnitude plots showing vortex formation.

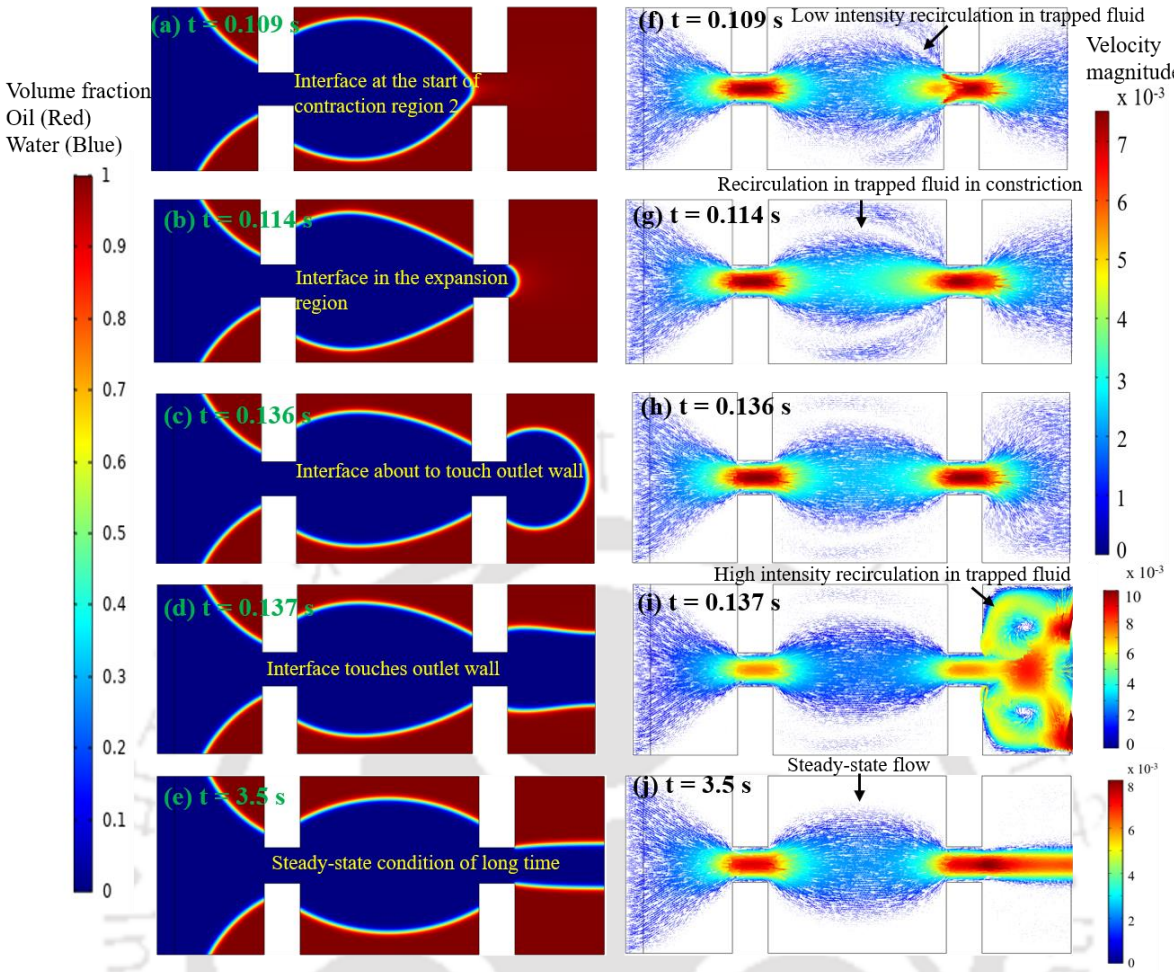

Figure 5. 16 Two-phase flow in the contraction-expansion model at a contact angle of 120° when the oil-water interface just entered the contraction region 2 ; (a), (b), (c), (d), (e) are volume fraction plot showing interface tracking with time, and (f), (g), (h), (i), (j) are the velocity magnitude plots showing vortex formation.

5.12 Summary

The dead-end pores consist of about 34-51% of the pore volume of the reservoir rock. During water flooding, a significant amount of oil is trapped in the complex pores, such as dead-ends and contraction expansion pores. Oil recovery from these pores is challenging. So numerical simulations are performed in these complex pore models to investigate the pore scale displacement mechanism and the effect of parameters such as viscosity, contact angle, water injection velocity, interfacial tension, and geometric parameters on oil recovery. Decreasing the contact angle (150° to 36°) recovers a small amount of oil (10.22%) from the dead-ends initially. However, further reducing the contact angle to 30° results in the complete displacement of oil. The oil recovery will be the highest from the dead-ends at a critical contact angle. It is comparatively difficult to displace the oil from the dead-ends. A significant amount of oil (61.23%) remained trapped after water flooding in the dead-end at a contact angle of 45°. However, complete displacement of oil is observed from the contraction expansion pore at the same contact angle. The change in viscosity ratio (0.09 to 10.65) does not significantly affect oil recovery (1% - 2.8%) in both cases. No significant change in oil recovery with IFT is observed in contraction expansion pores. The lower is API gravity of the trapped oil lesser is the oil recovery from the dead-end. However, decreasing the contact angle to ≤18° results in complete oil recovery irrespective of geometric parameters and API gravity of trapped oil. Higher injection velocity poses a high shear and drag force to remove the trapped fluid from the dead-ends, leading to additional oil recovery of 14.9% at a water injection velocity of 0.01 m/s. However, decreasing the injection velocity results increase in oil recovery of 12.1% from the contraction expansion pore. Geometric parameters, such as pore throat width, depth of the dead-ends, and distance between the two dead-ends, significantly affect the trapping and mobilization of oil. Increasing dead-end depth causes a reduction in the oil recovery. However, decreasing the contact angle up to 25°-18° helps in the almost complete displacement of oil

from the dead-end. The pore scale displacement process has been investigated in these complex pores, which shows the vortex formation in the trapped fluid due to partial momentum transfer from the displacing phase. These findings will develop a better understanding of pore scale flow dynamics and aid in designing optimum secondary and tertiary recovery processes.

Chapter 6. Pore-scale flow dynamics and heavy oil recovery using low saline water and chemical flooding

Enhanced oil recovery;

Micro-particle image velocimetry;

Core flooding;

Heavy oil;

Alkali polymer flooding.

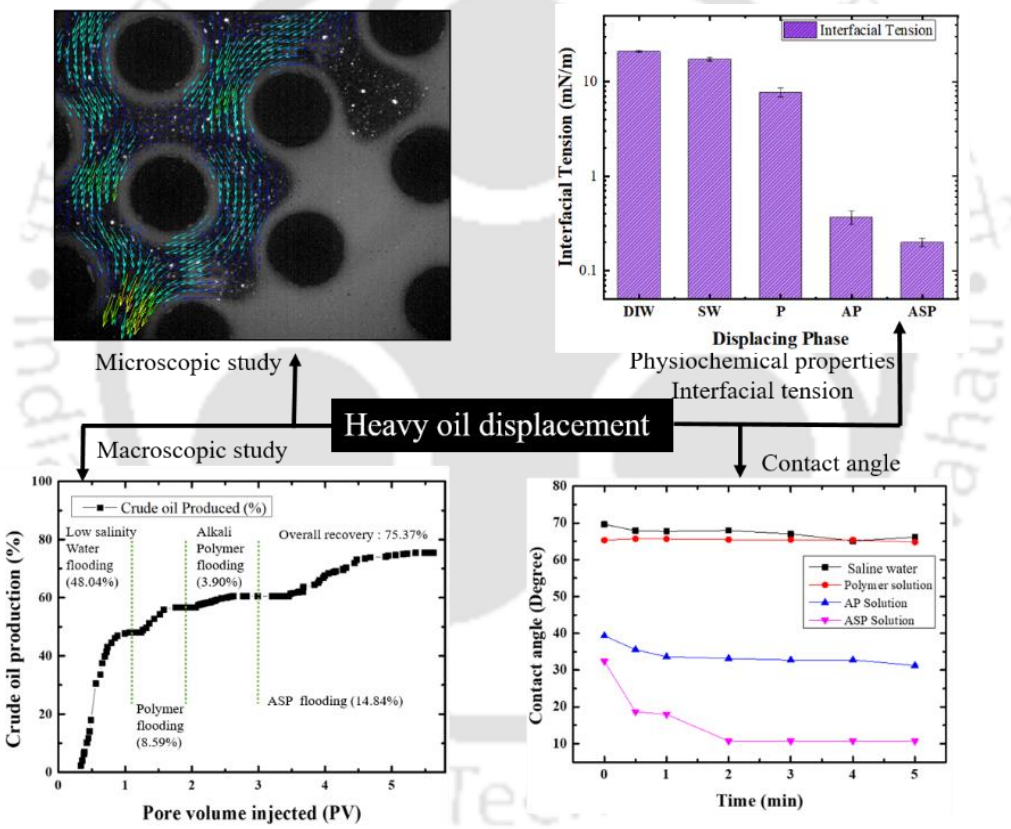

Pore-scale flow dynamics and heavy oil recovery using low saline water and chemical flooding

In this chapter, we report a quantitative analysis of pore-scale flow dynamics and displacement behavior of heavy oil at the micro and macro-scale to optimize different chemical flooding processes for enhanced heavy oil recovery. Microscopic studies are performed using micro-particle image velocimetry, whereas macroscopic studies are conducted using core flooding process. The phenomena such as fluctuating flow, flow direction reversal, viscous fingering, unsteady flow behavior, and sudden velocity jumps are observed during low salinity water flooding. Polymer solution follows the same preferential flow path generated during low salinity water flooding and results in no significant change in trapped oil saturation. Alkali-polymer solution injection improves oil recovery by in-situ emulsification, interfacial tension reduction, and wettability alteration to extremely water-wet conditions. Core flooding experiments are performed to investigate the heavy oil recovery by injecting different chemical slugs at simultaneous and separate injection modes. The core flooding results showed that the ultimate oil recovery is 75.37% by simultaneous injection of chemical slugs; however, a separate injection of individual chemical slugs yields lower oil recovery in the case of alkali-surfactant-polymer flooding. Here, the combined microscopic and macroscopic study provides information about the mechanisms and oil recovery by different chemical flooding processes through the porous medium.

6.1 Pore-scale experiments on 2D micromodel

The micromodel flooding experiments are performed in a sequence in which, initially, a low salinity water (LSW) flooding operation is conducted to understand the pore-scale phenomena and oil recovery mechanisms. The mechanisms such as wettability alteration, fines migration,

pH increase, multi-ion exchange, and salting-in effect contribute to enhanced oil recovery during low salinity water injection (Strand et al., 2009). Easy availability of water, low capital, and operating cost cause low salinity water flooding as one of the emerging techniques for enhanced oil recovery. However, significant oil trapping is observed within the porous medium due to the high mobility of the LSW. Therefore, LSW flooding is followed by polymer flooding to reduce the aqueous phase mobility and control the mobility ratio. However, it results in only a slight increase in the heavy oil recovery after LSW flooding. Hence, the polymer flooding is followed by alkali-polymer (AP) flooding to change matrix-fluid and fluid–fluid interaction, thereby improving the sweep efficiency. The heavy crude oil used in the experiments has a high acid value. During alkali-polymer flooding, an alkaline solution reacts with the petroleum acids present in the crude oil, resulting in in-situ surfactant generation at the interface of fluids. The in-situ surfactant accumulates at the interface, resulting in emulsification and interfacial tension (IFT) reduction. It also improves the matrix-fluid interaction by wettability alteration. After AP flooding, alkali-surfactant-polymer (ASP) flooding is performed to recover the leftover heavy oil. ASP solution further reduces the IFT and wettability and causes additional oil recovery. We have achieved maximum oil recovery using the flooding sequence followed in the current work. Non-wetting phase properties such as viscosity, density, and flow rate are mentioned in the Table 6.1.

Table 6. 1 Non-wetting phase viscosity, density, and flow rate.

Solution	**Viscosity (cSt)**	**Density (g/cm^3)**	**Flow rate (ml/min)**
Low saline water (LSW)	1	1.000	0.05, 0.1
Polymer solution	21.19	1.001	0.05, 0.1, 0.2
Alkali polymer	11.60	1.0072	0.05, 0.1, 0.2
Alkali surfactant polymer	5.08	1.0068	0.05, 0.1, 0.2

6.1.1 Low salinity water flooding

The water flooding process is performed in a two-dimensional porous micromodel. The porous medium is initially saturated with crude oil. Thereafter, low saline water (seeded with fluorescent tracer particles) is injected continuously at a flow rate of 0.05 ml/min into the micromodel to displace the crude oil. An ensemble of 500 images is captured at a frame rate of 24 fps and 4X magnification. The velocity vector map is obtained after pre and post-processing of the images using dynamic studio software. During LSW flooding, a significant difference in the viscosity between the two phases and excessive mobility of displacing phase results in finger formation (viscous fingering), leaving behind the oil in pore throats and around the micro-cylinders (Figure 6.1b). An oil film formation around the micro-cylinders is formed during the LSW flooding process. The film formation during LSW flooding elucidates the oil-wet nature of the micro-cylinder (Figure 6.1a). The thickness of the oil film around the micro cylinders is 63 μm during low salinity water flooding. A significant amount of oil (47.81 %) is left (trapped) in the porous medium after the LSW flooding. Similarly, Saw and Mandal, 2020 and Patil et al., 2018 observed oil recovery of up to 62.20 % and 68 %, respectively, during low salinity water flooding in the porous medium (Patil et al., 2008). The velocity vector map shows a fluctuating flow (back and forth movement) of the non-wetting phase in the porous medium, contributing to unsteady flow behavior, although the displacing phase is continuously injected. The fluctuating flow results in the flow direction reversal repeatedly for a fraction of second in the porous medium. It can be seen in Figure 6.1a, where the fluid flows in the counter-current direction, whereas in Figure 6.1b, the fluid flows in the actual flow direction. Similarly, our previous study observed a sudden reversal of the flow direction of the trapped ganglia as a droplet of the non-wetting phase moves nearby the porous medium during immiscible two-phase flow in the heterogeneous porous medium (Sharma et al., 2022). The

velocity magnitude during the LSW flooding process is not temporally consistent due to the fluctuating flow, flow direction reversal, or unsteady flow behavior (Figure 6.1d). However, it is consistent during single-phase flow in the porous medium. In some regions, a sudden increase in the velocity (ranging in 0.6–1.03 mm/s) and circulation around the micro-cylinder also contribute to unsteady flow behavior during the displacement process (Figure 6.1c). The unsteady behavior results in significant oil trapping in the porous medium (Figure 6.1). A sudden velocity jump, also called the Haines jump during two-phase flow, has been reported by Kazemifar et al., 2015 during the displacement of water from the homogeneous porous medium by CO_2 injection.

The velocity magnitude contour plots, vorticity map, and shear rate profile are further obtained to understand the displacement process within the porous medium during LSW flooding (Figure 6.2). The contour plots also confirm the finger formation during the LSW flooding process. Inconsistent velocity magnitude is observed in the time-resolved contour plot (Figure 6.2a). The displacement is also inconsistent during the LSW flooding process. In the viscous fingering front, the maximum velocity is observed at the center of the channel, whereas the minimum is at the cylinder wall. The shear rate is also inconsistent with time due to unsteady flow behavior. The highest shear is noticed at the cylinder wall due to the high-velocity gradient, whereas the low shear is in the middle of the flow path because of the low-velocity gradient (Figure 6.2b). The phenomena such as viscous fingering and inconsistent velocity magnitude result in unsteady flow behavior during flow through the porous medium. Similar observations have been obtained by others during immiscible two-phase flow (Blois et al., 2015; Kazemifar et al., 2016; Roman et al., 2016). The vorticity profile is also plotted to see any circulations during the flooding process. Although the two-phase flow during LSW flooding is very uneven, the flow pattern is roughly wavy or semi-sinusoidal (Figure 6.2c). The formation of a half vortex is often visualized through the vorticity profile. Similar vorticity

profiles have been observed by Blois et al., 2015 during immiscible two-phase flow through the porous medium. The tortuosity of the flow path during low salinity water injection is 1.208.

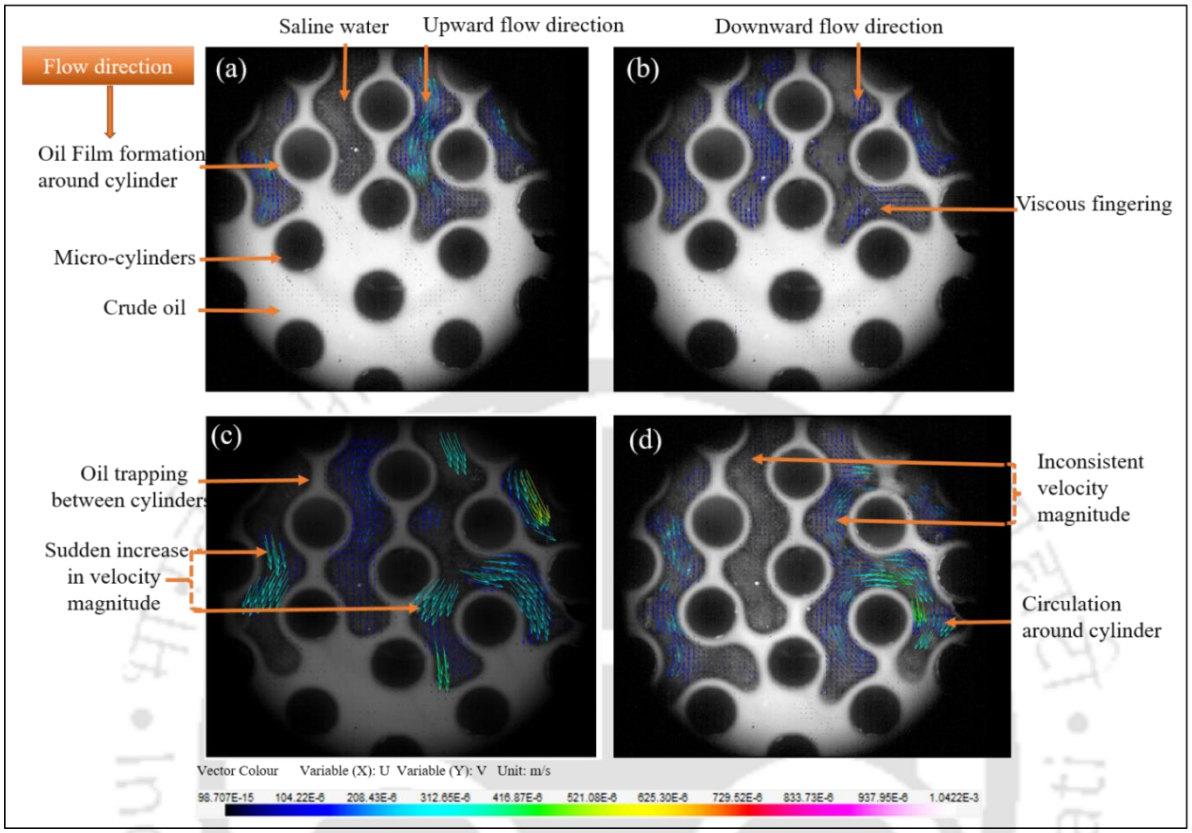

Figure 6. 1 Velocity vector field showing displacement of crude oil by low saline water, (a) oil film formation around the micro-cylinders, (b) viscous fingering during displacement process, (c) sudden increase in the velocity magnitude, (d) Inconsistent velocity magnitude

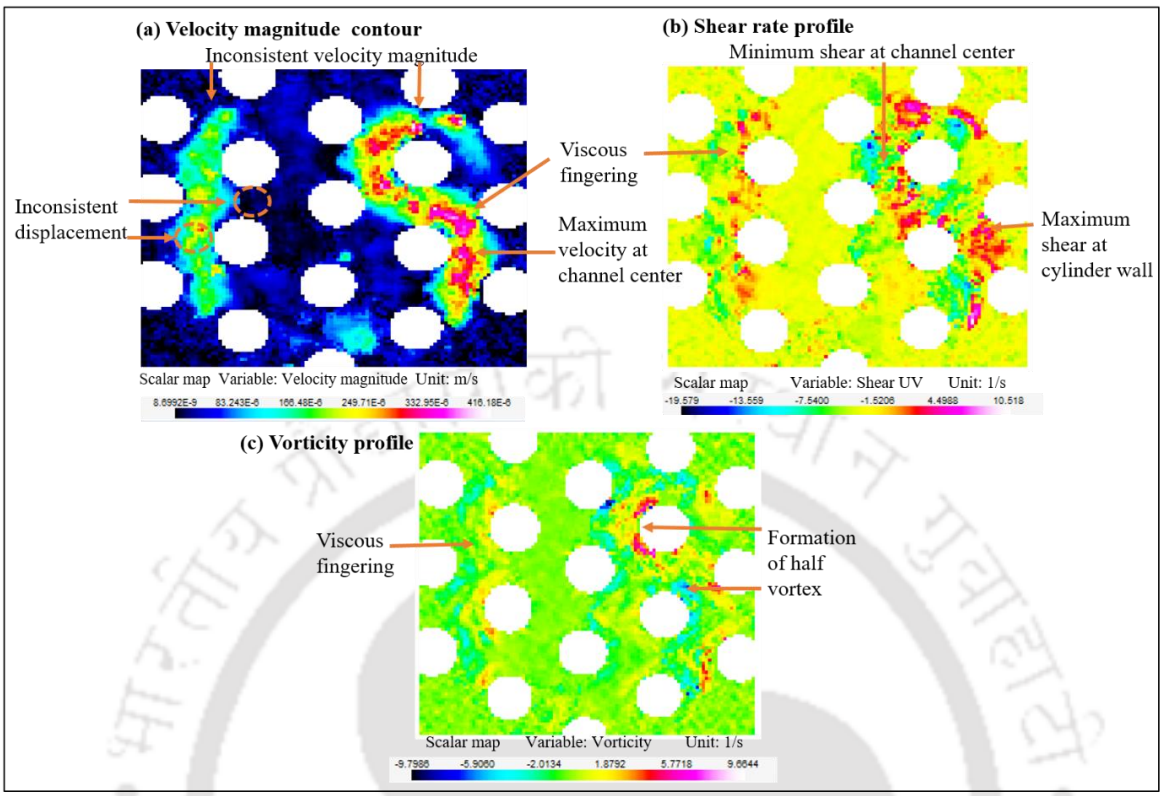

Figure 6. 2 Flow characterization during low salinity water flooding using (a) Velocity magnitude contour map showing viscous fingering, (b) shear rate map, (c) Vorticity map.

6.1.2 Polymer flooding

A significant amount of crude oil is bypassed during LSW flooding, causing viscous fingering. Generally, polymer flooding is conducted in the porous medium to control the mobility ratio by increasing the displacing phase viscosity, which causes a reduction in the viscous fingering (Sheng, 2010). The polymer solution exerts pressure on the trapped oil droplets and films. Hence oil can be pulled and pushed out of the pore constrictions and dead-ends (Sheng, 2010). Therefore, polymer (HPAM) is added to saline water to decrease the mobility of displacing phase and improve the mobility ratio. The polymer solution is injected into the porous medium at three different flow rates 0.05, 0.1, and 0.2 ml/min in a continuous mode to investigate their effect on reducing the trapped oil saturation. It is observed from the velocity vector map that

there is a negligible displacement of trapped oil using a polymer solution (Figure 6.3). This is because the polymer follows the same preferential flow path developed during LSW flooding. When the polymer solution is injected at flow rates of 0.05 ml/min, 0.1 ml/min, and 0.2 ml/min, the flow velocity through the porous medium is 0.5 mm/s, 1.1 mm/s, and 1.8 mm/s, respectively (Figure 6.3). The tortuosity of the flow path during polymer injection is 1.125. The polymer flooding results no change in the thickness of the oil film around the micro-cylinders.

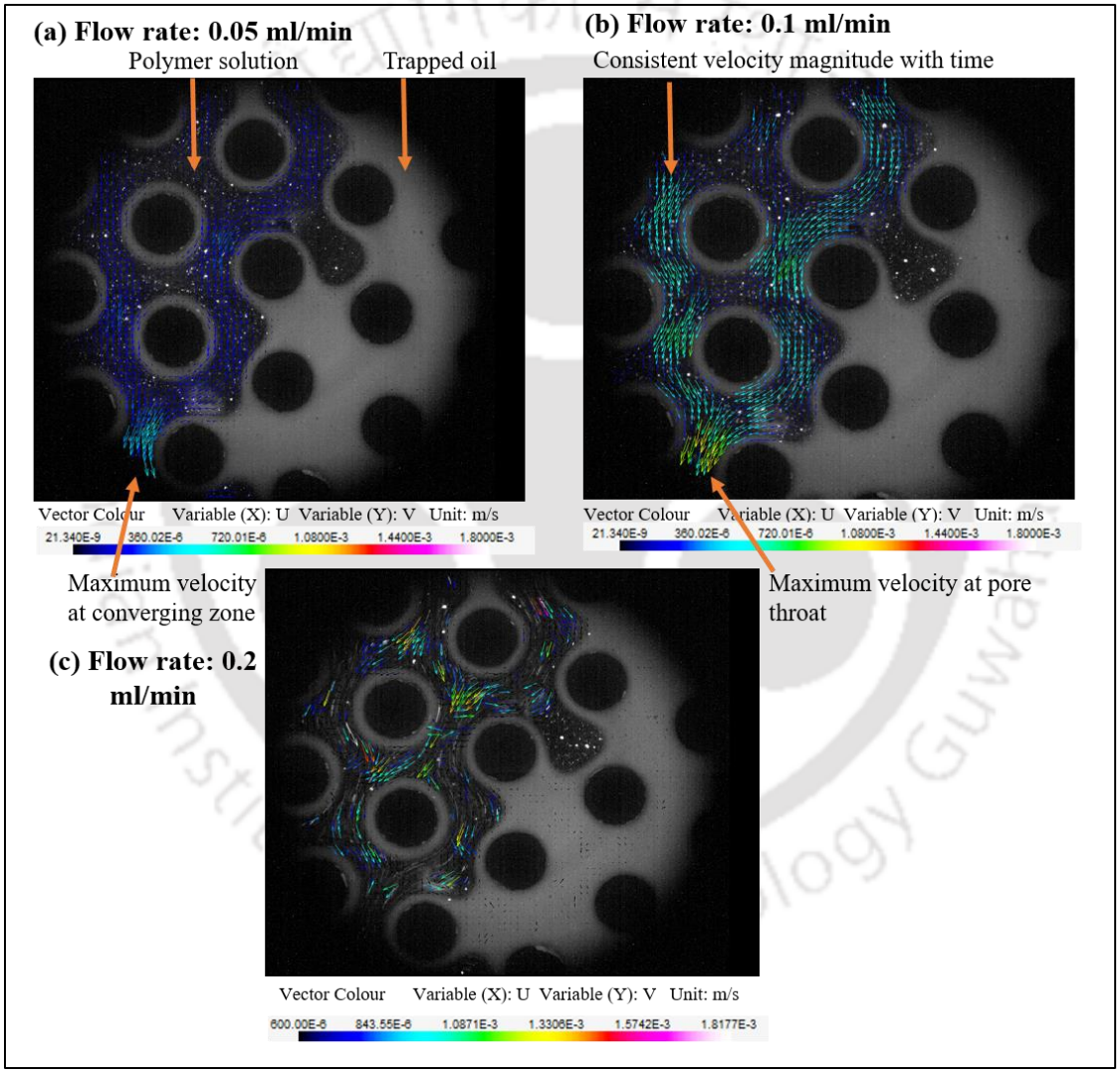

Figure 6. 3 The velocity field during polymer flooding (subsequent to LSW flooding) in porous micromodel at flow rates of 0.05 ml/min (a), 0.1 ml/min (b), and 0.2 ml/min (c).

The flow velocity of the polymer solution increases with an increment in flow rate, and it contacts only the interface of trapped oil. Hence, polymer flooding in the micromodel after low salinity water flooding has a negligible effect on the mobilization of trapped crude oil. A shear rate profile is obtained to quantify further the polymer-flooded porous medium. It is noticed that with an increment in the flow rate, the shear rate value also increases. The maximum shear rate is obtained as 16.638 s^{-1} at a flow rate of 0.05 ml/min, but as the flow rate increases to 0.2 ml/min, the maximum shear rate value reach 42.56 s^{-1} (Figure 6.4).

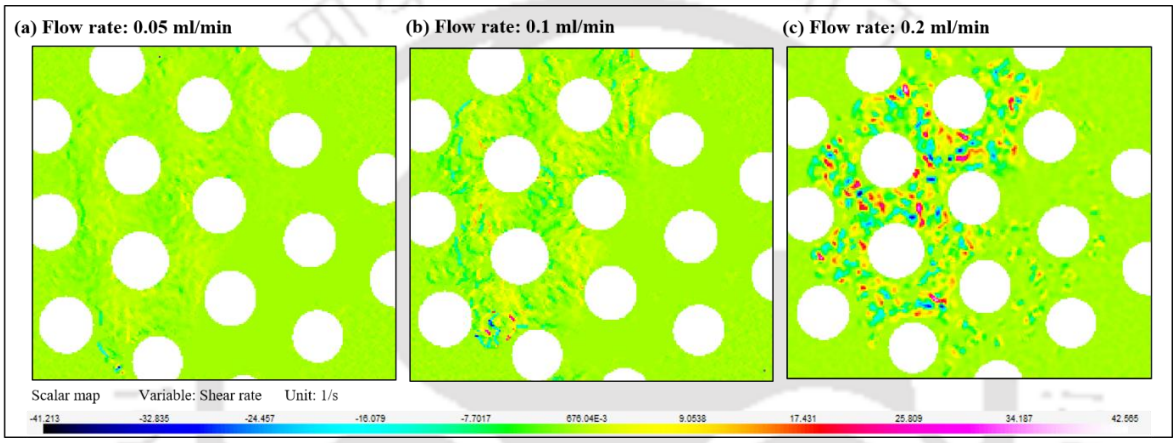

Figure 6. 4 Shear rate profiles at 0.05 ml/min (a), 0.1 ml/min (b), and 0.2 ml/min (c).

6.1.3 Alkali polymer flooding

Even after the polymer flooding in the porous medium, about 45.27 % of OOIP is remained trapped. This trapped oil can be recovered by improving the mobility ratio and decreasing the IFT. Therefore, the alkaline polymer flooding technique is adopted to reduce the residual oil saturation. Alkali and acidic components of crude oil form an in-situ surfactant at the water–oil interface and reduce the IFT value. The in-situ surfactants diffuse either into the crude oil or aqueous solution. The IFT reduction causes an emulsion formation that has a high viscosity value. The alkaline flooding also results in a wettability alteration to more water-wet conditions. The combination of alkali and polymer results in significant trapped oil recovery (Elyaderani and Jafari, 2019; Mehranfar and Ghazanfari, 2014; Sheng, 2010). The crude oil

trapped in the different regions of the porous medium is contacted by the alkali and produced as an emulsion. Polymer (HPAM) is added to augment the aqueous phase (alkali solution) viscosity; hence aqueous phase mobility can be controlled, and the problem of viscous fingering can be eliminated.

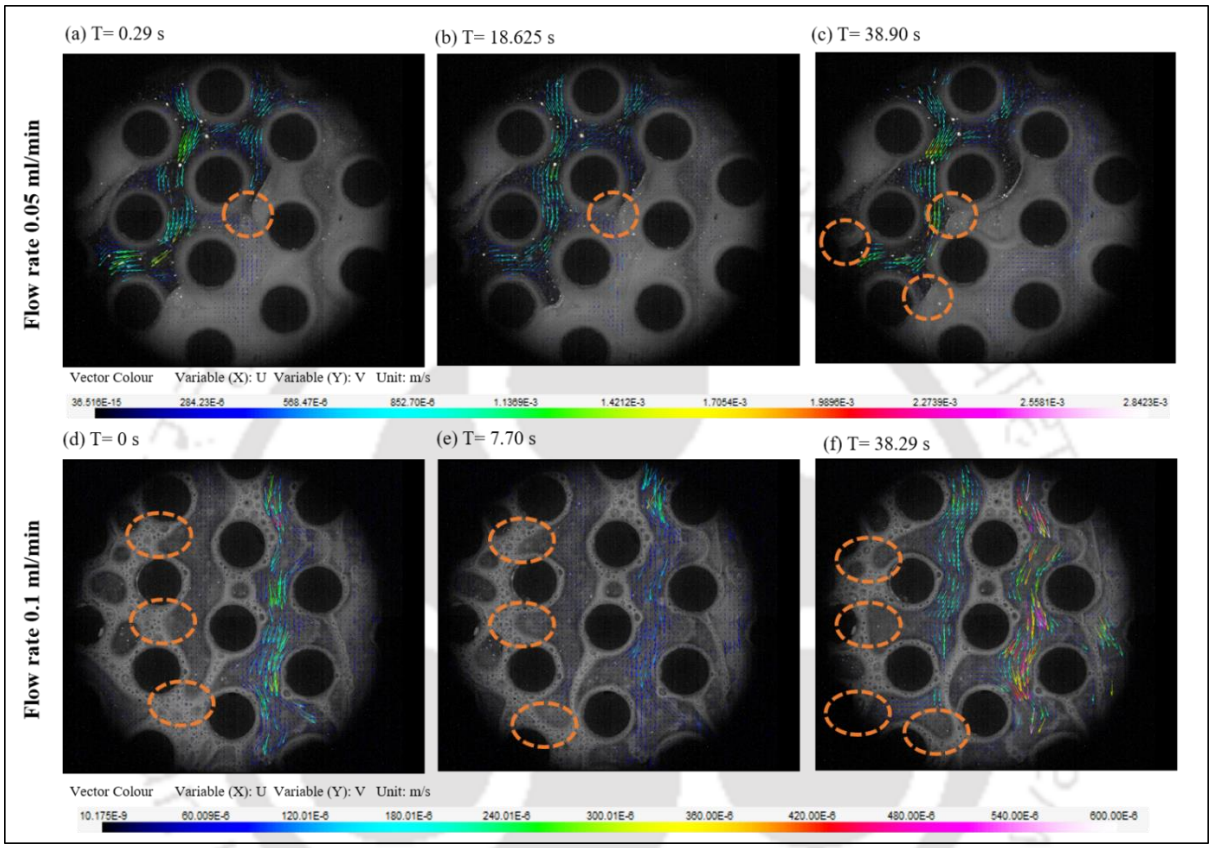

Figure 6. 5 Alkali polymer flooding in porous micromodel at the flow rates of 0.05 ml/min (a, b, c) and 0.1 ml/min (d, e, f). The non-wetting and wetting phase interface movement are marked as a circle in all the images.

Alkali-polymer flooding is conducted at three different flow rates, 0.05 ml/min, 0.1 ml/min, and 0.2 ml/min, sequentially at continuous injection mode, to understand the effect of flow rate on emulsion formation and displacement. The increase in the injection velocity during alkali-polymer flooding causes more supply of alkali to the trapped crude oil, which augments the

emulsification process. The emulsification process eliminates viscous fingering phenomena (Elyaderani and Jafari, 2019; Mehranfar and Ghazanfari, 2014; Sheng, 2010). The velocity field clearly shows the movement of the confined crude oil interface at different regions of the porous medium for a 0.05 ml/min flow rate (Figure 6.5). These movements of the interface result in the formation of multiple flow paths. It is noticed that the velocity magnitude at different regions of the porous medium is not consistent with the time. The formed emulsion also helped to recover the oil from the orthogonal directional to fluid flow. This way, the crude oil's maximum saturation can be recovered.

The alkaline polymer flooding initiates displacement in almost all directions where oil is trapped. The flow pattern can be seen with the help of the velocity vectors. A similar trend is observed when the flow rate is further increased. Even though at the flow rate of 0.1 ml/min, the displacement efficiency is significantly improved during AP flooding because of emulsion formation. The observed velocity (0.03–0.06 mm/ s) of AP solution is low due to emulsion formation, which causes a reduction in the mobility of the aqueous phase (alkaline polymer solution). However, in some regions where the oil is completely displaced, the AP solution moves at a high velocity ranging in 0.6 mm/s. As mobility decreases due to the interaction of AP solution and heavy oil, sweep efficiency is improved in the porous medium. However, the oil film around the cylinders still confirms a minor change in the wettability of the porous medium. The velocity vectors are inconsistent with the flow direction, meaning fluid starts to flow in many directions and sweep the trapped oil. The film thickness reduces during AP flooding with an increased flow rate. When the flow rate of the AP solution is further increased to 0.2 ml/min, oil is further displaced, and some saturation of the AP solution is trapped between the crude oil. During alkaline polymer flooding, it is observed that increasing the flow rate (0.05–0.2 ml/min) further decreases the flow velocity (2.8 mm/s − 0.3 mm/s) in the porous medium as crude oil and chemical slug reaction results in the emulsion formation (Figure 6.6).

During alkali-polymer flooding, the optimum injection velocity of 0.213 mm/s (at a flow rate of 0.1 ml/min) is observed, which eliminates the viscous fingering and improves sweep efficiency.

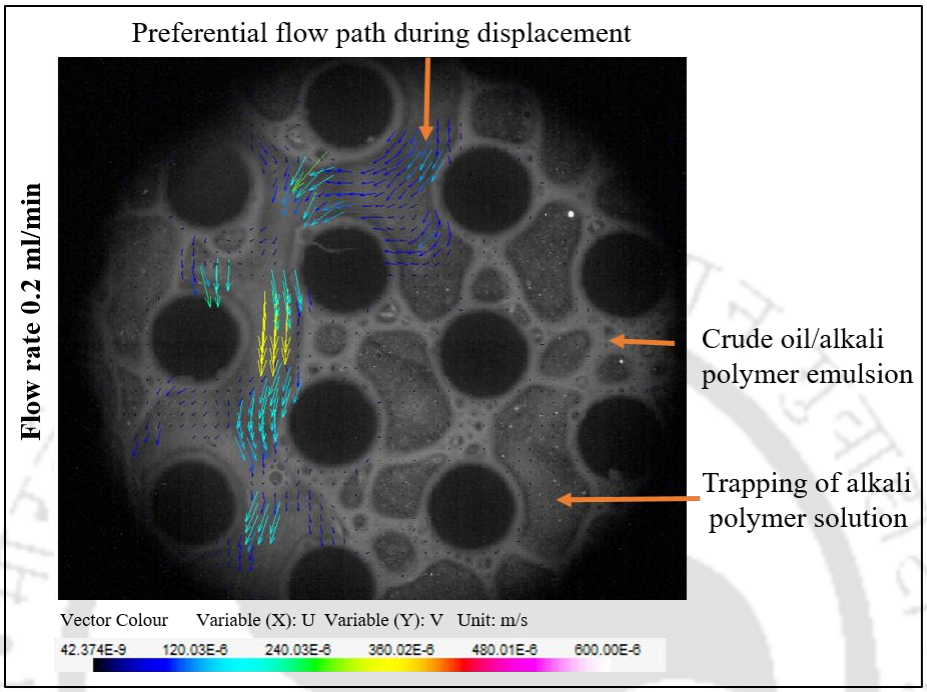

Figure 6. 6 Alkali Polymer flooding in porous micromodels at a flow rate of 0.2 ml/min.

The fluid flow during alkali-polymer flooding is further characterized using shear rate and vorticity profile. It is noticed that the shear rate decreases in the porous medium as the emulsion generation rate increases due to the reaction of alkali and crude oil. It can be seen in Figure 6.7a that initially, the shear rate (11.97 s^{-1}) is high in the regions nearby the flow path, but with an increase in the emulsion formation, the shear rate (3.094 s^{-1}) reduced drastically at almost every place due to the very low velocity of the emulsion (Figure 6.7a, b). Similar results are observed in the case of the vorticity profile. The vorticity decreases with time from 17.418 s^{-1} to 4.44 s^{-1} due to the slow velocity of the emulsion (Figure 6.7c, d). The

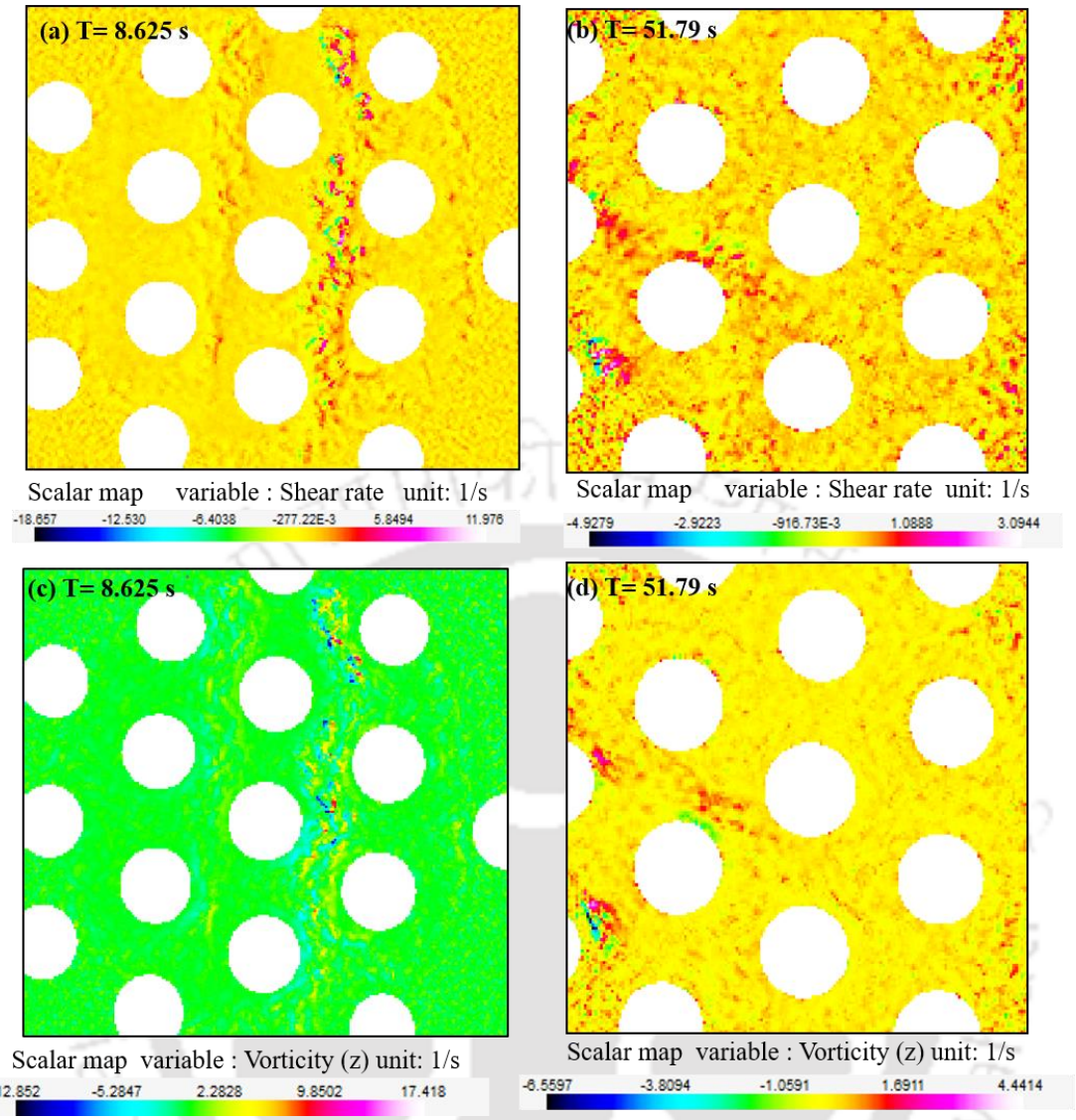

Figure 6. 7 Shear rate and vorticity map during alkali polymer flooding at 0.1 ml/min flow rate. (a), (b): shear rate map at T= 8.625 s and T= 51.79 s, respectively; (c), (d): Vorticity map at T= 8.625 s and T= 51.79 s, respectively.

6.1.4 Oil recovery during the micromodel flooding process

Total oil recovery by different flooding processes is measured using the thresholding function of image J software. Significant oil saturation (47.81 %) remains trapped in the porous medium after LSW flooding (Figure 6.8a). Polymer flooding is performed in the porous medium after LSW flooding to control the mobility of the aqueous phase (water). The polymer solution is injected at three different flow rates: 0.05, 0.1, and 0.2 ml/min, resulting in an additional oil

recovery of 2.54 %. A substantial amount (45.27 %) of oil was trapped in the porous medium after polymer flooding (Figure 6.8b).

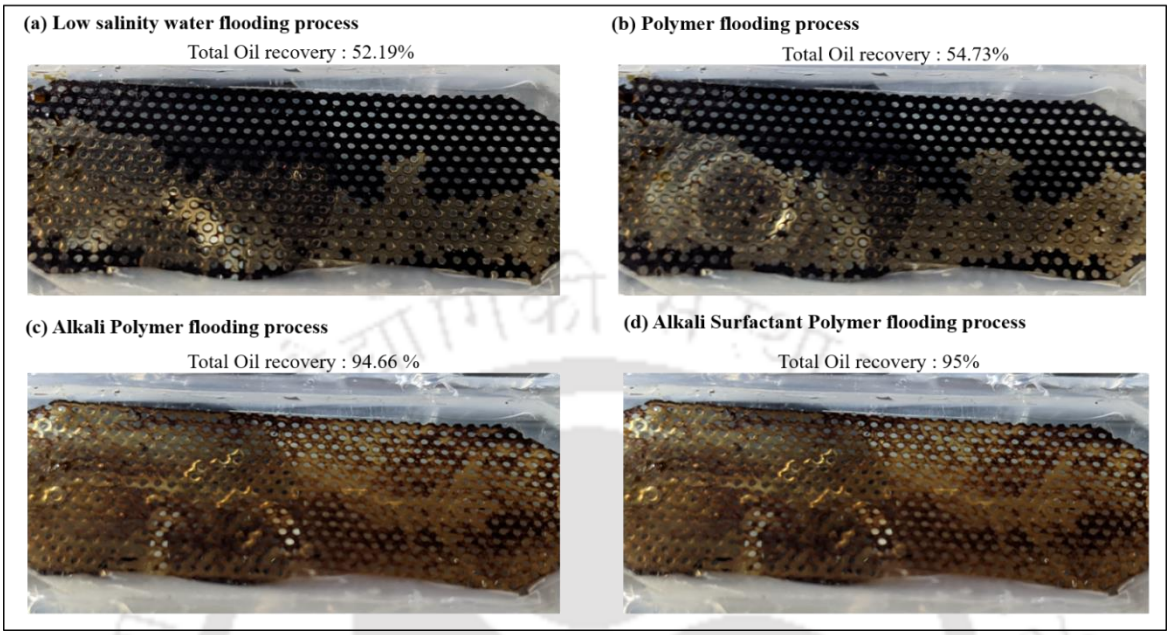

Figure 6. 8 Images of micromodel showing crude oil recovery during (a) Low salinity water flooding process, (b) Polymer flooding process, (c) Alkaline polymer flooding Process, and (d) Alkali Surfactant polymer flooding process.

It is observed that polymer flooding could not effectively displace the oil from the porous medium. Hence alkali-polymer flooding is conducted in the porous micromodel to improve fluid–fluid, and fluid–solid interactions, leading to an increase in sweep efficiency (Chen et al., 2015). During alkali-polymer flooding, cumulative oil recovery reached 94.66 % (Figure 6.8c). Due to the uniform and highly porous nature of the current system, higher recovery is obtained compared to Pie et al., 2014 (67.8 %) and Tang et al., 2013 (53.4 %). Significant interfacial tension reduction and wettability alteration also cause an increase in the oil recovery. The remaining oil is trapped in the porous medium in the form of an emulsion. Subsequently, alkali-surfactant-polymer flooding is executed to improve the oil recovery, but it is difficult to recover

the remaining oil from the porous medium. Hence ultimate oil recovery after alkali-surfactant-polymer flooding is 95 % from the 2D porous medium (Figure 6.8d).

6.2 Wettability alteration, interfacial tension, and in-situ emulsification analysis

The preference of any solid surface (rock, glass, or PDMS) to be wetted or adhered with one fluid in the presence of other immiscible fluids is called wettability. The relationships between wettability and capillary pressure ($P_c = 2\sigma Cos\theta/r$) at the pore-scale is critical for optimizing the oil recovery factor. If the contact angle is between 0°- 80°, 80°-100°, 100°-160°, and 160°-180°, then reservoir rock is characterized accordingly as water-wet, intermediate wet, oil-wet, and strongly oil-wet, respectively. The injection of a combination of chemical slugs can mobilize the trapped crude oil. The present work performs the contact angle measurement of low saline water, HPAM polymer, Alkali-polymer solution, and Alkali-surfactant-polymer solution on a sandstone pellet saturated with crude oil. The wettability study showed that the low saline water yielded a contact angle of 69.61°. This indicates that the rock surface under analysis is water-wet. Wettability alteration is one of the most important mechanisms of oil recovery using low-salinity water flooding (Saw and Mandal, 2020). The thermodynamic equilibrium between the crude oil and rock gets disturbed in the presence of low salinity water, resulting in cation desorption from the rock surface. The pH of the system increases with the release of cations, resulting in the removal of organic materials from the rock surface. The wettability of the rock surface is changed to a more water-wet condition in the presence of low-salinity water (Saw and Mandal, 2020; Saw et al., 2022; Strand et al., 2009). The average value of contact angle for polymer solution results in about 65.32°. No significant change in the wettability is observed using a polymer solution because of no significant fluid–solid interaction. A significant reduction of contact angle is observed in the case of an alkali-polymer solution, which is reduced to 39.3°. The reason for wettability alteration is the emulsification

process between crude oil and alkali-polymer solution, which results in trapped oil recovery in the form of emulsion from small pore constrictions (Mehranfar and Ghazanfari, 2014). Similarly, Saha et al., 2018a also observed the contact angle reduction up to 38.9° using an alkaline solution on a crude oil-saturated sandstone pellet. When the surfactant is added to the alkali-polymer solution, the contact angle is decreased up to 32.37° due to the interaction of the surfactant with the polar compounds in the crude oil. The surfactant recovers the trapped oil by altering the wetting nature of the rock to an extremely water-wetting condition (Figure 6.9). Similarly, the dynamic contact angle reduces to 17.6° using sodium ethyl ester sulphonate surfactant (SEES) in the displacing phase (Pal et al., 2018).

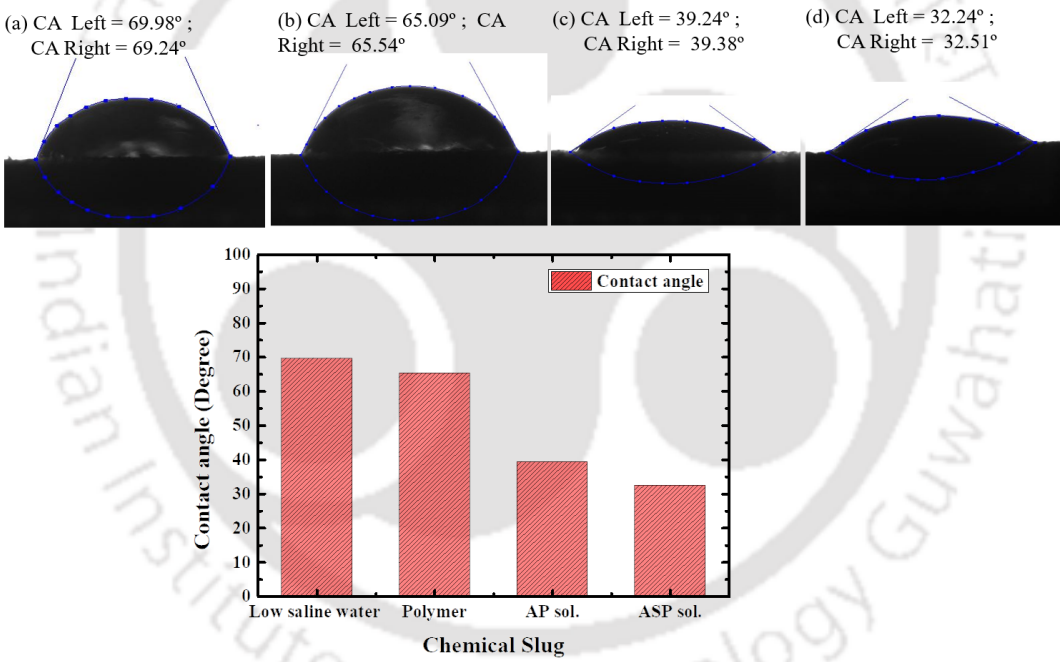

Figure 6. 9 Contact angle measurement on a sandstone pellet using (a) Low saline water, (b) Polymer solution, (c) Alkali polymer solution, and (d) Alkali surfactant polymer solution.

The comparative study reveals that the saline water has a large contact angle on the sandstone pellet. In contrast, the ASP solution has a minimal contact angle, showing high wettability

towards the rock pellet. The generation of in-situ surfactant and visualization of emulsion formation can be found in Sharma et al., 2021.

Measurement of wettability alteration with time shows a significant reduction in the contact angle for alkali-polymer and ASP solutions. However, minor changes in contact angle are observed using polymer solution. In the case of low salinity water, the contact angle reduced between 69.6° − 65.13° in five minutes. In the case of alkali-polymer and ASP solution, the contact angle ranges between 39.1°– 31.2° and 32.4° – 10.7°, respectively (Figure 6.10a).

The interfacial tension measurement showed that the heavy crude oil has the highest IFT of 20.86 mN/m with the DI water. The interfacial tension is reduced considerably for saline water, polymer solution, alkali-polymer solution (AP), and alkali-surfactant-polymer (ASP) solution. During low-salinity water injection, the organic material's solubility increases in the aqueous phase (salting-in effect). This results in IFT reduction between the two phases (Strand et al., 2009). The IFT is reduced to 17.18 mN/m using low salinity water in the porous medium. The IFT value between the polymer solution and heavy crude oil is obtained as 7.71 mN/m. Further, the IFT value of the alkali-polymer solution and crude oil reduces to 0.37 mN/m (Figure 6.10b) due to in-situ surfactant formation. For an alkali-surfactant-polymer solution and crude oil, the lowest IFT is achieved as 0.20 mN/m (Figure 6.10b). The significant IFT reduction is because of emulsion formation between the surfactant and crude oil. The droplet size in the emulsion remains small as the surfactant coats the emulsion droplets during the interaction, which reduces the coalescence of the droplets in the emulsion.

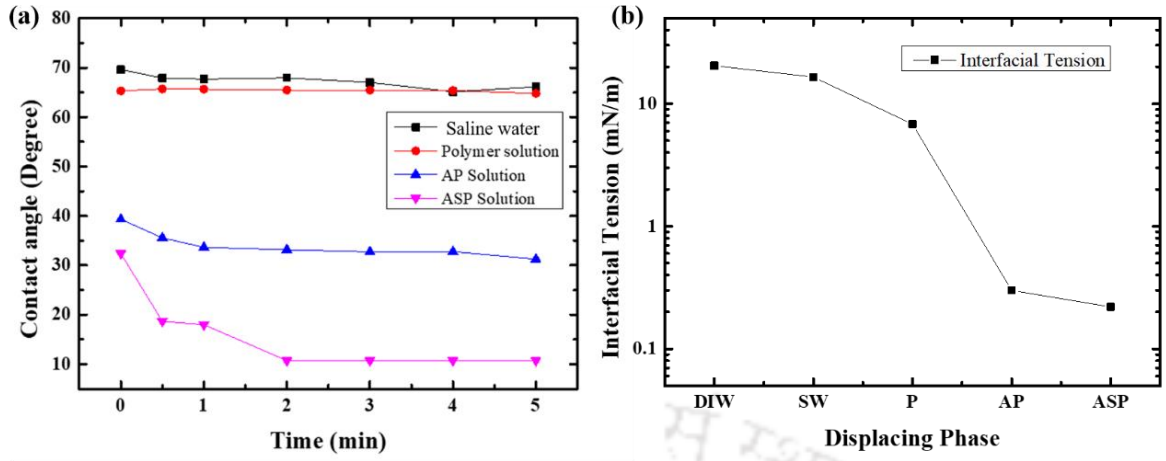

Figure 6. 10 Contact angle and interfacial tension measurement, (a) Comparative analysis of wettability alteration with time on sandstone pellet using low saline water, polymer solution, alkaline polymer solution, and alkali surfactant polymer solution, (b) interfacial tension analysis between heavy crude oil and different solutions.

6.3 Droplet size distribution of emulsion

Microscopic studies of different emulsions are performed to probe the emulsion stability based on droplet size distribution (Figure 6.11). The displacing phase (saline water/alkali-polymer/alkali-surfactant-polymer) is mixed in equal proportion with crude oil and stirred with an ultrasonic homogenizer for 20 min to formulate the emulsion. The emulsion is of oil in water (O/W) type emulsion between crude oil and ASP solution. Initially, the emulsion droplets are distributed uniformly and form a single continuous phase. The emulsion samples are transferred in graduated bottles for visual observation of the emulsion stability and phase behavior. The single-phase emulsion remains stable for more than 72 hrs after that, the phases start to separate (Figure 6.12). The crude oil-saline water emulsion, crude oil-polymer emulsion, crude oil-alkali polymer emulsion, and crude oil-alkali surfactant polymer emulsions remained stable for up to 3 days. After that, phase segregation begins because of the droplet

coalescence. However, the sample with the crude oil-alkali polymer solution and crude oil-alkali surfactant polymer solution had a meager settling at the end of day 3 (Figure 6.12). It is observed that with time after 10 days, the single-phase emulsion changes into the three-phase system in which the middle phase becomes narrow with time. As the droplet's coalescences increase with time, the top and bottom phases become thicker (Pal et al., 2018). In the case of polymer solution/ crude oil emulsion, the microscopic images show an average droplet size of 18.42 μm (Figure 6.11c). The droplet size distribution of ASP solution/crude oil emulsion shows an average droplet of 12.92 μm (Figure 6.11d). The overall average of droplet size (average of triplicate readings) for crude oil-polymer and the crude oil-ASP emulsion is 20.14 μm (standard deviation = 1.54 μm) and 12.13 μm (standard deviation = 0.80 μm), respectively. During crude oil and surfactant solution interaction, the breakdown of oil droplets takes place, and surfactant coats around the emulsion droplets and prevents the coalescence of the droplets (Pal et al., 2018). The droplet size is reduced because of the IFT reduction. The in-situ emulsification results in the miscibility between crude oil and ASP solution (Pal and Mandal, 2020; Pal et al., 2018). Therefore, the addition of alkali and surfactant in the aqueous phase help to displace the trapped non-wetting phase in a porous medium due to IFT reduction, simultaneous in-situ emulsification, and wettability alteration.

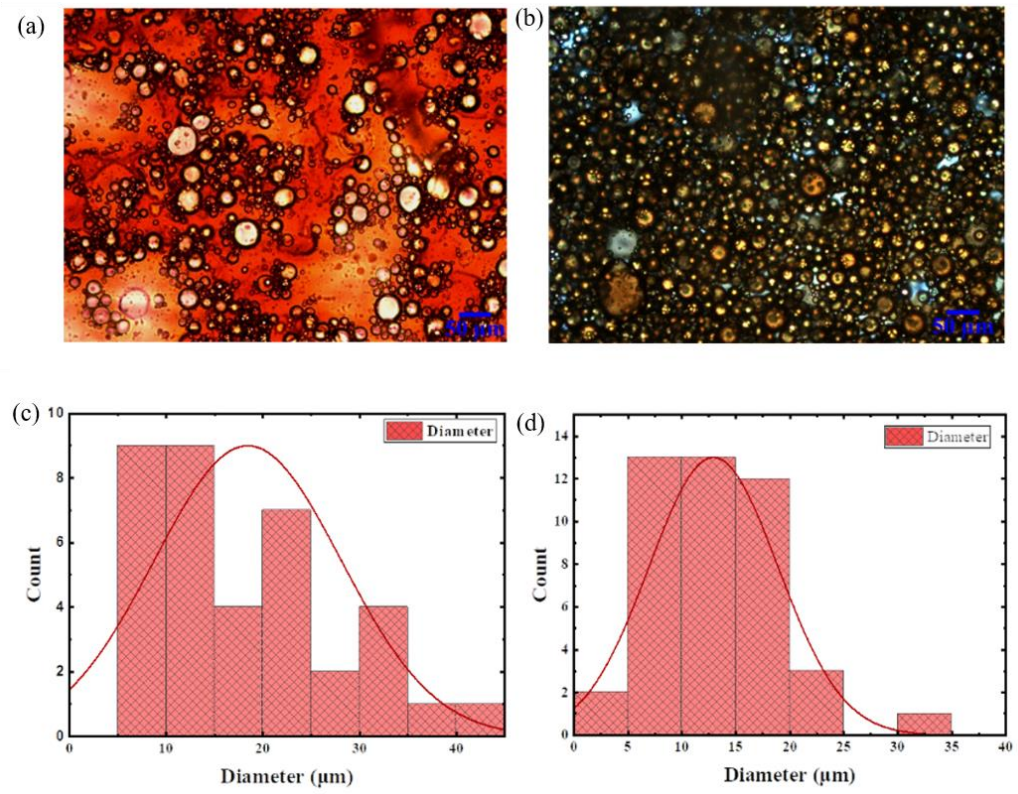

Figure 6. 11 Microscopic visualization of emulsion: between crude oil / HPAM polymer solution (a) and between crude oil /ASP solution (b). Droplet size distribution of crude oil/ HPAM polymer solution emulsion (c) and crude oil/ASP solution emulsion (d). The average droplet size was 18.42 μm and 12.92 μm for the crude oil / HPAM polymer solution emulsion and crude oil/ASP solution emulsion, respectively.

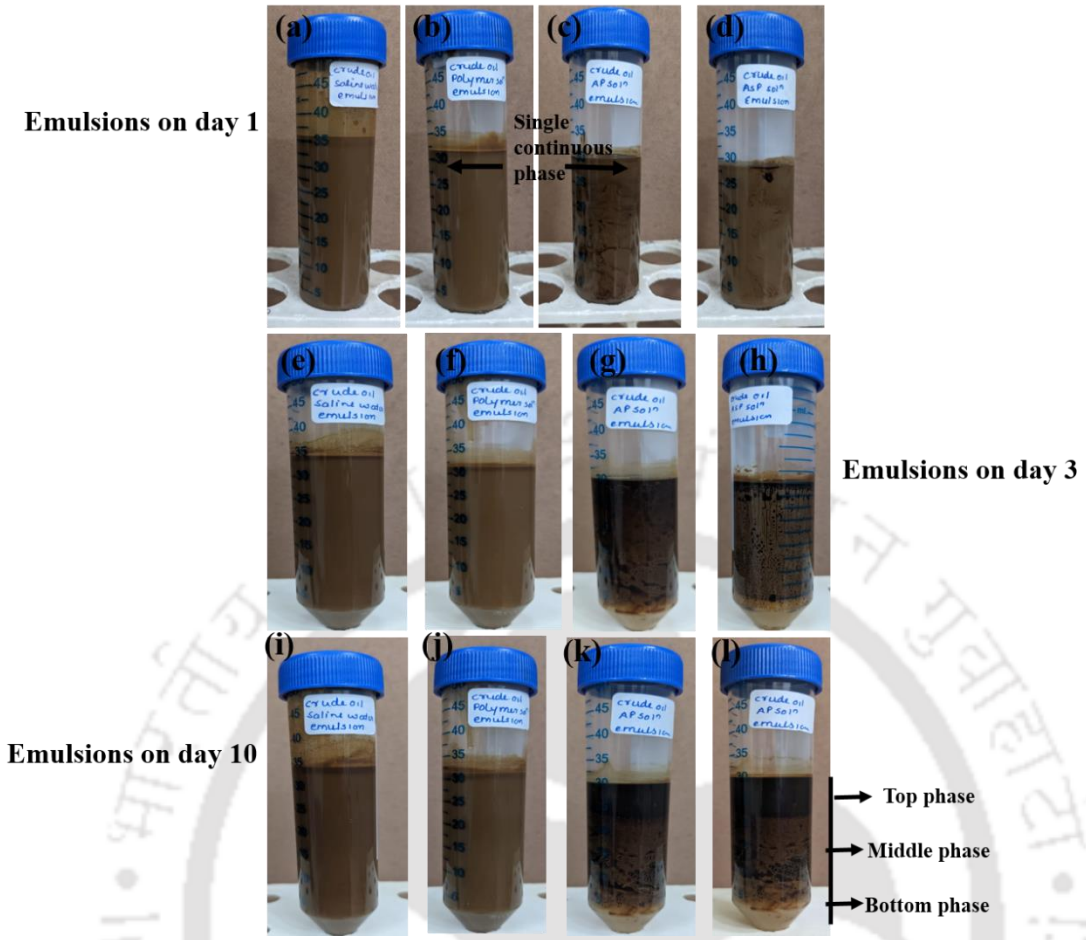

Figure 6. 12 Crude oil and different chemical slug emulsions stability analysis on day 1, day 3, and day 10.

6.4 Effect of salinity on interfacial tension and wettability

To understand the effect of salinity on interfacial tension and wettability alteration, the salinity of displacing phase is varied (from 0.1 wt% to 10 wt% NaCl). Interfacial tension measurement shows an increase in the interfacial tension from 13.13 mN/m – 19.17 mN/m, decreasing the salinity from 10 wt% to 0.1 wt% (Figure 6.13a). Literature shows that the IFT increases when the salinity of the displacing phase is decreased below 40000 ppm (Abdel-Wali, 1996). Saw and Mandal, 2020 also observed that in the presence of seawater, the interfacial tension initially reduced to the lowest value. Thereafter the interfacial tension increases with a further dilution of the seawater. The wettability alteration study is also conducted by increasing the salinity of

displacing phase from 0.1 wt% to 10 wt% NaCl. The contact angle measurement showed a change in contact angle from 73◦ to 62.23◦ while decreasing the salinity of the displacing phase from 10 wt% to 0.1 wt% of NaCl (Figure 6.13b). Low saline water disturbs the thermodynamic equilibrium and alters wettability to more water-wet conditions (Strand et al., 2009). Saw and Mandal, 2020 investigated the effect of salinity dilution on the wettability of a carbonate rock surface and found that the contact angle decreases significantly with the degree of dilution of seawater.

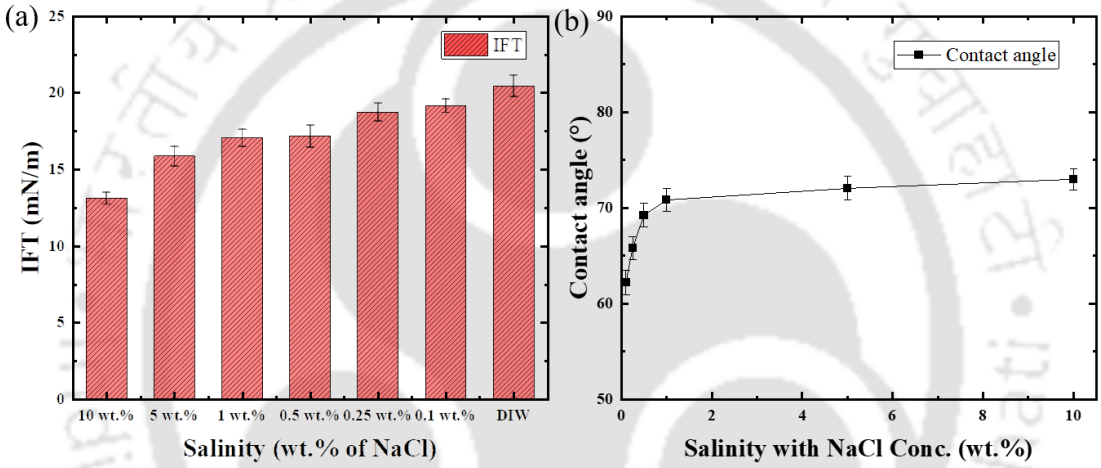

Figure 6. 13 Effect of salinity on (a) interfacial tension and (b) wettability alteration

6.5 Core flooding experiments

Different flooding processes, such as low salinity water flooding, polymer flooding, alkali-polymer flooding, and alkali-surfactant-polymer flooding, are executed on the Idaho core sample with a porosity of 28 %. Initially, the core is saturated with low salinity water for 24 hrs under the core holder. Heavy crude oil is injected into the core to displace the resident saline water and creates an initial reservoir condition with initial crude oil saturation of 91 % and connate water saturation of 9 %. A water flooding operation is performed, which results in a recovery of 48.04 % of the original oil in place. The mechanisms such as wettability alteration,

fines migration, pH increase, multi-ion exchange, and salting in contribute to enhanced oil recovery during low salinity water injection (Mahmoudzadeh et al., 2022). During low salinity water injection, reactions occur among oil/brine/rock resulting in an increase in the pH, which causes the generation of surfactant and reduction of the interfacial tension between oil and water. Hence, water wettability significantly improved, which led to higher oil recovery (Al-Shalabi and Sepehrnoori, 2016; Saw and Mandal, 2020; Sheng, 2010). An increased oil recovery of up to 68 % (overall) and 20 % (additional) using low salinity water flooding has also been reported by Patil et al., 2008 and Gamage and Thyne, 2011 respectively. Still, a considerable volume of oil remained confined in the pores of the reservoir rock. Further, polymer flooding is executed to improve the mobility ratio and control the aqueous phase mobility (Kalita et al., 2022). The polymer solution exerts pressure on the trapped oil droplets and films. Hence oil can be pulled and pushed out of the pore constrictions and dead-ends (Sheng, 2010). The flooding resulted in a recovery of almost 8.59 % of the original oil in place. However, 43.37 % of oil remained trapped in the pores of the reservoir rock. Hence alkaline polymer flooding is executed to change rock-fluid (wettability) and fluid–fluid (interfacial tension) properties. The flooding resulted in an oil recovery of 3.90 %. Even after the alkali-polymer flooding, 39.47 % of the oil remained trapped. Surfactant (SDS) is used with the aqueous phase to improve the wettability alteration and reduce the IFT. The execution of alkaline surfactant polymer flooding brings the best results in terms of oil recovery. The results show recovery of almost 14.84 % of original oil in place (OOIP) using ASP flooding. The alkali forms an in-situ surfactant, and the addition of an external surfactant further augments the IFT reduction to a significantly low value and forms a stable emulsion. The polymer increases the displacing phase (water) viscosity. Hence all three chemicals, alkali, surfactant, and polymer, work in synergy to reduce the residual oil saturation. Hence, after saline water and all chemical flooding execution on the Idaho core, the heavy oil recovery reached almost

75.37 % (Figure 6.14a). During the flooding process, maximum differential pressure of 6 psi is reached. The low differential pressure is just because of the high porosity of the Idaho core sample. Core flooding experiments are also conducted by separately injecting low salinity water, polymer solution, alkaline polymer solution, and alkali-surfactant-polymer solution in different experiments to investigate the crude oil recovery by individual fluids. Low salinity water injection recovers 48.04 % of crude oil (OOIP). Separate injection of polymer solution recovers 58.88 % of crude oil (OOIP), which is slightly higher than the oil recovery till polymer flooding in the previous case of simultaneous injection.

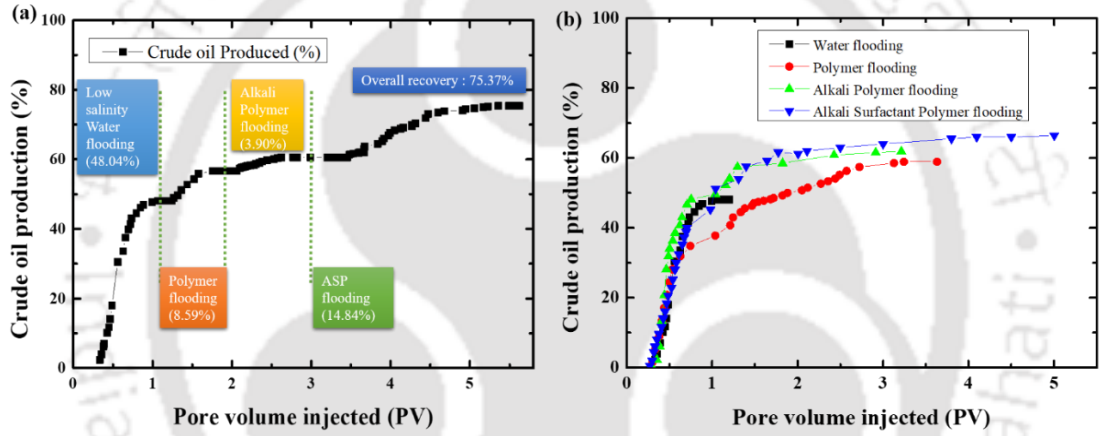

Figure 6.14 Crude oil recovery using core flooding in case of (a) various concurrent/simultaneous flooding processes, including Low salinity water flooding, polymer flooding, Alkali polymer flooding, and alkali surfactant polymer flooding, (b) Direct injection of various chemical solutions separately in different experiments.

Similarly, a separate injection of alkali-polymer solution results in a recovery of 61.85 % crude oil (OOIP), which is slightly higher (1.32 %) than the simultaneous injection of alkali-polymer (after polymer flooding) in the previous case. But the separate injection of ASP solution recovers 66.40 % of crude oil (OOIP), which is 8.97 % lower than the simultaneous injection

of ASP solution in the previous case. Hence it can be concluded that there is a reduction in oil recovery during separate injection of ASP solution compared to simultaneous injection. However, a slight increase in oil recovery is observed during separate injections of LSW, Polymer solution, and AP solution (Figure 6.14b) compared to simultaneous injection (Figure 6.14a).

6.6 Summary

In this study, pore and core-scale analyses of different flooding processes are executed to understand the flow behavior, such as displacement mechanisms and oil recovery. During low salinity water flooding, viscous instability, film formation around the cylinders, and inconsistent velocity magnitude are observed, causing unsteady flow behavior in the porous medium. Sweep efficiency is significantly reduced due to the unsteady flow behavior and viscous instability in porous micromodel. Polymer flooding is performed to control the displacing phase mobility. The polymer solution followed the same preferential flow path generated by LSW flooding, leading to no significant change in the confined fluid saturation in the porous medium. Even increasing the flow rate (from 0.05 to 0.2 ml/min) could not displace the trapped fluid. Alkali-polymer and ASP flooding were subsequently executed to improve fluid–fluid and matrix-fluid interaction. The alkali-polymer solution was introduced at three different flow rates. At low flow rates, the interface starts to move. Increasing the flow rate causes an increment in the emulsion formation, which moves in multiple directions, displacing the trapped oil from the pores in all directions. Due to in-situ emulsion formation, oil recovery increased significantly using ASP and alkali-polymer flooding. Contact angle measurement is conducted to investigate the wettability alteration by different chemical solutions. It is observed that using an alkali-polymer solution and ASP solution causes a significant improvement in wettability by reducing the contact angle. Core scale analysis is performed to estimate heavy oil recovery from the porous medium. The results showed that the

LSW flooding, polymer flooding, alkali-polymer flooding, and ASP flooding recovered 48.04 %, 8.59 %, 3.90 %, and 14.84 %, respectively. The overall heavy oil recovery from the core flooding is 75.37 %. The separate injection of ASP solution results in an oil recovery of 66.40 %, which is lower than the sequential injection of ASP solution in the core flooding process.

Chapter 7. Suspension transport through the porous medium

Suspension;

Shear-induced particle migration;

Porous medium;

Micro-particle image velocimetry;

Multiphase flow.

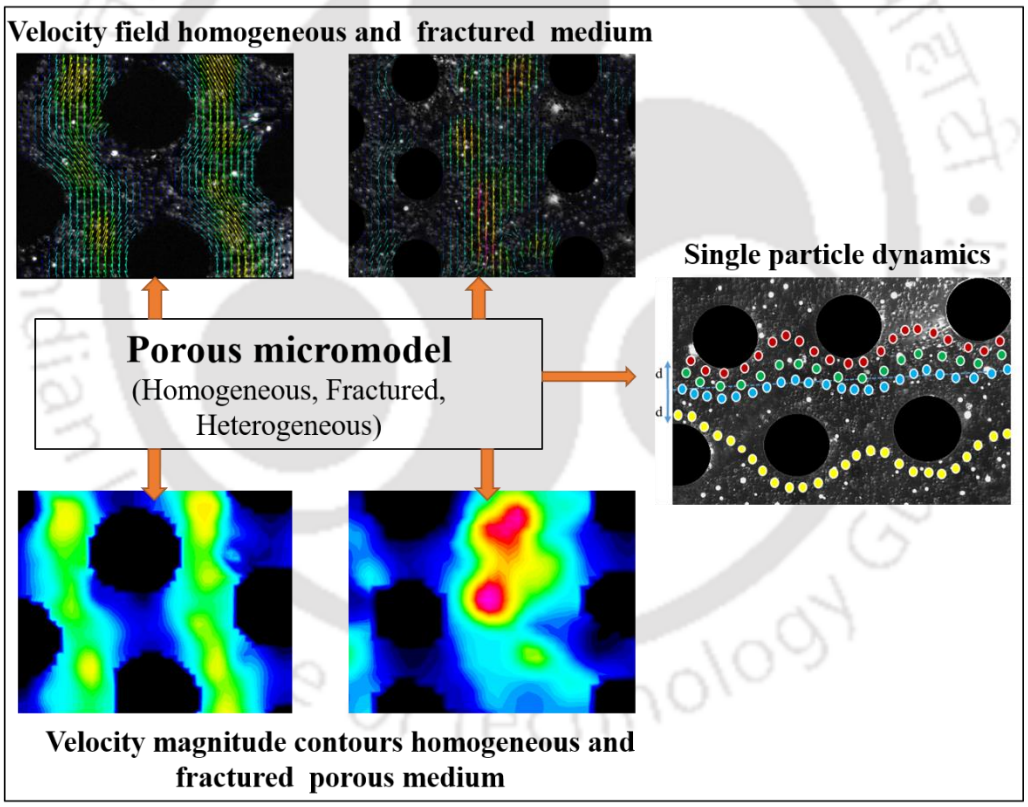

Suspension transport through the porous medium

This chapter presents visualization and quantification of suspension flow dynamics through the porous medium. Soft-lithography technique is used to fabricate the porous micromodels of homogeneous, heterogeneous, and fractured geometry to visualize the suspension flow through the porous medium. Single particle flow dynamics have been visualized, showing that the hydrodynamic interactions and inter-particle non-hydrodynamic forces between the moving and fixed grains particles strongly influence the particle trajectory. The effect of particle concentration within the suspension showed that at higher particle concentration, severe clusters formed in the porous medium resulting in a velocity drift. The phenomena of pore bridging, trapping, and shear-induced particle migration are also observed during multiphase flow in the heterogeneous porous medium.

7.1 Micromodels

Three porous micromodels, such as homogeneous, heterogeneous, and fractured, are used to investigate the effect of geometry on the suspension flow through the porous medium. The dimensions and the geometrical properties of the micromodels are mentioned in the following Table 7.1.

Table 7. 1 Geometrical characterization of porous micromodels

S.N.	Parameters	Micromodel 1	Micromodel 2	Micromodel 3
1.	Nature	Homogeneous porous medium	Fracture porous medium	Heterogeneous porous medium
2.	Length (l) Width (w) Height (h)	4.05 cm 1.95 cm 400 μm	4.05 cm 1.95 cm 400 μm	4.05 cm 1.95 cm 400 μm
3.	Porosity, φ (%)	78	70	53
4.	Micro-cylinder height (h) / Bead diameter, D (μm)	500	1000	500
5.	Fracture width & Length	-	1mm	-

7.2 Single particle flow dynamics

To understand particle dynamics in the porous medium, suspension with low particle concentration (2.5 %) is injected into the porous medium. The trajectory of the individual particles is tracked, which shows that the particle released from the center of the flow channel in the porous medium follows a less tortuous path while moving from the top to the bottom, hence taking less retention time. However, particles released near the fixed cylinders follow a highly tortuous path and have more retention time. The particles released from very near to the cylinders change their flow path by crossing from one channel to another. Similar flow behavior can be seen in the numerical simulations performed by De and Singh, 2020. Figure 7.1 shows the particle trajectories based on their release locations.

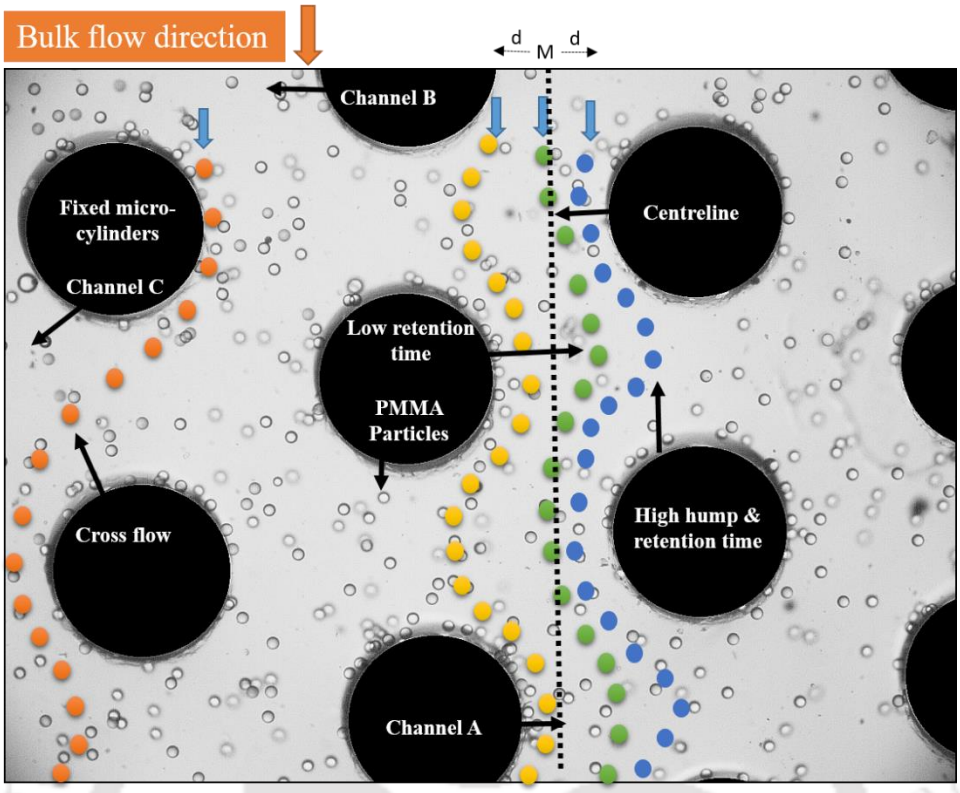

Figure 7. 1 Particle trajectories during low concentrated suspension flow through the porous medium.

Single particle dynamics experiments in the regular porous medium are validated by coupled laminar flow and particle tracing module in the COMSOL MULTIPHYSICS. Therefore a homogeneous porous medium (78% porosity) with a cylinder diameter and pore throat of 500 μm is prepared. The momentum and continuity equations are solved using fluid flow and tracing particles in the homogeneous porous medium.

PMMA particles of size 40 μm and a density of 1.18 g/cm^3 are used in the numerical simulations. Glycerol water solution (76:24) is injected into the porous medium. The bounce wall condition with gravity and drag forces are also considered while running the simulations. The numerical results showed a good agreement with the experimental results of single particle dynamics mentioned above.

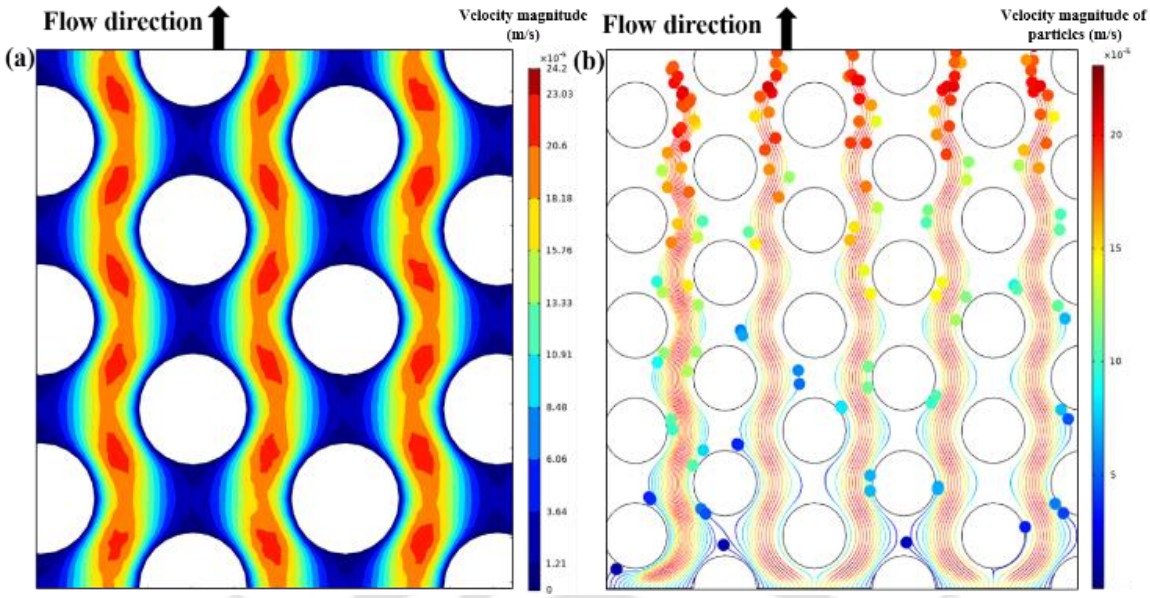

Figure 7. 2 Numerical simulations showing suspension flow through a porous medium, (a) Velocity magnitude contours during dilute concentration suspension flow, (b) Particle trajectories observed during the suspension flow.

Figure 7.2a shows the velocity magnitude profile (figure 7.2a) and particle trajectories (Figure 7.2b) during suspension flow through the porous medium. The experimental results of velocity magnitude in figure 7.4a (velocity magnitude) and simulation results in figure 7.2a, during dilute suspension flow through the porous medium, are compared. A qualitative symmetry of velocity magnitude is observed between the experimental and simulation results, as particle-particle interactions are not considered during simulations. However, particle trajectories are almost identical in experiments and simulations

7.3 Suspension flow through porous media

The experiments are conducted by injecting suspensions of different particle concentrations, including 2.5 %, 5 %, 7.5 %, and 20%, in the porous medium. When suspension with 2.5 % particle concentration is injected in the porous medium, no particle-particle interaction and cluster-free flow is observed (Figure 7.3a). Further, the concentration is increased to 5% suspension and injected in the porous medium. It is observed that some particles settle at the

bottom of cylinders, and few clusters are formed (Figure 7.3b). However, significant particle clustering is observed when the concentrated suspension of 7.5% particle is injected (Figure 7.3c). Further, an increase in the particle concentration up to 20% in the suspension results in severe particle clustering (Figure 7.3d).

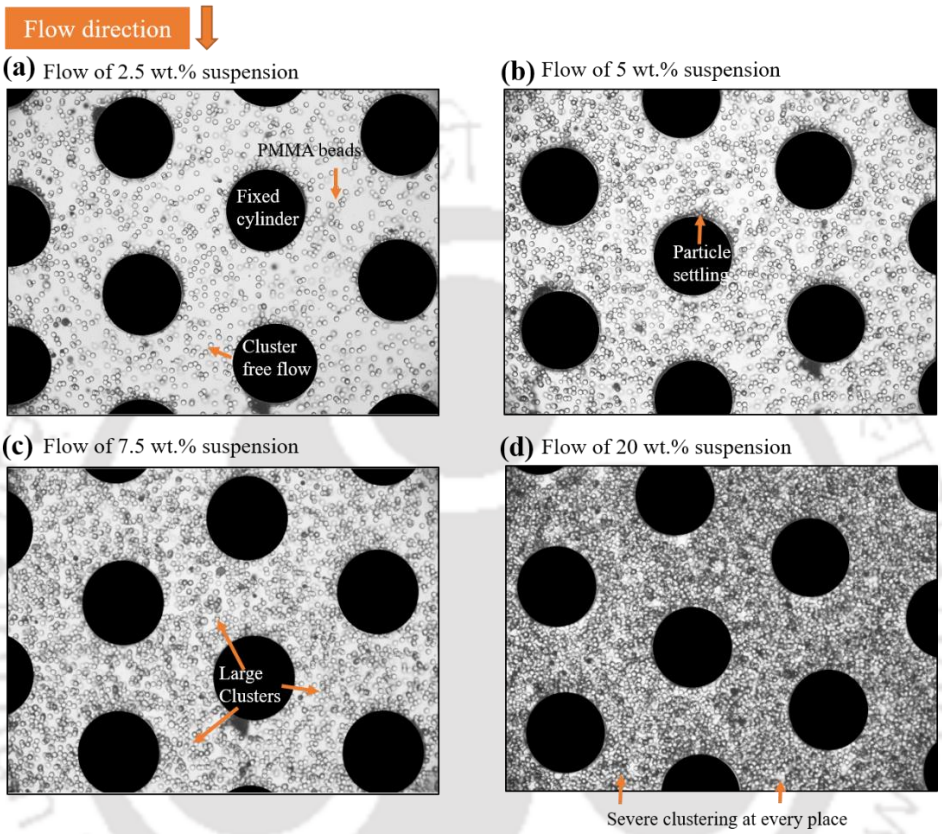

Figure 7. 3 Suspension flow through the porous medium, (a) Suspension with 2.5 wt% PMMA, (b) Suspension with 5 wt.% PMMA, (c) Suspension with 7.5 wt.% PMMA particles, and (d) Suspension with 20 wt. % PMMA.

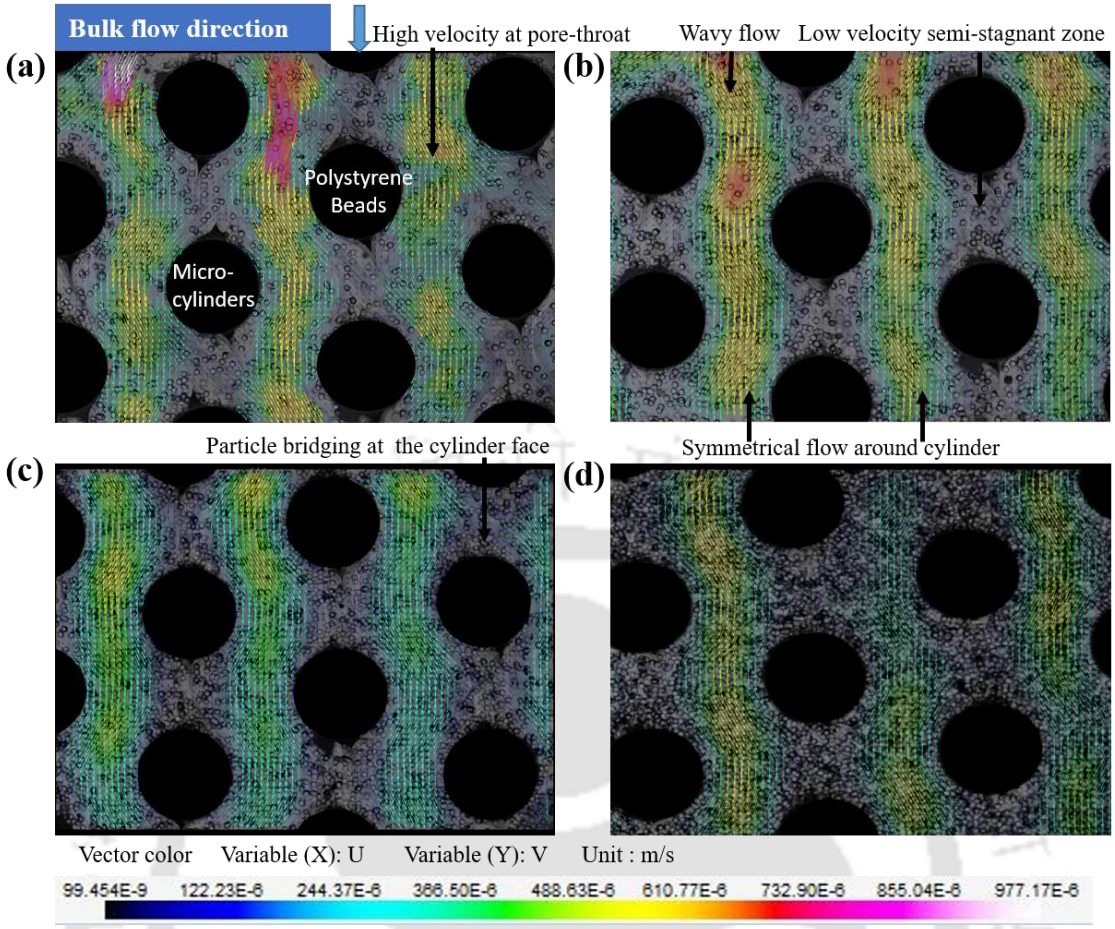

Figure 7. 4 The instantaneous velocity field for suspension infiltrating at 0.05 ml/min in the 2D porous micromodel (a) suspension with 2.5 wt.% PMMA, (b) suspension with 5.0 wt.% PMMA, (c) suspension with 7.5 wt.% PMMA, (d) suspension with 20 wt.% PMMA (Images captured at 24 FPS)

The velocity magnitude contour plots are prepared to analyze suspension flow in porous media at a flow rate of 0.05 ml/min. When suspension with 2.5 % particle concentration is injected into the porous medium, a high-velocity magnitude (0.97 mm/s) is observed because the particle is not colliding with each other (Figure 7.5a). Increasing the particle concentration up to 5 % in the suspension causes particle-particle collision during flow, resulting in a negative drift velocity. Hence the maximum velocity magnitude will decrease to 0.78 mm/s (Figure 7.5b). Further, an increase in the particle concentration to 7.5% in the suspension further increases a negative drift in the velocity, and the maximum velocity magnitude further

decreases to 0.53 mm/s (Figure 7.5c). However, when the particle concentration is significantly increased, the clusters of particles do not get any space to move in random directions. Hence particle clusters move in the flow direction and provide additional momentum to the particle moving forward, resulting in positive drift velocity. Hence the velocity magnitude increased to 0.572 mm/s in this case (Figure 7.5d).

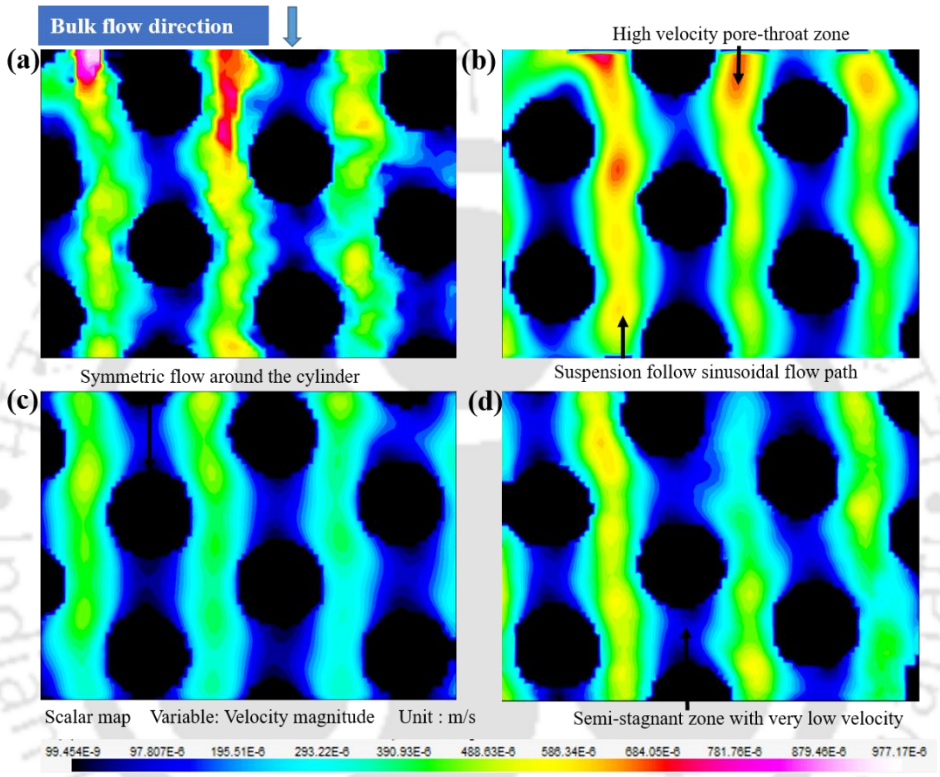

Figure 7. 5 Velocity magnitude contours of suspension with (a) 2.5 % PMMA particles, (b) 5% PMMA particle, (c) 7.5 % PMMA particles, (d) 20 % PMMA particles

The concentration contour plots of different suspensions (2.5 – 20 wt.%) flow through a homogeneous porous medium have been prepared to analyze the effect of particle concentration on suspension flow behavior in the porous media (Figure 7.6). A Matlab code is written to prepare the concentration contour plots. Concentration contours show the lowest particle concentration around the microcylinders and the maximum at the pore throat regions.

The high particle concentration is observed in the middle of the flow channel in the porous medium. The shear-induced particle migration is affected by the microcylinders. Particle concentration is not consistent at low-concentrations (2.5 wt.%). However, the concentration profile is consistent for 20 wt.% suspension flow. A symmetrical concentration flow profile is observed around the cylinder at 20 wt.%.

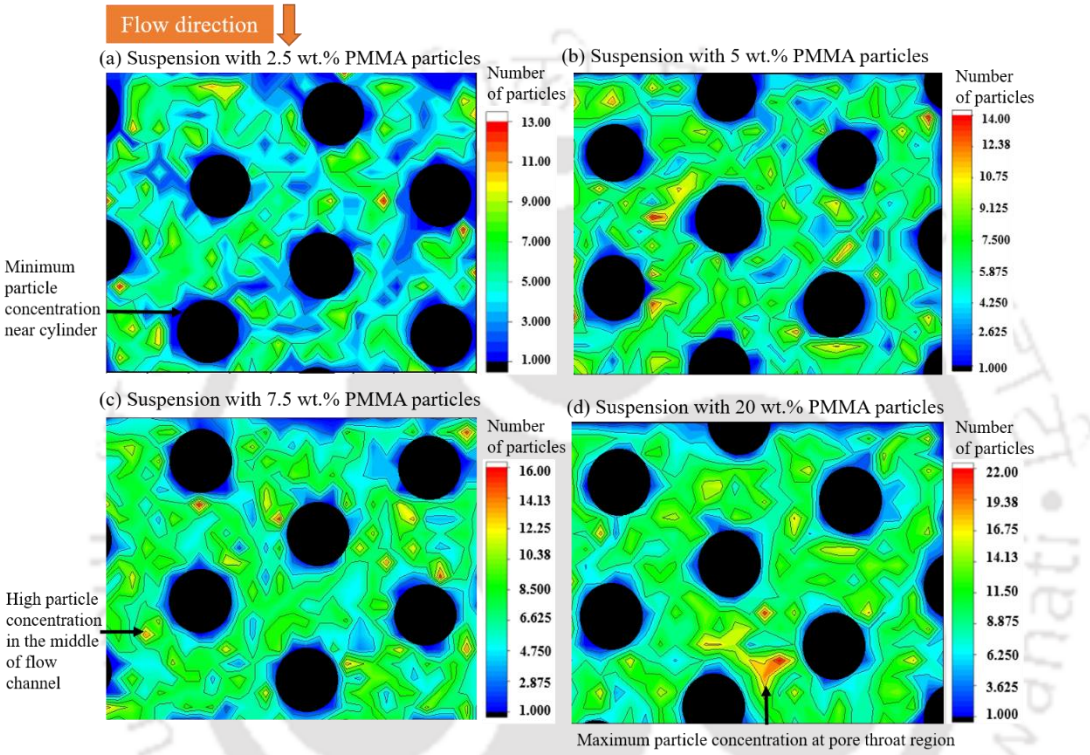

Figure 7. 6 Velocity magnitude contours of suspension with (a) 2.5 % PMMA particles, (b) 5% PMMA particle, (c) 7.5 % PMMA particles, (d) 20 % PMMA particles

Suspension (2.5 wt.%) flow behavior is characterized in the fractured porous medium using a time-resolved velocity vector (Figure 7.7). It is observed that the maximum velocity is observed at the fracture center, whereas the minimum velocity in the pore spaces. The velocity is almost double in the fracture compared to the pore region. The particles migrate from the high shear region to the center of the fracture, where the shear is small. Hence the concentration of particles is significantly increased at the center of the fracture. A high particle concentration

results in a higher drift, resulting in higher velocity at the center of the fracture compared to the porous medium (Figure 7.7a). The velocity vector map of suspension flow through porous medium shows the maximum velocity at the narrow pore throat regions. In contrast, minimum velocity is observed at the large pore bodies. The particles slow down and settle in the pore body region, resulting in pore bridging (Figure 7.7b,7.7c). Crossflow from the fracture to porous medium and fluctuating flow are also observed in suspension with 2.5 wt.% particles (Figure 7.7d).

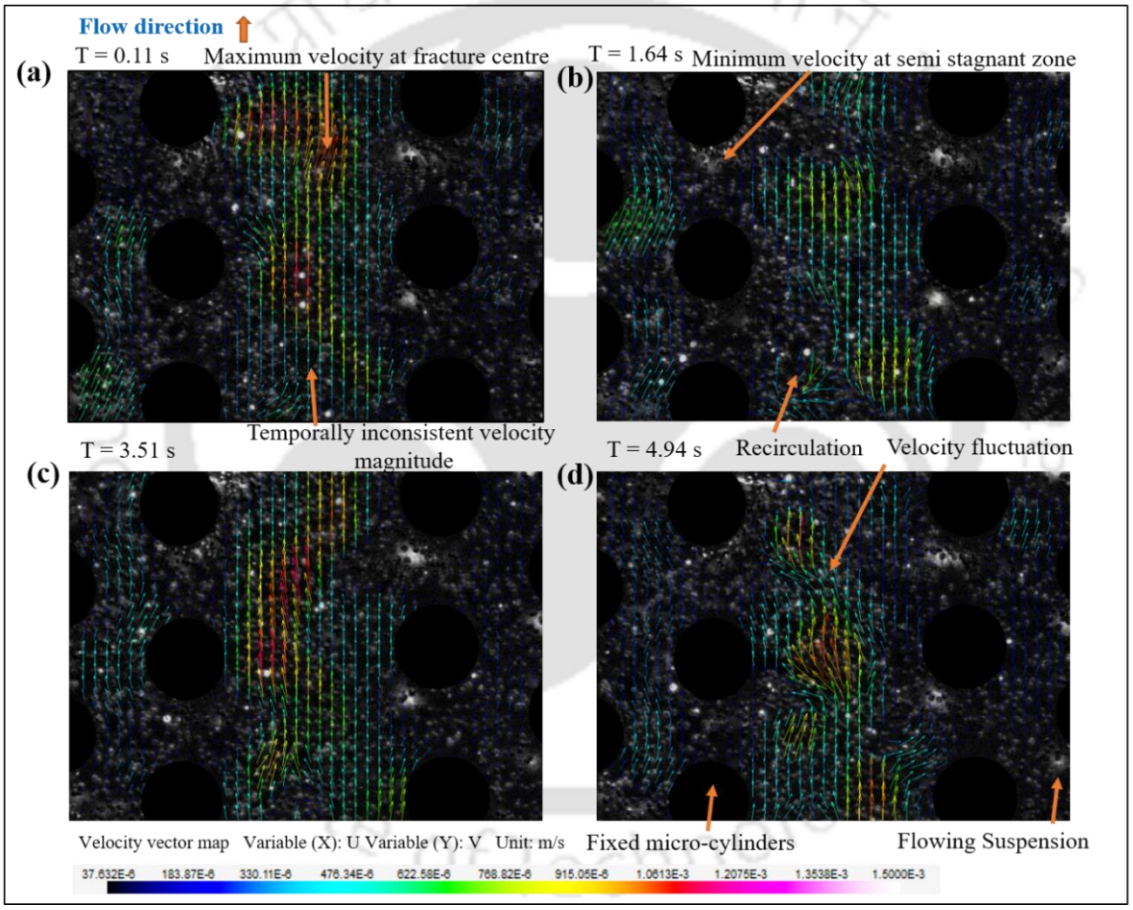

Figure 7. 7 Time-resolved velocity vector field showing 2.5 wt.% suspensions flowing in the fractured porous medium (a), (b), (c), (d) are the velocity vector field at T = 0.11 s, 1.64 s, T = 3.51 s, and T = 4.94 s respectively.

The suspension flow behavior through the fractured porous medium is also characterized at larger concentrations from 5 wt.% and 20 wt.%. The velocity magnitude profile along the line EF shows that the velocity magnitude is significantly larger in the case of higher concentration suspension flow in the porous medium (Figure 7.8a). The highest velocity magnitude of 0.72 mm/s is obtained for 5 wt.% suspension, whereas the highest velocity magnitude of 0.91 mm/s is observed in case 20 wt.% suspension flow through the fractured porous medium. It is also observed that in the middle of the fracture, the velocity is significantly higher compared to the boundaries of the fracture or near the cylinder due to frictional forces.

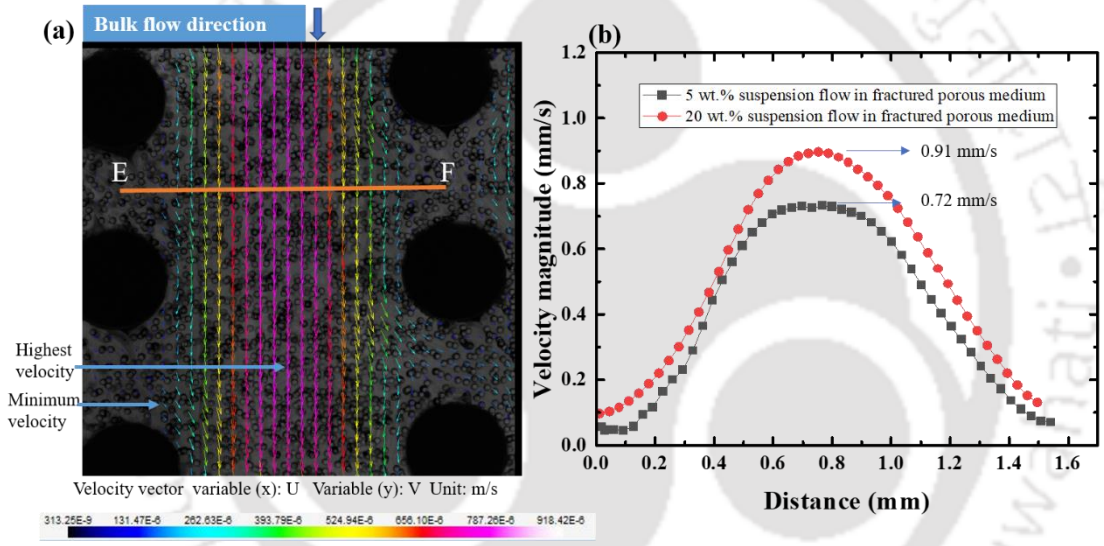

Figure 7. 8 Comparison of velocity magnitude along a line EF in the fractured porous medium, (a) velocity vector map showing along a line EF during 5 wt.% suspension flow in the fractured porous medium, (b) velocity magnitude profiles along line EF during 5 wt.% and 20 wt.% suspension flow through fractured porous medium section respectively.

Suspension flow behavior in the porous medium is investigated for change in velocity magnitude and concentration profile across the fracture line GH and along the line IJ in the porous medium (Figure 7.9a, b). The concentration profile for the fracture channel flow shows pronounced particle migration toward the center. Particles are migrating from higher-shear

regions to low-shear due to shear-induced migration. However, significant shear-induced migration was not observed in the case of flow through the porous channel region.

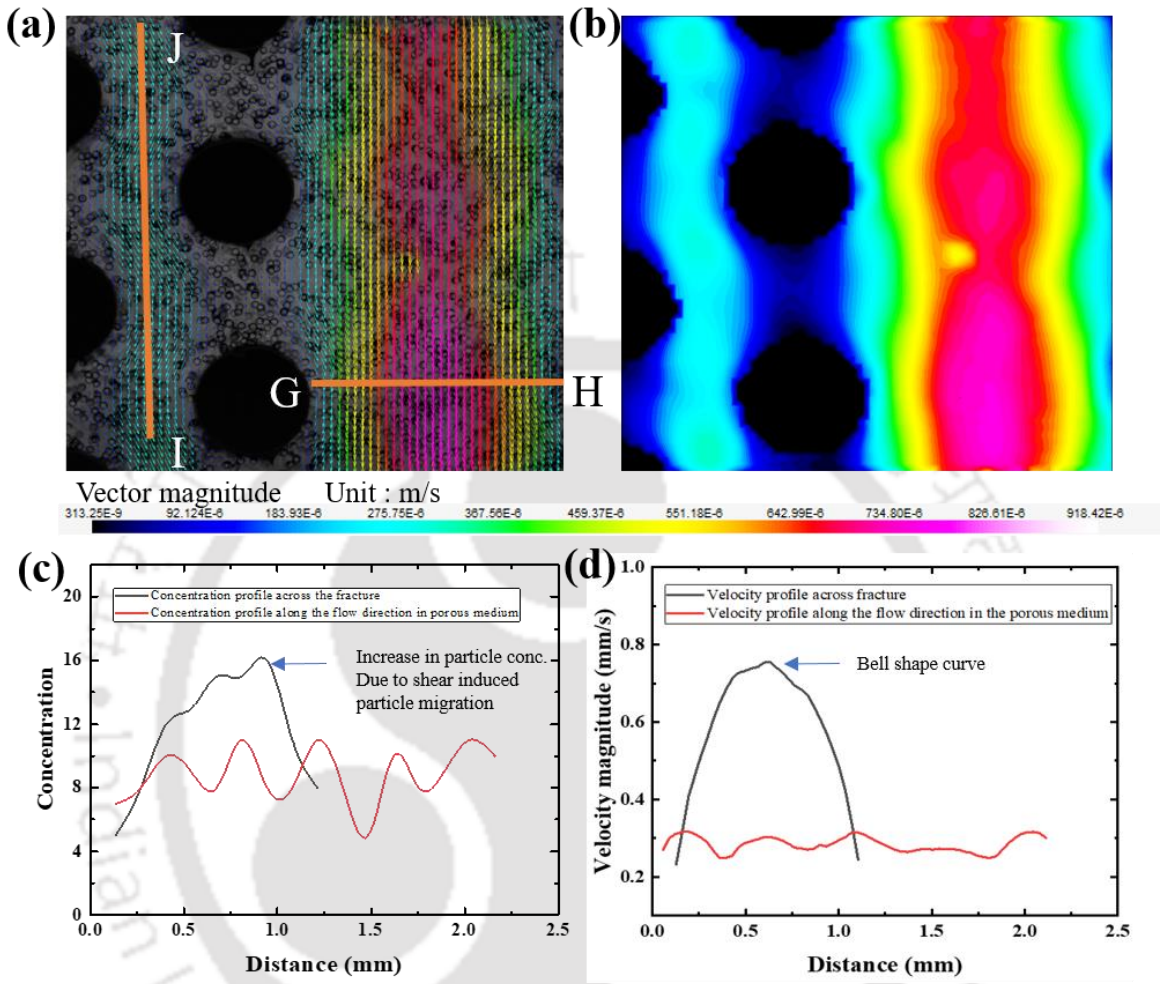

Figure 7. 9 (a), (b), (d) Velocity magnitude along the line GH and IJ, (c) Particle concentration along the line GH and IJ.

The periodic nature of the concentration profile in the porous channel is observed due to the periodic configuration of the grain particles. The migration of suspension particles towards the center of the channel (in the absence of any grain particles) produced a blunted concentration profile (Figure 7.9c). A larger suspension velocity was observed at the center of the channel due to higher particle concentration, and the shear rate was diminished at the center. It also

followed the bluntness of the velocity profile across the channel. However, the velocity profile for the porous medium is similar to its concentration profile (Figure 7.9d). The particle migration is well studied in the case of suspension flowing through tubes and channels. However, the migration in porous media has received less attention (De and Singh, 2020).

An analysis has been performed to study the velocity component along the flow direction (V_x) and the component perpendicular to the flow direction (V_y). The dependency of particle velocity on the number of particles encountered can be clearly depicted in the graph (Figure 7.10a). Experiments with different injection flow rates have been conducted to investigate its effect on root mean square average velocity (Figure 7.10b). The linear dependency of the RMS average velocity on the injection flow rate can be clearly seen.

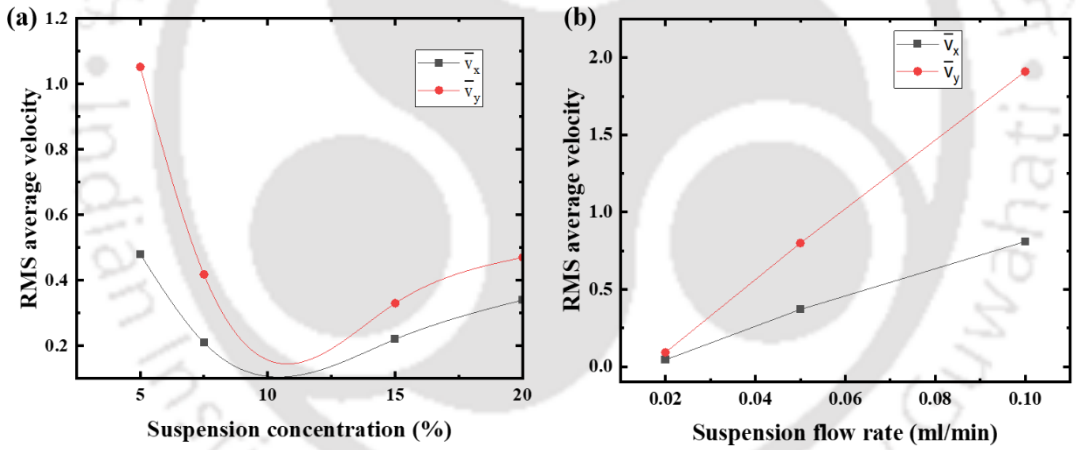

Figure 7. 10 Variation in time average root-mean-square average velocity with (a) concentration and (b) suspension average flow rate.

7.4 Multiphase flow

A multiphase flow study is also conducted by initially saturating the heterogeneous porous medium with concentrated suspension of 5 wt.% PMMA particles. Thereafter, n-decane is injected at 0.05 ml/min in the porous medium to displace the suspension. At the interface, particle accumulation occurs, and the highest particle concentration is observed at the

suspension / n-decane interface. As the interface moves, the shear-induced particle migration results in the maximum particle concentration in the center of the flow channel in the heterogeneous medium and lower at the wall of the beads (Figure 7.11a, 7.11b). Even fluctuating flow of suspension displacement through the porous medium is visualized due to unsteady flow behavior during multiphase flow in the heterogeneous medium.

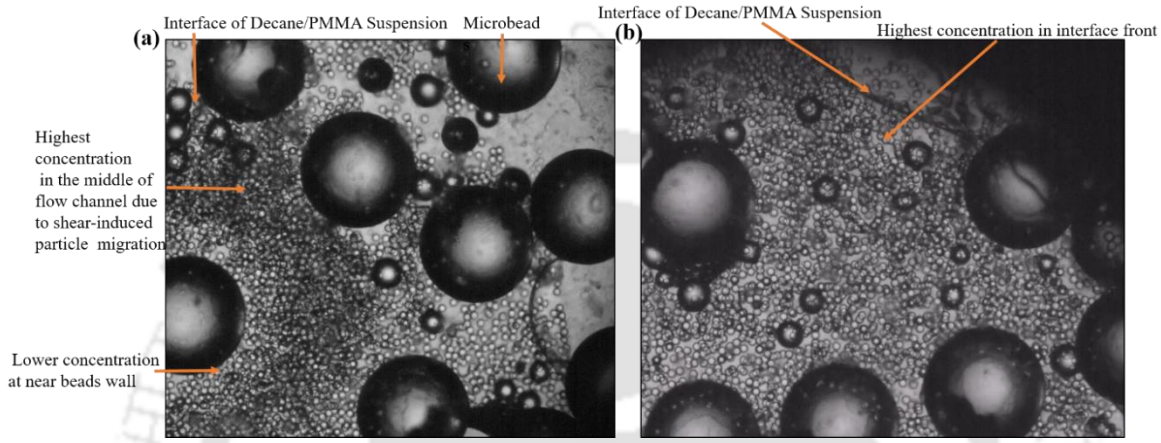

Figure 7. 11 Multiphase flow by displacing the 5 wt. % suspension by n-decane, (a) showing the highest particle concentration in the middle of the flow channel due to shear-induced particle migration, and (b) interface tracking of n-decane/PMMA suspension.

To further characterize the dense suspension displacement through the heterogeneous porous medium the interface is tracked, and velocity magnitude profiles/maps are plotted with time. It is observed that initially (t = 0 sec) the interface was at a fixed position and not moving (Figure 7.12a). But with time (t = 4.16 sec) as the interface starts to move due to injection of n-decane, the highest velocity is observed at the interface (figure 7.12b). This high velocity is observed in the center of the flow channel in the porous medium because of particles migrating from the high shear region to the low shear region in the channel center. Ahead of the interface, the velocity decreases, and in open pore bodies, velocity gradually decreases to a low value. The velocity magnitude is observed to be high at the small constriction in the porous medium

(Figure 7.12b, 7.12c, 7.12d, 7.12e, and 7.12f). The heterogeneity in the porous medium results in due to geometric factor (a pore throat-to-particle diameter ratio) resulting in particle trapping. The phenomena of particle cluster formation, particle bridging, and trapping are observed for suspension (5 wt.% PMMA particles) flow through a heterogeneous porous medium, resulting in no invasive flow through small pore constriction and throats (Figure 7.13a, 7.13b).

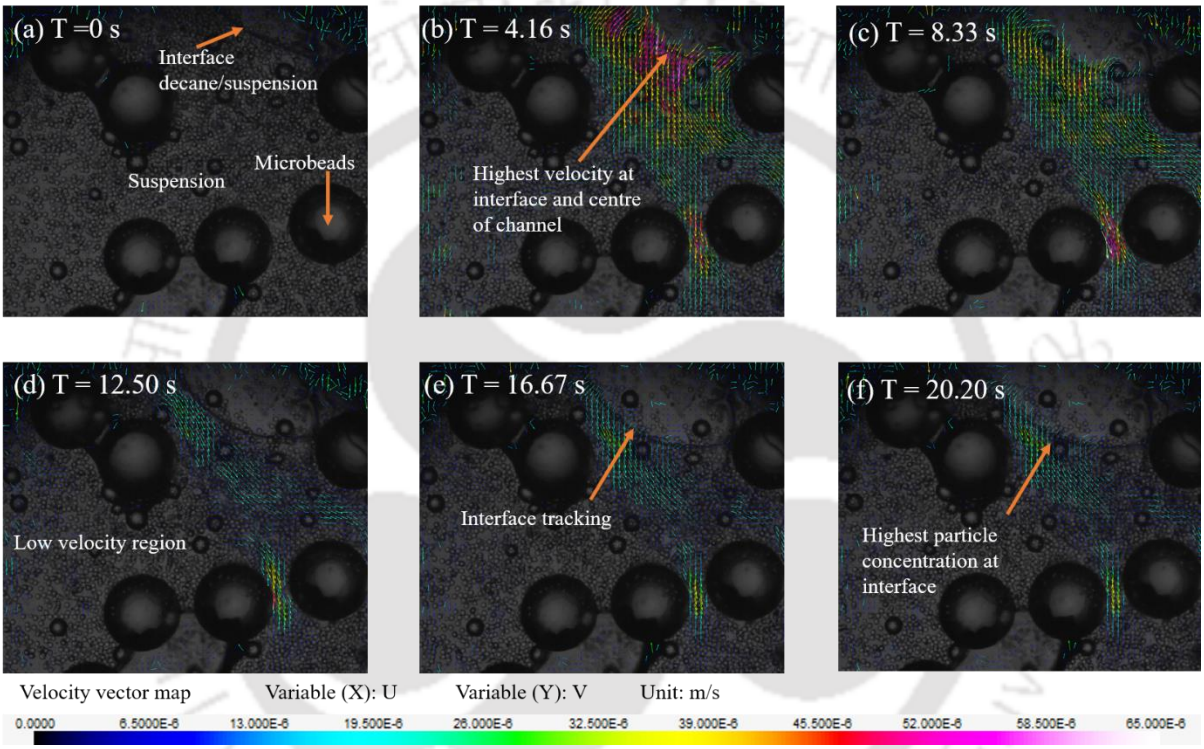

Figure 7. 12 Velocity vector field of Multiphase flow by displacing 5 wt. % suspension by n-decane.

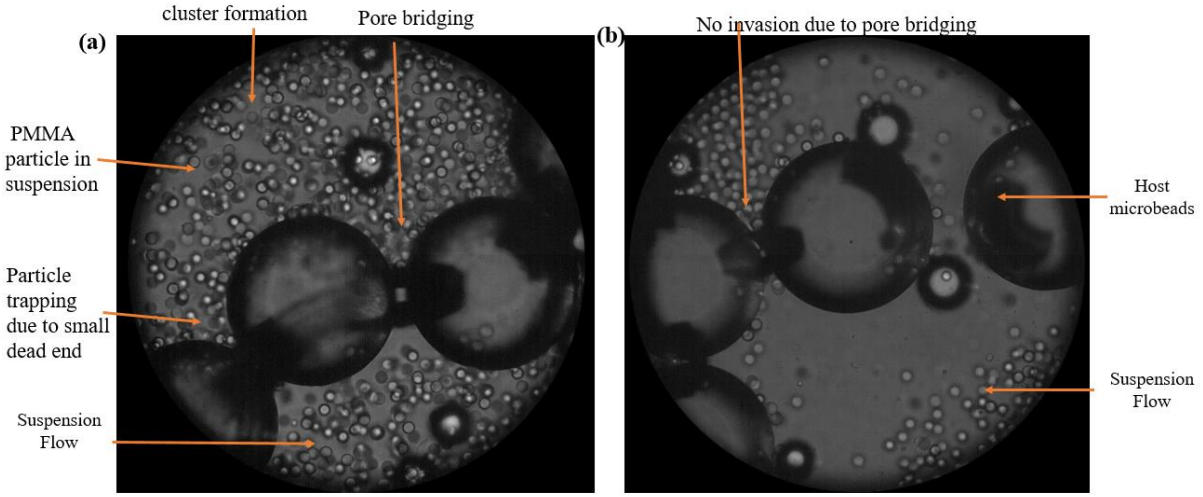

Figure 7. 13 displacement of suspension through the porous medium using n-decane, (a), (b) cluster formation, and pore bridging prevent the suspension flow through the pore throat.

7.5 Summary

Suspension flow through homogeneous, heterogeneous, and fractured porous mediums is studied using micro-particle image velocimetry. Suspension of low (2.5 wt.% particles) to high concentration (20 wt.% of particles) is injected into the porous medium to visualize and quantify suspension flow behavior in different types of the porous medium. It is observed that the concentrated suspension flow results in particle cluster formation, whereas dilute suspension (2.5 wt.% particles) shows cluster-free flow. The initial location of the mobile particle strongly influences the particle trajectories. When the particle is flowing from near the wall of the cylinder, the retention time significantly increases because of the highly tortuous path. Single particle dynamics is validated with the numerical simulations using coupling laminar flow and particle tracing. Symmetrical flow around the micro-cylinders and wavy flow are also observed during concentrated (20 wt.%) suspension flow in the porous medium. Significant velocity fluctuations are observed in the case of low concentration (2.5 wt.%) suspension flow. During suspension flow in the fractured medium, the maximum velocity is

observed at the fracture center, whereas the minimum velocity is in the semi-stagnant zones. The velocity is almost double in the fracture compared to the porous medium. The concentration profile showed that shear-induced particle migration is observed in the fractured medium because the particles experience high shear at the cylinder wall resulting in particle movement towards the center of the fractures where the shear is small. During multiphase flow, the phenomena of pore bridging, trapping, and shear-induced particle migration are also observed, which affect the displacement behavior in the heterogeneous porous medium.

Chapter 8. Conclusion and future directions

This chapter summarizes the overall conclusion drawn from the research work conducted in this dissertation. Furthermore, this chapter entails the scope of future research on the relevant area.

The content of the thesis dealt with pore-scale flow dynamics and displacement mechanisms during different chemical flooding processes both at the micro and macro-scale. Two-phase flow has been studied using micro-particle image velocimetry and fluorescence microscopy in porous micromodels. Pore-scale phenomena such as Haines jump, shear-induced circulations, fluctuating flow, and viscous fingering are investigated during immiscible two-phase flow and chemical flooding. The effect of different parameters such as interfacial tension, wettability, in-situ emulsification, and heterogeneity on trapping and mobilization of oil through a porous medium during different chemical floodings (low salinity water, polymer, alkaline, alkali polymer, alkali-surfactant-polymer flooding, and silica nanofluid flooding) have been investigated. The suspension flow behavior has been studied to investigate particle migration and trapping in the porous medium. Two-phase flow through complex pores has been studied to understand the displacement mechanisms and parameters affecting oil recovery. The major conclusions drawn from each part of the study are summarized as follows:

Silica nanoparticles in alkaline solution significantly affect the oil recovery by in-situ emulsification, IFT reduction, and wettability alteration. The dynamic IFT is reduced to a value of 0.01 mN/m, and the contact angle is reduced to 22° using silica nanofluid. The drainage and imbibition experiments are conducted using an alkaline and silica nanoparticle-assisted alkaline solution to understand their interaction with the crude oil. During drainage experiments, viscous instability is observed due to the unfavorable mobility ratio, resulting in

a large quantity of oil remaining trapped in the small pore constrictions. During the imbibition experiment, the alkaline solution interacts with the crude oil and forms a water/oil emulsion. The emulsion has a higher viscosity which significantly reduces the viscous fingering. The interaction of alkaline solution and crude oil in the porous medium disintegrates the continuous oil into several large droplets, which causes unsteady flow behaviour in the medium. However, diverging, converging, and stagnation zones are visualized, but these are not periodic. Imbibition experiment is also conducted using silica nanofluid. Crude oil interacts with the silica nanofluid, and a stable micro-emulsion is formed in the porous medium, resulting in a regular piston-like displacement and improving the sweep efficiency by preventing viscous instability.

To gain a fundamental understanding of flow dynamics and pore-scale phenomena in the heterogeneous porous medium, immiscible two-phase flow experiments are conducted in a bead-based porous micromodel. A significant amount of the non-wetting phase is trapped (due to viscous instability) within the small pore constrictions in the form of droplets and ganglia after water flooding. The phenomena of shear-induced circulation is observed in the trapped non-wetting phase due to partial momentum transfer by the displacing phase. These phenomena (shear-induced circulations and viscous fingering) are undesirable and result in unsteady flow behavior in the porous medium. The reason for unsteady flow behavior is the disintegration or integration of droplets from the ganglia. These disintegrated droplets move through the porous medium and cause flow direction reversal of trapped ganglia. To understand the effect of the flow rate, it is increased to displace the trapped fluid from the porous medium. However, it only increases the intensity of recirculation in the trapped ganglia. Increasing both the flow rate and viscosity of displacing phase results in the significant recovery of trapped fluid from the porous medium. It is observed that even at higher viscosity and flow rates of displacing phase,

the heterogeneous micromodel causes excessive trapping and minimum mobilization of the trapped non-wetting phase compared to the homogeneous micro model.

The effect of flow rate, viscosity ratio, interfacial tension, wettability alteration, and geometric ratio have been investigated on the trapped oil recovery from complex pores. Numerical simulation results show that the oil recovery will be the highest from the dead-ends at a critical contact angle (30°). It is difficult to displace the oil from the dead-ends compared to the contraction-expansion pores. A significant amount of oil (61.23%) remained trapped after water flooding in the dead-end at a lower contact angle (45°). However, complete displacement of oil is observed from the contraction-expansion pore at the same contact angle. The change in viscosity ratio (0.09 to 10.65) does not significantly affect oil recovery (1% - 2.8%) in both complex pores. No significant change in oil recovery with IFT is observed in contraction-expansion pores. Higher injection velocity poses a high shear and drags force to remove the trapped fluid from the dead-ends, leading to additional oil recovery of 14.9% at a water injection velocity of 0.01 m/s. However, decreasing the injection velocity results increase in oil recovery of 12.1% from the contraction expansion pore. Increasing dead-end depth causes a reduction in the oil recovery. However, decreasing the contact angle helps in the almost complete displacement of oil from the dead-end.

Chemical flooding (Low salinity water, Polymer, Alkali-Polymer) is performed to understand the flow behavior, such as displacement mechanisms and oil recovery. During low salinity water flooding, viscous instability, inconsistent velocity magnitude, and unsteady flow behavior are visualized in the porous medium. A significant amount of oil (47.81%) remained trapped after LSW flooding in the porous micro model. The polymer solution followed the same preferential flow path generated by LSW flooding, leading to no significant change (2.54%) in the trapped fluid saturation. Oil recovery significantly increased due to in-situ

emulsion formation at higher flow rates during Alkali polymer and ASP flooding. Alkali-polymer and ASP solution cause a significant improvement in wettability by reducing the contact angle to 39.3° and 32.37°, respectively. The core flooding analysis showed that the low salinity water (LSW) flooding, polymer flooding, alkali-polymer flooding, and ASP flooding recovered 48.04 %, 8.59 %, 3.90 %, and 14.84 % of heavy oil with an overall recovery of 75.37 %. The separate injection of ASP solution results in an oil recovery of 66.40%.

Suspension flow through the porous medium has been studied to understand the effect of particle concentration on flow behaviour. Concentrated suspension results in cluster formation, whereas diluted suspension (2.5 wt.% particles) shows cluster-free flow in the porous medium. Single particle dynamics showed hydrodynamic and non-hydrodynamic forces significantly influence particle trajectories. The particle trajectories are strongly influenced by the initial location of the mobile particle. When the particle is flowing from near the wall of the cylinder. The retention time will significantly increase because of the highly tortuous path. In case of concentrated (20 wt.%) suspension flow, temporally consistent high-velocity magnitude, symmetrical flow around the micro-cylinders, and wavy flow are observed in the porous medium. Significant velocity fluctuations, temporally inconsistent velocity magnitude and no symmetry in flow around the micro-cylinders are observed in the case of 2.5 wt.% suspension flow. The maximum velocity is observed at the fracture center, whereas the minimum velocity is in semi-stagnant zones of the porous medium. Shear-induced particle migration is observed in the straight fracture of the porous medium because the particles experience high shear at the cylinder wall. Therefore, the particles move toward the center of the fracture (low shear region). The phenomena of pore bridging, trapping, and shear-induced particle migration are also observed during multiphase flow in the heterogeneous porous medium. Our study provides an understanding of the transport of fine particles in porous media.

There are several pieces of work that can be undertaken as the continuation of the current research work. The effect of the injection and production patterns (such as five spot, seven spot) need to be understood to investigate the displacement efficiency. The temperature and pressure significantly affect the displacement process and fluid flow dynamics, which need to be understood. Monodisperse suspension flow behavior through a porous medium has been investigated in the current study. However, bidisperse and polydisperse suspension flow through a porous medium is not completely understood. Multiphase flow behavior using polydisperse suspension is critical to investigate as it replicated the flow of real reservoir fluid through the porous medium. Except for the experimental work, numerical simulations of polydisperse suspension flow in the heterogeneous porous medium need to be understood. For this purpose, Lattice Boltzmann Method (LBM), Discrete Element Method (DEM), and Immersed Moving Boundary (IMB) in coupling can be utilized.

Publications

Journal Publications

1. Sharma, V.K., Bhowmik, R., Tiwari, P. and Singh, A., 2022. Pore-scale investigation of immiscible fluid displacement process in randomly distributed bead-based porous micromodels using Micro-PIV. Journal of Petroleum Science and Engineering 212: 110301.
2. Sharma, V.K., Tiwari, P. and Singh, A., 2021. Micro-particle Image Velocimetry Measurements of Pore-Scale Velocity Field during Nanoparticle-Assisted Alkaline Flooding. Energy & Fuels, 35(16): 12957-12973.
3. Sharma, V.K., Tiwari, P. and Singh, A., 2023. An experimental study of pore-scale flow dynamics and heavy oil recovery using low saline water and chemical flooding. Fuel 334: 126756.

Manuscript under preparation

1. Sharma, V.K., Tiwari, P. and Singh, A. "A Review of Multiphase Flow Visualization in Porous Micromodels."
2. Sharma, V.K., Gupta, R., Tiwari, P. and Singh, A. “Numerical simulations of immiscible fluid displacement through complex pores”.
3. Sharma, V.K., Gupta, S., Tiwari, P. and Singh, A. “An experimental investigation of suspension transport through a porous medium.”

Conference Presentation

1. Sharma, V.K., Gupta, S., Tiwari, P., Singh, A., “Experimental investigation of suspension transport through porous medium” FMFP-2022, Indian Institute of Technology, Roorkee, India, 2022.

2. Sharma, V.K., Tiwari, P., Singh, A., and Gupta, R., "Numerical simulations of two-phase flow in complex pores (dead-ends) using Phase field method" CompFlu-2022, Indian Institute of Technology, Kharagpur, India, 2022.
3. Sharma, V.K., Tiwari, P., Singh, A., "Challenges in Multiphase flow measurement in porous micromodels using Micro-Particle image velocimetry," CHEMCON-2021, Institute of Minerals and Materials Technology, Bhubaneshwar, India, 2021.
4. Sharma, V.K., Tiwari, P., Singh, A., "Comparative study of nanoparticles for Enhanced Oil Recovery in micromodels," COMPFLU, IISER Bhopal, India, 2019.
5. Sharma, V.K., Tiwari, P., Singh, A., "Experimental investigation of the role of nanoparticles in interfacial tension reduction, wettability alteration, and rheology modification," NCUPE, IIT Guwahati, India, 2019.
6. Sharma, V.K., Tiwari, P., Singh, A., "Microscopic study of nanoparticles assisted alkaline flooding (NAAF)," Reflux 7.0, IIT Guwahati, India, 2019.
7. Sharma, V.K., Tiwari, P., Singh, A., "Silica nanoparticle suspended inorganic alkaline flooding for enhanced oil recovery," Research Conclave, IIT Guwahati, India, 2019.
8. Sharma, V.K., Haque, N., Singh, A., "Experimental study of alkaline flooding in porous micromodels," COMPFLU, IIT Roorkee, India, 2018.

References

[1] Kalita P, Sharma V, Pandey L, Tiwari P. Secondary and Tertiary Oil Recovery Processes. Microbial Enhanced Oil Recovery. Springer; 2022, p. 23-50.

[2] Ge J, Zhang X, Le-Hussain F. Fines migration and mineral reactions as a mechanism for CO2 residual trapping during CO2 sequestration. Energy 2022;239:122233.

[3] Jung J, Jang J, Santamarina J, Tsouris C, Phelps T, Rawn C. Gas production from hydrate-bearing sediments: the role of fine particles. Energy & fuels 2012;26(1):480-7.

[4] Muecke TW. Formation fines and factors controlling their movement in porous media. Journal of petroleum technology 1979;31(02):144-50.

[5] You Z, Bedrikovetsky P, Badalyan A, Hand M. Particle mobilization in porous media: temperature effects on competing electrostatic and drag forces. Geophysical Research Letters 2015;42(8):2852-60.

[6] Song W, Jinzhou Z, Yongming L. Hydraulic fracturing simulation of complex fractures growth in naturally fractured shale gas reservoir. Arabian Journal for Science and Engineering 2014;39(10):7411-9.

[7] Zarikos I, Terzis A, Hassanizadeh S, Weigand B. Velocity distributions in trapped and mobilized non-wetting phase ganglia in porous media. Scientific reports 2018;8(1):1-11.

[8] de Winter D, Weishaupt K, Scheller S, Frey S, Raoof A, Hassanizadeh S, et al. The Complexity of Porous Media Flow Characterized in a Microfluidic Model Based on Confocal Laser Scanning Microscopy and Micro-PIV. Transport in Porous Media 2020:136: 343-367

[9] Ekanem EM, Berg S, De S, Fadili A, Bultreys T, Rücker M, et al. Signature of elastic turbulence of viscoelastic fluid flow in a single pore throat. Physical Review E 2020;101(4):042605.

[10] Breuer KS. Microscale diagnostic techniques. New York: Springer; 2005.

[11] Mielnik MM, Saetran LR. Micro particle image velocimetry—an overview. Turbulence 2004;10:83-90.

[12] Song X, Gu M, Cao L, Tang Z, Xu C. A microparticle image velocimetry based on light field imaging. IEEE Sensors Journal 2019;19(21):9806-17.

[13] Heshmati M, Piri M. Interfacial boundary conditions and residual trapping: A pore-scale investigation of the effects of wetting phase flow rate and viscosity using micro-particle image velocimetry. Fuel 2018;224:560-78.

[14] Oughanem R, Youssef S, Bauer D, Peysson Y, Maire E, Vizika O. A multi-scale investigation of pore structure impact on the mobilization of trapped oil by surfactant injection. Transport in porous media 2015;109(3):673-92.

[15] Saha R, Uppaluri RV, Tiwari P. Silica nanoparticle assisted polymer flooding of heavy crude oil: emulsification, rheology, and wettability alteration characteristics. Industrial & Engineering Chemistry Research 2018;57(18):6364-76.

[16] Liu Z, Li Y, Luan H, Gao W, Guo Y, Chen Y. Pore scale and macroscopic visual displacement of oil-in-water emulsions for enhanced oil recovery. Chemical Engineering Science 2019;197:404-14.

[17] Maghzi A, Mohebbi A, Kharrat R, Ghazanfari MH. Pore-scale monitoring of wettability alteration by silica nanoparticles during polymer flooding to heavy oil in a five-spot glass micromodel. Transport in porous media 2011;87:653-64.

[18] Hilfer R, Øren P. Dimensional analysis of pore scale and field scale immiscible displacement. Transport in Porous Media 1996;22(1):53-72.

[19] Zhang C, Oostrom M, Wietsma TW, Grate JW, Warner MG. Influence of viscous and capillary forces on immiscible fluid displacement: Pore-scale experimental study in a

water-wet micromodel demonstrating viscous and capillary fingering. Energy & Fuels 2011;25(8):3493-505.

[20] Edery Y, Berg S, Weitz D. Surfactant variations in porous media localize capillary instabilities during haines jumps. Physical review letters 2018;120(2):028005.

[21] Follesø H. Fluid displacements during multiphase flow visualized at the pore scale using micromodels. Master Thesis, University of Bergen, Bergen. 2012.

[22] Sharma VK, Bhowmik R, Tiwari P, Singh A. Pore-scale investigation of immiscible fluid displacement process in randomly distributed bead-based porous micromodels using Micro-PIV. Journal of Petroleum Science and Engineering 2022;212:110301.

[23] Datta SS, Dupin J-B, Weitz DA. Fluid breakup during simultaneous two-phase flow through a three-dimensional porous medium. Physics of Fluids 2014;26(6):062004.

[24] Datta SS, Ramakrishnan T, Weitz DA. Mobilization of a trapped non-wetting fluid from a three-dimensional porous medium. Physics of Fluids 2014;26(2):022002.

[25] Krummel AT, Datta SS, Münster S, Weitz DA. Visualizing multiphase flow and trapped fluid configurations in a model three-dimensional porous medium. AIChE Journal 2013;59(3):1022-9.

[26] Sharma VK, Singh A, Tiwari P. An experimental study of pore-scale flow dynamics and heavy oil recovery using low saline water and chemical flooding. Fuel 2023;334:126756.

[27] Broens M, Unsal E. Emulsification kinetics during quasi-miscible flow in dead-end pores. Advances in Water Resources 2018;113:13-22.

[28] Unsal E, Broens M, Armstrong RT. Pore scale dynamics of microemulsion formation. Langmuir 2016;32(28):7096-108.

[29] Jafari I, Rokhforouz M-R. Numerical modeling of water oil two-phase flow during counter-current spontaneous imbibition in porous media at pore-scale. Petroleum Science and Technology 2020;38(24):1040-53.

[30] Zhu Z, Liu J, Liu H, Wu M, Song Z. Numerical investigation of single-and two-phase flow in porous media with a bifurcated fracture. Physics of Fluids 2021;33(5):052117.

[31] Roman S, Soulaine C, Kovscek AR. Pore-scale visualization and characterization of viscous dissipation in porous media. Journal of colloid and interface science 2020;558:269-79.

[32] Xia T, Feng Q, Wang S, Shu Q, Zhang Y, Sun Y. A numerical study of particle migration in porous media during produced water reinjection. Journal of Energy Resources Technology 2022;144(7):073002.

[33] Hendraningrat L, Li S, Torsæter O. A coreflood investigation of nanofluid enhanced oil recovery. Journal of Petroleum Science and Engineering 2013;111:128-38.

[34] De N, Singh A. Numerical simulation of particle migration in suspension flow through heterogeneous porous media. Particulate Science and Technology 2021;39(1):19-31.

[35] Yousif OS, Karakouzian M, Rahim NO, Rashed KA. Physical clogging of uniformly graded porous media under constant flow rates. Transport in porous media 2017;120(3):643-59.

[36] Zhou K, Hou J, Sun Q, Guo L, Bing S, Du Q, et al. A study on particle suspension flow and permeability impairment in porous media using LBM–DEM–IMB simulation method. Transport in Porous Media 2018;124(3):681-98.

[37] Feia S, Dupla JC, Ghabezloo S, Sulem J, Canou J, Onaisi A, et al. Experimental investigation of particle suspension injection and permeability impairment in porous media. Geomechanics for Energy and the Environment 2015;3:24-39.

[38] Jung J, Cao SC, Shin Y-H, Al-Raoush RI, Alshibli K, Choi J-W. A microfluidic pore model to study the migration of fine particles in single-phase and multi-phase flows in porous media. Microsystem Technologies 2018;24(2):1071-80.

[39] Liu Q, Zhao B, Santamarina JC. Particle migration and clogging in porous media: a convergent flow microfluidics study. Journal of Geophysical Research: Solid Earth 2019;124(9):9495-504.

[40] Yang Y, Yuan W, Hou J, You Z. Review on physical and chemical factors affecting fines migration in porous media. Water Research 2022;214:118172.

[41] Chatenever A, Calhoun JC. Visual examinations of fluid behavior in porous media-part i. Journal of Petroleum Technology 1952;4(06):149-56.

[42] Karadimitriou N, Hassanizadeh S. A review of micromodels and their use in two-phase flow studies. Vadose Zone Journal 2012; 11(3): 1-21

[43] Gong H, Li Y, Dong M, Ma S, Liu W. Effect of wettability alteration on enhanced heavy oil recovery by alkaline flooding. Colloids and Surfaces A: Physicochemical and Engineering Aspects 2016;488:28-35.

[44] Sharma VK, Tiwari P, Singh A. Micro-particle Image Velocimetry Measurements of Pore-Scale Velocity Field during Nanoparticle-Assisted Alkaline Flooding. Energy & Fuels 2021;35(16):12957-73.

[45] Gunda NS, Bera B, Karadimitriou NK, Mitra SK, Hassanizadeh SM. Reservoir-on-a-chip (ROC): a new paradigm in reservoir engineering. Lab Chip 2011;11(22):3785-92.

[46] Jahanbakhsh A, Wlodarczyk KL, Hand DP, Maier RR, Maroto-Valer MM. Review of Microfluidic Devices and Imaging Techniques for Fluid Flow Study in Porous Geomaterials. Sensors 2020;20(14):4030.

[47] Lake M, Narciso C, Cowdrick K, Storey T, Zhang S, Zartman J, et al. Microfluidic device design, fabrication, and testing protocols. Protoc Exch 2015;10(10.1038).

[48] Yun W, Ross CM, Roman S, Kovscek AR. Creation of a dual-porosity and dual-depth micromodel for the study of multiphase flow in complex porous media. Lab on a Chip 2017;17(8):1462-74.

[49] Dimou AP, Menke HP, Maes J. Benchmarking the viability of 3D printed micromodels for single phase flow using Particle Image Velocimetry and Direct Numerical Simulations. Transport in Porous Media 2022;141:279-294.

[50] Mohammadi S, Mahani H, Ayatollahi S, Niasar V. Impact of oil polarity on the mixing time at the pore scale in low salinity waterflooding. Energy & Fuels 2020;34(10):12247-59.

[51] Bartels W-B, Mahani H, Berg S, Menezes R, van der Hoeven JA, Fadili A. Oil configuration under high-salinity and low-salinity conditions at pore scale: a parametric investigation by use of a single-channel micromodel. Spe Journal 2017;22(05):1362-73.

[52] Ziaie B, Baldi A, Atashbar MZ. Introduction to micro-/nanofabrication. Springer handbook of nanotechnology. Springer; 2010, p. 231-69.

[53] Qin D, Xia Y, Whitesides GM. Soft lithography for micro- and nanoscale patterning. Nature Protocols 2010;5(3):491-502.

[54] Dijk P, Berkowitz B, Bendel P. Investigation of flow in water-saturated rock fractures using nuclear magnetic resonance imaging (NMRI). Water Resources Research 1999;35(2):347-60.

[55] Lebon L, Oger L, Leblond J, Hulin J, Martys N, Schwartz L. Pulsed gradient NMR measurements and numerical simulation of flow velocity distribution in sphere packings. Physics of Fluids 1996;8(2):293-301.

[56] Ogawa K, Matsuka T, Hirai S, Okazaki K. Three-dimensional velocity measurement of complex interstitial flows through water-saturated porous media by the tagging method in the MRI technique. Measurement Science and technology 2001;12(2):172.

[57] Berg S, Ott H, Klapp SA, Schwing A, Neiteler R, Brussee N, et al. Real-time 3D imaging of Haines jumps in porous media flow. Proceedings of the National Academy of Sciences 2013;110(10):3755-9.

[58] Kim GB, Lee SJ. X-ray PIV measurements of blood flows without tracer particles. Experiments in Fluids 2006;41(2):195-200.

[59] Liu D, Garimella SV, Wereley ST. Infrared micro-particle image velocimetry in silicon-based microdevices. Experiments in fluids 2005;38(3):385-92.

[60] Johnston W, Dybbs A, Edwards R. Measurement of fluid velocity inside porous media with a laser anemometer. The Physics of fluids 1975;18(7):913-4.

[61] Sinton D. Microscale flow visualization. Microfluidics and Nanofluidics 2004;1(1):2-21.

[62] Huang AY, Huang MY, Capart H, Chen R-H. Optical measurements of pore geometry and fluid velocity in a bed of irregularly packed spheres. Experiments in Fluids 2008;45(2):309-21.

[63] Kazemifar F, Blois G, Kyritsis DC, Christensen KT. A methodology for velocity field measurement in multiphase high-pressure flow of CO2 and water in micromodels. Water Resources Research 2015;51:3017-29.

[64] Lu X, Zhao Y, Dennis DJ. Flow measurements in microporous media using micro-particle image velocimetry. Physical Review Fluids 2018;3:104202.

[65] Roman S, Soulaine C, AlSaud MA, Kovscek A, Tchelepi H. Particle velocimetry analysis of immiscible two-phase flow in micromodels. Advances in Water Resources 2016;95:199-211.

[66] Wereley ST, Meinhart CD. Recent Advances in Micro-Particle Image Velocimetry. Annual Review of Fluid Mechanics 2010;42(1):557-76.

[67] Wiederseiner S, Andreini N, Epely-Chauvin G, Ancey C. Refractive-index and density matching in concentrated particle suspensions: a review. Experiments in fluids 2011;50(5):1183-206.

[68] Santiago JG, Wereley ST, Meinhart CD, Beebe D, Adrian RJ. A particle image velocimetry system for microfluidics. Experiments in fluids 1998;25(4):316-9.

[69] Haque N, Singh A, Saha UK. Experimental Visualization and Analysis of Multiphase Immiscible Flow in Fractured Micromodels Using Micro-Particle Image Velocimetry. Journal of Energy Resources Technology 2021;144(2):024501.

[70] Lindken R, Rossi M, Große S, Westerweel J. Micro-particle image velocimetry (μPIV): recent developments, applications, and guidelines. Lab on a Chip 2009;9:2551-67.

[71] Wereley ST, Gui L, Meinhart C. Advanced algorithms for microscale particle image velocimetry. AIAA journal 2002;40(6):1047-55.

[72] Blois G, Barros JM, Christensen KT. PIV investigation of two-phase flow in a micro-pillar microfluidic device. *10th International Symposium on Particle Image Velocimetry* 2013.

[73] Blois G, Barros JM, Christensen KT. A microscopic particle image velocimetry method for studying the dynamics of immiscible liquid–liquid interactions in a porous micromodel. Microfluidics and Nanofluidics 2015;18:1391-406.

[74] Saha R, Uppaluri RV, Tiwari P. Influence of emulsification, interfacial tension, wettability alteration and saponification on residual oil recovery by alkali flooding. Journal of industrial and engineering chemistry 2018;59:286-96.

[75] Dong M, Liu Q, Li A. Displacement mechanisms of enhanced heavy oil recovery by alkaline flooding in a micromodel. Particuology 2012;10(3):298-305.

[76] Pei H, Zhang G, Ge J, Jin L, Liu X. Analysis of Microscopic Displacement Mechanisms of Alkaline Flooding for Enhanced Heavy-Oil Recovery. Energy & Fuels 2011;25:4423-4429.

[77] Pei H, Zhang G, Ge J, Ma M, Zhang L, Liu Y. Improvement of Sweep Efficiency by Alkaline Flooding for Heavy Oil Reservoirs. Journal of Dispersion Science and Technology 2013;34:1548-56.

[78] Haines WB. Studies in the physical properties of soil. V. The hysteresis effect in capillary properties, and the modes of moisture distribution associated therewith. The Journal of Agricultural Science 1930;20(1):97-116.

[79] Moebius F, Or D. Interfacial jumps and pressure bursts during fluid displacement in interacting irregular capillaries. Journal of colloid and interface science 2012;377(1):406-15.

[80] Yuan H, Swanson B. Resolving pore-space characteristics by rate-controlled porosimetry. SPE Formation Evaluation 1989;4(01):17-24.

[81] Hlushkou D, Tallarek U. Transition from creeping via viscous-inertial to turbulent flow in fixed beds. Journal of Chromatography A 2006;1126(1-2):70-85.

[82] Kazemifar F, Blois G, Kyritsis DC, Christensen KT. Quantifying the flow dynamics of supercritical CO2–water displacement in a 2D porous micromodel using fluorescent microscopy and microscopic PIV. Advances in Water Resources 2016;95:352-68.

[83] Li Y, Kazemifar F, Blois G, Christensen KT. Micro-PIV measurements of multiphase flow of water and liquid/supercritical CO2 in 2D heterogeneous porous micromodels. *18th International Symposium on Applications of Laser and Imaging Techniques to Fluid Mechanics.* 2016.

[84] Jafari I, Masihi M, Nasiri Zarandi M. Experimental study on imbibition displacement mechanisms of two-phase fluid using micromodel: Fracture network, distribution of pore size, and matrix construction. Physics of Fluids 2017;29(12):122004.

[85] Zhu Z, Song Z, Shao Z, Wu M, Xu X. Simulation of imbibition in porous media with a tree-shaped fracture following the level-set method. Physics of Fluids 2021;33(8):082109.

[86] Pak T, Butler IB, Geiger S, Van Dijke MI, Sorbie KS. Droplet fragmentation: 3D imaging of a previously unidentified pore-scale process during multiphase flow in porous media. Proceedings of the National Academy of Sciences 2015;112(7):1947-52.

[87] Lenormand R. Liquids in porous media. Journal of Physics: Condensed Matter 1990;2(S):SA79.

[88] Alzahid YA, Aborshaid H, Asali M, McClure J, Chen C, Mostaghimi P, et al. Real-time synchrotron-based X-ray computed microtomography during in situ emulsification. Journal of Petroleum Science and Engineering 2020;195:107885.

[89] Gu Q, Zhu L, Zhang Y, Liu H. Pore-scale study of counter-current imbibition in strongly water-wet fractured porous media using lattice Boltzmann method. Physics of Fluids 2019;31(8):086602.

[90] Amiri HA, Hamouda AA. Pore-scale modeling of non-isothermal two phase flow in 2D porous media: Influences of viscosity, capillarity, wettability and heterogeneity. International Journal of Multiphase Flow 2014;61:14-27.

[91] Maaref S, Rokhforouz MR, Ayatollahi S. Numerical investigation of two phase flow in micromodel porous media: Effects of wettability, heterogeneity, and viscosity. The Canadian Journal of Chemical Engineering 2017;95(6):1213-23.

[92] Rokhforouz M, Akhlaghi Amiri H. Phase-field simulation of counter-current spontaneous imbibition in a fractured heterogeneous porous medium. Physics of Fluids 2017;29(6):062104.

[93] Saw RK, Mandal A. A mechanistic investigation of low salinity water flooding coupled with ion tuning for enhanced oil recovery. RSC advances 2020;10(69):42570-83.

[94] Mehranfar A, Ghazanfari MH. Investigation of the microscopic displacement mechanisms and macroscopic behavior of alkaline flooding at different wettability conditions in shaly glass micromodels. Journal of Petroleum Science and Engineering 2014;122:595-615.

[95] Strand S, Doust A, Puntervold T, Austad T. "Smart Water" as Wettability Modifier in Carbonate and Sandstone. *IOR 2009-15th European Symposium on Improved Oil Recovery*. European Association of Geoscientists & Engineers; 2009:cp-124-00040.

[96] Pei H, Zhang G, Ge J, Jin L, Ma C. Potential of alkaline flooding to enhance heavy oil recovery through water-in-oil emulsification. Fuel 2013;104:284-93.

[97] Lu X, Zhao Y, Dennis DJ. Fluid flow characterisation in randomly packed microscale porous beds with different sphere sizes using micro-particle image velocimetry. Experimental Thermal and Fluid Science 2020;118:110136.

[98] Sen D, Nobes DS, Mitra SK. Optical measurement of pore scale velocity field inside microporous media. Microfluidics and nanofluidics 2012;12:189-200.

[99] Armstrong RT, Georgiadis A, Ott H, Klemin D, Berg S. Critical capillary number: Desaturation studied with fast X-ray computed microtomography. Geophysical Research Letters 2014;41(1):55-60.

[100] Basirat F, Yang Z, Niemi A. Pore-scale modeling of wettability effects on CO2–brine displacement during geological storage. Advances in water resources 2017;109:181-95.

[101] Unsal E, Rücker M, Berg S, Bartels W-B, Bonnin A. Imaging of compositional gradients during in situ emulsification using X-ray micro-tomography. Journal of colloid and interface science 2019;550:159-69.

[102] Terzis A, Zarikos I, Weishaupt K, Yang G, Chu X, Helmig R, et al. Microscopic velocity field measurements inside a regular porous medium adjacent to a low Reynolds number channel flow. Physics of Fluids 2019;31(4):042001.

[103] Perrin C, Sorbie K, Tardy P, Crawshaw J. Micro-PIV–A New Technology for Pore Scale Flow Characterization in Micromodels (SPE94078). *67th EAGE Conference & Exhibition.* European Association of Geoscientists & Engineers; 2005:cp-1-00280.

[104] Zerai B, Saylor BZ, Kadambi JR, Oliver MJ, Mazaheri AR, Ahmadi G, et al. Flow characterization through a network cell using particle image velocimetry. Transport in porous media 2005;60(2):159-81.

[105] Gutiérrez J, Moura M, Carvalho M. Dynamics of viscoelastic flow through axisymmetric constricted microcapillary at high elasticity number. Journal of Non-Newtonian Fluid Mechanics 2020;286:104438.

[106] Li W, Nan Y, Wen X, Wang W, Jin Z. Effects of Salinity and N-, S-, and O-Bearing Polar Components on Light Oil–Brine Interfacial Properties from Molecular Perspectives. The Journal of Physical Chemistry C 2019;123(38):23520-23528.

[107] Parsa S, Santanach-Carreras E, Xiao L, Weitz DA. Origin of anomalous polymer-induced fluid displacement in porous media. Physical Review Fluids 2020;5(2):022001.

[108] Ott H, Kharrat A, Borji M, Arnold P. Fluid-phase topology of complex displacements in porous media. Physical Review Research 2020;2(2):023240.

[109] Ali JA, Kolo K, Manshad AK, Mohammadi AH. Recent advances in application of nanotechnology in chemical enhanced oil recovery: Effects of nanoparticles on wettability alteration, interfacial tension reduction, and flooding. Egyptian journal of petroleum 2018;27(10):1371-83.

[110] Rostami P, Sharifi M, Aminshahidy B, Fahimpour J. Enhanced oil recovery using silica nanoparticles in the presence of salts for wettability alteration. Journal of Dispersion Science and Technology 2020;41(3):402-13.

[111] Alvarado V, Manrique E. Enhanced oil recovery: an update review. Energies 2010;3(9):1529-75.

[112] Carcoana A. Enhanced Oil Recovery in Rumania. In: SPE Enhanced Oil Recovery Symposium, Tulsa. Oklahoma Publishing; 1982.

[113] Carcoana A. Applied enhanced oil recovery. Richardson, TX (United States); Society of Petroleum Engineers; 1992.

[114] Li Y, Kazemifar F, Blois G, Christensen KT. Micro-PIV measurements of multiphase flow of water and liquid CO2 in 2-D heterogeneous porous micromodels. Water Resources Research 2017;53(7):6178-96.

[115] Elyaderani SMG, Jafari A. Microfluidics experimental study in porous media applied for nanosilica/alkaline flooding. Journal of Petroleum Science and Engineering 2019;173:1289-303.

[116] Mohammadi M, Khorrami MK, Vatani A, Ghasemzadeh H, Vatanparast H, Bahramian A. Rapid determination and classification of crude oils by ATR-FTIR spectroscopy and chemometric methods. Spectrochimica Acta Part A: Molecular and Biomolecular Spectroscopy 2020;232:118157.

[117] Chen Z, Zhao X, Wang Z, Fu M. A comparative study of inorganic alkaline/polymer flooding and organic alkaline/polymer flooding for enhanced heavy oil recovery. Colloids and Surfaces A: Physicochemical and Engineering Aspects 2015;469:150-7.

[118] Pei H, Zhang G, Ge J, Jin L. The Effect of Oil Viscosity, Permeability, and Residual Oil Saturation on the Performance of Alkaline Flooding in the Recovery of Heavy Oil. Energy Sources, Part A: Recovery, Utilization, and Environmental Effects 2012;34(8):702-10.

[119] Pei H, Zhang G, Ge J, Tang M, Zheng Y. Comparative Effectiveness of Alkaline Flooding and Alkaline–Surfactant Flooding for Improved Heavy-Oil Recovery. Energy & Fuels 2012;26(5):2911-9.

[120] Pei H, Zhang G, Ge J, Zhang L, Wang H. Effect of polymer on the interaction of alkali with heavy oil and its use in improving oil recovery. Colloids and Surfaces A: Physicochemical and Engineering Aspects 2014;446:57-64.

[121] Sedaghat MH, Ahadi A, Kordnejad M, Borazjani Z. Aspects of alkaline flooding: oil recovery improvement and displacement mechanisms. Middle East J Sci Res 2013;18:258-63.

[122] Tang M, Zhang G, Ge J, Jiang P, Liu Q, Pei H, et al. Investigation into the mechanisms of heavy oil recovery by novel alkaline flooding. Colloids and Surfaces A: Physicochemical and Engineering Aspects 2013;421:91-100.

[123] Du Y, Zhang G, Ge J, Li G, Feng A. Influence of Oil Viscosity on Alkaline Flooding for Enhanced Heavy Oil Recovery. Journal of Chemistry 2013;2013:1-8.

[124] Sedaghat M, Mohammadzadeh O, Kord S, Chatzis I. Heavy oil recovery using ASP flooding: A pore-level experimental study in fractured five-spot micromodels. The Canadian Journal of Chemical Engineering 2016;94(4):779-91.

[125] Kumar N, Mandal A. Wettability alteration of sandstone rock by surfactant stabilized nanoemulsion for enhanced oil recovery—A mechanistic study. Colloids and Surfaces A: Physicochemical and Engineering Aspects 2020;601:125043.

[126] Raeini AQ, Blunt MJ, Bijeljic B. Modelling two-phase flow in porous media at the pore scale using the volume-of-fluid method. Journal of Computational Physics 2012;231(17):5653-68.

[127] Ambekar AS, Mattey P, Buwa VV. Pore-resolved two-phase flow in a pseudo-3D porous medium: Measurements and volume-of-fluid simulations. Chemical Engineering Science 2021;230:116128.

[128] Amiri HA, Hamouda AA. Evaluation of level set and phase field methods in modeling two phase flow with viscosity contrast through dual-permeability porous medium. International Journal of Multiphase Flow 2013;52:22-34.

[129] Hunter R. In RJ Hunter (Ed.), Foundations of colloid science. Oxford; 2001

[130] Papamichos E, Vardoulakis I, Tronvoll J, Skjaerstein A. Volumetric sand production model and experiment. International journal for numerical and analytical methods in geomechanics 2001;25(8):789-808.

[131] Anbari A, Chien HT, Datta SS, Deng W, Weitz DA, Fan J. Microfluidic model porous media: fabrication and applications. Small 2018;14(18):1703575.

[132] Lifton VA. Microfluidics: an enabling screening technology for enhanced oil recovery (EOR). Lab on a Chip 2016;16(10):1777-96.

[133] Auset M, Keller AA. Pore-scale processes that control dispersion of colloids in saturated porous media. Water resources research 2004;40(3); 1-13.

[134] Lei W, Li Q, Yang H-E, Wu T-J, Wei J, Wang M. Preferential flow control in heterogeneous porous media by concentration-manipulated rheology of microgel particle suspension. Journal of Petroleum Science and Engineering 2022;212:110275.

[135] VanNess K, Rasmuson A, Ron CA, Johnson WP. A unified force and torque balance for colloid transport: Predicting attachment and mobilization under favorable and unfavorable conditions. Langmuir 2019;35(27):9061-70.

[136] Benamar A, Ahfir N-D, Wang H, Alem A. Particle transport in a saturated porous medium: Pore structure effects. Comptes Rendus Geoscience 2007;339(10):674-81.

[137] De N, Singh A. Stokesian dynamics simulation of suspension flow in porous media. Transport in Porous Media 2020;131(2):473-502.

[138] Samanta A, Ojha K, Mandal A. Interactions between acidic crude oil and alkali and their effects on enhanced oil recovery. Energy & Fuels 2011;25(4):1642-9.

[139] Pauchard V, Sjöblom J, Kokal S, Bouriat P, Dicharry C, Müller H, et al. Role of naphthenic acids in emulsion tightness for a low-total-acid-number (TAN)/high-asphaltenes oil. Energy & fuels 2009;23(3):1269-79.

[140] Sabbagh R, Kazemi MA, Soltani H, Nobes DS. Micro-and Macro-Scale Measurement of Flow Velocity in Porous Media: A Shadow Imaging Approach for 2D and 3D. Optics 2020;1(1):71-87.

[141] Wang H, Wang P. An experimental investigation of the permeability in porous chip formed by micropost arrays based on microparticle image velocimetry and micromanometer measurements. Journal of Fluids Engineering 2017;139(2):021108.

[142] Ge J, Feng A, Zhang G, Jiang P, Pei H, Li R, et al. Study of the Factors Influencing Alkaline Flooding in Heavy-Oil Reservoirs. Energy & Fuels 2012;26:2875-82.

[143] Koh KS, Wong VL. Introductory Chapter: From Microemulsions to Nanoemulsions. Nanoemulsions: Properties, Fabrications and Applications. IntechOpen; 2019.

[144] Pal N, Mandal A. Oil recovery mechanisms of Pickering nanoemulsions stabilized by surfactant-polymer-nanoparticle assemblies: A versatile surface energies' approach. Fuel 2020;276:118138.

[145] Kumar N, Mandal A. Thermodynamic and physicochemical properties evaluation for formation and characterization of oil-in-water nanoemulsion. Journal of Molecular Liquids 2018;266:147-59.

[146] Maurya NK, Mandal A. Investigation of synergistic effect of nanoparticle and surfactant in macro emulsion based EOR application in oil reservoirs. Chemical Engineering Research and Design 2018;132:370-84.

[147] Berg S, Cense A, Hofman J, Smits R. Two-phase flow in porous media with slip boundary condition. Transport in porous media 2008;74(3):275-92.

[148] Berg S, van Wunnik J. Shear rate determination from pore-scale flow fields. Transport in Porous Media 2017;117(2):229-46.

[149] Lenormand R, Zarcone C, Sarr A. Mechanisms of the displacement of one fluid by another in a network of capillary ducts. J Fluid Mech 1983;135(34):337-53.

[150] Chen Y-F, Wu D-S, Fang S, Hu R. Experimental study on two-phase flow in rough fracture: Phase diagram and localized flow channel. International Journal of Heat and Mass Transfer 2018;122:1298-307.

[151] Patil SB, Dandekar AY, Patil S, Khataniar S. Low salinity brine injection for EOR on Alaska North Slope (ANS). *International Petroleum Technology Conference.* OnePetro; 2008.

[152] Sheng JJ. Modern chemical enhanced oil recovery: theory and practice. Gulf Professional Publishing; 2010.

[153] Saw RK, Pillai P, Mandal A. Synergistic effect of low saline ion tuned Sea Water with ionic liquids for enhanced oil recovery from carbonate reservoirs. Journal of Molecular Liquids 2022;364:120011.

[154] Pal N, Saxena N, Laxmi KD, Mandal A. Interfacial behaviour, wettability alteration and emulsification characteristics of a novel surfactant: Implications for enhanced oil recovery. Chemical Engineering Science 2018;187:200-12.

[155] Abdel-Wali A. Effect of simple polar compounds and salinity on interfacial tension and wettability of rock/oil/brine system. Journal of King Saud University-Engineering Sciences 1996;8(2):153-62.

[156] Al-Shalabi EW, Sepehrnoori K. A comprehensive review of low salinity/engineered water injections and their applications in sandstone and carbonate rocks. Journal of Petroleum Science and Engineering 2016;139:137-61.

[157] Mahmoudzadeh A, Fatemi M, Masihi M. Microfluidics experimental investigation of the mechanisms of enhanced oil recovery by low salinity water flooding in fractured porous media. Fuel 2022;314:123067.

[158] Shirazi M, Masihi M, Mahani H, Tamsilian Y. Impact of Temperature and Etching Methods on Surface Roughness, Topography, and Composition of Glass Micromodels. Energy & Fuels 2022;36(23):14066-78.

[159] Zhang Q, Wu J, Ma P, Cai J, Zhang Y. Acid value determination and pre-esterification of crude Euphorbia lathyris L. Oil. World Journal of Engineering and Technology 2015;3(02):70.

[160] Ahmed T. Reservoir engineering. Handbook(2nd ed) Houston, TX: Gulf Professional Publishing 2001.